The effects of radiation on ablative heat shields during atmospheric entry

THÈSE N^O 7681 (2017)

PRÉSENTÉE LE 2 JUIN 2017
À LA FACULTÉ DES SCIENCES ET TECHNIQUES DE L'INGÉNIEUR
GROUPE INTERDISCIPLINAIRE D'AERODYNAMIQUE
ET LABORATOIRE DE LA SCIENCE ET DE L'INGÉNIERIE DE L'ÉNERGIE RENOUVELABLE
PROGRAMME DOCTORAL EN ENERGIE

ÉCOLE POLYTECHNIQUE FÉDÉRALE DE LAUSANNE

POUR L'OBTENTION DU GRADE DE DOCTEUR ÈS SCIENCES

PAR

Nikhil BANERJI

acceptée sur proposition du jury:

Dr P. Ott, président du jury
Prof. S. Haussener, Dr P. Leyland, directrices de thèse
Prof. R. Morgan, rapporteur
Dr J. Barcena, rapporteur
Prof. A. Pautz, rapporteur

ÉCOLE POLYTECHNIQUE
FÉDÉRALE DE LAUSANNE

Suisse
2017

ABSTRACT

Spacecraft employ composite materials as Thermal Protection Systems (TPS) to survive entering a planetary atmosphere at hypersonic speeds. Under intense convective and radiative heating from the surrounding shock layer, these composites decompose and erode, transferring heat away from the payload. A risk-averse approach has long saturated the space industry, with the selection of unoptimised, dense, flight-qualified materials taking priority over novel TPS, tailored to the mission at hand. However, demanding flight trajectories and greater payload carrying capacity required on future missions call for contemporary research into lightweight composites. A better understanding of the high temperature response of these materials is needed to improve TPS sizing and optimisation. This thesis uses a combination of experimental testing and numerical simulations to understand the effects of thermal radiation on these composites, both inside the material and upon interacting with the surrounding aerothermal environment.

TPS material testing in arc-jets can be complemented by the use of impulse facilities to characterise flight-equivalent radiative heating in multiple atmospheres. Being a recent development, ablation testing in expansion tubes has so far used non-flight geometries and/or conditions. A methodology was therefore established to design and manufacture scaled composite aeroshells in the laboratory. The models were subjected to Earth and Venus hypersonic conditions and decomposed upon contact with the flow, allowing carbonaceous species to mix with the surrounding hot plasma. Radiation from the boundary layer was then measured using emission spectroscopy and compared to data collected from experiments using a cold steel model.

Computational fluid dynamics, finite-rate surface kinetics and radiation databases were then validated based on these spectral measurements. Results most suited for comparison with experimental data were mainly obtained using a combination of Park's reaction schemes, Suzuki's reduced nitridation surface kinetic rate and the NEQAIR radiation code for both flow conditions. Visible radiation was heavily underestimated by numerical models, while generated UV and IR spectra compared well with measurements. Two unique datasets for

Earth and Venus entry were thus created through experiment and numerical analysis.

The recent investigation into the volumetric nature of ablation makes understanding internal radiation of TPS materials a priority. This term is rarely included in contemporary thermal response codes. To accurately characterise effective morphological and radiative properties, pore-level simulations were carried out on real TPS material geometries, recorded using high-resolution synchrotron tomography. A library of spectrally resolved extinction and scattering coefficients and scattering phase functions was used to calculate macroscopic optical properties of a semi-infinite slab of each material. A greater increase in absorptance during resin decomposition was seen for the medium density carbon phenolic than for the dense graphite reinforced polymer composite. Combined with these properties, volumetric view factors were used to evaluate the radiative flux inside the TPS material, which was then supplied to the PATO thermal response code. Internal radiation was shown to have a demonstrable effect through the comparison of simulation and flight data, promoting its inclusion in future modelling.

Keywords : ablation, atmospheric entry, emission spectroscopy, impulse facilities, numerical simulations, radiation, thermal protection systems, X-ray computed tomography.

RESUMÉ

Lors d'une entrée atmosphérique mettant en jeu des vitesses hypersoniques, les sondes spatiales sont équipées de boucliers en composite de carbone, afin de protéger les charges utiles qu'elles transportent. Ces boucliers sont soumis à des flux de chaleur radiatif et convectif très élevés dus à la couche de choc rayonnante qui les entoure. La chaleur est évacuée grâce à la décomposition et l'érosion de ces matériaux composites. L'évolution de ces matériaux s'est effectué en réduisant les risques plutôt qu'en optimisant la masse. Une meilleure compréhension de ces matériaux et des phénomènes physico-chimiques est indispensable pour le développement de nouvelles protections thermiques plus légères et moins coûteuses. Cette thèse étudie de manière approfondie les effets du rayonnement sur ces matériaux ainsi que leurs interactions avec leur environnement aérothermique.

La réponse à haute température de ces matériaux est habituellement caractérisée par des essais à jet de plasma. Des informations complémentaires peuvent être déterminées par des essais dans des tubes à expansion. Ces expériences produisent des flux de chaleurs radiatifs similaires à ceux rencontrés en vol dans des atmosphères différentes. Jusqu'à ce jour, aucun essai n'a été effectué avec ce type de matériau dans des conditions de vol équivalents et avec une forme similaire à des sondes existantes. Par conséquent, une méthodologie a été établie pour la conception et la fabrication de modèles réduits ayant la forme d'une sonde. Ces modèles ont été testés dans des conditions de rentrée dans les atmosphères terrestre et vénusienne permettant la décomposition de leurs surfaces et le mélange des espèces carbonées avec le plasma dans la couche limite. Des mesures spectroscopiques ont été effectuées pour caractériser le rayonnement émit par la couche limite.

Les modèles numériques de mécanique des fluides, des réactions surfaciques et de rayonnement ont été validés par ces mesures spectroscopiques. Le rayonnement dans le domaine visible est sous-estimé par le modèle alors que les comparaisons dans l'UV et l'IR sont excellentes. Des données uniques sur l'interaction entre le bouclier thermique et l'atmosphère terrestre et vénusienne ont été obtenues par mesures expérimentales et simulations numériques.

Des études récentes sur la nature volumétrique de l'ablation ont montré l'importance du rayonnement interne dans les nouveaux matériaux composites utilisés pour les sondes actuelles et futures. Ce rayonnement interne est rarement inclus dans les modèles contemporains de réponse thermique. La géométrie exacte de deux échantillons, un à haute densité et le deuxième à basse densité, a été obtenue par tomographie à haute résolution aux rayons X synchrotron. Ces géométries ont été utilisées dans un modèle numérique à échelle microscopique pour caractériser précisément leurs propriétés optiques et morphologiques effectives. Ces propriétés effectives ont ensuite été utilisées pour déterminer l'absorptance de ces deux échantillons. L'augmentation de l'absorptance due à la pyrolyse est plus significative pour un matériau à basse densité, contenant plus de résine. Les facteurs de forme volumétriques ainsi que ces propriétés ont permis d'évaluer les flux radiatifs dans ces matériaux. L'inclusion de ces flux au modèle de réponse thermique indique un effet significatif, important pour la modélisation future.

Mots clés : ablation, bouclier thermique, simulations numériques, rayonnement, rentrée atmosphérique, spéctroscopie, tomographie aux rayons-X, tube à expansion.

ACKNOWLEDGMENTS

I have been lucky enough to be surrounded, both at work and at home, by a group of people who are intelligent and kind, and constantly push me to be the best I can.

I am grateful to my supervisors for giving me the clay with which to mould my own research expertise. Pénélope, thank you for introducing me to the world of hypersonics - it's brilliant! I really appreciate the opportunity I've had to work on a variety of different projects, while being able to travel the globe and meet and work with new people, not to mention lab ski days and barbecues. Sophia, thanks for letting us aerospace types take over your lab! Thanks for all the support, technical and moral, as well as the interesting discussions.

Richard, though not officially a supervisor, you allowed me the most rewarding experience by taking me in, sharing your exceptional technical knowledge and stories, and letting me run riot in the X-labs. And for actually having read my thesis! Thanks, Boss. PJ and Rowan, for doing the heavy lifting having developed and documented the incredible `eilmer` code, and for the support when I manage to kill it! David Buttsworth, for all the fascinating discussions and ideas. Thanks to the X2 operators and UQ workshop staff who got everything working in time. And to X2, she might be stubborn and need some coaxing at times, but what a machine!

Over the years at EPFL, I've shared some great times with some really great people: Val, Yann, Ermina, Rikkert, Gwen, Genna, Chris, Dutch (Floris), Toni (€3 hospital!), Oner, Loïc, Angelo and Gaffu. Pisa, for the great laughs we had and your love of dirty, *dirty* vodka martinis! David, thanks for helping with 'military' applications - it's a shame our time together was so limited! Yannick, thanks for the help with the French abstract! Jérémy, it's been fun sharing a *buro* for 4 years. Thanks for all the help and interesting work, but most importantly thanks for being a great friend, without whom, this would all have been a lot more tedious. Bon courage, *Jeremy*.

Thanks to my Aussie family, Peter, Pam, Sarah, Tom and the thousand other Fahys for their generosity, encouragement and Port (the fortified wine, not... y'know). My family, for raising me and supporting me and loving me. *Dadu* and *Thamma*, I wish you could have been here today. *Ma*, *Ba*, I am who I am because of you (nature **and** nurture!). You've always made sure to give me the best possible opportunity to follow my dreams and I've known for a long time this was it. Thank you from the bottom of my heart. *Nanu*, *Nani*, you always encouraged me to write. Although I will never be as prolific as you, here's my small contribution to global knowledge. This thesis is for the both of you.

Elise, *meri jaan*, this would have been impossible without you. I could spend another 200 pages listing the reasons why. You teach and inspire me every day and I feel so very lucky. Thank you for your amazing love, care and support. Let's go exploring!

CONTENTS

LIST OF FIGURES

LIST OF TABLES

NOMENCLATURE

C_H	Heat transfer coefficient $= \rho_e u_e C_h$	$\mathrm{kg \cdot m^{-2} \cdot s^{-1}}$
C_h	Stanton number for heat transfer	
α_w	Surface absorptivity	
$\dot{m}$	Mass flux	$\mathrm{kg \cdot m^{-2} \cdot s^{-1}}$
$\mathcal{Q}_k$	Effective diffusive heat flux	$\mathrm{J \cdot m^{-2} \cdot s^{-1}}$
$\underline{\underline{\mathbf{K}}}$	Permeability tensor	$\mathrm{m^2}$
$\underline{\underline{\mathbf{k}}}$	Conductivity tensor	$\mathrm{J \cdot m^{-2} \cdot s^{-1} \cdot K^{-1}}$
e	Specific energy	$\mathrm{J \cdot kg^{-1}}$

h	Enthalpy of phase	$J{\cdot}kg^{-1}$
$\dot{q}$	Heat flux	$W{\cdot}cm^{-2}$
$\hat{n}$	Outward-facing normal of control surface	
∂v	Bounding surface	
A	Absorptance	
A	Area of the cell boundary per unit radian in the circumferential direction	m^2
b^*	Reduced impact parameter	
d	Diameter or characteristic length	m
E_a	Activation energy	J
f	Image	
F_i	Inviscid flux vector	
F_v	Viscous flux vector	
f_v	Phase volume fraction	
g^*	Reduced relative kinetic energy	
g_i	Test parameter	
G_s	Safety factor	
GCI_{fine}	Finest grid convergence index	
I_i	Volume averaged radiative intensity in phase i	$W{\cdot}m^{-3}{\cdot}sr^{-1}$
I_ν	Spectral Intensity	$W{\cdot}m^{-2}{\cdot}nm^{-1}{\cdot}sr^{-1}$
j	Emission coefficient	$W{\cdot}m^{-3}{\cdot}nm^{-1}{\cdot}sr^{-1}$
k	Imaginary part of complex refractive index	
k_b	Boltzmann coefficient, $1.38064852 \times 10^{-23}$ $J{\cdot}K^{-1}$	
m_i	Particle mass of species i	

n	Real part of complex refractive index	
p	Pressure	Pa
p	Theoretical order of convergence	
Q	Source term	
$Q^{(l)*}(g^*)$	Reduced cross section	
R	Reflectance	
r	Overall refinement ratio	
r^*	Reduced intermolecular distance	
r_m^*	Reduced distance of closest approach	
s	Path length	m
T	Temperature	K
t	Time	µs
Tr	Transmittance	
V	Volume	m^3
v	Velocity	m·s^{-1}
x	Size parameter	
X_i	Mole fraction	

Greek Symbols

α	Thermal diffusivity	m^2·s^{-1}
β	Extinction coefficient	m^{-1}
$\chi(g^*, b^*)$	Reduced angle of deflection	
ϵ	Inter-potential well depth	J
Γ	Goulard number	
γ_i	Efficiency of reaction, i	

κ	Absorption coefficient	m^{-1}
λ	Wavelength	nm
μ	Electric dipole moment	Debye
μ_i	Viscosity coefficient	Pa·s
Ω	Solid angle	sr
ω	Scattering albedo	
$\Omega^{(l,s)\star}$	Dimensionless collision integral	
Φ	Scattering phase function	sr^{-1}
ρ	Density	$\mathrm{kg \cdot m}^{-3}$
ρ_r	Directional-hemispherical reflectivity	
σ	Hard sphere collision diameter	Å
σ	Stefan-Boltzmann coefficient, 5.670367×10^{-8}	$\mathrm{W \cdot m}^{-2} \cdot \mathrm{K}^{-4}$
σ_s	Scattering coefficient	m^{-1}
$\sqrt{\rho c k}$	Thermal effusivity	$\mathrm{kg \cdot s}^{-5/2} \cdot \mathrm{K}^{-1}$
τ	Extent of the pyrolysis reaction	
τ	Optical thickness	
$\varphi(r)$	Interaction potential	
φ^*	Reduced interaction potential	

Subscripts

av	Geometrical mean
BL	Boundary layer
capsule	Inside the capsule
c	Char material
e	Boundary layer edge

f	Controlling the forward reaction rate
v	Virgin material
ν	Frequency
i, j	Phase declarations
∞	Freestream
b	Blackbody
cal	Calibration
conv	Convective
d	Discrete scale
exp	Experimental
g	Gas phase
rad	Radiative
refl	Reflection
refr	Refraction
REV	Representative elementary volume
s	Solid phase
stag	Stagnation point
test	Steady test time
tr	Translational-rotational mode
ve	Vibrational-electron-electronic mode

ACRONYMS

CFD   Computational Fluid Dynamics

CMA   Charring Material Thermal Response and Ablation Program

CT   Computed Tomography

DSC   Differential Scanning Calorimetry

EDL   entry, descent and landing

EAST   Electric Arc Shock Tube

EPFL   École polytechnique fédérale de Lausanne

FIAT   Fully Implicit Ablation and Thermal response program

FWHM   full width at half maximum

ICCD   Intensified charge-coupled device

IMU   Inertial Measurement Unit

MSL   Mars Science Laboratory

MEADS   Mars Entry Atmospheric Data System

MEDLI   MSL Entry, Descent, and Landing Instrumentation

MISP   MEDLI Integrated Sensor Plug

NASA   National Aeronautics and Space Administration

PATO   Porous-Material Analysis Toolbox based on Open-FOAM

PICA   Phenolic Impregnated Carbon Ablator

QSS   Quasi-steady state

RTE   Radiative Transfer Equation

RCC   Reinforced Carbon-Carbon

SCEBD   Self-Consistent Effective Binary Diffusion

SSE   Sensor Support Electronics

TGA   Thermogravimetric analysis

TPS   Thermal Protection Systems

UV   ultraviolet

VnIR   visible and near infrared

INTRODUCTION

Space exploration is the outcome of humankind's thirst for knowledge, its enduring dream to reach the stars and to pursue the sublime. After centuries of wistfully gazing out into the vast openness of space, rapid advances in technology during the 20th century transformed this aspiration from reverie to reality. The first breakthrough was made by Robert Goddard, who successfully manipulated Newton's third law to launch liquid-fuelled, multi-staged rockets in the 1920*s*, thereby ushering in the dawn of the space age. Progress persisted via the military during the decades bookending the second World War, before the hunt for intellectual insight into the workings of our universe broke through this morally ambiguous barrier in the 1950*s*.

Astonishing technological feats were achieved back in an era when the unknowns vastly exceeded the knowns, requiring substantial belief in contemporary knowledge of science and engineering. Since then, myriad experiments have been sent into orbit, into interstellar space and to land on the surface of neighbouring moons, planets and asteroids. By touching down at Tranquility Base amongst the "magnificent desolation" of the lunar surface on 20 July 1969, the Apollo program secured its place in history among the greatest achievements of humankind. It bore witness to the immense scientific and technological challenges that were overcome, but especially to the strength of human collaboration and spirit. The critical challenge of the journey home still remained, requiring successful re-entry, safe deployment of the drogue parachutes and splashdown.

1.1 THE NEED FOR THERMAL PROTECTION

Before landing on the surface of a planet, entry vehicles must traverse the gamut of aerothermodynamic forces. The vehicle enters the planetary atmosphere at hypersonic speeds. The flow is highly non-equilibrium and rarefied in the upper echelons of the atmosphere. At lower altitudes, the vehicle encounters first non-equilibrium and then equilibrium continuum flow along its trajectory. Upon release of the drogue chute, the vehicle is subjected to the supersonic and subsonic flow regimes. The incoming flow dissipates the majority of its kinetic

energy in the form of heat, dissociating and if fast enough, ionising particles in the radiating shock layer which forms around the vehicle. The core drivers of entry vehicle design are the desired drag coefficient and aerodynamic stability, but most importantly, survivability under the extreme conditions for all flow regimes. A TPS is thus employed to minimise the heat transferred to the vehicle payload.

By the mid 1950*s*, engineers were leaving behind the idea of sharp leading edges for sustained hypersonic flight. As convective heating was found to scale with the inverse square of vehicle nose radius ($\dot{q}_{conv} \propto 1/\sqrt{R_n}$), they began employing blunt bodies to survive the extreme aerodynamic heating at these speeds [1]. In this way, a large drag surface-area is provided normal to the flow, decelerating the vehicle by static pressure forces rather than viscous forces. Rather than storing the dissipated energy in the boundary layer, it is transported away from the vehicle by a large mass of gas processed through the surrounding bow shock. For the manned spaceflight program, the National Aeronautics and Space Administration (NASA) needed to ensure the protection of human payload from the high heat fluxes experienced by the vehicle during re-entry. To this end, their predecessors built on testing conducted by the US armed forces for the *Polaris* program and favoured metallic heat sink technology.

The metal best suited for this purpose was beryllium, which was later flown on the unmanned Project FIRE interplanetary re-entry tests [2]. However, this technology was abandoned due to difficulties in fabrication [3], scarce availability of beryllium and the worry that any heat sink may "pressure cook" the occupant of the capsule [4]. Reservations were also held over the added weight and expense of the beryllium heat shield as well as the question of jettisoning it before landing. By the time it reached the lower atmosphere, the extreme temperatures attained by the heat sink would make it hazardous to retain after parachute deployment. It also increased the chances of forest fires in the case of a dry landing [4].

Concurrent effort was therefore allocated to the design of sacrificial ablative heat shields. Even though the understanding of the complex physics involved was incomplete, engineers found something appealing in the "less tidy" ablation principle [4]. After rigorous testing in an ambitious and hectic flight test program, the selection of ablative heat shields for the majority of hypersonic descents in planetary atmospheres has been justified.

1.1.1 *Ablation and Pyrolysis*

Under intense convective and radiative heating from the surrounding shock wave, the sacrificial TPS layer heats up and starts to ablate. These TPS materials are usually composed of carbon or glass fibres, with strong thermal insulation and scattering (re-radiation) characteristics, set in an organic resin matrix. They can be enhanced using cork or honeycomb structure to tailor certain characteristics such as structural integrity or density. The bulk material absorbs heat using a combination of endothermic phase change and temperature increase. This energy is then dissipated via removal of surface material through surface reactions, melting and pyrolysis. Mechanical erosion or spallation is also possible, but undesirable due to its inefficiency in evacuating heat from the system.
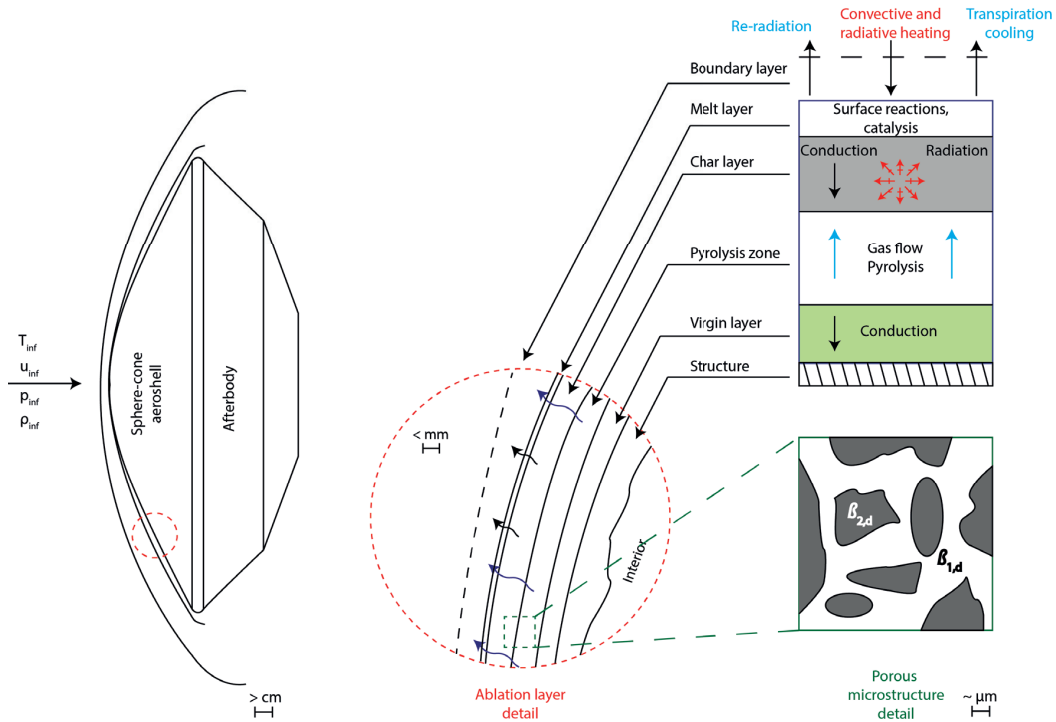
Figure 1.1: Schematic showing re-entry capsule (left), ablation and pyrolysis layers in TPS material (ablation layer detail) and detail of the two-phase medium with component designation.

As shown in Figure 1.1, three distinct layers are created in the TPS material. Its thickness is sized to keep the *virgin layer* at the lowest temperature due

to its proximity to the spacecraft payload, preventing the onset of material decomposition. The phenolic resin volatilises at approximately 600 K in the *pyrolysis zone*. This generates a gas rich in hydrocarbons and leaves behind carbon residue. The gas then convects through the thoroughly decomposed *char layer*, absorbing thermal energy before being injected into the boundary layer creating a transpiration cooling effect, blocking convective heat transfer [3]. The introduction of heavy carbonaceous species also modifies the optical properties of the boundary layer, radiatively cooling the flow. Strongly endothermic surface reactions such as sublimation [5] take place in parallel to oxidation and nitridation, resulting in surface recession as the material is consumed. The complex coupling effect between the strongly radiating plasma and the TPS material needs to be further understood to optimise the design of ablative heat shields.

Post-flight evaluation of the forebody heat shield on the Stardust capsule [6] and statistical modelling of modern, low density TPS material microstructure [7] have recently concluded that reactions, like oxidation, previously thought to occur solely on the surface, have a significant effect in depth. This volume ablation regime leaves the carbon preform exposed to its extreme operating environment, where internal radiation becomes a significant (and eventually, dominant) mode of heat transfer [5]. Similar to the modification of boundary layer optical properties post-pyrolysis, heavy molecules released during resin decomposition can significantly change the absorption properties of the gas phase. Combined with the opaque behaviour of the solid phase, $\beta_{2,\mathrm{d}}$, a strongly attenuating gas phase, $\beta_{1,\mathrm{d}}$, shown in Figure 1.1, has the potential to significantly alter the TPS material radiative behaviour and overall thermochemical response at high temperatures. A better grasp of the in-depth physical phenomena would help take a big step towards being able to predict their behaviour accurately, reducing the need for large safety factors.

1.1.2 *The Fall and Rise of Novel Heat Shield Design*

NASA's legacy missions (Gemini, Apollo and Viking) employed novel ablative materials tailored to the entry environment in question [8]. However, post-Viking, the agency concentrated its efforts into developing a reusable TPS for the Space Shuttle. The *LI-2200* and *LI-900* ceramic tiles were good insulators, relying on surface re-radiation to dissipate the incident heat loads, but could not compete with ablative TPS when it came to surviving super-orbital entry.

Consequently, there was a lull in the development and modelling of new ablative TPS materials until the turn of the century. A risk-averse philosophy was adopted, where flight-qualified materials were used with little or no optimisation for the mission at hand. This encouraged the use of large safety factors, increasing TPS mass penalty and decreasing allowance in the mass balance for scientific or human payload. For example, the Pioneer and Galileo probes employed dense, unoptimised carbon phenolic developed by the United States Air Force for ballistic missile applications [8]. Modern missions suffer from similar issues. An up-front program decision was made to size the thickness of the Phenolic Impregnated Carbon Ablator (PICA) [9] heat shield on the forebody of the Mars Science Laboratory (MSL) capsule at approximately 32 mm while aerothermal analysis and margining yielded a required thickness of just 24 mm [10].

In order to survive the demanding thermal protection requirements of future space exploration missions, space agencies are becoming more flexible with the use of low density ablators, reinvigorating research efforts applied to these materials. Understanding their response at extreme temperatures is imperative to evaluating their flight worthiness. Compared to the heyday of the space age, the current shoe-string budgets allocated for space research no longer make flight testing TPS materials a viable option. A combination of laboratory testing and numerical modelling is therefore being used to evaluate their behaviour in the extreme conditions faced during atmospheric entry.

1.2 PLANNED EXPERIMENTAL TESTING AND NUMERICAL SIMULATIONS

Ablation testing is carried out using a range of facilities, such as arc-jets, furnaces, inductive torches, plasma wind tunnels and expansion tubes, with each dataset allowing the study of different aspects of the material's response to its high enthalpy environment. With the ability to produce a radiating shock layer similar to flight over a scaled vehicle model for a short test time [11], the University of Queensland's expansion tube facilities lead the way in aerothermodynamic research. Traditionally used for shock layer radiation measurements, the smaller of the two facilities, X2, has been upgraded for ablation testing [12, 13, 14]. With the use of high speed video, emission spectroscopy and 2D intensity mapping, it is possible to measure the radiative signatures of TPS models subjected to a hypersonic flow. Computational aerothermodynamic simulations are able to then rebuild the quasi-steady expansion tube flow around

the TPS material sample, providing information on shock layer parameters that cannot be measured. Comparison of experimental results with those generated numerically allows for the validation of the simulations, the definition of areas in need of improvement and an addition to the understanding of hypervelocity atmospheric entry.

The volumetric effects of ablation which have recently been hypothesised are difficult to measure or visualise experimentally. Traditionally, TPS material behaviour has been predicted using one-dimensional finite difference or finite element heat transfer codes, tailoring material properties to match experimental data. However, by taking into account their exact geometries using Computed Tomography (CT), it is possible to numerically quantify the radiative properties of both solid and gaseous phases in an ablative material [15, 16, 17]. These properties can be applied to the Radiative Transfer Equation (RTE) and included in a state of the art charring ablator response code [18] to evaluate in-depth radiative effects.

1.3   AIM

The overall aim of this work is to determine the external and internal effects of thermal radiation on ablative TPS materials in a representative flight environment. In *Part I*, surface degradation of these materials similar to flight was reproduced by subjecting aeroshell models to strongly radiating hypersonic flows in the X2 expansion tube. By comparing the emitted radiation signatures with spectra generated using a combination of Computational Fluid Dynamics (CFD), surface kinetic and radiation modelling, it was possible to validate numerical models and increase confidence in computational analyses of shock layer aerothermodynamics for the considered cases.

In *Part II*, the effect of radiation on the internal heat transfer in charring ablators was assessed. The evolution of TPS material optical properties was tracked by conducting pore-level calculations on digitised morphologies of two-phase virgin and charred samples, obtained from CT images. These properties were then used in macroscopic calculations conducted by coupling radiation and the thermochemical response of the material. Flight data recovered from the forebody heat shield of the MSL entry capsule was used as a test case for this methodology.

1.4 OBJECTIVES

The aims of this thesis are achieved by the completion of the following objectives.

O.1 X2 testing of pyrolysing phenolic aeroshell model at a high enthalpy Venusian entry condition with ultraviolet (UV), visible and near infrared (VnIR) emission spectroscopy and high speed imaging.

O.2 X2 testing of pyrolysing phenolic aeroshell model at a high enthalpy Earth re-entry condition with UV and VnIR emission spectroscopy and high speed imaging.

O.3 CFD simulations and analysis of X2 experiments, including finite-rate surface kinetic models, radiation analysis and calculation of numerical spectra for comparison with experimental data.

O.4 Characterisation of effective radiative properties of porous TPS material samples with two semi-transparent phases.

O.5 Use of Monte Carlo algorithm to calculate divergence of radiative flux within the TPS material and coupling to a thermochemical response code, PATO.

O.6 Comparison of results with flight data from the heat shield of the MSL mission.

1.5 SCOPE

In *Part I*, a reusable carbon phenolic aeroshell was designed and manufactured with the versatility to be used with all existing X2 flow conditions. The models were not dimensioned to match scaled models of any particular flown entry vehicle. The measured data was therefore not comparable to radiation signatures measured in flight. In *Part II*, the aim of including radiation in the PATO calculation was to evaluate its effect on the overall material response. Radiative flux divergence was supplied to the overall energy equation for a participating material domain. The effective properties were weighted by phase volume fraction and extent of the pyrolysis reaction.

1.6   THESIS OUTLINE

Chapter 2 presents a review of ablation testing in experimental facilities. The focus is kept on the non-traditional use of the X2 expansion tube facility for ablation testing, relevant past test campaigns and studies numerically rebuilding experiments using a combination of CFD and radiation modelling.

Chapter 3 presents the methodology used for the design and manufacture of carbon phenolic aeroshells, X2 condition selection and testing, the set-up of the imaging systems and discussion and analysis of calibrated experimental data.

Chapter 4 defines and justifies the underlying assumptions and models selected for numerical rebuilding of X2 experiments using the `eilmer3` CFD code, radiation modelling and implemented finite-rate surface kinetic boundary conditions. Flowfield results are presented for both Earth and Venus conditions studied and used as an input for the radiation model. Numerical spectra generated by line of sight radiation calculations are presented for both conditions and compared to the experimentally recorded spectra from *Chapter 3*.

Chapter 5 presents a review of the study of heat transfer in ablative TPS materials, detailing the rise in modelling complexity with the continued exclusion of radiative heat transfer mechanisms. It discusses recent methodologies used to add radiation to these models and characterisation of in-depth optical properties required to fully evaluate these effects. An overview of instrumented entry vehicles is presented, concentrating on MSL as it gives the best opportunity to validate heat transfer codes against flight data.

Chapter 6 provides a library of optical properties for both virgin and charred carbon phenolic and graphite material samples, with two semi-transparent phases, calculated by solving the coupled volume averaged RTEs. The given values include the effect of scattering within the phases, as well as wavelength dependence of macroscopic optical properties.

Chapter 7 describes the methodology used to evaluate the divergence of radiative flux inside an ablative material via a path-length Monte Carlo method, using the effective optical properties calculated in *Chapter 6*. By supplying the calculated data to the state of the art TPS thermochemical response code, Porous-Material Analysis Toolbox based on Open-FOAM (PATO), comparisons are made with

data recovered from MSL's heat shield during its entry and descent to the Martian surface.

Chapter 8 concludes the thesis, underlining the addition to state of the art knowledge of the topic and proposing future research which would add to this understanding.

Part I

AEROTHERMAL HEATING

ABLATION IN RADIATIVE SHOCK LAYERS: A REVIEW

2.1 ABLATION TESTING IN AEROTHERMAL ENVIRONMENTS

An entry capsule pierces the atmosphere at speeds much larger than the local speed of sound, forming a bow shock around its blunt body. The hypersonic flow dissipates its enormous kinetic energy into the surrounding shock layer, driving up its temperature. This results in high energy collisions, dissociation and ionisation of the particles and equilibrium or non-equilibrium (finite-rate) gas chemistry. These collisions transfer energy from the freestream to the shock layer, primarily exciting the translational thermal mode. This leads to a state of thermal non-equilibrium as vibrational, rotational and electronic internal energy modes play catch-up during the collisional exchange of energy processes [19, 20].

Collisions between excited species can also emit energy carrying photons, which can then be absorbed by the gas. This gives rise to radiative heating or cooling effects. This phenomenon is proportional to shock layer thickness, which increases with an increase in body diameter. At the stagnation point, the magnitude of radiative flux is directly correlated to vehicle nose radius. The spectral distribution of the incoming radiation is heavily dependent on the composition of the atmosphere in question as well as that of the ablative products present in the boundary layer. As a result, for an equivalent trajectory and vehicle geometry, radiative heating is much higher in a CO_2-N_2 Mars or Venus gas mixture, as compared to air. Conversely, for a Jovian atmosphere with a H_2-He gas mixture, a vehicle would require an entry velocity greater than $35\,km\cdot s^{-1}$ to receive radiative fluxes of similar order to those experienced while re-entering the Earth's atmosphere at approximately $11\,km\cdot s^{-1}$ [21]. Representative heating rates for planetary missions given in Figure 2.1 are meant to give the reader a better idea of the velocities and heat fluxes in question.

An appreciation of the suitability of an ablative material to its entry environment is paramount in optimising TPS sizing and design [8]. This suitability is assessed by subjecting the material to flight-equivalent thermal, chemical and mechanical environments. If an entry vehicle's thermal envelope is dominated
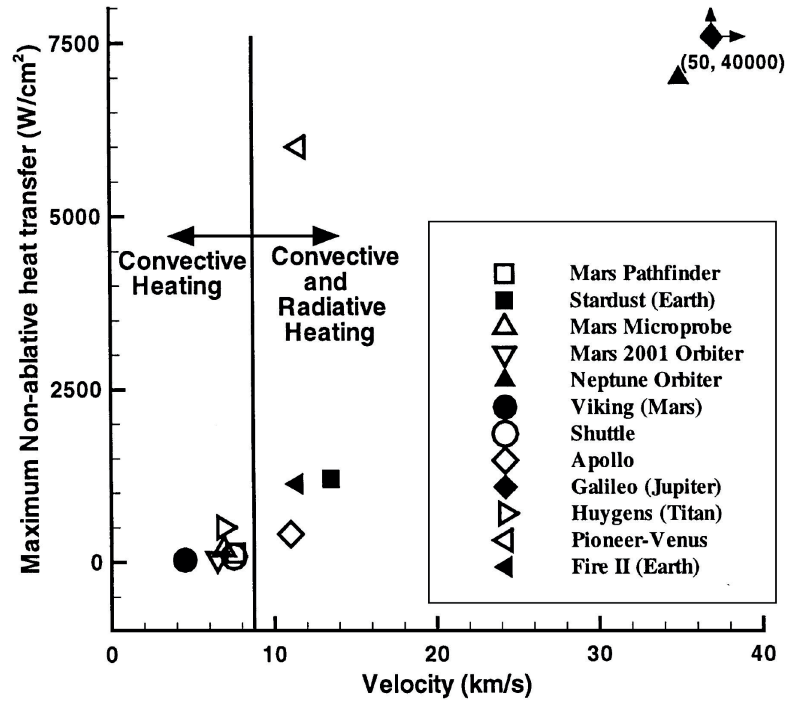
Figure 2.1: Non-ablative peak heating rates versus velocity for flown and planned entry vehicles from Gnoffo [21].

by convective heating, as it is during Earth re-entry, then it must be tested and characterised in high convective heat flux environments. If thermal radiation is the dominant heat transfer mechanism, for example during Jupiter entry, then a suitable facility providing high radiative heating should be used.

The most affordable and simplest method of testing thermal response of ablative materials is via the use of an oxy-acetylene torch [22, 23]. The torch, which can attain temperatures of up to $3000\,\mathrm{K}$ and heat fluxes up to $900\,\mathrm{W}{\cdot}\mathrm{cm}^{-2}$, can only simulate one set of conditions at a time and this is unable to match the effects of chemistry or enthalpy during atmospheric entry. This makes it an ineffective methodology for predicting material behaviour in disparate entry environments. However, it can be used as a preliminary test to deselect unsuitable materials before more refined tests are conducted [22].

2.1.1 *Testing in Long Duration Facilities*

Once suitable insulators are identified, they must be tested in advanced facilities for their expected aerothermal environment. Unfortunately, no single ground test facility has the versatility to produce all the required flight parameters [24]. Arc-jet facilities are the most versatile and have the longest legacy in TPS testing and qualification [25]. Material coupons are instrumented with thermocouples and subjected to high enthalpy, subsonic or supersonic nozzle exhaust flows for durations of up to 30 minutes. These experiments allow measurement and analysis of surface recession [26], surface emission [27, 28], in-depth temperatures [25, 28] and spallation [29].

Though these facilities are able to produce a wide range of conditions, they are, according to Venkatapathy *et al.* [30], unable to "simultaneously duplicate the scale, pressure, aerodynamic shear, heat flux, and enthalpy experienced in flight." The samples are limited in size and cannot have flight-equivalent geometries. Simulation of accurate time resolved heat fluxes is difficult. Investigation of the combined effects of radiative and convective heating is impossible. Often, little accurate data is available regarding the freestream conditions, which handicaps any numerical rebuilding of experiments.

Until the Mars Science Laboratory in 2012, NASA spent over 30 years employing the same TPS for each Mars landing [31]. After the dismantling of their Giant Planets installation, their arc-jet facilities no longer had the ability to operate in realistic extra-terrestrial atmospheres [32]. Theoretically, arc heaters are capable of heating virtually any gas mixture [30]. However, in attempting to upgrade their facilities for use with CO_2 gas mixtures, NASA engineers discovered that toxicity of cyanide as well as inflammability of carbon monoxide were causes for concern [33]. Recently, the HYMETS facility has been upgraded for use with Martian gas mixtures and managed to safely work with a CO_2-N_2 mixture in a $75\% - 25\%$ ratio by volume [31]. The system, however, does not yet seem robust.

In Europe, the Plasmatron at the von Kármán Institute [34] as well as the Plasma Wind Tunnels at the Institute for Space Systems [35] have previously conducted experiments using CO_2 gas mixtures at stagnation pressures equivalent to Mars entry, but lack the conditions required for Venus entry. Simulation of gas giant entry requires use of hydrogen and helium and is dangerous due to gas inflammability, but could potentially be achieved with the requisite care applied.

TPS ground testing has also been carried out in radiative facilities [36, 37]. These installations are especially interesting as they can help define heat flux failure mode boundaries [30]. Thermocouple data at high heat fluxes are of great value when combined with relevant convective heating data from arc-jet experiments. However, due to the lack of a flow, the pressure, chemistry and convective transport at the test surface is artificial or absent. The Sandia solar tower facility has been used for systems level testing of TPS [38] as well as characterisation of PICA radiative properties [36]. High energy laser facilities have also been used [37], but are limited to a single wavelength, which is dissimilar to flight.

The effect of pyrolysis on heat transfer and shock structure has also been investigated in conventional supersonic wind tunnels. Gollnick [39] found the heat flux at the surface of a hemispherical model to be severely reduced upon injection of a gas into a flow at Mach 3.53. A reduced temperature gradient was created at the wall due to displacement of the hot boundary layer resulting from pyrolysis gas injection. This phenomenon caused convective blockage when coupled to the changed thermal properties of the injected gas and its effect on Reynolds stresses. This blockage was found to be independent of the composition or rate of injection (blowing rate) of the pyrolysis gas. In a similar study, Kaattari [40] researched the effects of pyrolysis gas injection through a porous hemispherical model into hypersonic flows at Mach 3 and 5. Unlike Gollnick, he found surface heating to be inversely proportional to the blowing rate. Using shadowgraphs, he also observed an increase in shock stand-off upon mixing of pyrolysis and boundary layer gases. In both studies, flow velocity was too low to account for radiative heating or blockage.

The aforementioned facilities can all reproduce realistic convective heating rates with test times sufficient to achieve thermal equilibrium via aerothermal heating. However, they lack the ability to sufficiently recreate the non-equilibrium hypersonic flow surrounding an entry vehicle and its coupling to the ablative and radiative processes [41], especially in the case of non-Earth entries. They are therefore used primarily for material characterisation [41]. Alternatively, hypersonic impulse facilities, which produce shock layer radiation similar to flight, are used to test scaled models of entry vehicles [42].

2.1.2 *Testing in Impulse Facilities*

The X2 free-piston driven expansion tube at the University of Queensland is considered world class in the field of atmospheric entry research. Along with its larger sibling, X3, these facilities are unique in their ability to provide accurate aerothermodynamic data for superorbital flow [43]. A range of test gases have been used to simulate entry into atmospheres of the Earth [44], Mars [45], Titan [46], Venus [47] and the gas giants [48].

Its heritage and operation have been described in detail by Gildfind, Morgan and Jacobs [49], thus will only be briefly summarised here. Figure 2.2 includes a schematic of X2, coupled with a position-time ("x-t") diagram of the longitudinal wave processes that occurred during the experiments conducted during this work, investigating ablative planetary entry. From left to right, X2 is configured with a freely sliding piston located in the compression tube, a shock tube, an acceleration tube and a nozzle exiting into a test section where the model is mounted. The piston acts as a physical separator between the reservoir and driver gases. The shock tube is separated from adjacent sections at the two diaphragm stations. Typically, the primary and secondary diaphragms are made from 2 mm thick steel and a single sheet of aluminium foil respectively. The entire facility is sealed and the tube is evacuated forward of the primary diaphragm. Both the acceleration tube and test section are filled with air at a low pressure, while the shock tube is filled with the test gas, which depends on the atmosphere being studied. A light driver gas composed of helium, or a mixture of helium and argon, is filled at 92.8 kPa between the piston and primary diaphragm. A large volume of high pressure air at 6.85 MPa is pumped in behind the piston.

Once released, the high pressure reservoir air accelerates the piston to high speeds, compressing the light driver gas in front of it. It then transfers all of its kinetic energy to the gas, driving up the pressure and temperature past the point when reservoir and driver pressures are equal, until the gas explodes through the steel diaphragm [49]. X2 relies on piston momentum and inertia to maintain barrel pressure after diaphragm rupture through extra compression of the driver gas, to compensate for the mass lost through venting into the shock tube. The driver burst condition (state 4) undergoes a steady expansion due to the area change at the primary diaphragm station, before unsteadily expanding into the shock tube (state 3). The strong shock wave created by this explosion

Figure 2.2: Schematic and position-time diagram of X2. Published with permission from James *et al.* [48].

causes the test gas to compress and accelerate down the shock tube, processing it from state 1 to state 2. The test gas, now at a high temperature and pressure, explodes through the secondary diaphragm and suddenly encounters the low pressures in the acceleration tube. A secondary shock wave is then driven through the accelerator gas (state 5), processing it to state 6. The abrupt change in pressure induces an unsteady expansion in the test gas (state 7) adding total enthalpy and pressure to the flow. A Mach 10 diverging nozzle is then used to increase the test-gas core flow diameter via a steady expansion (state 8), accelerating the test gas towards the test section at speeds of up to $20 \, \text{km} \cdot \text{s}^{-1}$ [49].

When the expanded test gas interfaces with the model in the test section, it creates a radiating bow shock which can be quantified using optical diagnostics when quasi-steady. The test duration is short, usually in the order of $100 \, \mu\text{s}$ and ends upon the arrival of the noise reflected from the driver gas surface, u+a

wave reflections from the piston face and contact surface, the test gas unsteady expansion or driver pressure decay. These facilities differ from conventional shock tubes by injecting energy into the flow through both the primary shock wave and the unsteady expansion from which the facility gets its name. They are therefore able to minimise dissociation and radiative losses. They can also produce much higher enthalpy and chemically clean test flows which compare well with hypersonic flow experienced in flight [44].

Radiating shock layers can be characterised and understood through advanced optical diagnostics. The suite of such techniques available for use with X2 has grown to include VUV [50], UV [45] and IR [44, 13] spectroscopy, high speed video imaging [13, 51], pyrometry [13] and two dimensional intensity mapping of the flow through narrow band filters [44]. The greatest advantage of radiation measurement during ground testing involves comparison to flight. Data describing the shock layer around entry vehicles can only be measured from a distance via spectroscopic methods in the form of emission spectra. As shown by Fahy [44], when coupled with the aforementioned techniques, X2 is able to match flight data well, within the limits of uncertainty.

Since the late 1990s, there has been interest in simulating the effects of ablation in X2 to support superorbital sample return missions such as Stardust and Hayabusa. Morgan *et al.* [52] first simulated pyrolysis in X2 by injecting hydrogen from the surface of a scaled model of the Hayabusa capsule. A proof of concept was achieved and interferograms were used to measure the change in shock layer density due to pyrolysis gas injection. Hoogland [53] attempted the simulation of pyrolysis via hydrogen injection through a laser drilled plate prior to flow establishment. This methodology did not simulate a continuous layer of pyrolysis gases over the model forebody, as in flight. Instead, this resulted in the production of discrete streams of gas being ejected from the surface. Flow contamination and timing of gas injection were cited as obstacles to fulfilment of the experimental objectives.

The Achilles' heel of impulse facilities is their inability to sustain the flow for a sufficient duration to accurately reproduce ablation and pyrolysis. Buttsworth *et al.* [51] circumvented the timing obstacle entirely and tested scaled stainless steel models of the Hayabusa capsule, layered with an epoxy resin. Upon encountering the hot hypersonic flow, the resin started to decompose. This effect was visualised through the presence of CN in boundary layer radiation

measurements. An increase in shock layer intensity was also measured adjacent to the epoxy-coated models via high speed imaging. The epoxy was used for its low melting point and thermal diffusivity, to ensure pyrolysis. Although of similar composition to phenolic, it has a higher thermal conductivity, providing dissimilar surface reaction rates to decomposing phenolic. There is also a strong possibility that contamination of CN band emission could have been caused by use of a Mylar secondary diaphragm, made from polymeric resin. The flight-equivalent velocity of the flow was approximated at $9.0\,\mathrm{km\cdot s^{-1}}$, putting the model at a point on the capsule's trajectory where surface charring and ablation is more likely than resin decomposition. This work marked the beginning of studying radiative blockage in X2, due to ablative species present in the boundary layer.

In flight, quasi-steady wall temperatures are achieved through a heat and mass transfer balance between the flow and interacting wall. The temperatures change along the flight path, but at a chosen trajectory point, values approximate to an equilibrium thermal balance, with wall temperatures typically of the order of thousands of Kelvin for ablative TPS. Such conditions take the order of tens of seconds of flight time to achieve and cannot be achieved by aerodynamic heating alone in shock tunnels. By electrically pre-heating the walls internally, it is possible to reach wall temperatures characteristic of flight, so that surface chemistry interactions with the flow can be correctly reproduced, but the flow of volatiles driven by the internal temperature gradients below the wall surface will be much different. Several attempts have been made to utilise electrical pre-heating in X2 tests, as described below. Typically, the flow of current was kept on during these tests, causing a small perturbation to the internal temperature profile that propagates inwards on the order of $50\,\mathrm{\mu m}$ from the surface. Therefore, there is an absence of the one-to-one coupling with external heating and ablation rate found in flight. However, correct surface reaction rates are assumed, as representative wall temperature and boundary layer state are present.

In an attempt to eliminate the initial time requirement, Hunt [12] developed graphite ablation gauges that were ohmically heated to approximately $1600\,\mathrm{K}$ prior to flow establishment, to investigate surface chemistry. The design aimed to quantify ablation and recession of the gauges via monitoring of the alteration in electrical resistance. As before, major difficulties were observed in correct timing of the pre-heating mechanism. Zander *et al.* [13] built on the work

by Hunt [12] to electrically heat a thin hemi-cylindrical strip of Reinforced Carbon-Carbon (RCC) to approximately 2300 K prior to flow establishment, showing an increased production of CN due to wall temperature. Lewis *et al.* [14] investigated CN Violet emissions for the same model for wall temperatures ranging from 1770 K to 2410 K. More recently, Lewis [54] used similar models heated to 3200 K, to evaluate the difference in CN production between air and nitrogen flows (see Figure 2.3). His results indicate a divergence from traditional surface kinetic models by demonstrating a decrease in oxidation rate above 2500 K.

Though valid as a proof of concept, the existing shape is not realistic in planetary entry scenarios. The surrounding flow and heat flux incident on the model is artificial due to the difference in geometries compared with entry vehicles. It is unusable for comparison with flight away from the stagnation line. The asymmetric nature of the surrounding flow makes it difficult to simulate numerically, proving unhelpful for the creation of more accessible two dimensional test cases, as shown by Mora-Monteros *et al.* [55].
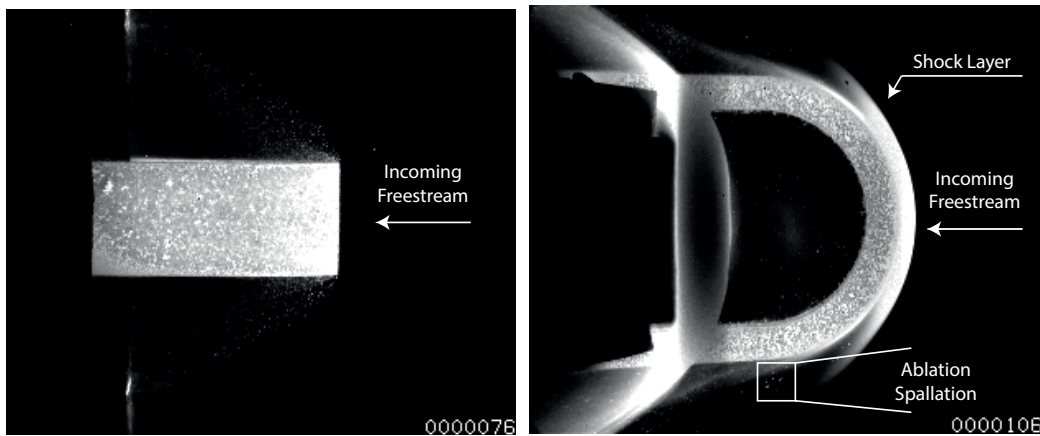
a) Visible spallation during shock arrival (top).   b) Quasi-steady shock layer (side).

Figure 2.3: High speed footage of flow establishment over semi-hemispherical model at 3200 K. Reprinted with permission from Lewis [54].

Condition Selection

Given that Venus' hot, dense atmosphere will prove a stern test for any entry vehicle, a better understanding of its entry environment is imperative for future

mission design. As explained in Chapter 5, the dense carbon phenolic employed on Pioneer-Venus was not developed or optimised specifically for the mission. It nevertheless managed to match the mission thermal requirements, while at the same time avoiding the imposition of a significant mass penalty on the payload. However, the heat shield used a carbon cloth derived from a specific rayon fabric produced in the 1970s which is unlikely to still be available [8]. NASA is also evaluating the use of aerocapture to place an orbiter around Venus. This process involves lower peak heat fluxes compared to atmospheric entry, but significantly higher heat loads [56]. Using the heritage dense carbon phenolic for aerocapture missions would impose a significant mass penalty, as TPS thickness is proportional to integrated heat load. It is therefore imperative that a medium density carbon phenolic is assessed for this role. A Venusian entry condition will therefore be studied in addition to an Earth re-entry condition, to augment the sparse database of existing radiation data of ablating atmospheric entry.

2.2   NUMERICAL MODELLING

Computational aerothermodynamic simulations are required in parallel to experimental testing to fully understand the complex physics encountered during atmospheric entry. These simulations comprise Computational Fluid Dynamics (CFD) simulations as well as radiation and TPS thermal response modelling. The simulations provide peak temperatures, heat fluxes and heat loads mapped across the vehicle surface which are essential to TPS design. Aerodynamic forces and pressure distributions can be simultaneously calculated, helping to define and optimise vehicle shape contours as well as contributing to trajectory estimation, flight dynamics and thermal control [21].

Being a great deal more economical than ground or flight tests, computational aerothermodynamics are used to study feasibility, design and margining as well as post-flight analyses. Anderson [1] identified the ablative heat shield used on the Galileo probe as the first to have been designed using numerical methods. However, this choice was most likely enforced due to an entry velocity of $47\,km{\cdot}s^{-1}$, which is to date unattainable in ground testing facilities. Unfortunately, these tools underpredicted heat flux at the frustum, leading to heavy recession at the shoulder [57]. It is thus generally accepted across the community that further development, verification and validation is required before numerical simulations can supplant the wind tunnel.

The flow is modelled using numerical solutions to the governing equations de-scribing the conservation of mass, momentum and energy. The free-molecular flow first encountered upon entering a planetary atmosphere is modelled by solving the Boltzmann equation using statistical methods [58]. Lower heating rates at high altitudes mean that these analyses are reserved for aerodynamic evaluations. Critical to heat shield design, the point of peak heating occurs fur-ther along the trajectory in the continuum hypersonic flow regime. This flow is well described by the compressible Navier-Stokes equations, which are derived by the application of the continuity equation to the conserved quantities of mass, momentum and energy (further detailed in Section 4.2) and will be the area of focus for this thesis. This equation set must be mathematically closed using ap-propriate physical models for the high temperature shock layer [59].

2.2.1 *Physical Models*

Gnoffo [21] put the choice of physical models for an aerothermodynamic flow simulation down to a combination of "flight environment, TPS and desired accuracy". Computational cost is directly proportional to the accuracy of physical modelling. Even though computational aerothermodynamics continues to evolve and develop and has vastly improved in accuracy since the the Galileo probe, entry vehicle design is still largely based on semi-empirical correlations, simplified tools and a heavy dose of conservatism. Various assumptions such as thermochemical equilibrium, frozen flow, tangent slab radiation transport or a viscous shock layer are made to reduce the calculation time [21].

To achieve the requisite accuracy in resolving the complex physico-chemical processes occurring in a shock layer with acceptable computational cost, nu-merical calculations tend to simulate a single point along a vehicle's trajectory in steady state. The chemistry model is defined to include all component species, reactions and kinetics and closely linked to the selected equation of state. Thermal non-equilibrium is accounted for by energy exchanged between thermal modes. Critical to the calculation of heat fluxes for TPS material design, transport properties are defined to describe the formation of flow and energy gradients in the gas via diffusion. High accuracy modelling of these properties is often based on collision data for all the binary interactions occurring in the gas mixture, as a function of temperature [60, 61]. The majority of relevant *collision integrals* have already been widely studied [62, 63, 64].

Simulating the interactions between the plasma and the ablating TPS material further increases modelling complexity. Prior knowledge of the evolution of the TPS material along its flight trajectory is required to be able to calculate surface temperatures and mass flux rates and species concentrations for pyrolysis and char injection into the flow. State of the art thermal response models [18, 65] are used to obtain these values by solving for the conservation of mass, momentum and energy inside the material, accounting for convective and radiative heating at the material surface. The equations used are detailed in Section 7.2.1. The calculated values can then be supplied to the flow simulation via a boundary condition for each conservation equation. Attempts have been made to strongly couple the material response and CFD simulations [66], but this is still a work in progress. Reactions occurring on the material surface, such as oxidation, nitridation and sublimation are often modelled using equilibrium or finite-rate kinetic models [64, 67].

If a significant fraction of the flowfield energy is employed in radiative excitation, a radiative source term should be included in the governing equations of the flow simulation. This avoids saturation of chemical and internal energy mode excitation which then overpredicts the radiation in the flow [68]. According to Gnoffo [21], "the high-fidelity simulation of a radiating flowfield is daunting." Addition of radiation takes an already stiff equation set, comprising the Navier-Stokes equations with finite-rate chemistry and thermal non-equilibrium, and increases the number of physical processes to be modelled by several orders of magnitude. The inclusion of ablation affects the gas composition and fluid gradients and thus adds to the complexity.

Radiation intensity can be studied by solving the radiative transfer equation (Equation 4.19, further detailed in Section 4.4), either along a line of sight or across the flow for a relevant spectral range. Emission and absorption coefficients are required as inputs to this equation. These are calculated by coupling the flowfield solution to external radiation databases such as Photaura [69], PARADE [70] and NEQAIR [71], which model the equilibrium and non-equilibrium excited state population distributions, energy levels and transitions. This data is often based on experimental or theoretical formulations which are not always applicable to the velocity range or atmosphere of interest [68]. Flight or experimental radiation measurements of ablating shock layers provide the best available opportunity for direct comparison with numerically generated intensity spectra. It is thus an extremely active research domain [72, 73],

to validate these both the flow and radiation modelling and reduce uncertainties.

The aim of this work is not to develop these modelling techniques and hypotheses further, but rather to implement them and evaluate their suitability on a case-by-case basis. A brief summary of relevant physico-chemical processes is supplied in Section 4.2.2. Gnoffo [68] presents a comprehensive review of planetary-entry gas dynamics. There is a legacy of simulating radiation measurements in the X2 expansion tube, by use of the `eilmer3` compressible flow CFD code, developed in-house at The University of Queensland [74]. Since this collection of codes was employed in this thesis, the reader is also directed to work by Gollan [20] on the thermochemistry and Potter [69] and Fahy [44] on radiation modelling, for further details on theory and methodology.

2.2.2 Simulation of Experiments

As mentioned in Section 2.1, characterisation of ablative samples such as PICA is often conducted in arc-jets, measuring surface emission and recession, in-depth temperatures and even spallation. It is common to use these measurements for validation of numerical codes. Known pressure conditions, cold-wall heat fluxes estimated using Gardon gauges and the material surface temperature are supplied as boundary conditions to material response codes such as `FIAT` [65]. This allows the comparison of measured data and numerical predictions of in-depth temperature measurements and surface recession. Milos and Chen [75] developed and validated the thermal property database for `FIAT` based on many arc-jet tests over a range of conditions. They obtained good comparisons for thermocouple data with tuned thermal properties. Driver *et al.* [76] however, found recession rates to be underpredicted by between 50 and 150% by `FIAT` during arc-jet shear tests of wedge and swept cylinder samples of PICA. This directly affected the sizing of the PICA heat shield used for the 2012 MSL mission, which was made more conservative.

From the heater to the test section, the flow in an arc-jet is complex and three dimensional, coupled to various non-equilibrium processes and difficult to characterise. Recently, Zhang *et al.* [77] coupled a magneto-hydrodynamic (MHD) solver to a multi-temperature fluid model to describe the evolving flow in a Plasmatron. They showed the often used assumption of local thermodynamic equilibrium to be incorrect for these facilities, particularly at low pressures, potentially leading to mischaracterisation of the flow. Inflow conditions are

often estimated based on a combination of local heat transfer simulation theory [78], experimental measurements and CFD simulations [79, 80]. Mahzari [32] improves on inflow parameter estimation by use of an inverse method. Using this data, he finds better comparison between FIAT simulations and thermocouple data of PICA testing in an arc-jet.

Radiation codes can be validated via comparison with emission spectroscopy measurements from the ablation layer during arc-jet testing. Winter *et al.* [73] fitted numerical spectra to experimental data to estimate post-shock rotational and vibrational temperatures of between 7000 K and 9000 K, suggesting thermal equilibrium in the flow. Macdonald *et al.* [28] compared intensity spectra measured from surface emissions of ASTERM samples heated in an inductively coupled plasma torch to ones calculated by the radiation code SPECAIR. Using black body temperatures estimated by fitting measured intensities to Wein's law, and the chemical equilibrium composition of air, they found good agreement between both data sets. This methodology, however, gives little information about the flow state. Coupling of CFD simulations with radiation databases better describe the flow state and radiative effects in arc-jet experiments is not common.

Gökçen *et al.* [80] conducted coupled fluid-material response analyses of PICA coupons tested in a 33 cm arc-jet nozzle flow. By comparing experimental data with numerical predictions of shape change, surface recession and material thermal response, they showed the importance of numerical analysis to fully understanding the test flow. However, the simulations did not study effects of injection of pyrolysis products into the boundary layer or their interaction with the flowfield. Davuluri *et al.* [81] have coupled a spallation solver to a solution from a hypersonic CFD code to calculate the dynamics and chemical interactions of spalled particles in air and argon arc-jet flows. They studied the production of carbonaceous species upstream and downstream of the shock by varying the spalled particle diameters and ejection velocities.

Accurate prediction of nozzle exit conditions for expansion tubes is equally complex as for arc-jet flow characterisation. James *et al.* [48] have developed Pitot, an equilibrium expansion tube and shock tunnel analysis code that uses the tube configuration parameters and measured shock velocities as an input to calculate the inflow conditions. Alternatively, the one-dimensional Lagrangian L1d solver, used to model piston dynamics, diaphragm rupture and the complex interactions of X2's primary shock wave, has been coupled to CFD simulations

to model the unsteady expansion through the nozzle for high pressure scramjet flows [49], as well as Earth and Mars entry flows [44, 69]. However, good quality comparison to experimental data is hard to attain, due to the complexity of the transient flow processes involved [49]. Thought is also being given to analysing the flow using MHD simulations [82] to better understand its complex interactions.

Palmer *et al.* [83] used CFD coupled to NEQAIR to simulate the relaxation of volumetric radiance measured over a hemispherical model subjected to Mars and Titan flows in X2. Freestream conditions were estimated from measurement of experimental shock speed and pressure. Adequate comparison was seen for experiments with a shock speed of $5.7\,\text{km}\cdot\text{s}^{-1}$. However, once this speed was increased to $7.6\,\text{km}\cdot\text{s}^{-1}$, the quality of the comparison degraded heavily. This discrepancy was attributed to NEQAIR's implementation of the Boltzmann distribution for Mars and Titan flows, which were not able to correctly simulate the non-equilibrium radiation profiles at higher speeds. This feature has been implemented in more recent versions of NEQAIR, and will be used in the numerical simulations proposed in this thesis.

Given the rarity of ablation experiments in expansion tubes, numerical rebuilding of these experiments is not common. Alba *et al.* [84] simulated CN band radiation measurements obtained from the aforementioned experiments by Lewis [14], coupling a 3D CFD solution to NEQAIR. Accurate calculation of the RCC model's material response was not required due to the complex heating environment and extremely short test time. Gas-surface interactions were therefore simulated using finite-rate surface kinetic models, developed by Park *et al.* [64] and Zhluktov and Abe [67], supplied with the temperatures measured at the model surface. The Park model constantly overpredicted radiative heat fluxes. Tuning the nitridation rate, according to values defined by Suzuki *et al.* [85], allowed for better comparison. At the lower end of the range of wall temperature studies, the Zhluktov and Abe model displayed good agreement with the radiative heat fluxes. At higher wall temperatures, the comparison was less adequate. The lack of a nitridation mechanism in this model is suggested as the reason for this discrepancy.

Potter [69] calculated spectra for comparison with shock layer radiation measurements in X2 for a cylindrical model in a Mars atmosphere and a scaled model of the Hayabusa capsule for an Earth re-entry condition. Freestream

conditions were estimated for the flow over the models as mentioned above, by first simulating the primary shock processes using `L1d` and then using `eilmer3` to perform a 2D axi-symmetric simulation of the expansion tube nozzle and test section. A two-temperature model was implemented along with finite-rate gas chemistry to include non-equilibrium effects occurring due to the unsteady expansion. The calculated flow parameters were then used to describe the high enthalpy, non-equilibrium flow over the models. The CFD solution was coupled to the in-house radiation code, `Photaura`, to compare simulated shock layer radiation to experimental spectra. The calculated intensities were found to be one to two orders of magnitude greater than the experimental data in both cases. Good qualitative agreement was however found for the shock stand-off distance (between 9 and 22% less) compared to values inferred from measured spectra.

Fahy [44] compared radiation data from the Hayabusa and Stardust re-entry flights to radiation data obtained from CFD simulations and expansion tube testing at matched conditions. Freestream conditions were estimated using `L1d` and `eilmer3` as above, comparing assumptions of equilibrium and finite rate chemistry. Differences in the flow properties, including temperature, density, pressure rise and velocity, stemming from thermochemical model selection, were deemed to have an insignificant effect on the shock layer properties over an aeroshell model. The equilibrium assumption was therefore selected due to its increased computational efficiency. Lines of sight were drawn through the flow solution, using the `PARADE` and `Photaura` codes to calculate spectral intensities for comparison to experiment and flight. Inadequate comparison was seen between CFD simulation of X2 experiments and the measured data. This was attributed to imperfectly scaled inflow conditions stemming from an incomplete understanding of the flow processes in the expansion tube. Good comparison was found between experimental measurements and CFD of the full-scale flight vehicles and flight measurements, indicating the plausibility of the ground testing methods involved.

Potter [69] allocates the discrepancies between experimentally measured and numerically calculated radiation data to faults in spectrometer calibration. Given that similar discrepancies are found by Fahy [44] with a changed experimental setup, there is a strong suggestion that incorrect characterisation of the fundamental inflow properties and modelling inaccuracies are at fault for weak comparison between the two data sets. To optimise computational efficiency, the numerical simulations proposed in this thesis will therefore use the `Pitot` code in

experimental mode, to characterise the inflow, as it does not quantifiably affect the quality of radiation results.

2.3 SUMMARY

Due to the operating envelope of existing facilities traditionally used for TPS testing, the dearth of accurate experimental data is even more severe for extra-terrestrial conditions. These facilities can attain flight-equivalent peak heating rates and pressures in air by varying the concentration of oxygen. Though this procedure allows accurate simulation of thermodynamic mechanisms, the relevant shock and boundary layer chemistry of alternative atmospheres cannot be recaptured. This affects the accuracy of predictions of phenomena such as surface catalycity and mass loss. The radiative heating rates are typically decoupled and simulated in high-energy laser facilities or solar towers, although the spectrum of incident radiation is not representative.

Characteristic convective and radiative heating can both be simultaneously simulated in the X2 expansion tube. Limited by the short test time, it is the equivalent of simulating the aerothermal environment around a vehicle at a single trajectory point. This review, in part, summarises previous X2 campaigns which provide a good foundation for further investigation of resin decomposition and radiative blockage due to carbonaceous species in the boundary layer. Though an interesting and useful concept, application of the electrical pre-heating methodology to representative aerothermal testing in expansion tubes requires further tweaking. More representative comparisons are to be found using flight-equivalent geometries, justifying the design, manufacture and testing of phenolic aeroshell models in this work.

The ample suite of available imaging techniques on X2 will be used to evaluate the effects on boundary layer radiation of pyrolytic species from the phenolic aeroshells. All previous ablation experiments in X2 have been conducted under Earth re-entry conditions, at post-peak heating velocities, where pyrolysis would cease to occur. A high speed Venusian entry condition will be studied in addition to an Earth re-entry condition, to augment the sparse database of existing radiation data of ablating atmospheric entry, as per *Objectives O.1* and *O.2*.

Computational aerothermodynamics is proposed as a replacement for ground and flight testing due to its improved economics and time frames. However, be-

fore this is possible, these tools need to be rigorously verified and validated to an acceptable level. A good foundation already exists for the simulation of X2 experiments using CFD, finite-rate surface kinetic and radiation modelling. The difficulty lies in the correct characterisation of the freestream parameters, which can drastically effect the final result. Several methodologies have been proposed and applied, with equivalent results. For computational efficiency, the proposed numerical study of both Earth and Venus conditions will estimate freestream properties using `Pitot`. In order to achieve *Objective O.3*, 2D axisymmetric simulations of the decomposing phenolic aeroshells will be carried out on the `eilmer3` compressible CFD code comparing two finite-rate surface kinetic models to represent the decomposing model. Radiation will be modelled along a line of sight representative of the experimental layout, for spectral comparison.

EXPANSION TUBE TEST CAMPAIGN[1]

3.1 INTRODUCTION

Experiments were carried out in the X2 expansion tube to evaluate the radiative emission and blockage caused by the injection of pyrolysis gases, formed by the decomposing phenolic aeroshell models, into the hot boundary layer. The design and manufacture of these models along with tested heating methodologies are discussed in this chapter. For sizing and development of spacecraft TPS, it is most important to know the behaviour of these materials under extreme thermal duress. The selection and testing of flow conditions, representative of high heating rates for Earth and Venus entry, is discussed. As mentioned in Section 2.1.2, UV and IR emission spectroscopy and high speed video were used to capture the radiation emitted from the high temperature boundary layers. The set-up, alignment, calibration and imaging procedures are outlined. The operation of the X2 facility is then detailed, including triggering of the measurement systems as well as post-test shock speed calculation. Finally, all experimental results and analyses are presented and discussed.

3.2 EXPERIMENTAL METHODOLOGY

3.2.1 *Model Development and Bench Testing*

An attempt was made to reuse the electrical pre-heating technique [13, 14] for which a fibreglass reinforced phenolic sphere-cone was cast (Figure 3.1a) with a nose radius of 19.5 mm, diameter of 60 mm and a sphere-cone angle of 60°. The chosen shape was similar to that of the Stardust capsule, deviating from previous pre-heating studies in X2, which used semi-hemispherical

---

1 Material from this chapter has been submitted for publication in the following articles,

- N Banerji, P Leyland, E J Fahy and R G Morgan. Venus Entry Flow Over a Pyrolyzing Aeroshell in the X2 Expansion Tube. Journal of Thermophysics and Heat Transfer, 2017.

- N Banerji, P Leyland, E J Fahy and R G Morgan. Earth Re-entry Flow Over a Pyrolyzing Aeroshell in the X2 Expansion Tube. Journal of Thermophysics and Heat Transfer, 2017.

models. The experiments were designed with ease of numerical rebuilding in mind, facilitated by the axisymmetry of the aeroshell shape and resulting two-dimensional behaviour of the surrounding flow. The aim was not to scale the exact capsule geometry, as matching flight conditions was not in the scope of this thesis. Model versatility was a requirement in its design, as it was used in both Venusian and Earth entry conditions.

Due to its low thermal and electrical conductivity, the use of a fibreglass shell ensured the preservation of model structural integrity, allowing the models to be reused several times. Approximately 25% by weight fibreglass content was used. Sixteen plies were laid up in a $[0/90]_{4s}$ cross-plied configuration and the model was vacuum treated (Figure 3.1b) and then cured for 60 min at 60 °C (Figure 3.1c). The mould was designed with a draft angle of 1° to allow for easy removal of the model after curing. The initial composite was then de-moulded, as shown in Figure 3.1d, after which it was baked once more at 80 °C for 240 min to allow the resin to set fully.

A 10 mm wide and 2 mm deep groove was then milled across the surface, with two 5 mm diameter holes drilled on each end of the groove. Six nichrome wires, attached in parallel, were set in these grooves, to be connected to electrodes behind the model. Nichrome was chosen over carbon fibre (previously used for electrical pre-heating in X2) for several reasons. The malleability of nichrome made it easy to manipulate in the groove and small diameter holes. The temperatures needed to produce phenolic pyrolysis are between 600 K and 900 K, well within the operating temperature range of nichrome (up to 1400 K). The extra heating allowed by the carbon fibre was therefore not needed. A large number of carbon fibre plies would also have been required to reduce electrical resistance to allow a significant flow of current through the system. This would have decreased ease of manufacturing. Further details of the materials used to manufacture the phenolic aeroshells are given in Table C.1. Technical drawings of the mould and models are provided in Appendix D.

Phenolic resin mixed with chopped fibres was then layered over the wires, filling in the groove. The model was cured in the mould as before. The result is shown in Figure 3.1e. A DC rectifier, capable of supplying up to 250 A at 12.5 V was connected to the circuit. The aim was to resistively heat the wires just prior to the flow establishment in X2 and heat the phenolic resin, which was to decompose and outgas at a predetermined temperature (see Figure 3.2b). Due to the
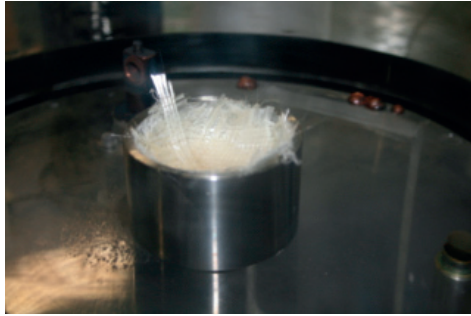
a) Fibreglass shell allowed to set in aeroshell shaped mould.
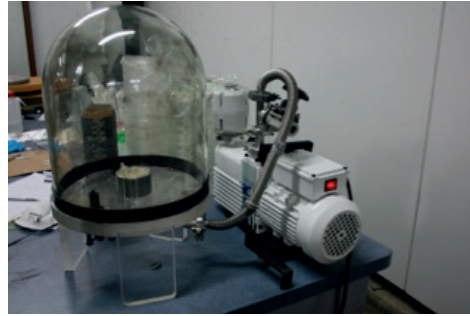
b) Fibre-resin mixture vacuum treated to remove air bubbles.

c) Composite structure cured at 60 °C for 60 min.
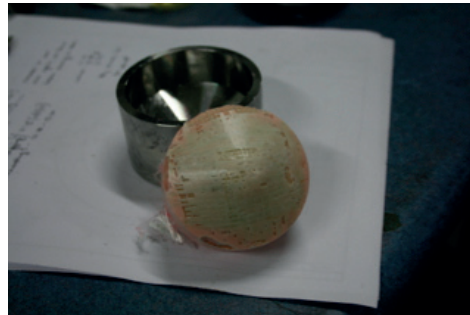
d) Initial composite shape taken out of mould before being baked once more at 80 °C for 240 min.
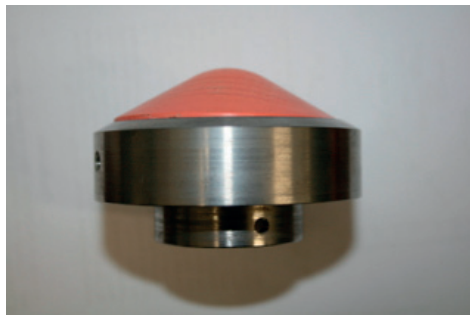
e) Final phenolic aeroshell model, mounted in holder.

Figure 3.1: Model manufacture.

a) Phenolic model mounted in the X2 test section.

b) Pyrolysing model during heating under atmospheric pressure.

c) Charred model, with cracked and dispersed phenolic above heated strip.
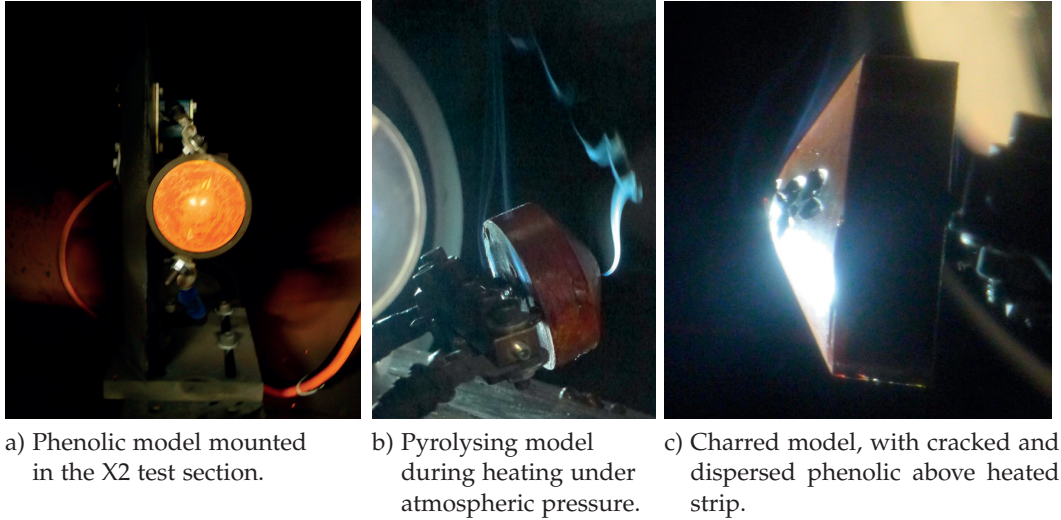
Figure 3.2: Bench top heating tests of the carbon phenolic composite model.

brittleness of the phenolic resin, pre-heating the model caused significant fracture and dispersion at the surface (Figure 3.2c), shifting the model nose from the spectrometer slit. Therefore, the radiation measurements taken were no longer of the desired region. Chopped fibre volume fraction was increased in the flow facing layer to delay resin break-up. However, its occurrence was still unpredictable and sudden, making it impossible to control surface temperature. The model was therefore shock heated similarly to Buttsworth *et al.* [51]. The hot flow increased the surface temperature and caused the model to pyrolyse.

3.2.2 *Condition Selection and Testing*

Development of a flight-equivalent condition for an expansion tube requires rigorous and detailed analysis [44, 48] and is not within the scope of this work. High enthalpy conditions were therefore selected from the existing database, to be able to evaluate phenolic pyrolysis at a proximity to peak-heating rates for Venus and Earth entry. A test condition developed by de Crombrugghe [47] for high speed Venus entry, named V1 in this work, was thus applied. For Earth entry, a condition close to peak heating on the trajectory of the Hayabusa capsule, developed by Fahy [44], named E1, was also adopted. For both conditions, the tube was sealed with the shock tube separated from adjacent sections by the pri-

mary and secondary diaphragms, made of 2 mm thick mild steel and aluminium foil respectively. The gas fill pressures for both conditions are summarised in Table 3.1.

Table 3.1: Gas compositions and fill pressures and mean experimental shock velocities.

	Reservoir	Driver	Shock tube	Acceleration tube	Primary shock speed	Secondary shock speed
Earth (E1)	6.85 MPa, air	92.8 kPa, 100% He	13 500 Pa, air	17 Pa, air	4545 m·s^{-1} ±42	9805 m·s^{-1} ±105
Venus (V1)	6.85 MPa, air	92.8 kPa, 100% He	3600 Pa, 96% CO$_2$ - 4% N$_2$	40 Pa, air	5300 m·s^{-1} ±43	9347 m·s^{-1} ±96

Venus Condition

The acceleration tube and test section were held at a pressure of 40 Pa, while the shock tube was filled with 3.6 kPa of the Venus-like 96% CO$_2$- 4% N$_2$ test gas. Air was pumped in behind the piston at 6.85 MPa and the 100% helium driver gas was added at 92.8 kPa. Test flow conditions were estimated, prior to the main experiments, from nine 15° pitot cone-heads in a vertical rake spaced at 18 mm and positioned just downstream of the nozzle exit plane. This also allowed an estimation of steady test time, which can be estimated as $t\sim$ 70 μs from Figure 3.3. Pitot transducers 3 to 9 collect similar data, giving a core flow diameter of approximately 108 mm, which is then the limiting factor for the diameter during model design. The flow Mach number of 10.6 is within the design range of the facility nozzle. Both radiation and pressure measurements were triggered using a photodiode aimed at the nozzle exit combined with a trigger connected to a databox. Once triggered (Figure 3.3), a delay of 40 μs was allowed for the flow to settle before it was considered steady.

Earth Condition

To simulate Earth re-entry, the selected condition required the acceleration tube and test section to be held at a pressure of 17 Pa, while the shock tube was filled with 13.5 kPa of air. Air was pumped in behind the piston at 6.85 MPa and the 100% helium driver gas was added at 92.8 kPa. From the pitot rake, as before, core flow diameter was estimated as 144 mm. Test time is estimated as 100 μs
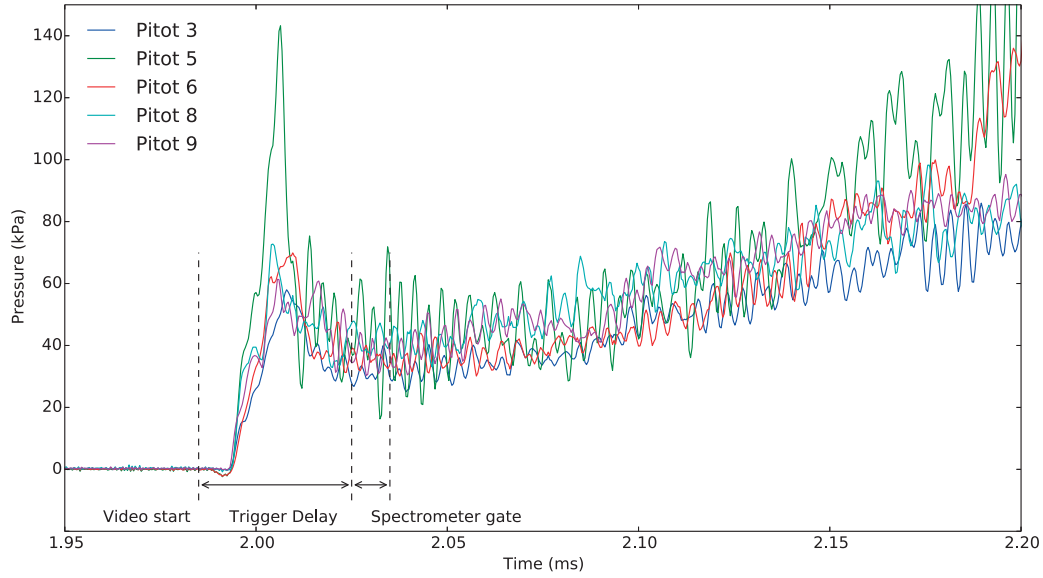
Figure 3.3: Pitot traces for V1 condition test shot x2s2488 (raw data from de Crombrug-ghe *et al.* [47]).
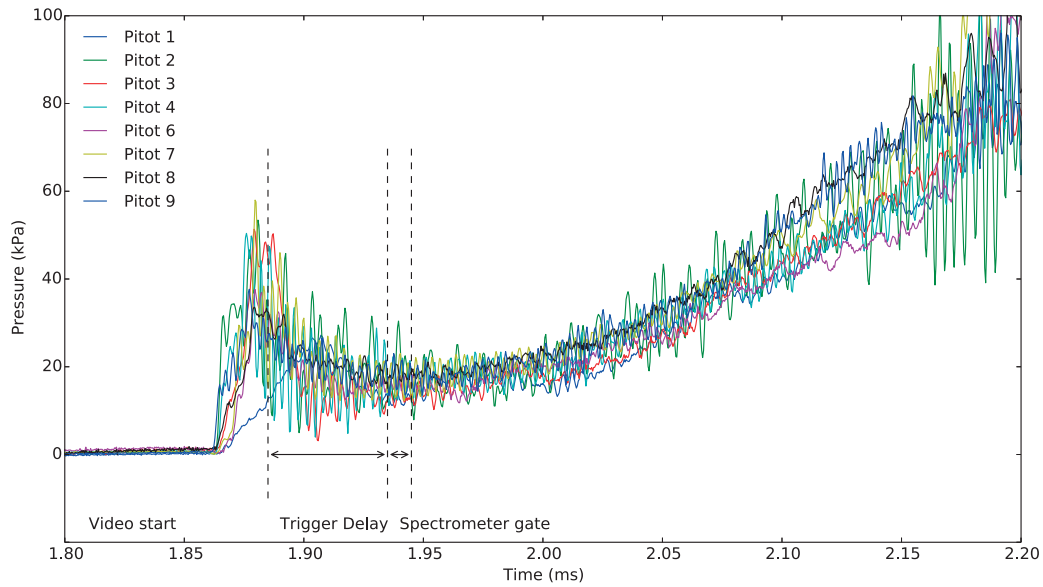
Figure 3.4: Pitot traces for E1 condition test shot x2s2312 (raw data from Fahy [44]).

from Figure 3.4. The calculated flow Mach number of 12.6 is larger than the nozzle design Mach number of 10. However, since the Mach 10 nozzle is the only one currently available for X2 and previous successful studies have been conducted using it, it is assumed that the nozzle will perform predictably. Once triggered (Figure 3.4), a delay of 50 µs was allowed to avoid the flow establishment period and to allow it to steady.

Freestream Characterisation

Freestream conditions are needed to be able to characterise the flow over the model. This is especially important for the numerical rebuilding conducted in Chapter 4. As discussed in Section 2.2.2, several methodologies have been used to obtain these values. The first method uses the `Pitot` tool [48], an equilibrium expansion tube and shock tunnel analysis code. It has the ability to rapidly obtain information about the flow state using simple inviscid analytical methods by modelling only the primary physical processes. Using an iterative process, the code helps experimenters design the flow conditions in theoretical mode. However, in experimental mode, it works in reverse, using the tube configuration parameters and measured shock velocities as an input to calculate flow temperature, density and chemical composition. However, the inherent assumption of an inviscid flow across the unsteady expansion does not account for the boundary layer formation in the tube and nozzle, which directly affects the flow. This is accounted for by manually adapting the nozzle area ratio in the code, checking the nozzle exit pressure against those measured by the pitot cone-heads during testing.

The more rigorous method includes coupling a one dimensional Lagrangian solver, which describes the primary shock processes, to a full scale CFD simulation of the nozzle and test section, to describe the unsteady expansion [44, 49, 69]. This method should be able to capture important flow effects possibly masked by `Pitot`. However, as shown by Fahy [44], this strategy, though more detailed and computationally intensive, does not significantly decrease the error in the calculation of numerical spectra, which is the ultimate aim of this work.

For simplicity, the freestream conditions were therefore calculated using `Pitot` and are presented in Table 3.2. For each experiment, the shock speeds were evaluated by resolving the rise in pressure with time as measured by the PCB pressure transducers set into the walls of the shock and acceleration tubes. Pri-

mary shock speeds were measured in the shock tube. Secondary shock speeds were measured across the final three transducers in the acceleration tube, before the nozzle entrance. The mean shock speeds across the entire test campaign are provided in Table 3.1. The larger standard deviation for the E1 condition demonstrates a higher variance in shock speeds when compared to the V1 condition. This is most likely due to difficulty in achieving and then stabilising at the lower pressures in the acceleration tube and test section for the E1 condition.

Table 3.2: Free stream parameters for Venus (V1) and Earth (E1) entry conditions in X2, estimated using `Pitot`.

	T_∞ (K)	p_∞ (Pa)	ρ_∞ (kg·m^{-3})	v_∞ (m·s^{-1})	X_{CO_2}	X_{CO}	X_{N_2}	X_{NO}	X_{O_2}	X_O
Venus (V1)	2780.9	4064.0	5.1×10^{-3}	9347.2	0.2622	0.4433	0.0193	0.005	0.168	0.1023
Earth (E1)	1976.1	1447.5	2.5×10^{-3}	9805.1	-	-	0.7858	0.0069	0.2053	0.002

Wall Temperature Estimation

Since the thermal properties of the actual phenolic resin supplied were unknown, mean values from literature were used [86]. The thermal diffusivity of a typical carbon phenolic TPS is $\alpha \sim 10^{-6}$ m^2·s^{-1}, giving a penetration distance of approximately $\sqrt{8\alpha t_{test}} \sim 24$ µm for the V1 flow condition with a steady test time, $t_{test} \sim 70$ µs. For the E1 condition, with a test time of approximately 100 µs, a penetration distance of 28 µm is similarly calculated. It is therefore reasonable to estimate the rise in surface temperature using the one dimensional semi-infinite approximation described below,

$$\Delta T_{test} = \frac{2\dot{q}_{stag}}{\sqrt{\pi}\sqrt{\rho ck}}\sqrt{t_{test}} \tag{3.1}$$

Using Sutton and Graves' empirical correlation [87] for stagnation-point heat transfer in CO_2-N_2 atmospheres, heat flux incident on the model, $\dot{q}_{stag}$, is estimated as 7900 W·cm^{-2} for the V1 condition. Taking thermal effusivity as $\sqrt{\rho ck} \sim$ 2200 kg·s$^{-5/2}$·K^{-1} [86], a temperature rise of between $300 - 350$ K is estimated, resulting in a wall temperature of approximately 600 K. For the E1 condition, the model surface temperature is similarly calculated for an incident heat flux of 5900 W·cm^{-2} to also be approximately 600 K for a test time of $t_{test} \sim 100$ µs.

3.2.3 *Optical Setup*

Emission Spectroscopy

Once the model was mounted in the X2 test section, the optical systems were set up. The aim of both sets of experiments was to measure emission from the phenolic products added to the flow through surface reactions. To achieve this aim, radiation from the ablation layer was measured in the ultraviolet and visible-near infrared wavelength ranges. Oxidation and nitridation of the phenolic surface makes it prudent to search for CN, C_2 and C emissions in the ultraviolet. Due to the existing predominance of CO_2 in the V1 condition, relative changes in the concentrations of these species is important. For the E1 condition condition, carbonaceous species are only present in trace amounts due to contamination in the tunnel and therefore measuring the absolute emission of the aforementioned species is of great interest. The layout of the optical setup is illustrated in Figure 3.5, with the UV spectrometer to the left of the tunnel and the high speed camera and IR spectrometer to its right. VnIR radiation from the ablation layer was measured through a perspex window for a narrow horizontal strip parallel to and including the stagnation streamline. Ultraviolet radiation was similarly measured through a fused silica window.

Table 3.3: Summary of distances (in mm) between optical components along the light path for both spectroscopy systems to achieve a magnification of 2 : 1.

Component	Model - Focusing mirror	Focusing mirror - Turning mirror	Turning mirror - Periscope (top)	Periscope (top) - Periscope (bottom)	Periscope (bottom) - Spectrometer
UV	750	151	480	230	633
IR	750	270	380	180	670

Due to the small size of the models and the consequent narrow boundary layer, a magnification of 2 : 1 was achieved by focusing the radiation using a concave spherical mirror with focal length 500 mm. A turning mirror and a periscope assembly (consisting of two flat mirrors) were then used to rotate the image by 90° onto the vertical spectrometer slit. The captured light was spectrally resolved with an Acton Research Spectro Pro 2300I spectrograph using a 600 lines/nm diffraction grating coupled to a Princeton Instruments PI-max Intensified charge-coupled device (ICCD) camera. The horizontal plane imaged by the cameras is shown in Figure 3.6. All optical components are detailed in Table 3.4. The path
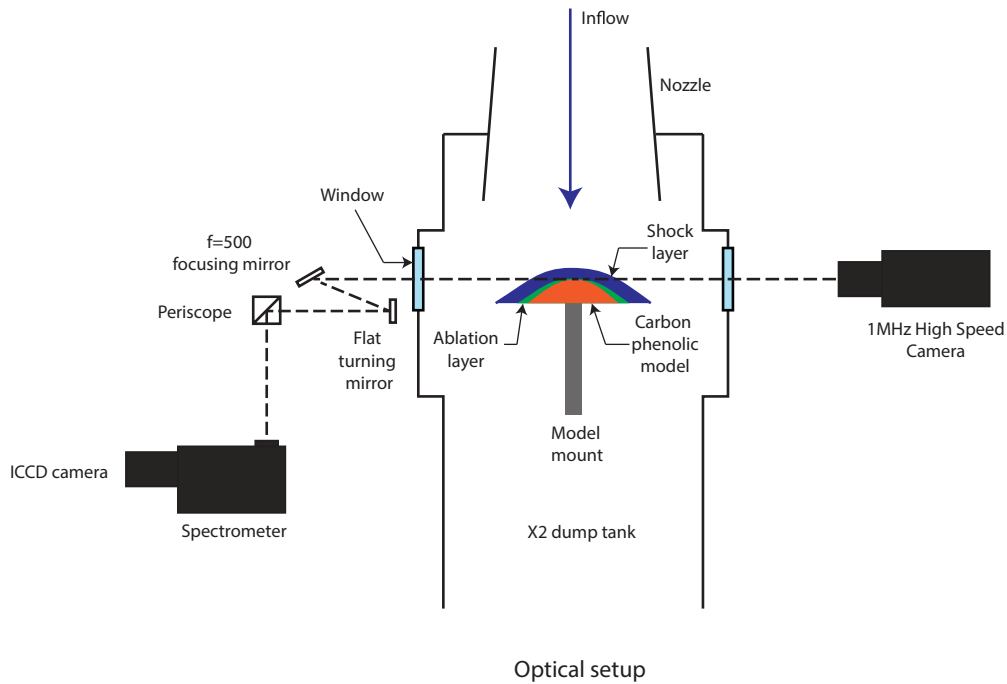
Optical setup

Figure 3.5: Illustration of the optical setup utilised for UV and VnIR radiation measurements (adapted with permission from Fahy *et al.* [44]). Both spectroscopy systems have the same layout on opposite sides of X2. The VnIR system on the right of the tube has been omitted for clarity.

lengths set between optical components are given in Table 3.3. The settings for both spectrometers are provided in Table 3.5.

High Speed Video

A Shimadzu HPV-1 high speed camera fitted with a Zoom Nikkor $100-300\,\mathrm{mm}$ f/5.6 s lens was positioned on a raised mount to image the model via a flat silver coated turning mirror placed above the test section. The data was used to evaluate the steadiness of the flow and visualising any erosion of the phenolic model surface. After correction of the image for orthogonality and contrast, shock stand-off distances were estimated during steady flow via use of the Canny Edge detection method [88] which identifies intensity gradients across pixels. The camera has the capacity to store 100 frames of data at a resolution of 312×260 pixels. For all the experiments conducted in this test campaign, a frame rate of $500\,\mathrm{MHz}$ was used, with zero delay from the trigger signal and
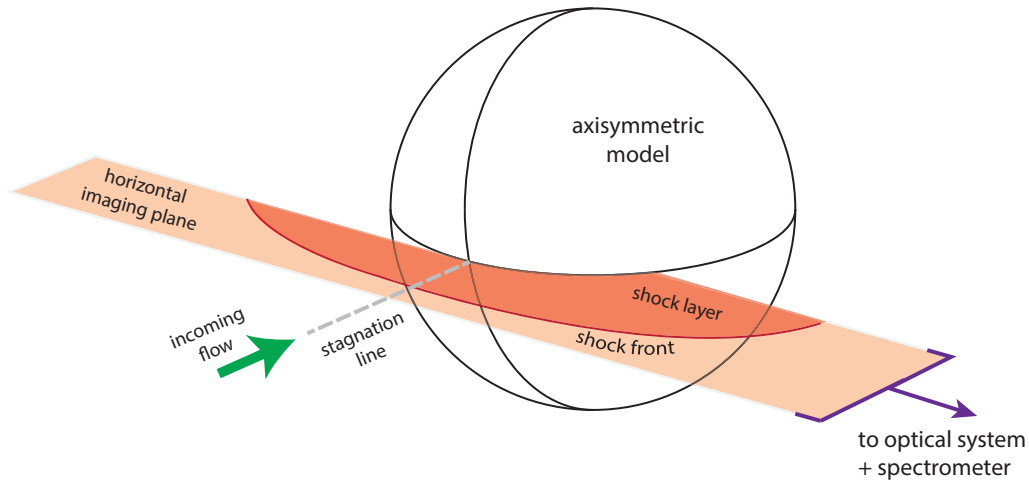
Figure 3.6: Illustration of the horizontal plane imaged via UV and VnIR spectroscopy systems. Used with permission from Fahy [11].

20 frames kept pre-trigger. Using an exposure time of 1 µs, the chosen settings recorded a frame every 2 µs, starting about 40 µs before shock arrival. Typically, for each shot, the HPV−1 recorded the arrival of the primary shock wave and then the establishment of the test gas bow shock around the model, the entire steady test time followed by the arrival of the driver gas.

Table 3.4: Summary of optical components used in both spectroscopy systems.

	Component	Radius	Material/Coating	Supplier Code	Number
UV	Tunnel window	97 mm	Fused Silica	-	1
	Flat turning mirror	25.4 mm	Enhanced aluminium	Thorlabs PF20 − 03−F01	4
	Concave focusing mirror	25.4 mm	Enhanced aluminium	Newport 20DC1000AL.2	1
IR	Tunnel window	97 mm	Perspex	-	1
	Flat turning mirror	25.4 mm	Protected silver	Thorlabs PF20 − 03−P01	3
	Concave focusing mirror	25.4 mm	Protected silver	Newport 20DC1000ER.2	1
	Periscope assembly	-	-	-	2

Table 3.5: Spectrometer settings.

Spectrometer	Venus		Earth		
	UV	IR	UV	IR	IR
Centre Wavelength (nm)	440	656	415	656	780
Gain (dB)	110	150	220	150	150
FWHM (Å)	4.1	4.5	2.5	2.0	3.0
$\Delta\lambda$ (nm/pixel)	0.14	0.137	0.14	0.134	0.126
Δx (µm/pixel)	26		26		
Grating (lines/mm)	600		600		
Effective wavelength range (nm)	80		80		
Slit width (µm)	50		50		
Exposure time (µs)	10		10		
Trigger delay (µs)	40		50		

Calibration

Measured radiation data is quantified via intensity calibration for later comparison with numerically simulated spectra. The ICCD detector recorded a signal in counts related to the radiation emitted from the ablation layer during the steady test time. This signal was converted to spectral radiance (in $W \cdot m^{-2} \cdot nm^{-1} \cdot sr^{-1}$ or similar) via calibration by comparison with a light source of known intensity. Using Equation 3.2, a calibration factor is applied to the ratio of the experimental, f_{exp}, and calibration images, f_{cal}. This term is then multiplied by the ratio of exposure times t_{cal} and t_{exp}.

$$I(\lambda, z) = C \cdot \frac{f_{exp}(\lambda, z)}{f_{cal}(\lambda, z)} \cdot \frac{t_{cal}}{t_{exp}} \qquad (3.2)$$

Intensity calibration can be conducted using two types of light sources, one with a known spectral irradiance at a specific distance from the source, and the second with a known spectral radiance. Using a light source with a known spectral irradiance such as a tungsten lamp, results in a complicated procedure (detailed by Jacobs [89]) for the calculation of the calibration factor, C, where each optical component in the system needs to be calibrated individually. On the other hand, by placing a light source with a known spectral radiance in the position of

the object to be imaged (i.e. the stagnation point), the calculation of C is greatly simplified by accounting for the solid angle, magnification, reflectivity and transmissivity of the whole system at once. The calibration factor is then a function of lamp spectral radiance as a function of wavelength, L_{cal},

$$C_i = L_{cal}(\lambda) \tag{3.3}$$

A comparison of the two methodologies has been conducted by Fahy [44] and by Lewis [90], showing them to be equivalent. Therefore, to calibrate the data recorded in the experiments presented in this work, a Labsphere CSTM-LR-2Z-4 Integrating Sphere of a known spectral radiance (Figure 3.7) was placed in the position of the model, accounting for all of the components along the optical path in the recorded image. From this image and the known spectral radiance profile of the source, a pixel-by-pixel calibration matrix was used to quantify the raw data. At 2 : 1 magnification, the integrating sphere image through the spectroscopy system illuminated the entire ICCD.

Background counts occur due to thermal noise even though the ICCD is cooled to 253 K during all experiments. These were therefore recorded from the regions on the ICCD not exposed to incoming light, and subtracted from the images during post-processing. Cosmic rays occasionally cause bright spots on the ICCD, but these could also be removed during post-processing. Wavelength calibration was performed using a light source with two known spectral lines, such as a fluorescent lamp.
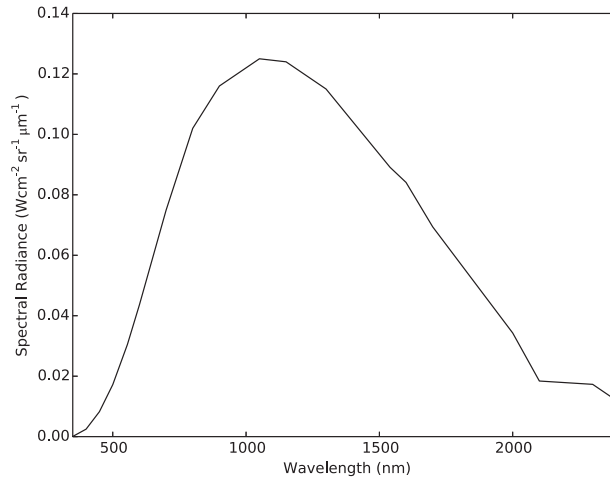
Figure 3.7: Integrating Sphere spectral radiance.

3.3   results and analysis

The experimental campaign consisted of a total of 24 shots, with half investigating the V1 condition and the remainder reserved for the E1 entry condition. For each condition, half the shots were fired on to a cold steel model, as a control for comparison with the shock heated carbon phenolic models, which were in place for the remaining shots. This allowed for repeated tests using the same conditions. The majority of shots gave good quality data, the best of which were selected for further analysis and presented in this thesis. In this section, spectra are first presented from the V1 condition test campaign, and later from the Earth campaign. The spectra are presented first in absolute units and then normalised, for relative comparison between the steel and phenolic models. The atomic emission lines were identified by comparison with the NIST Atomic Spectra Database [91] and molecular emission features were identified by referring to previous work [45, 92]. All spectra are extracted from radiation measurements taken at a distance of 0.1 mm from the respective model surface, which are spatially averaged over ±1 pixel, giving an averaged spatial resolution of 0.08 mm.

3.3.1   *Venus Condition*

Stills taken by the Shimadzu HPV-1 high speed camera demonstrate the start and end of the steady test time during the V1 flow condition, shown in Figure 3.8a and 3.8c respectively. The shock stand-off distance can be estimated at approximately 1.9 mm through use of a Canny edge detection filter as seen in Figure 3.8e. Experimental UV spectra centred at 440 nm are presented in Figure 3.9. These data are measured horizontally along the stagnation line, at a distance of 0.1 mm from the steel and composite model surfaces. In both spectra, CN Violet and C_2 Swan bands are visible as well as the N_2^+ bandhead. There are two peaks at 394.4 nm and 396.2 nm corresponding to Al contamination due to residue from the burst secondary diaphragm. Eichmann [45] studied the sources for contamination in X2 experiments and attributed the Fe and Fe^+ lines to the steel models used. However, these lines are just as evident while using the phenolic model. The majority of this contamination must be iron stripped from the tunnel walls or from the primary diaphragm.

In Figure 3.10, the two spectra have been normalised by the maximum intensity of their highest Al peak to remove the effect of temperature differences caused by shot to shot variation. It can be seen that the N_2^+ First-Negative $\Delta v = 0$

bandhead gains in intensity, CN Violet intensity is unchanged, while the C_2 Swan bands lose intensity in the presence of the composite model. A similar phenomenon was noted by Eichmann [45] who suggested reduced CO_2 concentration of the test gas as a reason for weak CN and C_2 band structure in Martian flows. A reduction in CO_2 could be caused by a leak in the gas mixture storage facility and would leave more unreacted N_2 in the flow to ionise. Given the high density and velocity of the V1 flow investigated, along with the comparatively high test section pressure of 40 Pa (compared to 10 Pa used by Eichmann), this is certainly a possibility. However, given the stasis of CN Violet band intensities between shots, C_2 dissociation could also be linked to creation of other carbon based species after reaction with hydrocarbon components of the phenolic resin that are not picked up in this spectrum, or masked by the contaminants.

Spectra recorded in the visible wavelength range centred at 656 nm, for the cold steel and composite models are presented in Figure 3.11. Both spectra show the presence of O and C atomic lines, as well as CN Red bands. The higher level of background radiation seen in both plots is inherent in measuring radiation in the visible spectrum and likely stems from extraneous sources.

Both of these spectra are normalised and compared in Figure 3.12. No change is observed for the CN Red band and C atomic line spectra between the two data sets. However, an increase in peak spectral radiance for the atomic O line at 645.598 nm is seen in the presence of the composite model. This could be attributed to differences in the secondary shock speed, which affects the post shock temperature resulting in changes in chemistry, species concentrations and atomic emission. However, in Figure 3.11 the quoted values of $v_{s,2}$ are nearly identical. Inaccurate selections in pressure trace rises for shock speed calculations could mask variations in shot speed. Other causes for this discrepancy could be inconsistencies in fill pressures, small leaks or faults in the diaphragm materials or manufacturing process or a shift in imaging location under vacuum.
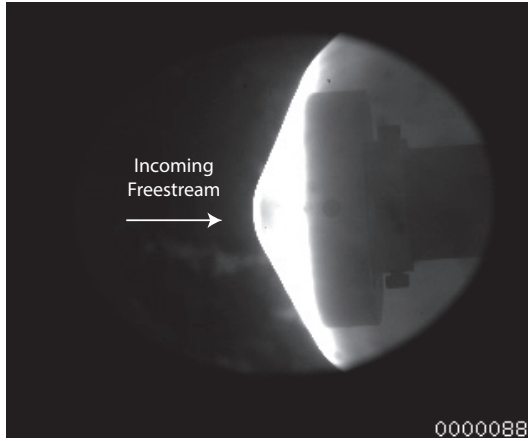
a) Steady test time during V1 flow.
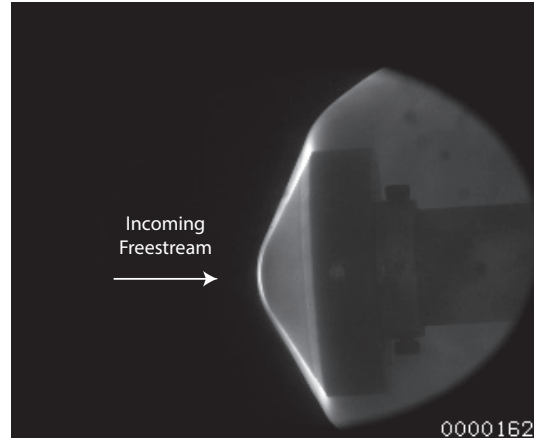
b) Steady flow over steel model in E1 flow.
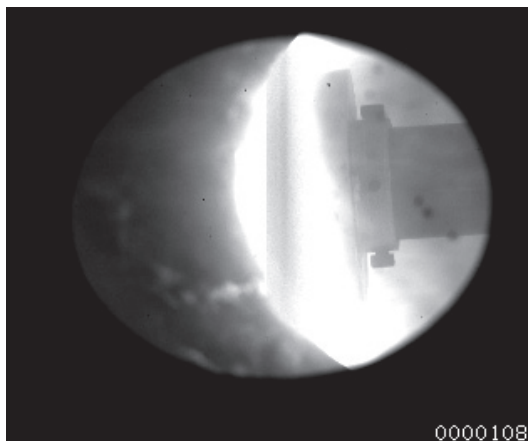
c) End of steady test time during V1 flow.
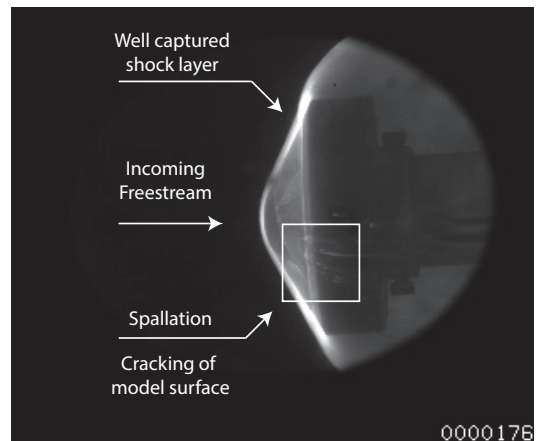
d) Steady flow over phenolic model in E1 flow.
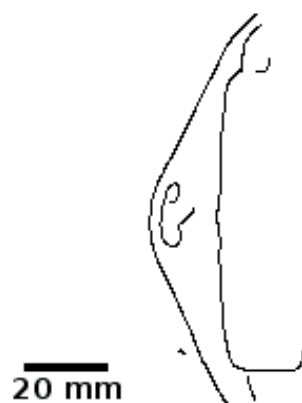
e) Canny edge detection results for a HPV-1 image showing V1 flow steady test time with a shock stand-off of 1.9 mm.
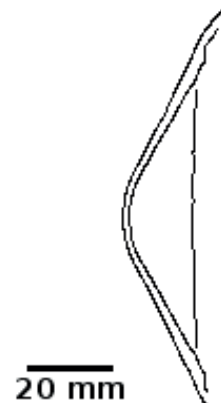
f) Canny edge detection results for a HPV-1 image showing E1 flow steady test time with a shock stand-off of 1.35 mm.

Figure 3.8: Side-on view taken by HPV-1 camera during V1 and E1 flows.
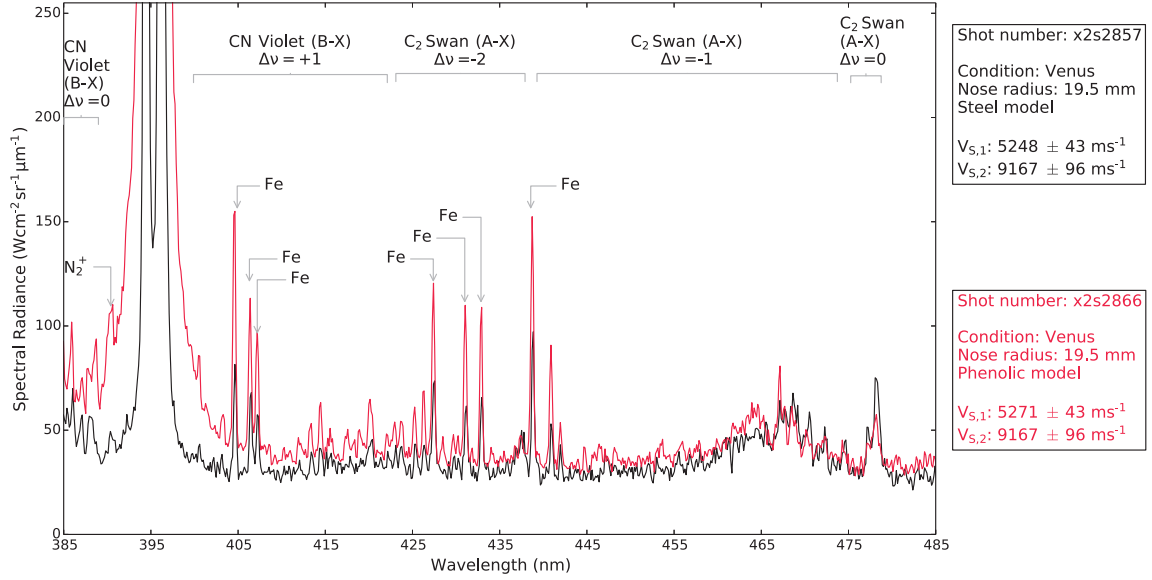
Figure 3.9: UV emission spectra measured at 0.1 mm upstream of steel and phenolic aeroshell model surface for the V1 condition with N_2^+, CN and C_2 Swan band radiation in evidence.
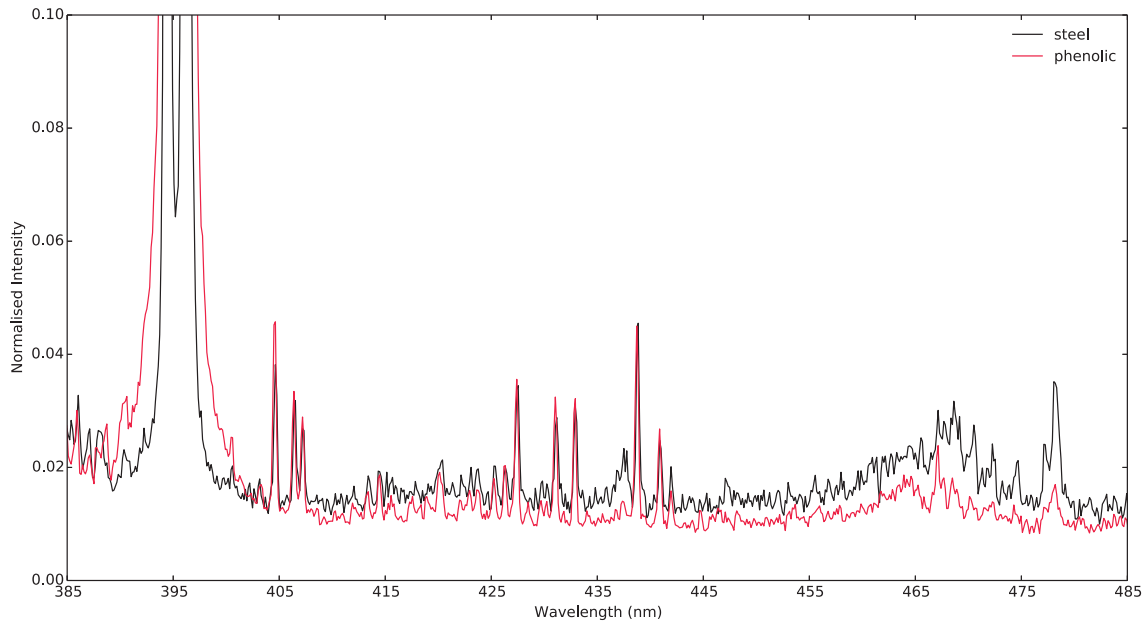
Figure 3.10: Normalised spectra in the UV for the V1 condition with an increase in N_2^+ and a decrease in C_2 Swan band radiation for the phenolic model.
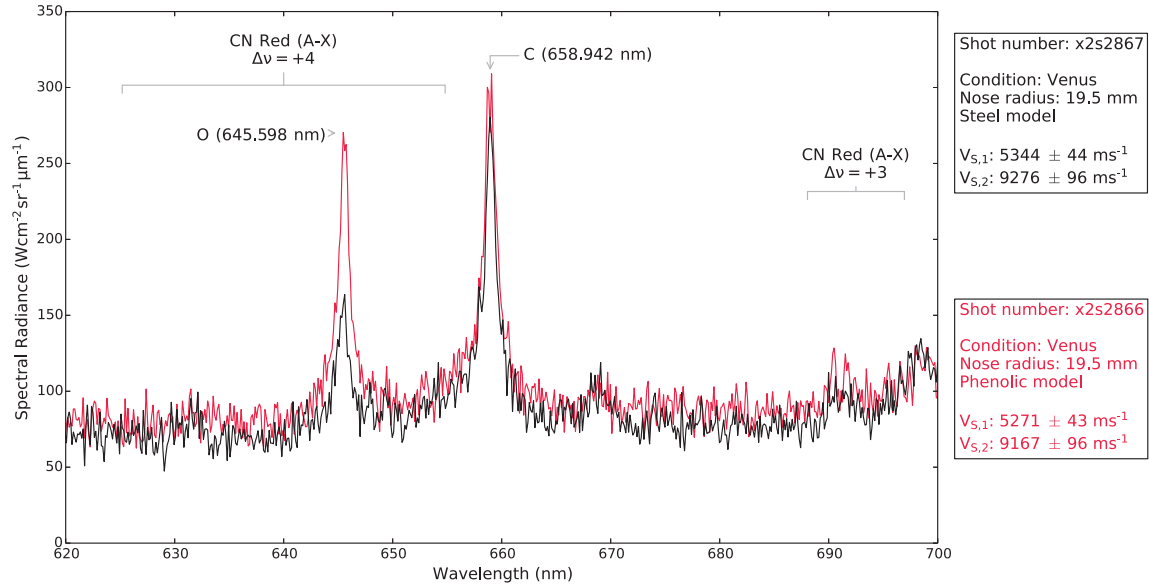
Figure 3.11: Visible emission spectra measured at 0.1 mm upstream of steel and phenolic aeroshell model surface, for the V1 condition with O, C and CN Red band radiation in evidence.
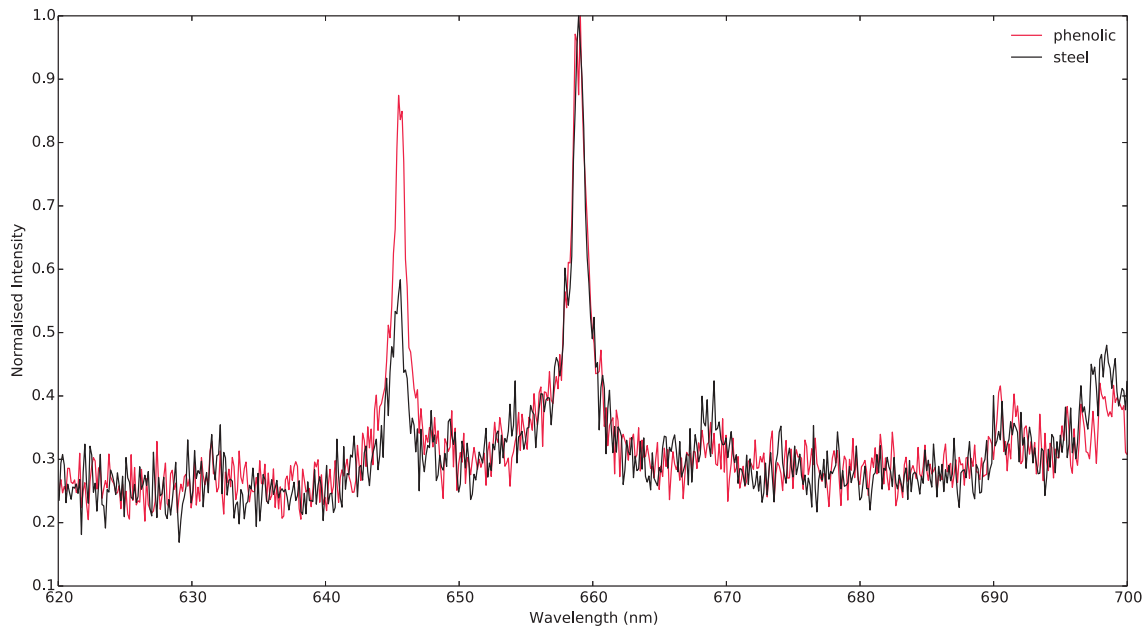
Figure 3.12: Normalised spectra in the visible for the V1 condition showing an increase in O line intensity for the phenolic model.

3.3.2 *Earth Condition*

Experimental UV spectra centred at 415 nm, taken horizontally along the stagnation line, at a distance of 0.1 mm from the steel and composite model surfaces, are presented in Figure 3.13. In this case, the models are subjected to the hypervelocity E1 condition. Once again, the highest intensity lines in both spectra are Al lines emit from the secondary diaphragm. Using the steel model, the only line of interest emitted by the plasma belongs to the N_2^+ First-Negative $\Delta v = 0$ bandhead at 391.22 nm, which is an important marker for non-equilibrium. With the composite model in place, CN Violet $(B - X)$ $\Delta v = 0$ and CN Violet $(B - X)$ $\Delta v = +1$ bands show strong emission. Being present only in trace amounts in the non-equilibrium flow, these carbonaceous species are demonstrably produced by surface reactions caused by interaction of the hot flow and the phenolic resin. Both of the above spectra are normalised and compared in Figure 3.14. The introduction of CN via phenolic pyrolysis is evident in the composite plot.

Experimental spectra centred at 656 nm, measured horizontally along the stagnation line, at a distance of 0.1 mm from the steel and composite model surfaces, are presented in Figure 3.15. Both spectra show oxygen atomic line spectra at 615 nm and 645 nm and a strong N atomic line at 648 nm. The spectra are normalised and plotted in a composite image in Figure 3.16. The presence of the composite model is seen to have an insignificant effect on the visible spectrum. Experimental spectra centred at 780 nm, taken horizontally along the stagnation line, starting at a distance of 0.1 mm from the surfaces of the steel and composite models, are presented in Figure 3.17. The oxygen triplet at 777 nm is the highest intensity line in both sets of data. The presence of three strong N lines between 740 nm and 750 nm is also noted. As above, both spectra are normalised to remove effects stemming from shot-to-shot variations and plotted in a composite image in Figure 3.18. It is seen that the presence of the composite model has an insignificant effect on the near infrared. Stills taken by the Shimadzu HPV-1 high speed camera demonstrate the steel and phenolic models during the steady test time for the E1 flow condition, shown in Figures 3.8b and 3.8d respectively. When the phenolic model is subjected to the E1 flow, signs of surface cracking as well as spallation are noted. The shock stand-off distance can be estimated at approximately 1.35 mm through use of a Canny edge detection filter as seen in Figure 3.8f.
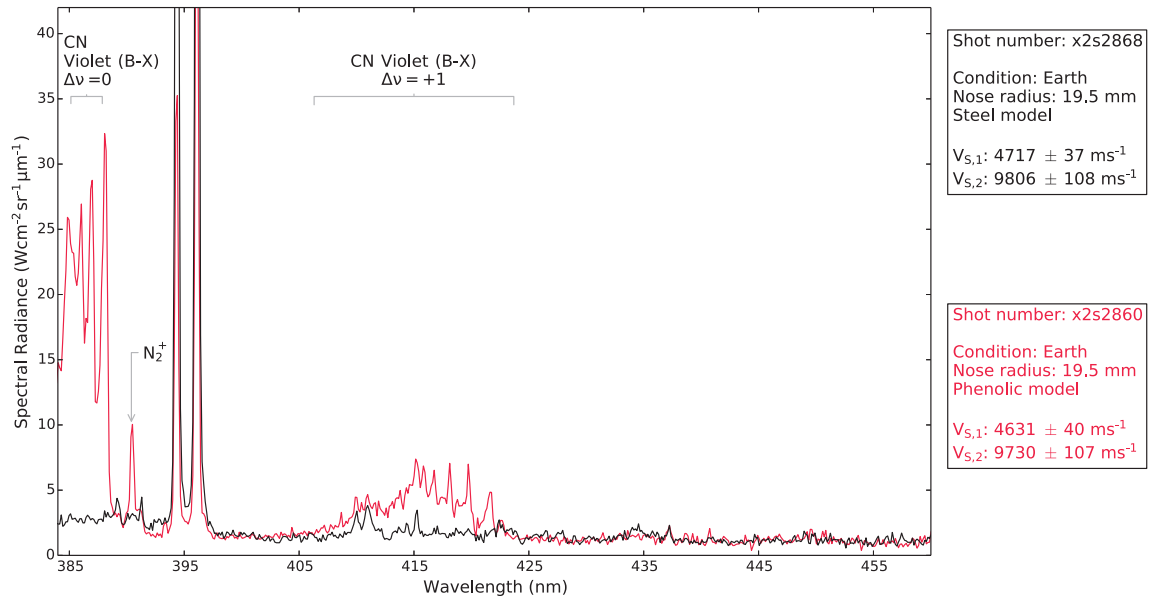
Figure 3.13: UV emission spectra measured at 0.1 mm upstream of steel and phenolic aeroshell model surface, for the E1 condition with CN Violet band radiation in evidence.
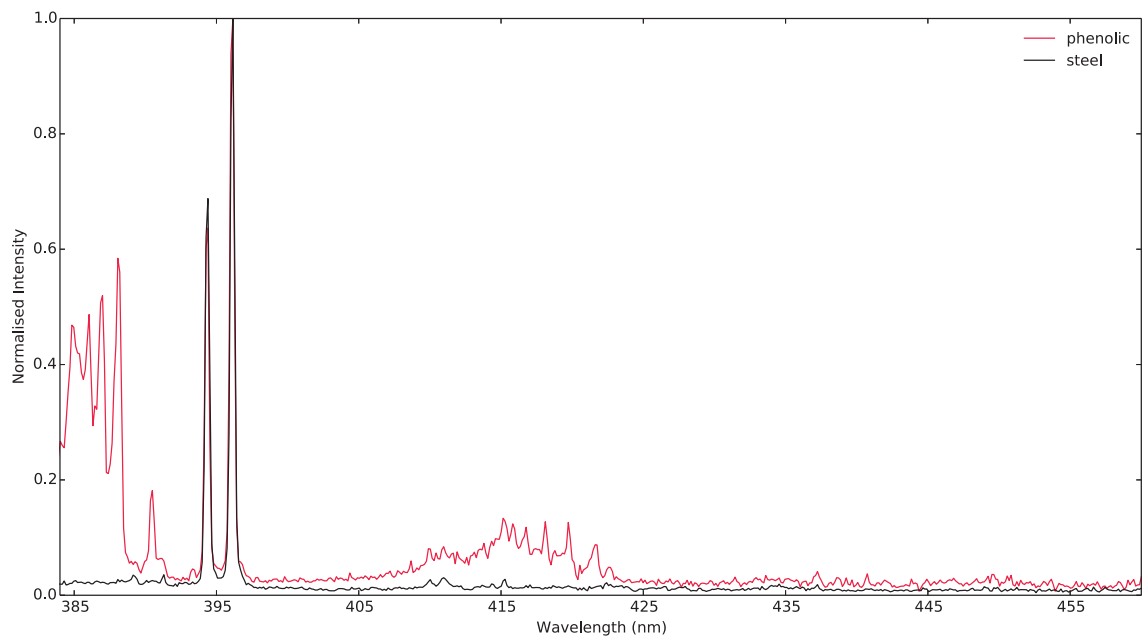
Figure 3.14: Normalised spectra measured in the UV for the E1 condition. Note the presence of CN Violet radiation for the phenolic model.
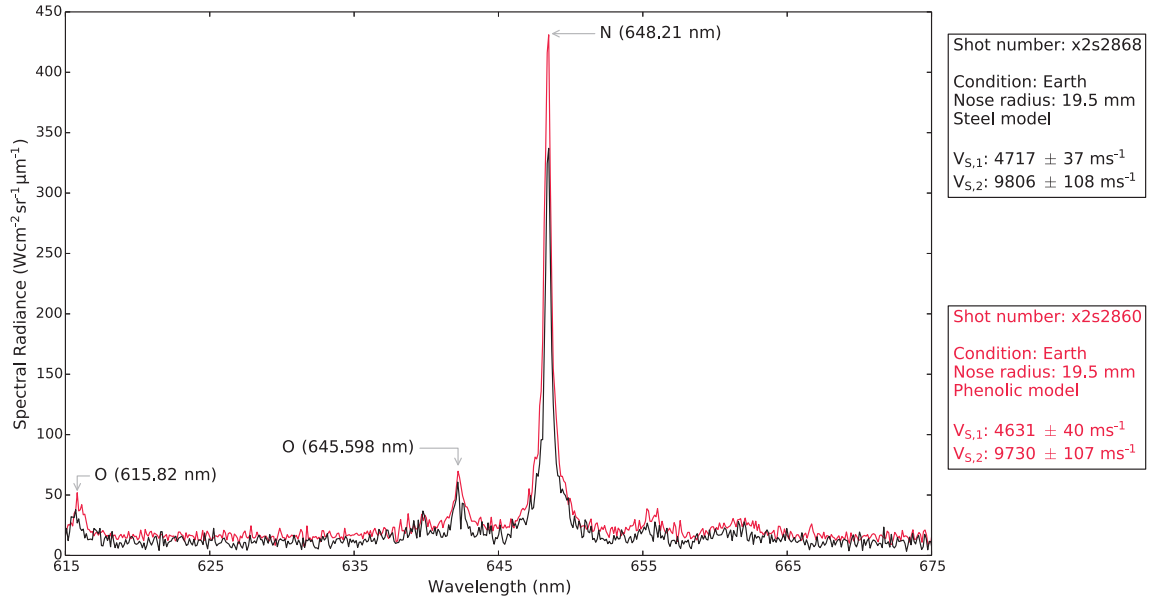
Figure 3.15: Visible emission spectra measured at 0.1 mm upstream of steel and phenolic aeroshell model surface, for the E1 condition with N and O radiation in evidence.
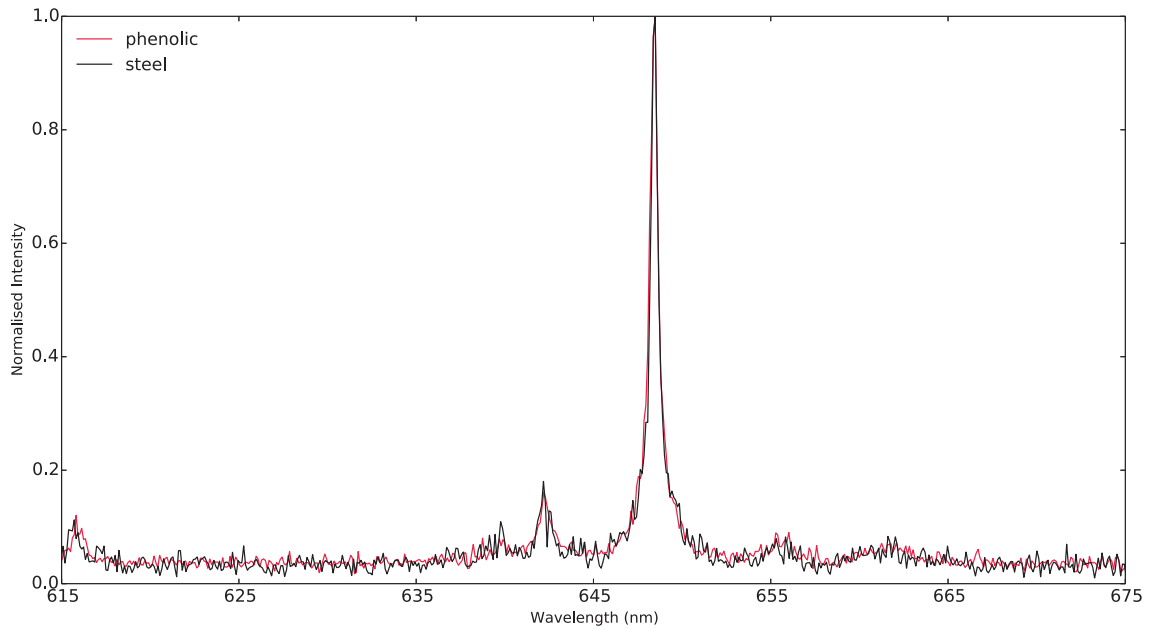
Figure 3.16: Normalised spectra measured in the visible wavelength range, for the E1 condition.
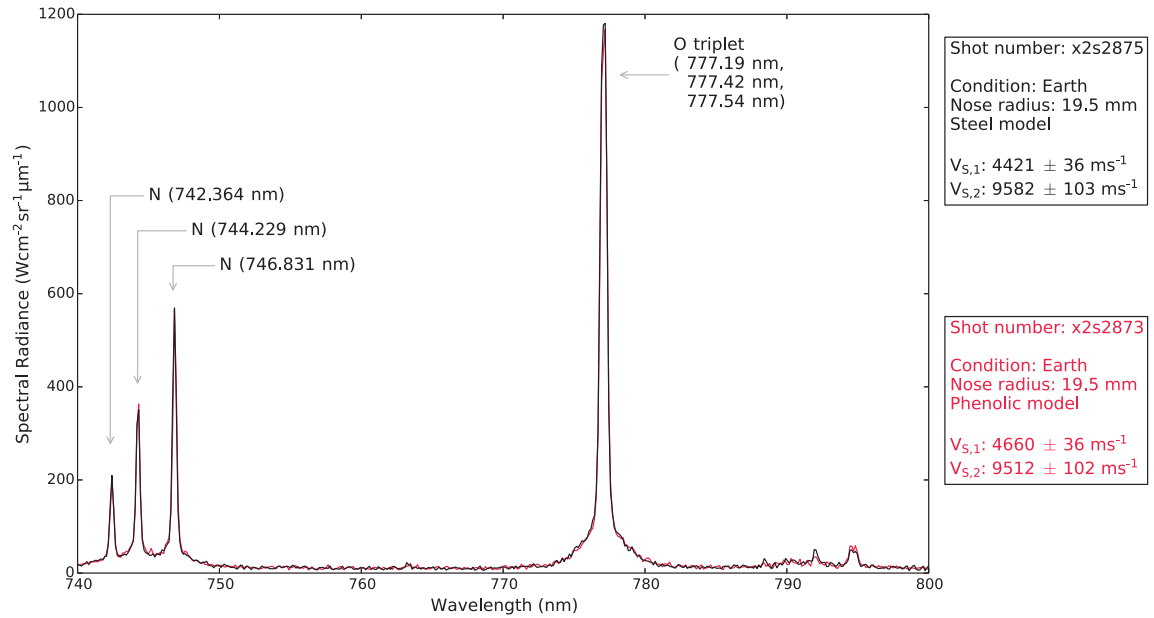
Figure 3.17: IR Emission spectra measured at 0.1 mm upstream of steel and phenolic aeroshell model surface, for the E1 condition with atomic N and O lines in evidence.
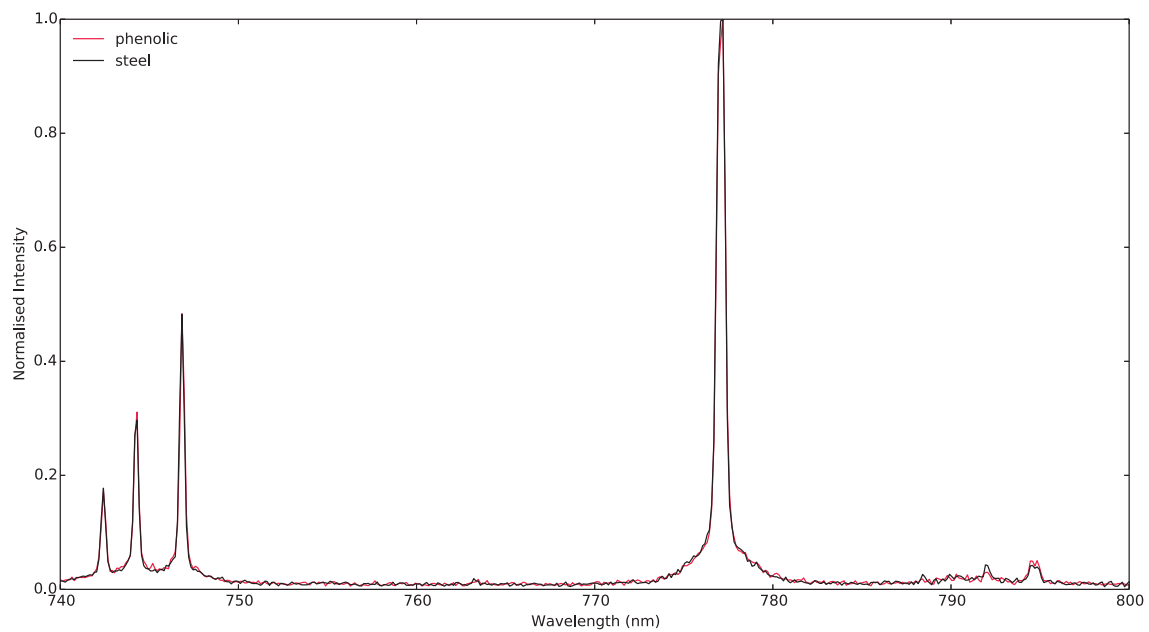
Figure 3.18: Normalised spectra measured in the IR for the E1 condition.

a) CN-Violet (B-X) $\Delta \nu = +1$ b) CN-Violet (B-X) $\Delta \nu = 0$ and $N_2{}^+$
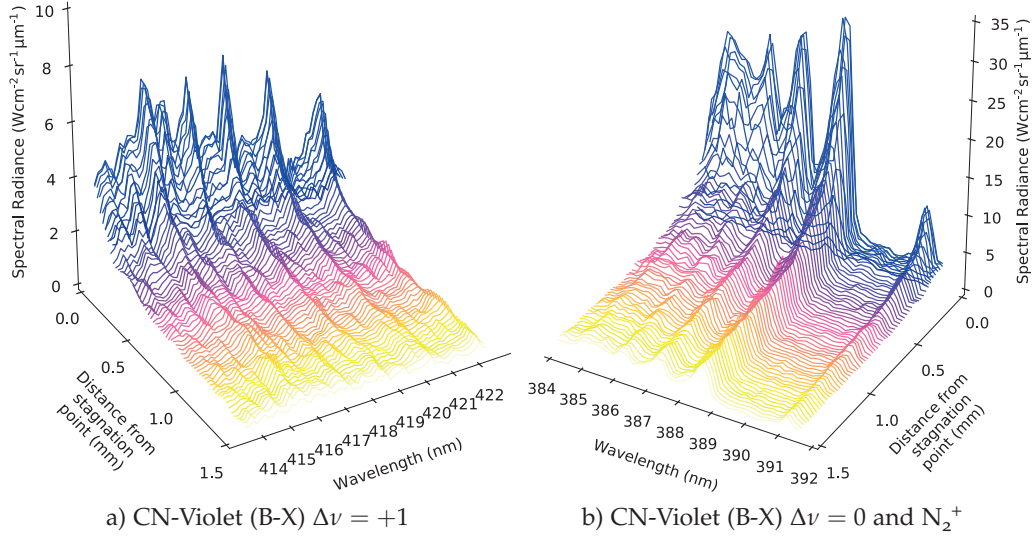
Figure 3.19: Variation in CN-Violet and $N_2{}^+$ emissions with axial distance from the model surface to the edge of the shock layer. Data from shot x2s2860 with the phenolic model in place. Colour for illustration purposes only. Note difference in scales on the z-axes.

The variation in UV radiation with distance from the phenolic model surface is shown in Figure 3.19. The data has been spatially averaged over ± 2 pixels for every point shown in the shock layer. Emission from the selected features is seen to be strongest at the phenolic model wall and drops quickly with increasing distance from the stagnation point. CN-Violet $\Delta \nu = 0$ and $N_2{}^+$ band radiation is measured across the entire distance investigated (Figure 3.19b) while CN-Violet $\Delta \nu = +1$ ceases to emit a strong radiation signature approximately 0.8 mm into the shock layer.

3.4   conclusions

The methodology used to design and manufacture reusable carbon phenolic aeroshell models with electrical pre-heating capability for use in experiments in the X2 expansion tube was established in this chapter. The success of applying the pre-heating technique was limited by the brittleness of the phenolic resin, causing it to crack and disperse at the surface above the heated strip. The model was shock heated in the X2 expansion tube, successfully simulating surface nitridation and oxidation in high enthalpy Venus and Earth entry conditions.

A representative selection of calibrated spectral intensities in the ultraviolet, visible and near infrared wavelength ranges are presented for both flow conditions in the second part of this chapter, thereby completing *Objectives O.1* and *O.2*. As ablation studies in CO_2-N_2 conditions are rare, given the inability of most experimental facilities to reproduce the required conditions, a unique dataset is presented here. By subjecting a phenolic model to a high enthalpy Earth re-entry flow, it was also possible to add to the sparse database of ablation spectra for terrestrial re-entry. Emission spectroscopy was used to measure the change in intensity of CN band radiation in the flow, due to reactions on the decomposing model surface. These calibrated spectra will be used for comparison with numerical spectra, calculated in Chapter 4.

NUMERICAL REBUILDING AND COMPARISON[1]

4.1 INTRODUCTION

As shown in previous studies by Potter [69], Alba [84] and Fahy [44], spectra recorded from experiments in X2 can be numerically rebuilt, within the limits of uncertainties in selected freestream conditions, numerical methods and experimental data. This was attempted for the aforementioned model in the respective V1 and E1 flow conditions, tested in X2. CFD calculations were used to model the hypersonic, non-equilibrium flow surrounding the model. This solution was then coupled to a radiation database, to calculate the line of sight spectra that were compared to the experimental spectra.

4.2 FLOWFIELD MODELLING

eilmer3 is the compressible flow computational fluid dynamics code developed by The University of Queensland, with contributions from École polytechnique fédérale de Lausanne (EPFL) and other research institutes. The solver uses a cell-centred, finite volume approach to the integral form of the compressible Navier-Stokes equations on 2D or 3D structured multi-block grids [74]. The time resolved integration of the conserved quantities from the mass, momentum and energy fluxes through a specified area along with any included source terms is given in Equation 4.1. The source terms, Q, are a combination of geometry (for axisymmetry), chemistry, thermal energy exchange and radiation components. These terms are applied using a split-operator approach, allowing each to be loosely coupled and solved separately.

---

1 Material from this chapter has been submitted for publication in the following articles,

- N Banerji, P Leyland, E J Fahy and R G Morgan. Venus Entry Flow Over a Pyrolyzing Aeroshell in the X2 Expansion Tube. *Journal of Thermophysics and Heat Transfer*, 2017.

- N Banerji, P Leyland, E J Fahy and R G Morgan. Earth Re-entry Flow Over a Pyrolyzing Aeroshell in the X2 Expansion Tube. *Journal of Thermophysics and Heat Transfer*, 2017.

The conserved quantities, U, include overall and species densities, momentum per volume in x and y directions as well as energy per volume. The flux vectors are divided into inviscid and viscous contributions. For a clear and detailed discussion and definition of the terms included in Equation 4.1, as solved by eilmer3, the reader is referred to work by Potter [69] and Gollan and Jacobs [74, 20].

$$\frac{\partial}{\partial t} \int_V U dV = - \oint_{\partial v} \left(\overline{F}_i - \overline{F}_v \right) \cdot \hat{n} \; dA + \int_V Q \; dV \qquad (4.1)$$

The split-operator approach allows the chemistry and radiation to be solved using optimised time stepping schemes, during which the flow solution is considered steady [74]. Both of these source terms require fairly intensive computation to be accurately solved. To ensure the stability of the overall flow simulation during this process, the allowable timestep is constrained by the Courant-Friedrichs-Lewy (CFL) criterion. By setting the CFL number, the user can select an appropriate timestep and limit the propagation of flow information to distances smaller than the width of a single cell [20]. It is therefore crucial to the successful completion of a simulation in eilmer3.

eilmer3's core is constructed using C++ and lua scripts are employed to interface with the user to define customised wall boundary conditions, reaction and energy exchange schemes. Python scripting is used for pre and post-processing the simulation as well as creating the main input file, which defines the gas model, inflow conditions, mesh and controls of the simulation parameters such as time step, CFL number and solution output frequency. The simulation can be ordered to run in serial, or as was most often the case for aeroshell simulations due to the fine mesh and hypersonic flow conditions, in parallel using either OpenMPI or IntelMPI. Once the simulation has terminated, the post-processor outputs results for visualisation, or data files containing flow properties along a specified slice through the flowfield.

4.2.1 *Meshing and Grid Resolution*

An axisymmetric structured grid was used for all simulations. This included the model forebody and shoulder, as radiation measurements in X2 were taken only from the stagnation line. Potter [69] found that including the afterbody in the domain did not affect the flow upstream of the model, but added complexity via turbulent effects and increased simulation time. Sizing the computational

domain to capture the bow shock and all its effects required some trial and error. The mesh was built outwards from the model geometry, defined by a series of points, with the shock stand-off distance estimated iteratively by changing the size of the domain to fully include all of the important flow features. Once the domain was sized, the cells were clustered towards the wall and around the shock in the x-direction to resolve the viscous effects in the boundary layer and strong non-equilibrium region respectively, as shown in Figure 4.1. The final simulation for the V1 condition was conducted with 120×190 cells, weakly clustered towards the stagnation line in the y-direction.
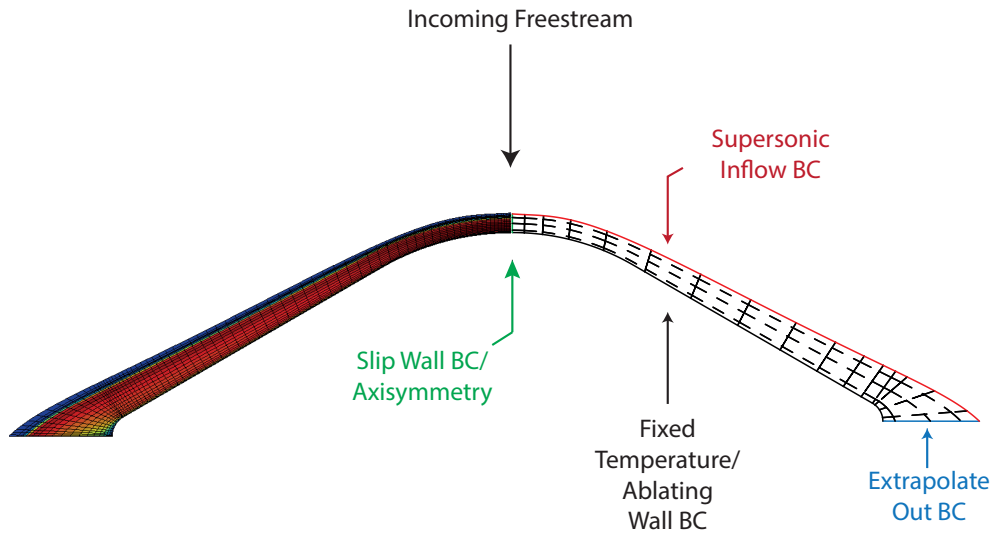
Figure 4.1: Typical grid and block layout for model forebody domain. On the left is the cell layout (with reduced clustering and number of cells for clarity) with an overlaid colour map defining T_{tr}. On the right is the block layout and boundary conditions mapped onto the respective blocks.

Given the small diameter of the model ($d = 60$ mm), it was seen that the simulation maintained, or somewhat improved, its fidelity by clustering only to the wall, but increasing the number of cells in the x-direction to 350. The complexity of the previous mesh arose from the transition between the smaller, clustered cells resolving the shock and the larger cells upstream and downstream of this region. Without fail, it was observed that the simulation dropped its time step significantly when resolving this region, increasing instability as a consequence.

This new strategy, however, was seen to decrease simulation time while significantly increasing stability. A final grid of 350×210 cells clustered to the model wall was therefore employed for all simulations for the E1 condition. The two meshes are indistinguishable by the image detail available and therefore the one used for the E1 simulations is omitted here. For computational efficiency, the domain was split up into 64 blocks mapped over the mesh, with each block distributed to a single processor.

A grid convergence study [93] was conducted on both final meshes, using two coarser grids with 50 % and 25 % of cells in both x and y directions, to give an overall refinement ratio of $r = 4$. For the V1 condition, temperatures calculated 0.38 mm upstream of the stagnation point were used as the test parameter, g_i, for each of the three grids studied. These values were taken from within the region of thermal equilibrium. Richardson extrapolation was used to calculate a theoretical temperature at zero grid spacing of 10 198 K with an error of 0.12 %, as shown in Figure 4.2. The theoretical order of convergence was calculated as $p = 1.033$. Using the finest grid convergence index [94] given in Equation 4.2, using a safety factor of $G_s = 1.25$ for the three grids under consideration, the calculated order of convergence was determined to be sufficiently close to a theoretical value of 1 for simulations involving a shock layer [93].

$$GCI_{\text{fine}} = \frac{G_s}{r^p - 1} \frac{g_i - g_{i+1}}{g_i} \tag{4.2}$$
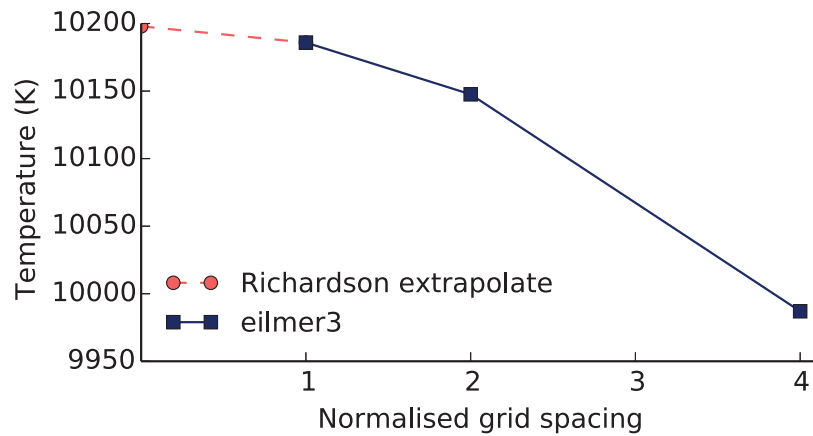
Figure 4.2: Spatial convergence of mesh used for model simulations of the V1 condition.
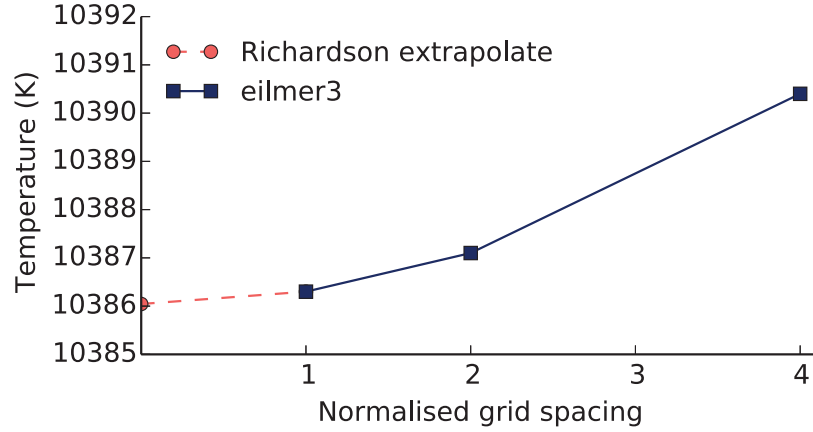
Figure 4.3: Spatial convergence of mesh used for model simulations of the E1 condition.

As seen by the results presented in Section 4.3 for the E1 condition, the CFD solution shows an absence of a thermal equilibrium zone. Only a single point exists, where the two temperature modes cross. It is at this point, 0.24 mm upstream of the stagnation region, that the calculated temperatures were used as the test parameter for the grid convergence study for the second mesh. Richardson extrapolation was used to calculate a theoretical temperature at zero grid spacing of 10 386 K with an error of 0.007 %, shown in Figure 4.3. The calculated order of convergence was $p = 1.022$. Using Equation 4.2 with a safety factor of $G_s = 1.25$, the solution is seen to be within the asymptotic range of convergence. Grid spatial convergence for the E1 simulations is better than for V1. This is likely due to a combination of the higher complexity of both the thermochemistry of the V1 flow and the mesh refinement strategy.

4.2.2 *Thermochemistry*

The chemistry and thermal energy exchange source terms input into the Navier-Stokes equations (Equation 4.1) are defined by the user in `eilmer3` and are heavily dependent on simulation requirements. Firstly, to be able to calculate the thermodynamic pressure, an equation of state was selected. The effects on gas chemistry of the elevated temperatures involved in hypersonic flow are well approximated by chemical non-equilibrium models [68]. In this state, the time taken for the chemical species to attain their equilibrium concentrations, τ_c, is said to be comparable to the transit time of the flow and to have an effect on the

flow properties. This model defines the thermodynamic pressure as the sum of the partial pressures of each thermally perfect constituent of the gas mixture and of electrons.

The strong bow shock that forms around a blunt body in hypersonic flow separately excites each of the thermal modes : translational, rotational, vibrational, electron and electronic, resulting in a state of thermal non-equilibrium. Park's [95] suggestion of combining the translational and rotational modes (T_{tr}) together as well as the vibrational, electron and electronic modes (T_{ve}) is applied to this work. This allows an increase in modelling accuracy compared to using an all encompassing single thermal mode without being overly penalised on computational efficiency. The total energy of the gas, E is composed of of thermal energy per unit mass, specific to each mode, e, as well as the kinetic energy.

$$E = e_{tr} + e_{ve} + \frac{1}{2}\vec{v} \cdot \vec{v} \tag{4.3}$$

The total energy continuity equation is therefore,

$$\frac{\partial \rho E}{\partial t} + \nabla \cdot (\vec{v}(\rho E + p)) = \nabla \cdot (\tau \cdot \vec{v}) - \nabla \cdot \vec{q} \tag{4.4}$$

where p is the gas pressure and τ is the viscous stress tensor. The heat flux vector, $\vec{q}$ is made up of conductive terms specific to the thermal mode, diffusive and radiative terms,

$$\begin{aligned} \vec{q} &= \vec{q}_{cond,tr} + \vec{q}_{cond,ve} + \vec{q}_{diff} + \vec{q}_{rad} \\ &= -K_{tr}\nabla T_{tr} - K_{ve}\nabla T_{ve} + \sum_s h_s \vec{J}_s + \int_\nu \vec{I}_\nu d\nu \end{aligned} \tag{4.5}$$

with K, the total conductivity coefficient, h_s, the species enthalpy and spectral radiative intensity, $\vec{I}_\nu$. Use of the two-temperature model also introduces a vibrational-electron-electronic energy continuity equation,

$$\frac{\partial \rho e_{ve}}{\partial t} + \nabla \cdot (\vec{v}(\rho e_{ve} + p_e)) = -\nabla \cdot \vec{q}_{ve} + \dot{\Omega}_{VT} + \dot{\Omega}_{ET} + \dot{\Omega}_{VC} + \dot{\Omega}_{EC} \tag{4.6}$$

where $\dot{\Omega}_{VT}$, $\dot{\Omega}_{ET}$, $\dot{\Omega}_{VC}$, $\dot{\Omega}_{EC}$ are terms for vibration-translation exchange, electron-translation exchange, vibration-chemistry coupling and electron-chemistry coupling respectively. The vibrational-electron-electronic heat flux vector, $\vec{q}_{ve}$ is defined as,

$$\begin{aligned} \vec{q} &= \vec{q}_{cond,ve} + \vec{q}_{diff,ve} + \vec{q}_{rad} \\ &= -K_{ve}\nabla T_{ve} + \sum_s h_{s,ve}\vec{J}_s + \int_\nu \vec{I}_\nu d\nu \end{aligned} \tag{4.7}$$

Compared to modelling a single temperature, additional equations are not needed for the two temperature model, since the species mass, total momentum and total energy equations hold with only minor adjustments [69]. For simulations using CO_2-N_2 gas mixtures, Park recommends the use of a one temperature assumption, since rapid relaxation of thermal modes was found in Mars and Venus flows [96, 97]. However, due to the high enthalpy of the freestream in X2, thermal non-equilibrium was expected in the shock layer [84, 44], excluding the use of this one-temperature assumption for the V1 simulations. Using the same logic, the two-temperature model is appropriate for the E1 simulations.

Individual thermal modes of a shock processed gas equilibrate over a characteristic relaxation time, τ_v, via elastic and inelastic collisions. This relaxation time was calculated using Millikan and White's correlation [98] with Park's high-temperature correction for vibrational relaxation [99]. These values were then applied to the Landau-Teller equation [100] to model energy exchanged between vibrational and translational thermal modes ($\dot{\Omega}_{VT}$ in Equation 4.6). The Appleton-Bray equations [101] were applied to model the energy exchanged by the translational and electronic modes via elastic collisions between heavy particles (ion or neutral) and electrons ($\dot{\Omega}_{ET}$ in Equation 4.6). Energy exchanges including the rotational mode are not accounted for, as it is assumed to relax readily to the translational temperature in the order of tens of collisions, compared to the tens of thousands of collisions required for translational-vibrational relaxation [19, 20]. Through inelastic collisions with molecules, free electrons can produce excited vibrational states. These exchanges would be accounted for by applying a complex three temperature model, using a Laundau-Teller form of the rate equation.

Reaction schemes are crucial for an accurate understanding of the mechanisms by which chemical species in the shock layer exchange particles or charge. These are implemented by the user in `eilmer3` using `lua` scripts. For the V1 condition, Park *et al.*'s Mars reaction model [96] was modified to contain 17 species and 43 reactions, omitting the inclusion of Ar as it was only present in trace amounts in the tunnel. The species considered were as follows:

$$CO_2, CO, O_2, O, N_2, N, C_2, C, CN, NO, C^+, N^+, O^+, O_2^+, NO^+, CO^+, e^-$$

A comparison was made with Johnston and Brandis' [102] reaction scheme for CO_2-N_2 flows comprising the same species but only 34 reactions. Tuned kinetic

rates were matched to CO Fourth-Positive and CN Violet band radiation measured at NASA's Electric Arc Shock Tube (EAST) facility to within an error of $\pm$ 30%. The tuned-rate model was developed through an optimisation procedure that minimised error between simulated and experimental non-equilibrium radiance profiles. The shock tube measurements were taken at pressures and velocities ranging from $0.1 - 10$ Torr and 6-8 km·s^{-1}. The reactions for which kinetic rates provided by Johnston diverge from Park's heritage values are presented in Table 4.1. The factor F_i is the new rate divided by the heritage rate at 8000 K. Significant modifications to kinetic rates for neutral exchange reactions J6 and J7 are most relevant to the rebuilding of boundary layer UV emission spectra for the V1 condition, detailed later in this chapter. Although freestream conditions investigated in X2 are different to the range studied by Johnston, it is still interesting to evaluate the suitability of the tuned rates.

Table 4.1: Johnston's modifications to Park's Venus reaction rates [102].

	Reaction	A	n	E_a	T	F_i
J1.	$CO + M \longleftrightarrow C + O + M$	1.8×10^{21}	-1.0	1.29×10^5	T_{av}	5.2
J2.	$C_2 + M \longleftrightarrow 2C + M$	4.5×10^{18}	-1.0	7.15×10^4	T_{av}	1.25
J3.	$CN + M \longleftrightarrow C + N + M$	6.0×10^{15}	-0.4	7.10×10^4	T_{av}	0.66
J4.	$NO + M \longleftrightarrow N + O + M$	4.4×10^{16}	0.0	7.55×10^4	T_{av}	0.4
J5.	$CO_2 + O \longleftrightarrow O_2 + CO$	2.71×10^{14}	0.0	3.38×10^4	T_{tr}	6
J6.	$CO + N \longleftrightarrow CN + O$	1.0×10^{15}	0.0	3.86×10^4	T_{tr}	10
J7.	$CN + C \longleftrightarrow C_2 + NO$	3.0×10^{14}	0.0	1.81×10^4	T_{tr}	3.2
J8.	$CN + O \longleftrightarrow NO + C$	1.6×10^{12}	0.1	1.46×10^4	T_{tr}	0.1
J9.	$CN + O \longleftrightarrow NO + C$	6.0×10^{13}	0.1	3.8×10^4	T_{tr}	1.9
J10.	$O_2 + N \longleftrightarrow NO + O$	2.49×10^9	1.18	4.01×10^3	T_{tr}	2.2

For air at high temperatures, the gas mixture is commonly described by eleven species including atomic and diatomic oxygen and nitrogen, NO and their re-

spective ions [99, 103]. Park, Jaffe and Partridge [64] have proposed a model agglomerating the eleven species in air with nine hydrocarbon species, representing ablative products. Suzuki, Fujita and Abe [104] proposed a model with an additional six species representing pyrolysis gases in the boundary layer, giving 52 reactions between permutations of 26 species, shown below.

$$N_2, O_2, N, O, NO, NO^+, N^+, O^+, N_2^+, O_2^+, C, C_2, C_3, CO_2, CO, CN, CO^+, C^+, H,$$
$$H_2, HCN, HCO, C_2H_2, C_2H, CH, e^-$$
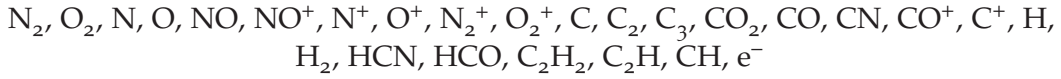
For the original eleven air species, this model uses commonly applied reaction rates and mechanisms defined by Gupta and Yos [103]. For interactions between the ablative and pyrolytic species, Suzuki *et al.* use a combination of reaction rates defined by Blottner [105], Lewis and Song [106], Westbrook *et al.* [107] and Heicklen [108]. The chemistry model proposed by Suzuki *et al.* will be referred to in this work as Abe's model to avoid confusion with the finite-rate surface ablation reactions also detailed by Suzuki (Section 4.2.4), which are used in parallel.

In comparison, Park's reaction scheme comprises 20 species and 21 reactions, omitting the polyatomic hydrocarbons and CO_2 but including H^+. Supplementary reactions included by Abe's model for relevant species, not present in Park's reaction scheme, are provided in Table 4.2. Most relevant to the rebuilding of UV emission spectra, detailed later in this chapter, are charge exchange reactions A10 and A11. Park's model-specific kinetic rates, reactions and coefficients are detailed in aforementioned relevant literature and are therefore not presented here. Both models were applied to the numerical simulations of the experiments conducted in X2 for the E1 condition.

Arrhenius formulations are used as a basis to define the non-equilibrium chemical source term. The generalised form for forward-rate coefficients is given in Equation 4.8, where E_a is the activation energy, T_f is the forward-rate controlling temperature, A and n are model-specific parameters and k_B is the Boltzmann coefficient. Using this forward-rate coefficient, it is then possible to calculate the reciprocal reverse-rate coefficient. This requires knowledge of the equilibrium constant, for concentrations evaluated at the reverse-rate controlling temperature, using the Gibbs' free energy minimisation approach [69].

$$k_f(T_f) = AT_f^n \exp(\frac{-E_a}{k_b T_f}) \tag{4.8}$$

Table 4.2: Additional reactions included in Abe's model compared to Park.

	Reaction	A	n	E_a	T_f	Reference
A1.	$CO + M \longleftrightarrow C + O + M$	2.3×10^{20}	-1.0	1.29×10^5	T_{av}	[96]
A2.	$NO + M \longleftrightarrow N + O + M$	5.0×10^{15}	0.0	7.55×10^4	T_{av}	[96]
A3.	$CO + CO \longleftrightarrow C_2 + O_2$	9.2×10^{11}	0.75	1.63×10^5	T	[105]
A4.	$CO + CO \longleftrightarrow CO_2 + C$	1.0×10^3	2.0	7.24×10^4	T	[105]
A5.	$CO + N \longleftrightarrow C + NO$	9.0×10^{16}	-1.0	5.32×10^4	T	[105]
A6.	$CO + NO \longleftrightarrow CO_2 + N$	1.0×10^3	2.0	2.1×10^4	T	[105]
A7.	$N_2 + CO \longleftrightarrow CN + NO$	1.0×10^3	2.0	9.20×10^4	T	[105]
A8.	$C + O \longleftrightarrow CO^+ + e^-$	8.8×10^8	1.0	3.31×10^4	T_{ve}	[96]
A9.	$O + O \longleftrightarrow O_2^+ + e^-$	7.1×10^2	-1.84	1.41×10^5	T_{ve}	[99]
A10.	$N_2 + N^+ \longleftrightarrow N + N_2^+$	1.0×10^{12}	0.5	1.22×10^4	T	[19]
A11.	$N_2 + O^+ \longleftrightarrow O + N_2^+$	3.4×10^{19}	-2.0	2.3×10^4	T	[103]
A12.	$N + NO^+ \longleftrightarrow NO + N^+$	1.0×10^{19}	-0.93	6.1×10^4	T	[103]
A13.	$O + NO^+ \longleftrightarrow NO + O^+$	3.6×10^{15}	-0.6	5.08×10^4	T	[19]
A14.	$O + NO^+ \longleftrightarrow O_2 + N^+$	1.0×10^{12}	0.5	7.72×10^4	T	[19]
A15.	$O_2 + NO^+ \longleftrightarrow NO + O_2^+$	2.4×10^{13}	0.41	3.26×10^4	T	[19]
A16.	$O + O_2^+ \longleftrightarrow O^+ + O_2$	4.0×10^{12}	0.09	1.8×10^4	T	[19]

For a two-temperature approximation, the forward-rate controlling temperature used for charge exchange, associative ionisation as well as neutral exchange reactions is T_{tr}. For electron impact ionisation reactions, T_{ve} is used to control the Arrhenius rates. Rate controlling temperatures for heavy particle dissociation reactions are modelled using a weighted version of Park's geometric average temperature [99], as in Equation 4.9. The justification for this model is that the energy required for dissociation is obtained in approximately equal proportions

from the vibrational mode of the dissociating molecule and the translational energy of the colliding molecule.

$$T_{av} = T_{tr}^s \, T_{ve}^{1-s} \qquad (4.9)$$

The original geometric average temperature model proposed by Park [99] sets $s = 0.5$, which holds true for CO_2-N_2 mixtures and is used for V1 simulations in this work. However, da Silva *et al.* [109] found improved performance by weighting the geometric average temperature by setting $s = 0.7$ for conditions of strong translation-vibration non-equilibrium in nitrogen dominated gas mixtures, such as air. This modification has therefore been adopted for E1 condition simulations. Reverse-rates are governed by T_{tr} when applied to recombination reactions.

The change in thermal energy due to the creation and destruction of atoms, molecules and ions needs to be accounted for in the governing equations. As vibrational species change in concentration due to the relevant chemical reactions, their average vibrational energy will also be altered. Preferential dissociation of molecules occurs from higher vibrational energy levels, reducing the average vibrational energy among unreacted molecules. As soon as a gas is processed by a shock, its translational temperature is high, while its vibrational temperature remains at its pre-shock value. This decreases the speed of dissociation, due to a slowed reaction. By using a modified equilibrium reaction rate, it is possible to model the slowed reaction [20]. Treanor and Marrone's preferential dissociation model is applied to account for this chemistry-vibration coupling [110], included by the term $\dot{\Omega}_{VC}$ in Equation 4.6. Additionally, electron impact ionisation ($\dot{\Omega}_{EC}$ in Equation 4.6) can deplete energy from modes other than heavy particle translation and therefore is taken into account according to reaction rates provided by Park [99].

Park [111] details the limitations of the two-temperature model, including an inability to correctly simulate the shock stand-off distance, which affects the pressure distribution across the model surface. Subsequent errors occur on calculation of aerodynamic coefficients and most importantly for this work, on the calculation of species number densities. Multiple reaction schemes were explored for both V1 and E1 flow conditions, to evaluate which matches experimental results best, even given the limitations of the underlying two-temperature model.

4.2.3 *Transport Properties*

Evaluation of mass, momentum and energy fluxes in a high temperature, non-equilibrium environment is highly dependent on the calculation of transport properties within the gas mixture. This is especially crucial for the evaluation of convective heating of the TPS surface. Collision integrals are required to efficiently and accurately model these properties [60, 61]. Implementation in the `eilmer3` thermochemistry module is relatively simple, only requiring the input of the reduced collision integral values, $\Omega^{(1,1)\star}$ and $\Omega^{(2,2)\star}$, relating to thermal conductivity and mixture viscosity. Given that ablative species are mainly carbonaceous in nature, available datasets defined by Laricchiuta [62] and Wright [63] for a CO_2 - N_2 gas mixture conveniently account for all interactions with pyrolytic species. These readily available values were therefore implemented to rebuild the V1 condition, using both the Park and Johnston reaction schemes.

For computational simulations of the E1 condition, Park *et al.* [64] provide the relevant reduced collision integral values to go with their reaction scheme, thus simplifying implementation. Abe's chemistry model [104] lacks the collision integrals required, as the authors used empirical values, curve fits and the Wilke mixing rule to calculate thermodynamic and transport properties of the gas mixture. Values for the neutral-neutral interactions of ablating species in Abe's model are therefore calculated, for temperatures ranging from $2000\,K$ to $32\,000\,K$. The foundations for the current calculations at EPFL were laid by Savajano [112] who thoroughly details the underlying equations and theory, which are therefore only very briefly presented here. As explained by Mora-Monteros [113], a collaborative effort was made to develop an in-house code in `Python`, for the calculation of the missing collision integral sets required for use with Abe's model. This code has been made available in the *Compressible Flow CFD Project* repository, housed by the University of Queensland.

In order to accurately model the binary interactions that define transport properties, several interaction potentials ($\varphi(r)$) have been proposed. The Lennard-Jones $(6-12)$ potential is one of the simplest and most commonly used approaches for neutral-neutral interactions, however, it is not without its limitations. One of these is the modelling of interactions between polar molecules which results in poor accuracy when a dipole moment is present in the binary collision. In this case, the Stockmayer potential (Equation 4.10) is a good alternative as it is angle-dependent, with an additional third term that takes into account the

dipole moment induced in the colliding pair [114]. Equation 4.10 also defines the Lennard-Jones potential for $\delta^* = 0$.

$$\varphi^*(r^*) = 4[(\frac{1}{r^*})^{12} - (\frac{1}{r^*})^6 - \delta(\frac{1}{r^*})^3)]$$

(4.10)

$$\delta^* = \frac{\mu_1 \mu_2}{2\epsilon\sigma^3}$$

μ_1 and μ_2 are the electric dipole moments in *esu-angstroms* for the two molecules under consideration and are presented in Table 4.3. ϵ is the inter-potential well depth in *Joules* and σ is the hard sphere collision diameter in *Angstroms*, both calculated as the average of the values for the colliding pair of molecules.

In order to calculate the collision integrals, four quantities are evaluated. The reduced distance of closest approach, r_m^*, the reduced angle of deflection, $\chi(g^*, b^*)$, and $Q^{(l)*}(g^*)$ the reduced cross section. $\Omega^{(l,s)\star}$ is the dimensionless collision integral, reduced as in equation 4.15, which indicates the deviation of any particular molecular model from the idealised rigid-sphere model [60]. This allows for easy comparison between models and implementation in eilmer3. g^* is the reduced initial relative speed of two colliding molecules and b^* is the reduced impact parameter, i.e. the closest distance of approach of two particles in the absence of potential. To calculate viscosity and thermal conductivities, it suffices to set l and s both to 1 or 2 respectively. These quantities are evaluated by solving the following equations as defined by Hirschfelder [60].

$$0 = 1 - \frac{\varphi^*(r_m^*)}{\frac{1}{2}\mu g^{*2}} - \frac{b^{*2}}{r_m^{*2}}$$

(4.11)

$$\chi(g^*, b^*) = \pi - 2b^* \int_{r_m^*}^{\infty} \frac{dr^*/r^{*2}}{\sqrt{1 - \frac{b^{*2}}{r^{*2}} - \frac{\varphi^*(r^*)}{g^{*2}}}}$$

(4.12)

$$Q^{(l)*}(g^*) = \frac{2}{1 - \frac{1+(-l)^l}{2(1+l)}} \int_0^{\infty} (1 - \cos^l\chi)b^* db^*$$

(4.13)

$$\Omega^{(l,s)\star}(T^*) = \frac{2}{(s+1)!T^{*s+2}} \times \int_0^{\infty} e^{-g^{*2}/T^*} g^{*2s+3} Q^{(l)*}(g^*) dg^*$$

(4.14)

$$\Omega^{(l,s)\star} = \frac{[\Omega^{(l,s)}]}{[\Omega^{(l,s)}]_{\text{rig sph}}}$$

(4.15)

φ^* is the reduced interaction potential calculated using Equation 4.10. A triple integral is thus resolved from Equations 4.12, 4.13 and 4.14, using the trapezoidal method, to calculate the collision integral values. The integration parameters are, r^*, the reduced intermolecular distance, b^* the reduced impact parameter and g^*, the reduced relative kinetic energy.

Certain arbitrary corrections have been proposed for the Lennard-Jones potential by Park [64] for atom-molecule and atom-atom interactions (Equation 4.16) and by Kim [115] for molecule-molecule reactions (Equation 4.17) to better fit the quantum mechanical models. The applied method makes use of these same corrections. The calculated values are presented in Appendix E.

$$\Omega^{(l,s)\star} = 0.9\Omega^{(l,s)\star}\left(\frac{T}{2000}\right)^{-0.25} \tag{4.16}$$

$$\Omega^{(l,s)\star} = \left[0.45\left(\frac{T}{2000}\right)^{-0.25} + 0.5\right]\Omega^{(l,s)\star} \tag{4.17}$$

Table 4.3: Electron dipole moments (μ) implemented for polar molecules included in current model; as well as non-polar molecule data not included by Park [64].

Species	σ (Å)	ϵ/k (K)	μ (Debye)	Reference
CO_2	3.941	195.2	-	[116]
C_2H_2	4.1	208.9	-	[117]
CO	3.690	91.7	0.112	[114, 64]
CN	3.856	75.0	1.45	[114, 64]
CH	3.370	68.6	0.88	[114, 64]
HCN	3.63	569.1	2.985	[114, 64]
HCO	3.59	498.0	1.35	[114, 64]
NO	3.599	91.0	0.0672	[114, 64]

Where possible, the code was validated against the results of Wright *et al.* [118], Kim *et al.* [115], Park *et al.* [64] and the Mutation library [119], available with

the open-source distribution of COOLFluiD. The reduced collision integrals for the H−O interaction pair are shown in Figures 4.4a and 4.4b. Both thermal conductivity and viscosity integrals are overestimated compared to Park and Kim's results. The discrepancies, between 1 and 17%, are most likely caused due to a difference in chosen integration parameters and method, as the overall methodologies are the same. The values taken from Mutation are significantly lower than those calculated in this study. This is most likely due to the significant difference in methodologies used. Bellemans *et al.* [120] explain Mutation's use of the Sokolova sewing method to combine the Born-Mayer (at high temperatures) and Lennard-Jones (at low temperatures) potentials to cover both long and short range interactions respectively. The current methodology uses the same fit coefficients across all interactions and corrects for the potential parameters ϵ and σ instead.

In Figures 4.5a and 4.5b, the reduced collision integrals are compared for the interaction of polar molecules CO−CN. The use of Stockmayer's potential function accounts for the overestimation when compared to the values found in literature. It includes the effect of molecule polarisability in the calculation while not affecting computational efficiency. Kim's correction has not previously been used in combination with the Stockmayer potential, but seems suitable as good correlation is seen compared to literature values.

NASA's CEA2 program [121] calculates transport properties from collision integrals obtained via several different sources including empirical potentials, computational chemistry calculations and Svehla's experimental measurements. Svehla [116] uses pure species binary interactions to derive the transport coefficients for certain species - this would be the case for several binary interactions involving ablative species (especially C_2H, HCO), as they were not included in the experiments. The model developed in this work is therefore expected to be of higher accuracy than that of CEA2, however a comparison is still useful for model validation.

The Gupta-Yos mixture rule [103] is applied to the calculated collision integrals to solve for the dynamic viscosity of a multicomponent phenolic gas mixture for comparison with values calculated by CEA2. The mixture rule is given in Equation 4.18, where $T_{tr,i}$, X_i and m_i are the translational temperature, mole-fraction and particle mass of the species i respectively and k_b is Boltzmann's constant. The mixture viscosity is then calculated as the sum of all the species viscosities.
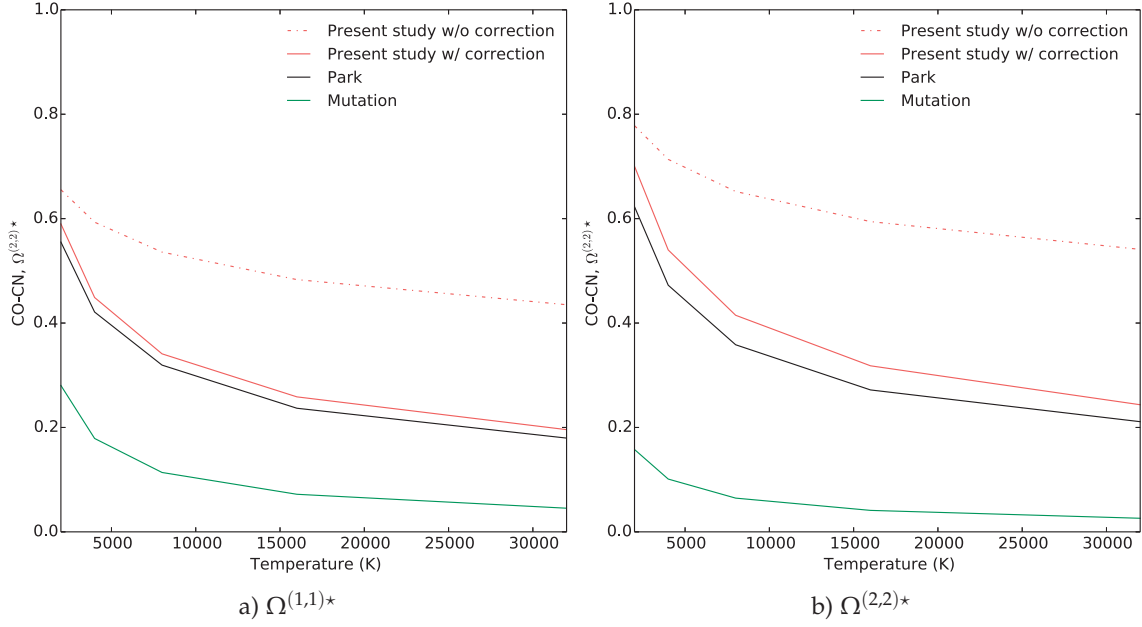
Figure 4.4: Comparison of calculated collision integrals for interactions between non-polar H and O atoms, calculated using the Lennard-Jones potential, with those from literature.

No ionised species were included in this calculation due to the comparatively low temperature range studied, which is representative of the ablation layer where dissociation dominates ionisation.

$$\mu_i = \frac{X_i m_i}{\sum\limits_{j}^{N_{\text{species}}} X_j \Delta_{ij}^{(2)}(T_{\text{tr},i})} \tag{4.18}$$

$$\Delta_{ij}^{(2)}(T) = \frac{16}{5}\left[\frac{2m_i m_j}{\pi k_b T(m_i + m_j)}\right]^{\frac{1}{2}} \pi\sigma^2 \Omega_{i,j}^{(2,2)\star}(T)$$

Data presented in Figure 4.6 demonstrates an underestimation in viscosity by the present model for the temperature range studied, in comparison to literature values. This is expected due to the higher value of the collision integrals generated. Around 3000 K, there are two points of inflexion, caused
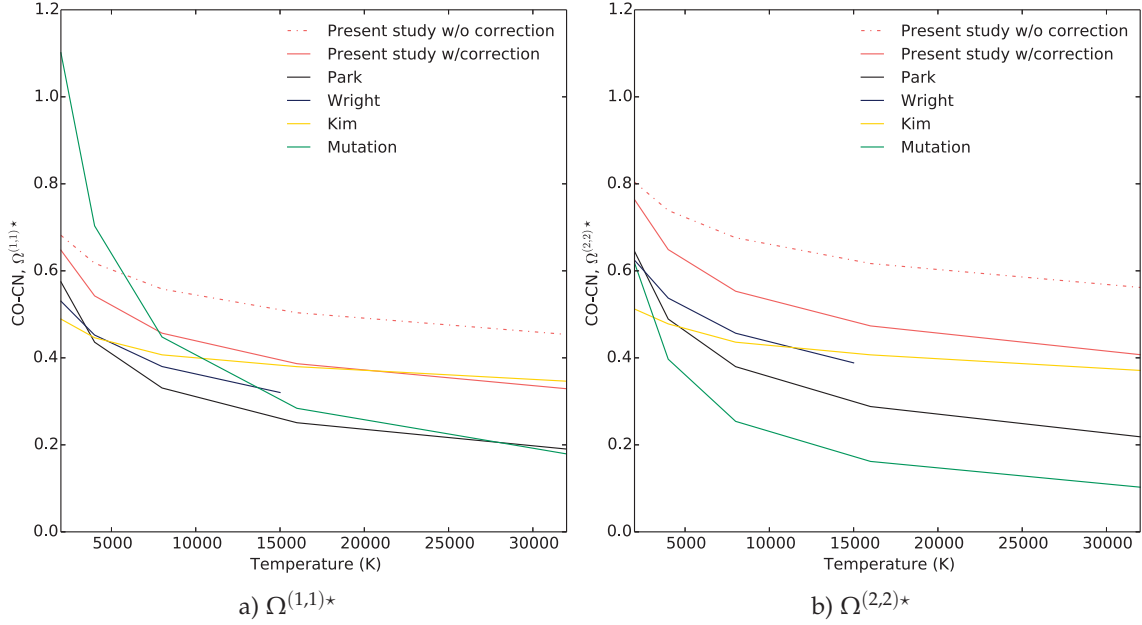
Figure 4.5: Comparison of calculated collision integrals for interactions between polar CO and CN molecules, calculated using the Stockmayer potential, with those from literature.

by significant dissociation of molecular hydrogen into atomic hydrogen. The calculated set of collision integrals predict a smaller decrease in viscosity around 3000 K, when compared with those provided by Park [64] and CEA2. This is due to the inclusion of CH, HCN and HCO, which reduce the mass fraction of atomic hydrogen, post H_2 dissociation. Park does not take these species into account. The use of pure species binary interactions to derive transport coefficients for all species reduces the fidelity of the CEA2 calculation.

The calculated set of reduced collision integrals are therefore implemented in eilmer3's thermochemistry module, as an input to the Gupta-Yos mixing rule for calculation of gas mixture transport properties using Abe's reaction scheme. Ramshaw and Chang's [122] Self-Consistent Effective Binary Diffusion (SCEBD) approximation to the Stefan-Maxwell equations was used to calculate mass diffusion. The fundamental idea behind an effective binary diffusion approximation is to estimate diffusive flux by simplifying the multicomponent mixture to be a binary mixture of species and a complementary composite species representing
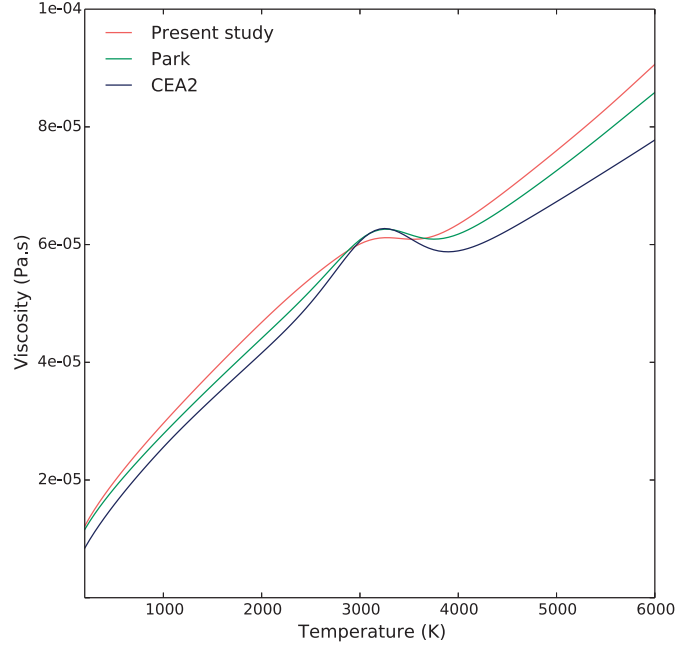
Figure 4.6: Viscosity for the 18 species ablation mixture with equilibrium concentrations, at 0.1 atm, compared to CEA2 and Park's values. Initial composition C:H:N:O = 0.2838 : 0.5749 : 0.0085 : 0.1328

the remaining species. Since every particle moves with a different velocity, the effective velocity of the composite species should be some appropriate weighted average of the velocities it represents. Ramshaw and Chang express the weighting factors in terms of the friction coefficients rather than using arbitrary values (as was done previously). Duffa [5] claims good precision and computational efficiency with the SCEBD approximation.

4.2.4   *Boundary Conditions*

For a simulation of the model forebody, the computation domain is enveloped by an inflow condition, a symmetry axis, a model wall and an outflow boundary, as shown in Figure 4.1. The hypersonic inflow is defined by the freestream conditions, calculated in Section 3.2.2. The axis of symmetry is represented by a slip-wall boundary condition, imposing a lack of viscous effects due to the absence of shear stress. The outflow condition extrapolates values from cells

adjacent to it and works best when the conditions are supersonic. This is usually achieved by the time the flow encounters the model shoulder. The aeroshell wall can have a catalytic effect on reactions of flowfield species in the boundary layer. `eilmer3` supports two catalytic boundary conditions: super catalytic, where species fully recombine to freestream values and non-catalytic, where the wall has no influence on the chemical behaviour of the boundary layer. Preliminary simulations were carried out with both conditions, with negligible differences in the flowfield solution data set. The non-catalytic wall was therefore used to represent the steel model.

A wall temperature of 600 K was used for all the simulations. The implemented surface-reaction boundary condition was limited to oxidation and nitridation of surface carbon, as per the equations and kinetic rates provided by Park [64]. Reactions involving C_3 were excluded from the model, as its abundance does not become significant until surface temperatures reach 3000 K [123]. The Arrhenius coefficients of the equations used are given in Table 4.4. The importance of nitridation to surface mass loss and radiative heating has resulted in several different models, summarised by Alba *et al.* [84]. The modification to Park's surface reaction model by Suzuki *et al.* [85], proposed a reduced efficiency of nitridation for lower temperatures, showing better agreement with efficiencies obtained experimentally. In this work, both surface kinetic models were considered.

Table 4.4: Surface ablative reactions and Arrhenius rate parameters.

	Reaction	γ_i	E_a (kJ·mol^{-1})	Reference
1.	$O + C(s) \longrightarrow CO$	0.63	9.644	[64]
2a.	$N + C(s) \longrightarrow CN$	0.30	0	[64]
2b.		$8.441 \times 10^{-3} \exp\left(\frac{2322}{T_w}\right)$	0	[85]

4.2.5 *Simulation Parameters*

Table 4.5 provides a summary of the parameters chosen for the simulation of the experiments conducted in X2. The methodology followed is summarised in Figure 4.7.

Table 4.5: Simulation Parameters.

	Venus (V1)	Earth (E1)
Gas model	17 species CO_2-N_2 mixture	20 and 26 species ablative air
Reaction scheme	Park; Johnston	Park; Abe
Chemistry-energy coupling	Treanor-Marrone and electron impact ionisation.	
Equation of state	Chemical non-equilibrium.	
Thermal modes	Translational-rotational and vibrational-electron-electronic.	
Thermal energy exchange	Vibrational-translational : Millikan-White Electronic-translational : Appleton-Bray	
Transport properties	Gupta-Yos mixing rule with relevant collision integrals.	
Diffusion model	Ramshaw-Chang	
Wall boundary conditions	Non-catalytic cold and reacting wall.	
Turbulence model	None [69, 84, 44].	
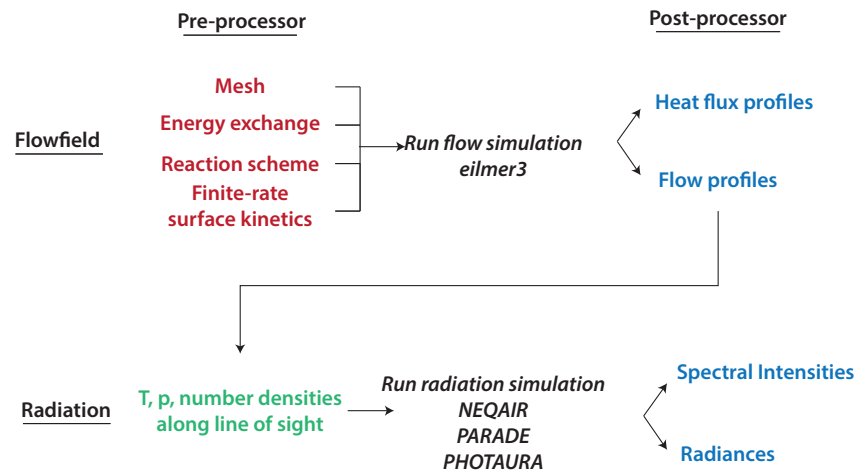
Figure 4.7: Methodology for numerical rebuilding of X2 experiments using the `eilmer3` compressible CFD code and a selection of radiation databases.

4.3 FLOWFIELD RESULTS

4.3.1 *Venus Condition*

Flowfield results for the aeroshell model in a simulated Venus entry flow in X2 are detailed in this section. The stagnation line profiles for translational-rotational (T_{tr}) and vibrational-electron-electronic (T_{ve}) temperatures using both Park (solid lines) and Johnston's (dashed lines) models are presented in Figure 4.8. Using the Park model, a shock stand-off distance of approximately 1.36 mm was noted, with a peak in T_{tr} of 44 300 K. Over a non-equilibrium region of approximately 1.08 mm, both thermal modes relaxed to an equilibrium temperature of 10 162 K. The equilibrium region then continued until the model wall. Modelling the gas chemistry using the Johnston model, a decrease in shock stand-off distance was observed (1.23 mm), with a lower peak T_{tr} of approximately 39 726 K. The two thermal modes equilibrated approximately 0.35 mm from the model wall at the same temperature as that obtained using the Park model. The effect of the finite-rate surface chemistry models on these profiles was negligible. The stagnation pressure was higher at 432 kPa using the Johnston model, compared with 429 kPa using the Park model (Figure 4.9). Compared to the experimentally measured shock stand-off distance of 1.9 mm (Figure 3.8e), Park and Johnston's reaction schemes underestimate this value by 28% and 35% respectively.

The stagnation-line species number densities are displayed in Figures 4.10, 4.11 and 4.12. For both models, the majority of species attained chemical quasi-equilibrium at a distance of 0.6 mm from the wall, further out from the zone where thermal equilibrium was achieved. Though a smaller shock thickness was calculated using Johnston's model, the species relaxed more rapidly to their equilibrium values. CO_2 and CO did not attain equilibrium and experienced continuous dissociation until the boundary layer, where an increase in concentration of these two species along with CN, O_2 and NO was observed, likely due to recombination. Using the Johnston model, increased dissociation was observed for CO_2 and CO, which was to be expected given the higher dissociation rates compared to those provided by Park. This, in turn, led to an increase in concentration of CN and C_2 in the shock layer.
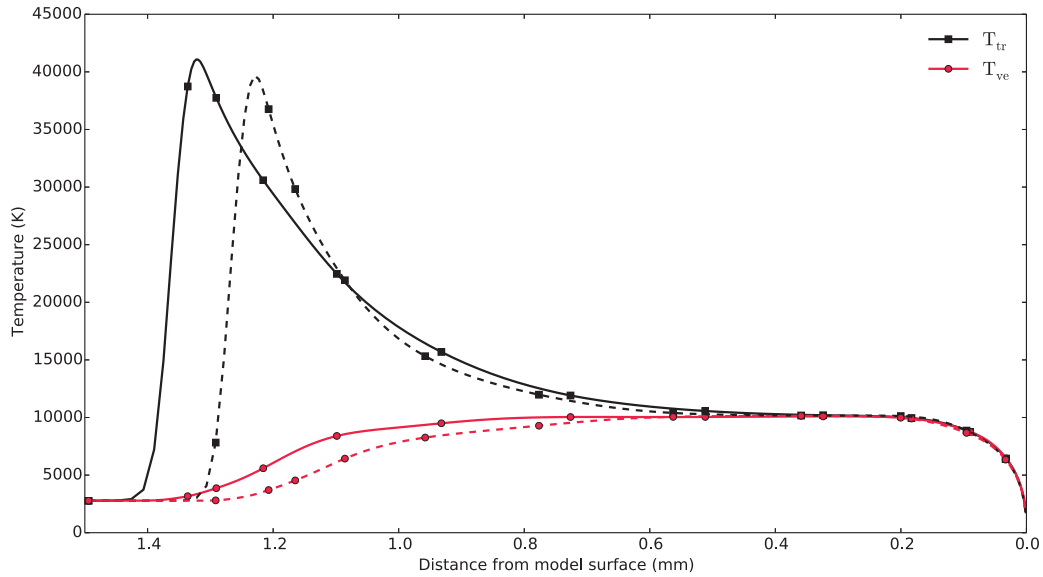
Figure 4.8: Stagnation line temperature profiles using the Park (solid) and Johnston (dashed) reaction schemes.
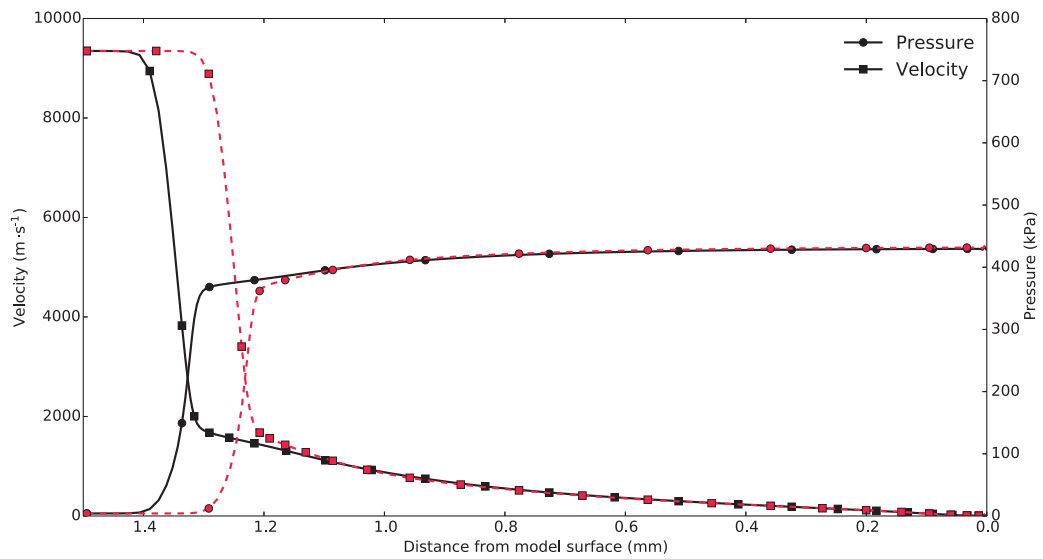
Figure 4.9: Stagnation line pressure and velocity profiles using the Park (solid) and Johnston (dashed) reaction schemes.
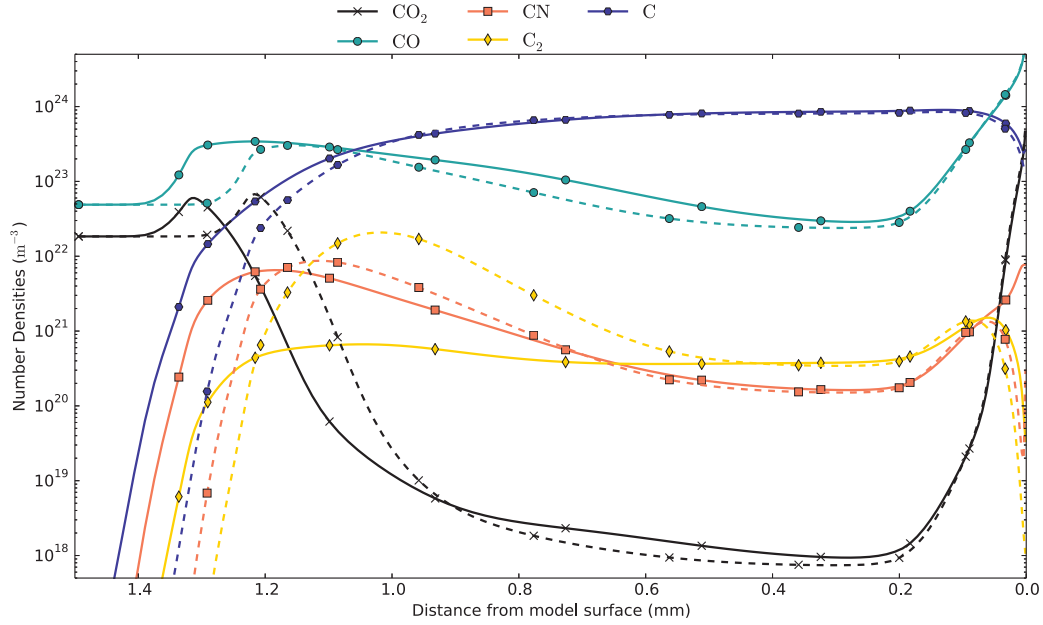
Figure 4.10: Stagnation line species number density profiles for carbonaceous species in V1 flow using the Park (solid) and Johnston (dashed) reaction schemes with a non-catalytic wall at 600 K.
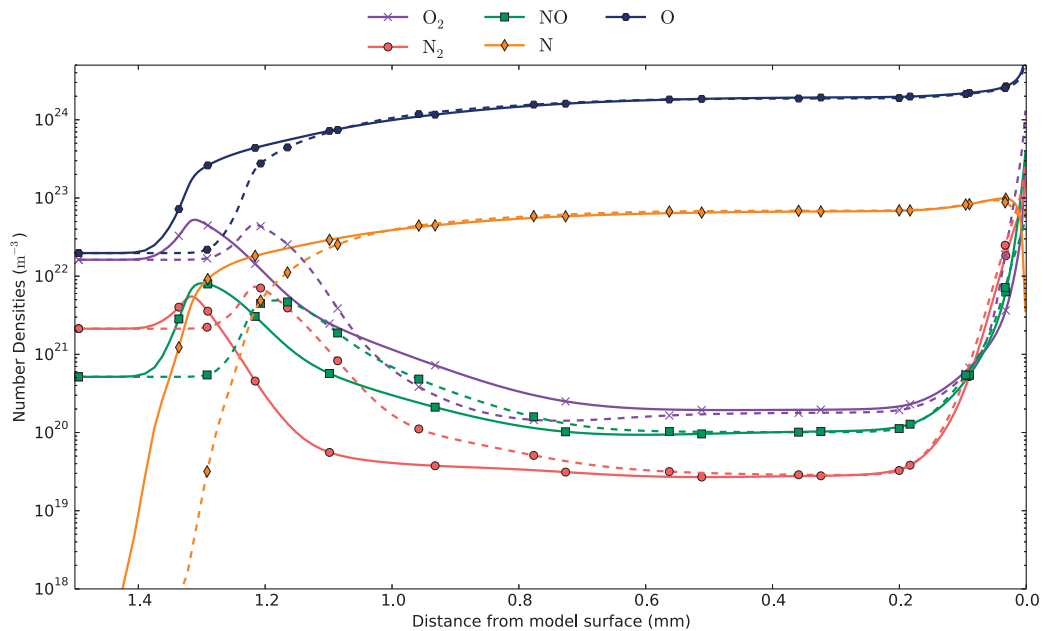
Figure 4.11: Stagnation line number density profiles for air species in V1 flow using the Park (solid) and Johnston (dashed) reaction schemes with a non-catalytic wall at 600 K.
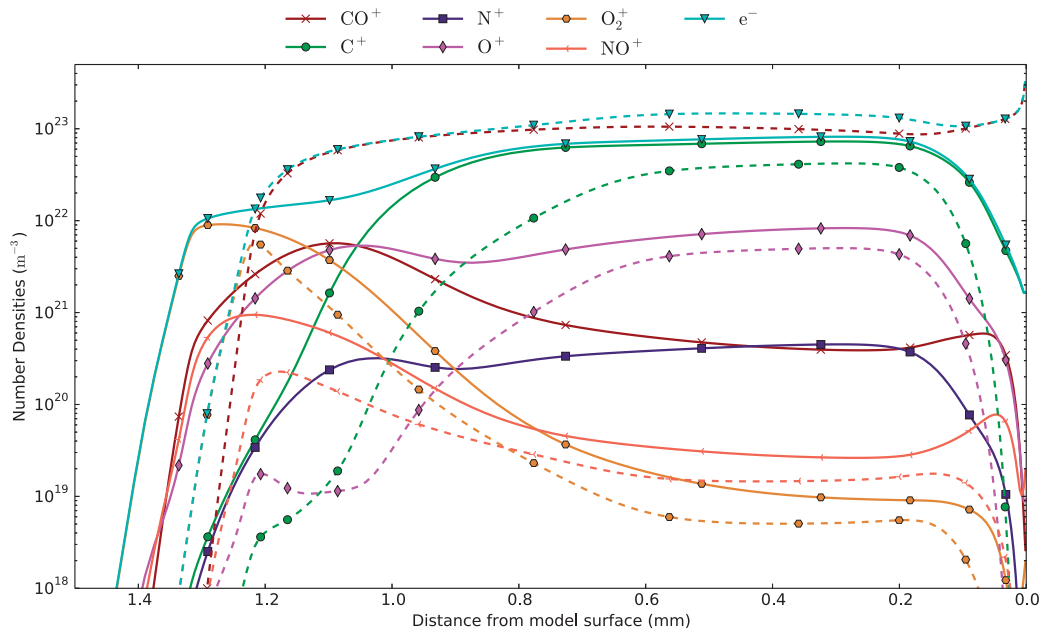
Figure 4.12: Stagnation line number density profiles for ionised species in V1 flow using the Park (solid) and Johnston (dashed) reaction schemes with a non-catalytic wall at 600 K.
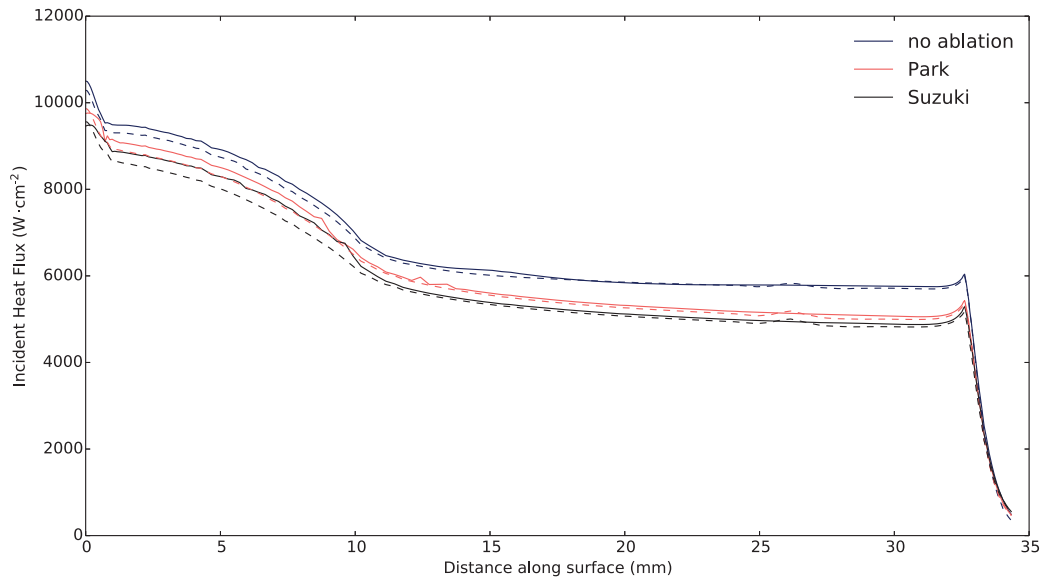
Figure 4.13: Profile of incident heat flux along the model surface with a non-catalytic wall and an ablating wall using both Park and Suzuki's surface kinetic rates. The Park (solid) and Johnston (dashed) reaction schemes are used.

In the boundary layer, higher recombination was observed using the Johnston model, where O_2, N_2 and NO (Figure 4.10) had higher concentrations than their Park counterparts. Conversely, atomic carbon, nitrogen and oxygen, as well as CN and C_2 (Figure 4.11), had lower number densities than values calculated with the Park model. A significantly higher electron density and as well as CO^+ concentration in the shock layer using the Johnston model is shown in Figure 4.12.

Convective heat flux incident on the model wall is presented in Figure 4.13, depicted from the stagnation point to the shoulder following the contours of the aeroshell. A comparison is made between the effect of the surface kinetic rates proposed by Park and by Suzuki, along with the underlying comparison between Park and Johnston's reaction schemes for CO_2-N_2 gas mixtures. First of all, it can be seen that from stagnation point to shoulder, a lower incident convective heat flux is calculated for the cases with surface reactions as compared to the non-catalytic case. This phenomenon can be attributed to convective blockage, an expected result of surface reactions. The largest difference is calculated near the model shoulder (12.8% decrease, compared to 3.5% at the stagnation point) where the lower temperature and gradients are seemingly conducive to increased production of CN and CO. The lowest heat flux value is associated with Suzuki's reduced reaction efficiency, as compared to the one provided by Park. Interestingly, heat fluxes associated with Johnston's model differ significantly from Park's model mainly around the stagnation point, in the region of highest temperatures and gradients. Near the shoulder, both models equilibrate to similar heat flux values. Compared to the heat flux incident on a non-reacting wall of 7900 W·cm^{-2} calculated in Section 3.2.2 using Sutton and Graves' empirical correlation, the CFD-computed stagnation-point heat flux differs by 21% using Park's model and 18% using Johnston's model.

In data presented in Figure 4.13, there is a local irregularity in the heat flux profile near the stagnation line ($x = 0$ mm). This feature can be attributed to the carbuncle phenomenon, a local displacement of the shape of the bow shock that is most prominent in the blunt nose region of a capsule and strongly affects heat transfer to the vehicle [124]. Even when the shock wave structure and calculated flow properties themselves show no sign of carbuncle, as is the case here, significant errors in the calculation of surface properties still commonly occur [124]. The problem remains unsolved and difficult to resolve. Some successful *quick-fixes* include the addition of numerical dissipation across the axis of symmetry

as well as realignment of the computation mesh with the location of the bow shock. As mentioned above in Section 4.2.1, a different mesh was therefore used for the E1 simulations, reducing the effect of the carbuncle, as seen in Figure 4.18.

4.3.2   *Earth Condition*

Flowfield results for the aeroshell model in a simulated Earth entry flow in X2 are detailed in this section. The stagnation line profiles for T_{tr} and T_{ve} using both Park (solid) and Abe's (dashed) reaction schemes are presented in Figure 4.14. Using the Park model, a shock stand-off distance of approximately 1.17 mm was noted, with a peak in T_{tr} of 37 734 K. Over a non-equilibrium region of approximately 0.93 mm, both thermal modes relaxed to an equilibrium temperature of 10 312 K. Past this convergence point, both thermal modes diverge once more, until they meet at the model wall. Thermal separation is also visible in the boundary layer, as both modes relax differently to the wall temperature. Modelling the gas chemistry using the Abe model, a decrease in shock stand-off distance was observed (1.14 mm), with a lower peak T_{tr} of approximately 33 203 K. Faster relaxation of T_{tr} is seen compared to Park's model, converging with T_{ve} approximately 0.24 mm from the model wall. Thermal separation is once again visible in the boundary layer. The effect of the finite-rate surface chemistry models (Table 4.4) on these profiles was negligible. A stagnation pressure of 236 kPa was calculated using both models (Figure 4.15). Good comparison is found between the experimentally measured shock stand-off distance of 1.35 mm (Figure 3.8f) and those calculated using Park and Abe's reaction schemes, which underestimate this value by 13% and 15% respectively.

The stagnation-line species number densities are displayed in Figure 4.16 for molecular species and Figure 4.17 for ionised species. The shock layer is dominated by free electrons as well as atomic N, O and their ions, which reach a state of quasi chemical equilibrium between 0.2 and 0.7 mm from the wall. Very similar concentrations are calculated for these species using both chemistry models. Due to the strong recombination of N_2 and O_2 in the boundary layer, there are negligible N and O atom concentrations at the wall for catalycity to act on and enhance heat transfer. When combined with the higher temperature calculated in the boundary layer using Park's reaction model, this results in higher emissions for comparison with experimental spectra.
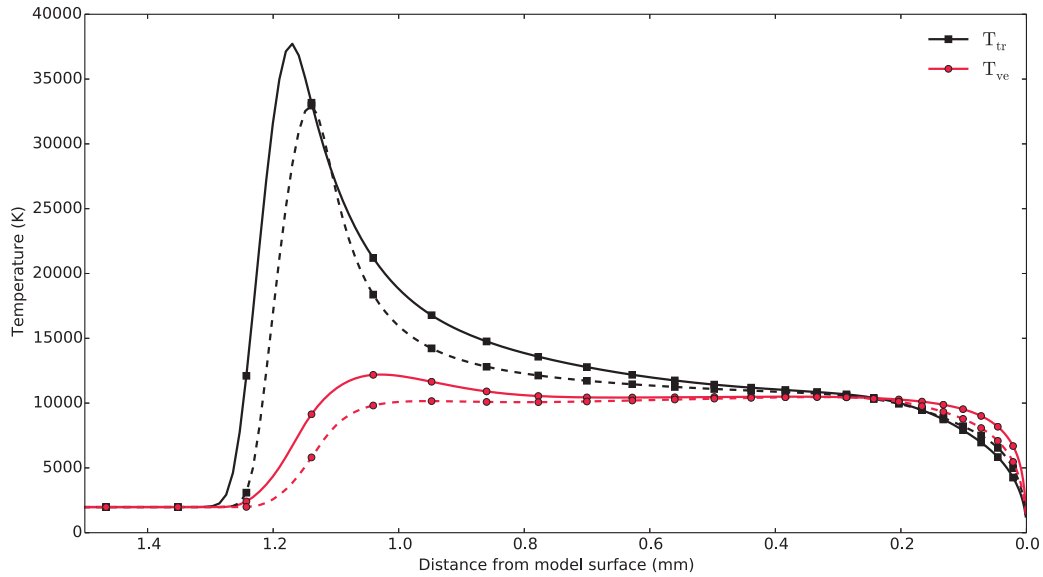
Figure 4.14: Stagnation line temperature profiles using the Park (solid) and Abe (dashed) reaction schemes.
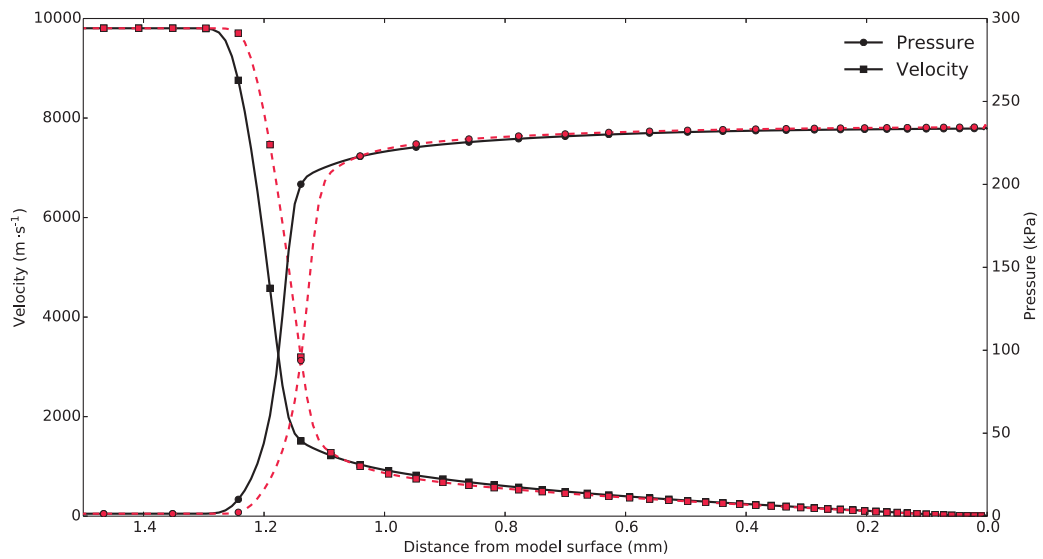
Figure 4.15: Stagnation line pressure and velocity profiles using the Park (solid) and Abe (dashed) reaction schemes.
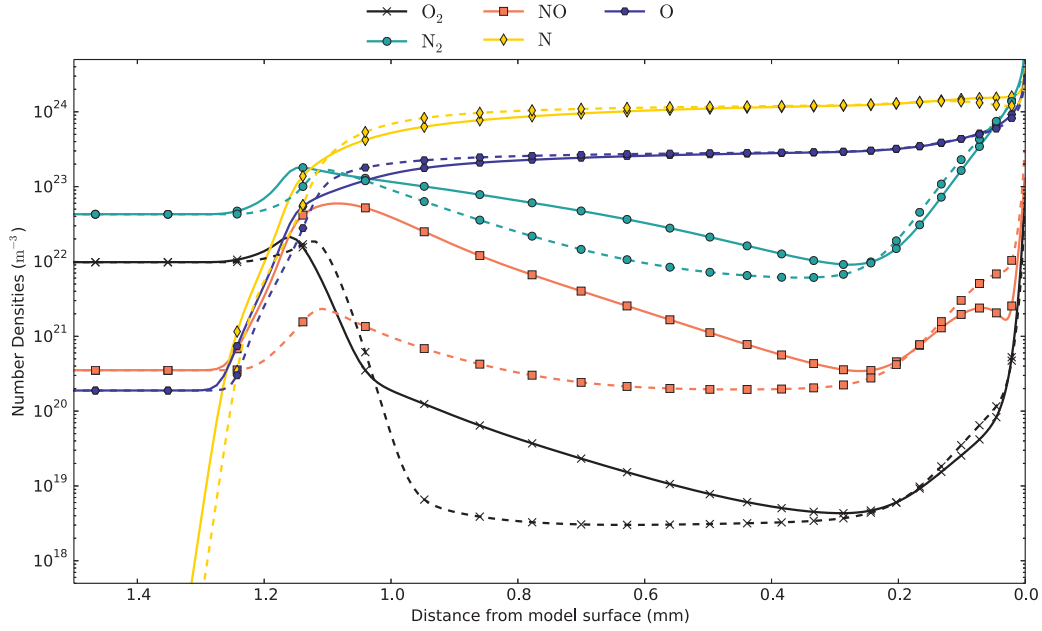
Figure 4.16: Stagnation line species number density profiles for heavy particle species in E1 flow using the Park (solid) and Abe (dashed) reaction schemes with a non-catalytic wall at 600 K.
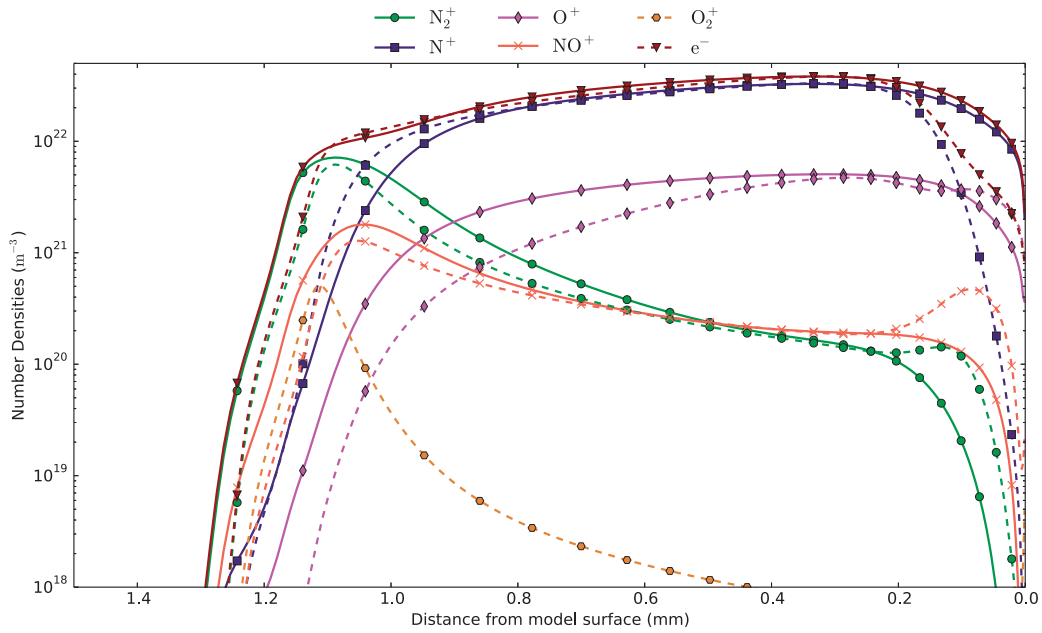
Figure 4.17: Stagnation line number density profiles for ionised species in E1 flow using the Park (solid) and Abe (dashed) reaction schemes with a non-catalytic wall at 600 K.

All other species exist in a state of chemical non-equilibrium. Simulations using Abe's model show rapid dissociation of molecular O_2, N_2 and NO. Though dissociation rates are much lower for Park's model, number density magnitudes reach near-identical levels close to the boundary layer. O_2^+, included only in Abe's model, is the only species that is created across the shock but rapidly depletes, while other ionised species reach the wall. N_2^+ concentration drops off rapidly while approaching the model wall using Park's model, but is present in larger abundance using Abe's model.

Convective heat flux incident on the model wall is presented in Figure 4.18, depicted from the stagnation point to the shoulder following the contours of the aeroshell. A comparison is made between the effect on heat flux of surface kinetic rates proposed by Park and Suzuki, along with the underlying comparison between Park and Abe's reaction schemes for ablative-air mixtures. Once again, it can be seen that from stagnation point to shoulder, a lower incident convective heat flux is calculated for the cases with surface reactions as compared to the non-catalytic case, due to convective blockage. A difference of approximately 15% is calculated near the model shoulder, compared to only 9% at the stagnation point. Using both Suzuki and Park's surface kinetic rates, the computed heat flux values are identical. Heat fluxes associated with Abe's model differ significantly from Park's model mainly around the stagnation point, in the region of highest temperatures and gradients. Near the shoulder, both models equilibrate to similar heat flux values. Compared to the heat flux incident on a non-reacting wall of $5900\,\text{W·cm}^{-2}$ calculated in Section 3.2.2 using Sutton and Graves' empirical correlation, the CFD-computed heat flux at the stagnation-point differs by 19% using Abe's model and 16.5% using Park's model.

The stagnation line number density profiles of carbonaceous species in the boundary layer are given in Figure 4.19. These species are created by oxidation and nitridation reactions on the model surface, whose production rates are governed by kinetic models proposed by Park (dashed) and Suzuki (dot-dash) defined in Table 4.4. Concentrations are shown for simulations using Park (Figure 4.19a) and Abe's (Figure 4.19b) flowfield chemistry models. In both cases, it can be seen that atomic N and O retain their pre-ablation concentrations (solid lines) and attain a quasi-equilibrium state. This similarity should mean that for comparison with experimental data from Chapter 3, the strength of the emission lines produced by these atoms in the visible and IR wavelength ranges should

depend mainly on temperature. All carbonaceous species are abundant in higher concentrations using Park's surface kinetic rates compared to Suzuki's reduced rates. This difference is more evident in Figure 4.19a, where Park's flowfield chemistry model is employed. CO, CN and C are produced in similar amounts using both surface kinetic models. The biggest difference is in the production of C_2, which is more prominent in simulations using Abe's model (Figure 4.19b). However, due to its low number density, it is unlikely to show up in the numerical spectra, thus agreeing with the experimentally obtained UV radiation data for the E1 condition.
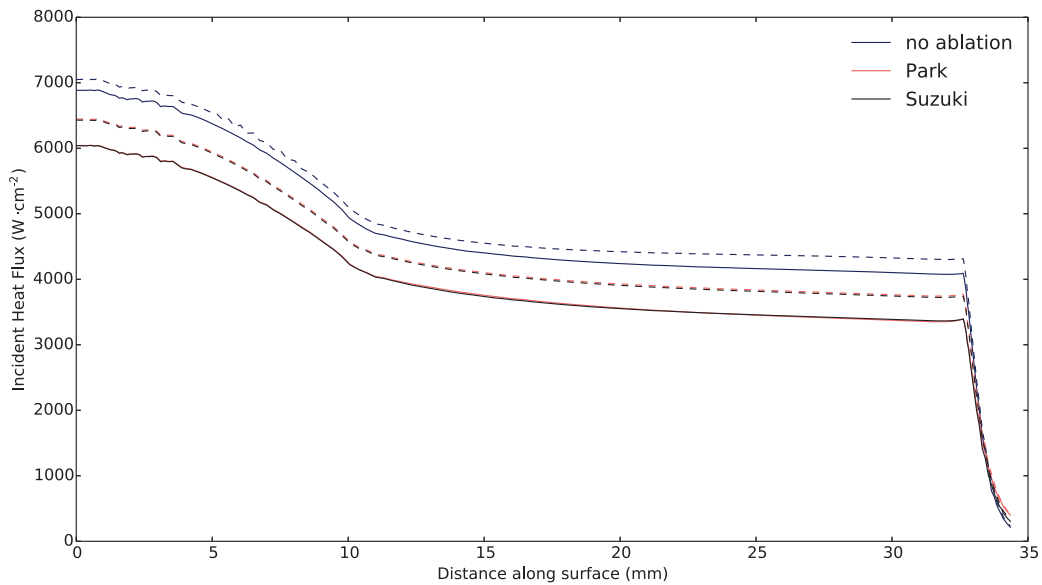
Figure 4.18: Profile of incident heat flux along the model surface with a non-catalytic wall and an ablating wall using both Park and Suzuki's surface kinetic rates. The Park (solid) and Abe (dashed) reaction schemes are used.

4.4   RADIATION MODELLING

To rebuild the exact data recorded by the spectrometers, the RTE was solved along a line of sight, chosen to mimic the experimental view at 0.1 mm from the model surface. Shown in Equation 4.19, the applied RTE ignores both scattering in weakly ionised plasmas due to low gas density, as well as transient terms due to the speed of light being far greater than the shock speed. The frequency-
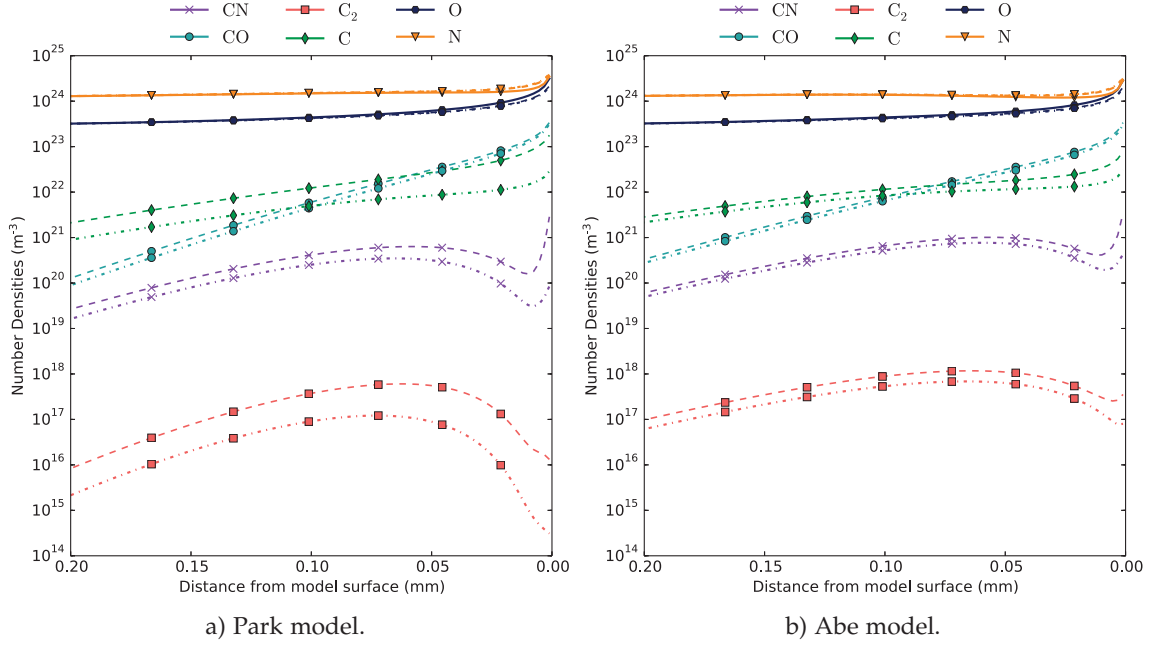
Figure 4.19: Boundary layer number density profiles for ablative species, comparing Park (dashed), Suzuki (dot-dash) reacting and non-reacting (solid) cases.

dependent intensity, I_ν was solved for as a function of path length s, as well as emission and absorption coefficients, j_ν and κ_ν.

$$I_\nu(s) = I_\nu(s_0)e^{-\kappa_\nu(s_0,s)} + \int_{s_0}^{s} j_\nu(s')e^{-\kappa_\nu(s',s)}ds' \qquad (4.19)$$

To evaluate these values, first the number of atoms and molecules that populate a particular electronic state were defined through the use of a radiation database. Using temperature and species number densities from the CFD solution as an input for each spatial point, these state populations can be calculated using two methods. The first method assumes the existence of a Boltzmann distribution for each species, but is not valid in regions of thermochemical non-equilibrium. Alternatively, a collisional-radiative (CR) calculation can be applied, simultaneously solving up to 35 coupled equations for atomic species, while requiring hundreds of rates, most of which have high uncertainties [125]. Quasi-steady state (QSS) modelling was therefore used, combining the two methods. Emission and absorption coefficients account for atomic bound-bound (atomic lines),

bound-free (photoionisation) and free-free (Bremsstrahlung) transitions as well as molecular bound-bound transitions. Based on the obtained electronic state populations, the coefficients could be calculated by linearly summing the transition mechanisms for each species.

The Photaura [69], PARADE v3.2 [70] and NEQAIR v14 [71] radiation databases were used for the above calculations, with differences in the databases resulting in different calculated intensities. The result that best matches the experimental spectra is always the one presented (Appendix B). A spectral resolution of 100 points per nm was used over a wavelength range from from $380 - 500$ nm in the ultraviolet, $615 - 700$ nm in the visible and $700 - 800$ nm in the near infrared.

The effects of Doppler and pressure broadening mechanisms on the physical flow [126], as well as effects caused by the instrument, were numerically reproduced by applying a convolution function in the spectral dimension. All of the radiation codes employed in this work allow the application of a Voigt function and a Voigt-square root function post-calculation, with Gaussian and Lorentzian line widths equivalent to the full width at half maximum (FWHM). These values were obtained using a combination of parametric studies and experimental techniques described by Cruden *et al.* [127] and are listed in Table 3.5. The square root of the Voigt function was found to best fit the experimental line shape in the wavelength range of interest and was thus employed in all calculations.

eilmer3 allows the inclusion of a radiative source term in the Navier-Stokes equations (Equation 4.1), which is required based on the degree of radiation-flowfield coupling. The extent of coupling can be estimated via the Goulard number, Γ, which is the conversion of the freestream energy flux to radiative energy flux. This is shown in Equation 4.20 below, where q_{rad} is the incoming radiative heat flux and ρ_∞ and u_∞ are the density and velocity of the freestream respectively. The radiative heat fluxes were obtained by post-processing the eilmer3 solution via the code's inbuilt radiation database, Photaura. The tangent-slab approximation was applied to the cells closest to the stagnation line, parallel to the axis of symmetry and normal to the model wall. This method models emission and absorption in the gas along discretised lines directed outwards from the wall, without having to integrate the local intensity field for all solid angles. The wall directed heat flux at point z along a line of sight is thus given by Equation 4.21 where z_s is the shock-front coordinate, j_ν is the emission coefficient, $\tau(s,z)$

is the optical thickness accounting for the absorption coefficient, κ_ν, and E_3 is the third order exponential integral, specified by Johnston [128].

$$\Gamma = \frac{2\dot{q}_{\text{rad}}}{\frac{1}{2}\rho_\infty u_\infty^3} \tag{4.20}$$

$$\vec{q}_{\text{rad}} = 2\pi \int_{s=z}^{s=z_s} j_\nu \left| \frac{dE_3[\tau(s,z)]}{d\tau} \right| ds \tag{4.21}$$

As a rule of thumb, when $\Gamma > 0.01$, the flow is said to be strongly coupled to radiative effects [129]. In this case, photons emitted from excited heavy particles can be adiabatically transported out of a control volume or be re-absorbed by the heavy ablative species present. In doing so, they would significantly alter the state of the flow. It would therefore be necessary to include the divergence of the radiative flux in the energy equation. The calculated radiative heat fluxes and Goulard numbers are presented in Table 4.6. For the V1 and E1 conditions, the Goulard numbers were estimated at 0.003 and 0.001 respectively, both below the nominal threshold. Inclusion of the radiative term was therefore thought to have a negligible effect on the flowfield and was consequently excluded from this work.

Table 4.6: Goulard numbers for E1 and V1 conditions.

	$\dot{q}_{\text{rad}}$ (W·cm^{-2})	Goulard number
Venus (V1)	317.79	0.003
Earth (E1)	51.77	0.001

4.5 COMPARING CFD AND EXPERIMENT

4.5.1 *Venus Condition*

The measured absolute spectral intensities in the ultraviolet compared with numerical spectra calculated using the NEQAIR code are presented in Figure 4.20. The experimental spectra were measured approximately 0.1 mm upstream of the stagnation point and numerical spectra were calculated at an equivalent distance from CFD solutions using both the reaction schemes introduced in Section 4.2.2. Simulated temperature profiles along the selected line of sight are presented in Figure 4.27b. Spectra calculated with NEQAIR were chosen as

they best matched the experimental results, while PARADE and Photaura overestimated all peak intensities present. A possible reason for this overestimation is that both PARADE [130] and Photaura [69] were developed and validated for Mars and Titan entry conditions, which generally occur at lower densities and velocities when compared to Venus entry. A truncated x-axis is presented in Figure 4.20 to remove all the contaminant Al and Fe peaks emanating from diaphragms and the tunnel wall, which otherwise serve only to clutter the plot. No lines of interest visible in the experimental spectra (Figure 3.9) were lost in this truncation. Several large Fe peaks still remain between $425 - 445$ nm in the experimental data, but are not modelled in the numerical spectra and therefore are not labelled.

Using the Park model, good correlation is seen for the C_2 Swan bands in Figure 4.20, matching peak intensities and line widths. However, spectral radiance was substantially overestimated for the CN Violet $v = 0$ band. This was most likely due to significant CN Violet self-absorption, which has been noted in a past study by Boubert *et al.* [131], and not accounted for by any of the radiation databases considered. This overestimation was slightly reduced when the Johnston model was applied, but was still significant. With the Johnston model, CN Violet $v = +1$ peak intensities were better matched than with the Park model, however all C_2 Swan band peaks were severely overestimated due to the increase in concentration along the line of sight. Both the implemented reaction schemes excluded N_2^+ due to Park's [96] hypothesis that its concentration and effect on the rate processes is insignificant. The N_2^+ is produced across the shock and would not significantly affect the chemical composition of the boundary layer, but it is an effective marker for non-equilibrium in the flow. Given its intensity was of similar order of magnitude to that of the CN Violet band, its inclusion in numerical models for CO_2-N_2 flows in X2 is recommended.

Experimental spectra measured in the visible wavelength range, 0.1 mm from the phenolic and the steel model surface, were compared to numerical spectra calculated using the PARADE database in Figure 4.21. In this case, the Photaura and NEQAIR databases were not presented due to severe underestimation of spectral radiances at these wavelengths. The most intense lines identified were an O atomic line at 645.59 nm and a C atomic line at 658.94 nm. Several weak CN Red bands were also present. Use of both Park and Suzuki's finite-rate surface kinetic models had no significant effect on the generated spectra, which closely resembled the non-ablating case.
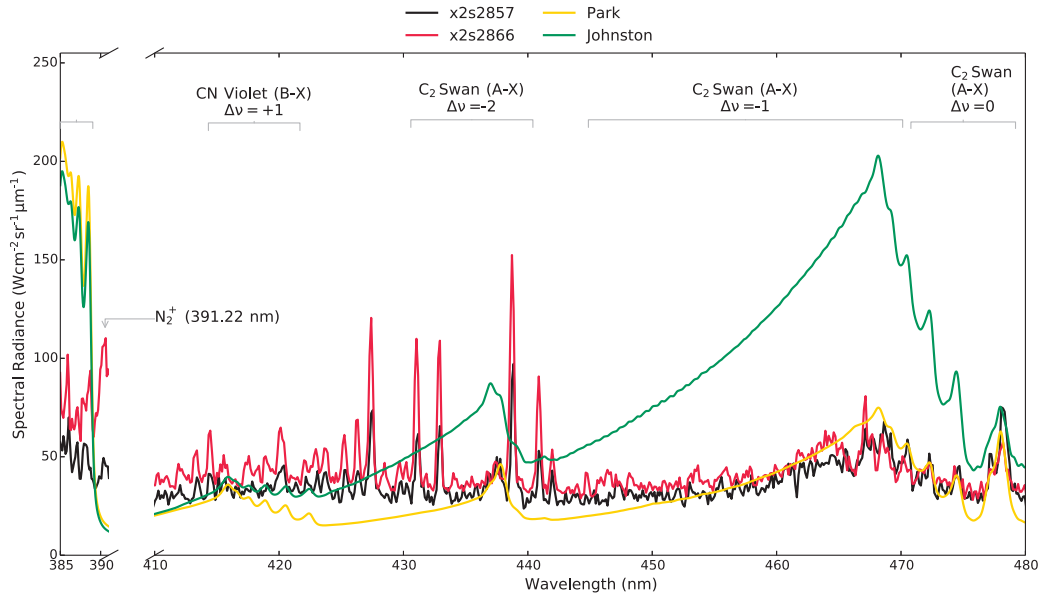
Figure 4.20: Comparison of experimental spectra taken 0.1 mm upstream of carbon phenolic (x2s2866) and steel (x2s2857) model surface with numerical spectra calculated using NEQAIR with the Park and Johnston reaction schemes.
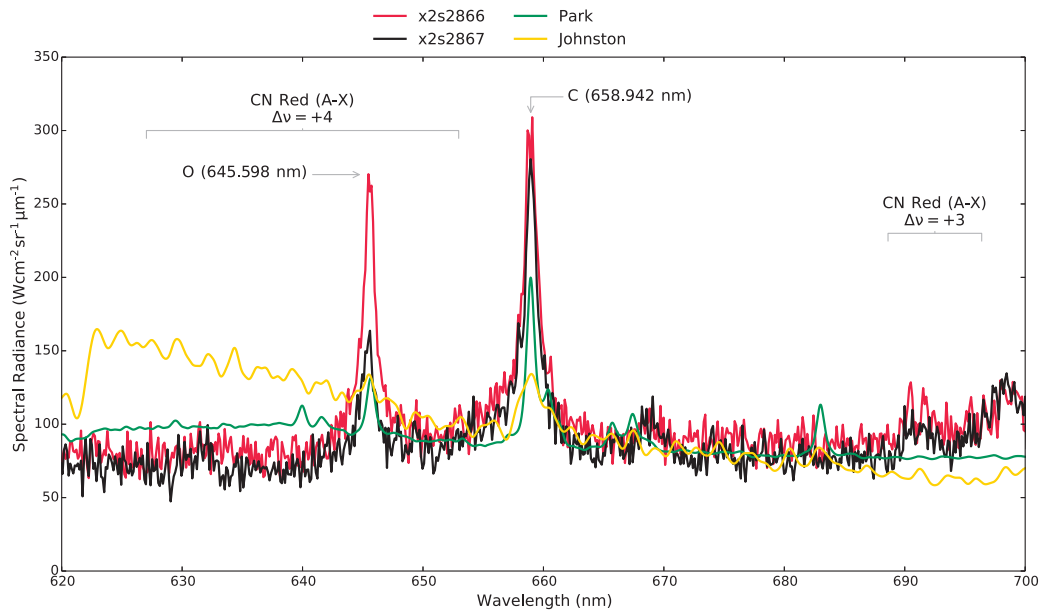
Figure 4.21: Comparison of experimental spectra taken 0.1 mm upstream of carbon phenolic (x2s2866) and steel (x2s2867) model surfaces with numerical spectra calculated using PARADE with the Park and Johnston reaction schemes.

The significantly higher level of background radiation and noise in the experimental spectra is an inherent disadvantage of measuring radiation in the visible wavelength range, as contamination from extraneous light sources is present, even after background subtraction. The numerical spectra calculated using Park's reaction scheme were therefore shifted up to account for this background radiation. This shift was achieved by the addition of the mean value for baseline experimental radiation to the numerical spectral radiances. In addition to this, the radiation codes do not sufficiently model the noise and extra broadening in the spectral line wings, which have been attributed to additional contributions from neutral Bremsstrahlung by Cruden *et al.* [132]. Spectra calculated using the Johnston model had a much higher average intensity, matching the background radiation for much of the studied range, overestimating radiance below 640 nm and underestimating it above 690 nm.

4.5.2 *Earth Condition*

Experimental spectra measured in the visible wavelength range, 0.1 mm from the model surface, are compared to numerical spectra in Figure 4.22 for the E1 condition. Simulated temperature profiles along the line of sight are provided in Figure 4.27a. All radiation calculations shown for this section were conducted using NEQAIR, as it achieved closest comparison to experimental results, as well as being the most recently updated and most stable code. The highest intensity line identified in this wavelength range belongs to atomic nitrogen at 648.21 nm as well as two less intense atomic oxygen lines at 615.82 nm and 645.59 nm. These lines are also present in the numerical spectra, calculated using both flowfield chemistry models, but at much lower intensities. The spectral comparison was once again inconclusive for visible wavelengths, with the computational results underestimating all peak intensities. Use of finite-rate surface kinetic models had no significant effect on the generated spectra, as there is no obvious radiation emitted by ablative species at these wavelengths.

When compared to the visible radiation measured for the V1 condition (Figure 3.11), the level of background radiation is significantly lower, but still present. It is hypothesised that the higher freestream and post-shock temperatures of the V1 condition (Figure 4.8) cause its flow to radiate mainly at visible wavelengths, compared to the E1 condition, where the majority of the flow radiates in the near infrared. This is not visible in the calibrated spectral intensities recorded, as the entire visible spectrum is not covered. However, this hypothesis is further

backed up by images taken of the two conditions using the high speed camera, given in Figures 3.8a and 3.8b respectively, which is limited to measuring visible radiation. The average optical densities across all pixels can be obtained via histograms of the recorded 8-bit images and used to compare mean visible radiation emitted by the two conditions. For the V1 condition, mean optical density of $\sim$ 23, which is significantly higher than $\sim$ 13 obtained for the E1 condition.

Comparison of experimental and numerical spectra in the near IR is presented in Figure 4.23. The significant emission lines of interest belong to the atomic oxygen triplet at 777.19 nm, 777.42 nm and 777.54 nm, as well as three atomic nitrogen lines at 742.36 nm, 744.23 nm and 746.83 nm. Once again the relevant emission lines are present in the numerical spectra and qualitatively speaking, the line shapes are relatively well matched. The only downside being the insufficient modelling of the increased background and subsequent extra broadening in the wings of the experimental spectra, attributed to the code's aforementioned lack of ability to model the free-free neutral-ion interactions (neutral Bremsstrahlung) [132]. It is positive to note the excellent comparison in the magnitude of spectral radiance between the experimental and numerical datasets. Similar comparison was found between numerical and experimental IR spectra using Photaura and PARADE by Fahy [44], for a larger model with higher intensity emissions in X2. Modelling the flowfield with Abe's reaction scheme results in an underestimation of spectral intensities, while Park's scheme gives near identical values to experiment.

Ultraviolet spectra are most interesting for comparison due to the presence of emission bands generated by carbonaceous species abundant in the boundary layer due to resin decomposition. Due to the plurality of the datasets generated, this comparison has been broken down into three different parts. Comparisons of experimental and numerical spectra are given in Figure 4.24 for the non-reacting wall and Figure 4.26 for the reacting wall. A comparison of the numerical spectra generated with different combinations of surface reaction and flowfield chemistry models is shown in Figure 4.25. Similar to Figure 4.20, the x-axis has been truncated in each case, to remove extraneous emission lines from contaminant species, Al and Fe. It is however interesting to note the lack of high intensity Fe peaks in the remainder of the spectrum, as found in UV measurements with the V1 condition (Figure 4.20). It is therefore quite likely that the Fe lines come from the tunnel walls being stripped by the hotter V1 condition.
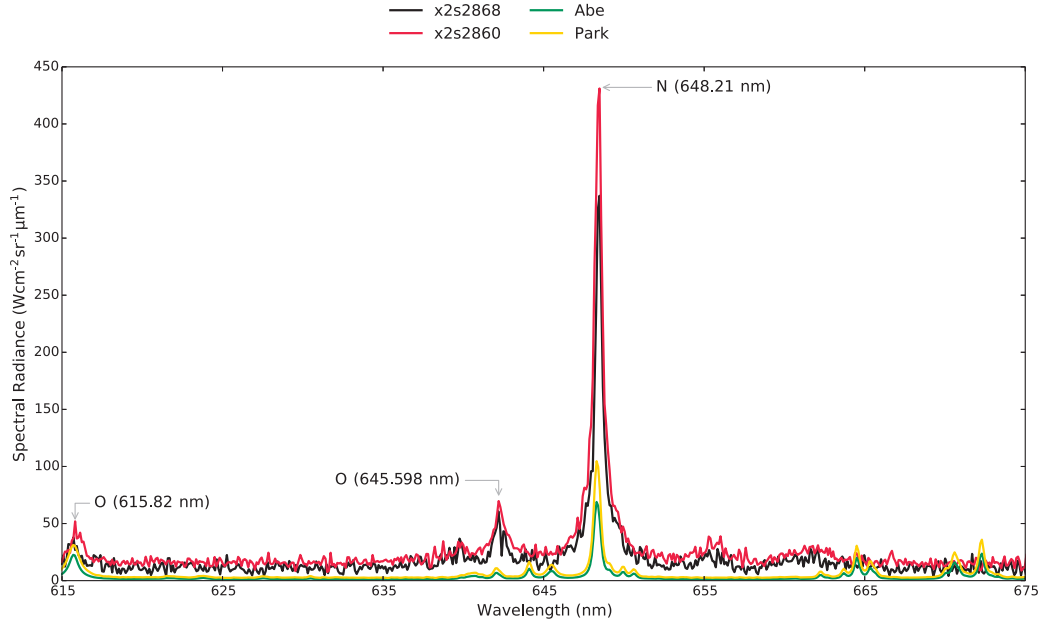
Figure 4.22: Comparison of visible experimental spectra taken 0.1 mm upstream of carbon phenolic (x2s2860) and steel (x2s2868) model surfaces with numerical spectra calculated using NEQAIR with the Park and Abe reaction schemes.
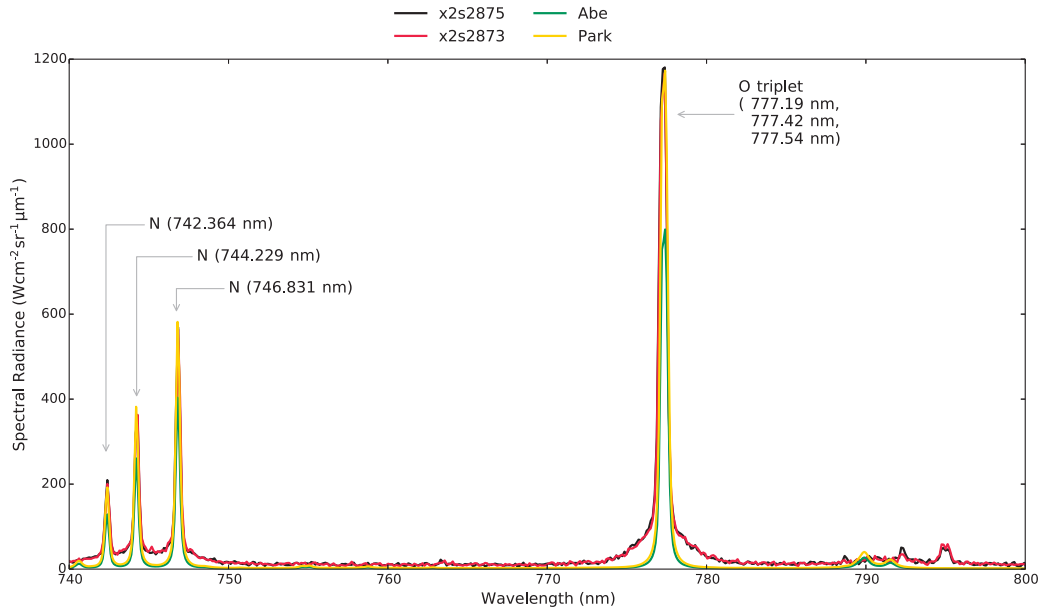
Figure 4.23: Comparison of IR experimental spectra taken 0.1 mm upstream of carbon phenolic (x2s2873) and steel (x2s2875) model surfaces with numerical spectra calculated using NEQAIR with the Park and Abe reaction schemes.
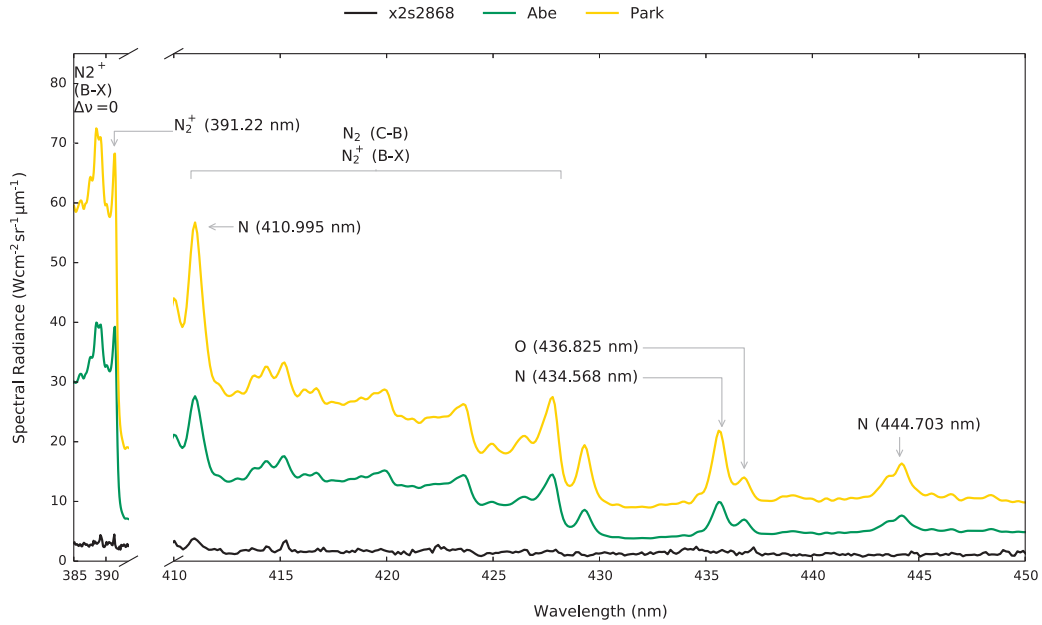
Figure 4.24: Comparison of UV experimental spectra taken 0.1 mm upstream of steel model surface (x2s2868) with numerical spectra calculated using NEQAIR with the Park and Abe reaction schemes.
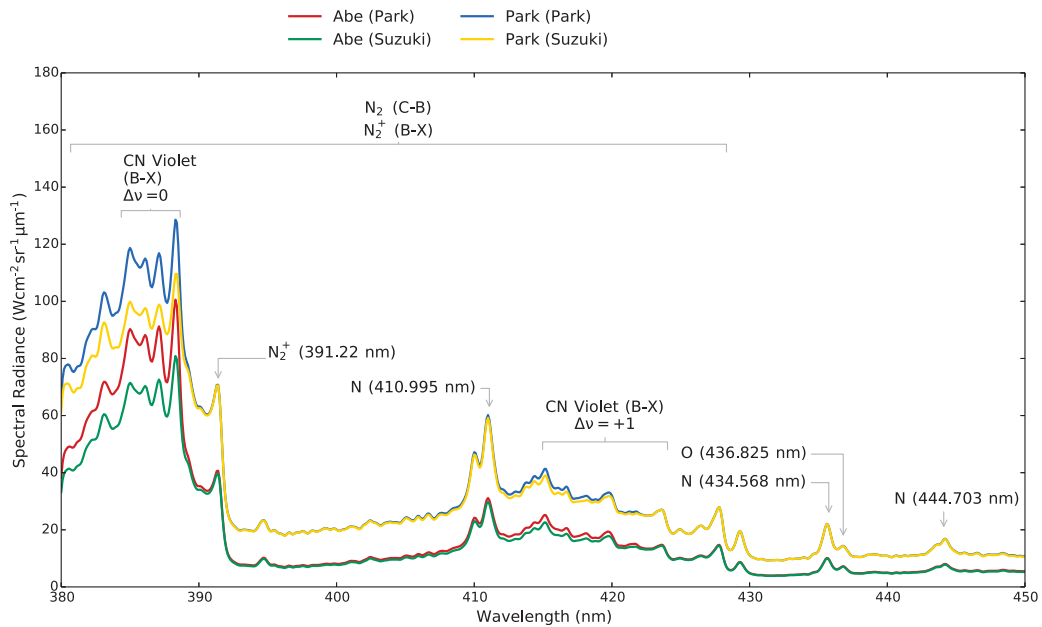
Figure 4.25: Comparison of numerical spectra calculated, using NEQAIR, in the UV, 0.1 mm upstream of the reacting model wall, for E1 condition for the used combinations of surface and flowfield reaction schemes and rates.
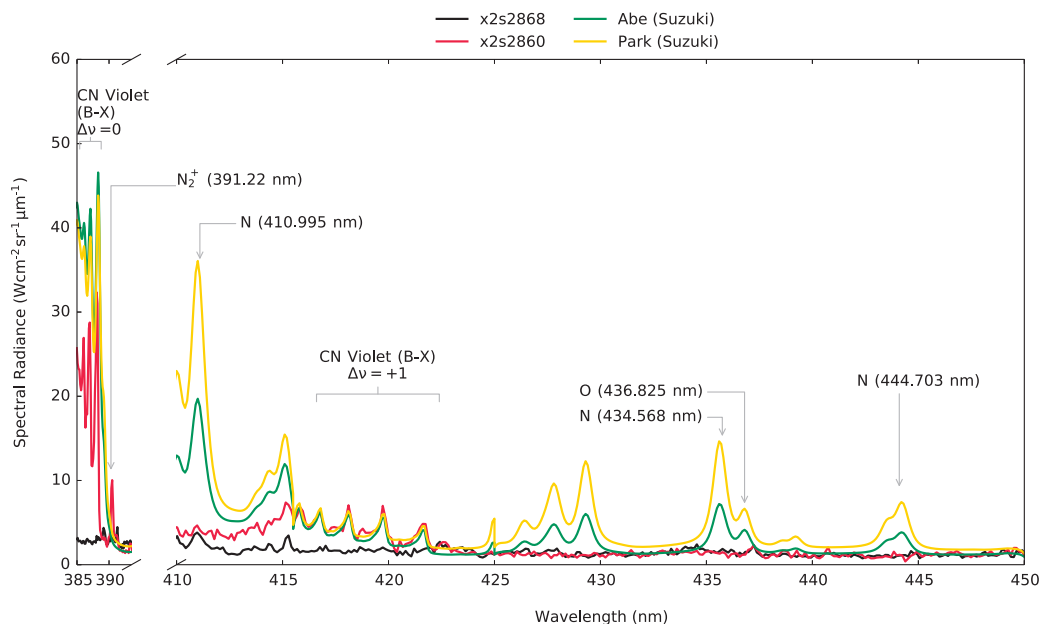
Figure 4.26: Comparison of UV experimental spectra taken 0.1 mm upstream of carbon phenolic (x2s2860) and steel (x2s2868) model surfaces with numerical spectra calculated using NEQAIR with the Park and Abe reaction schemes, having removed N_2^+ radiation.

From Figure 4.24, it is clear that from 385 nm to 450 nm, there are few significant emission features measured at a distance of 0.1 mm from the surface of the steel model in X2. Small peaks are seen for atomic nitrogen at 410.995 nm, as well as the N_2^+ First-Negative $\Delta\nu = 0$ bandhead at 391.22 nm. However, the numerically generated spectra show significant emission in this wavelength range, stemming mainly from N_2^+ $(B - X)$ and N_2 $(C - B)$ band radiation, as well as peaks of atomic oxygen and nitrogen which are unclear in the experimental data. The Park chemistry model leads the Abe model in severe overestimation of spectral radiance for this case. Given that the radiation is already largely overestimated for the non-phenolic case, emissions due to carbonaceous species produced by surface reactions would only serve to further exaggerate the discrepancies.

A comparison of numerically generated spectra was therefore carried out to select which model would best fit the experimental data recorded at a distance of 0.1 mm from the decomposing phenolic model surface. Out of the four

sets of CFD results shown in Figure 4.25, the flowfield gas chemistry of two sets was modelled using Park's reactions and the remaining simulations used Abe's reactions. The surface reactions, employed to simulate resin decomposition through oxidation and nitridation of the phenolic have already been described in Table 4.4 and are displayed in brackets in the figure legend. As expected, both surface reaction models introduce CN Violet bands into the emission spectra. Suzuki's reduced nitridation rate results in lower intensity CN bands and is thus more suited to comparison with low intensity experimental bands (Figure 3.13). Following on from Figure 4.24, the Park model predicts a higher spectral radiance than the Abe rates. This is due to the substantial overestimation of N_2^+ radiation, which was similarly noted by Fahy [44].

It is hypothesised that the over-prediction of N_2^+ stems from the use of the two-temperature approximation, where reaction rates are governed by a combination of thermal modes. Across the shock wave, where N_2^+ is produced, there is a large spike in the translational, rotational and vibrational modes, while the electronic modes lag behind, since the plasma is weakly ionised [69]. Since N_2^+ forms from direct ionisation of the N_2 molecule, its formation should mainly depend on the electronic temperature mode. However, using T_{ve} to control production rates creates a non-linear spike in the Arrhenius type reaction (Equation 4.8). This is also seen when comparing the lower levels of N_2^+ radiation computed using the Abe model, which is at a much lower post-shock temperature compared to Park's model (Figure 4.14) and thus produces less N_2^+ (Figure 4.17). This could possibly be resolved via the complex implementation of a three temperature model, which separates translational-rotational, vibrational and electronic thermal modes. This in turn could allow ionisation reactions to be controlled by the electronic temperature, which would be more suitable.

It was therefore decided to remove N_2^+ from the radiation model, to investigate whether the generated spectra would be a closer fit to the experimental results. A severe reduction in intensity can be seen in Figure 4.26, across the entire wavelength range. The CN band lines and shapes are faithfully reproduced using a FWHM of 0.25 nm. The CN Violet $\nu = 0$ band radiation is over-predicted by a factor of 1.5. Atomic nitrogen and oxygen lines are also over-predicted by the numerical spectra. However, the CN Violet $\nu = +1$ band radiation reproduces experimental line shape and intensity extremely well.

Sources of Uncertainty

a) E1 condition.   b) V1 condition.
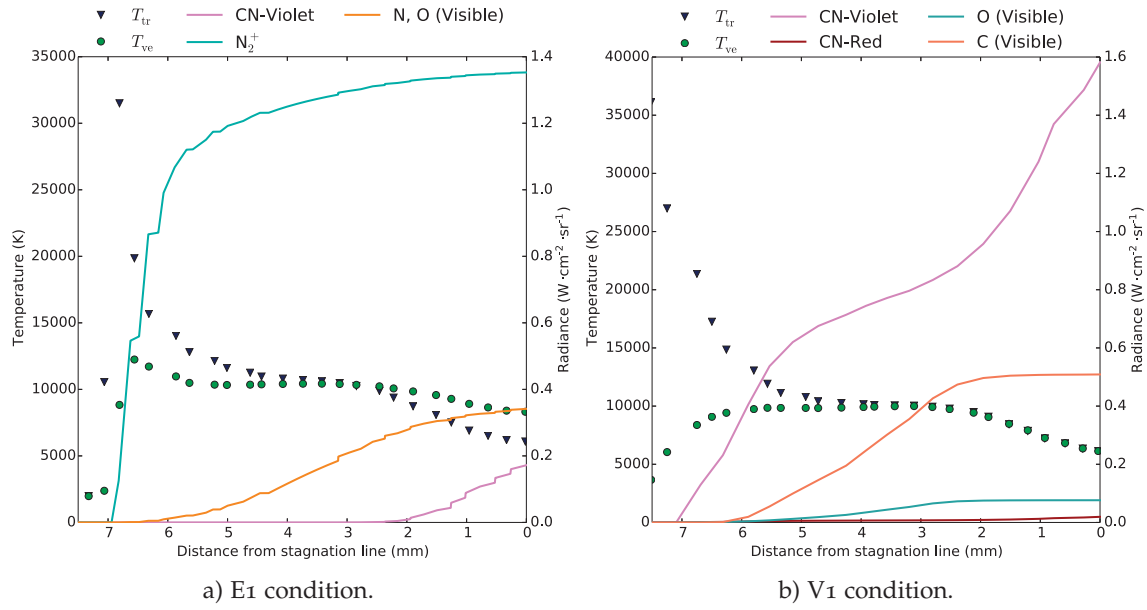
Figure 4.27: Selected radiance and temperature profiles along the line of sight (taken axially 0.1 mm from the stagnation point), from the stagnation region ($x = 0$ mm) out towards the periphery of the flow ($x = 7.5$ mm) leading to the spectrometers ($x \gg 7.5$ mm, omitted from plot).

Line of sight temperature profiles have been provided for both conditions, in Figure 4.27, along with the radiance of the bands under investigation. For the E1 condition, in Figure 4.27a, it can be seen that the majority of the flowfield is in a state of thermal non-equilibrium. This subsequently requires the radiation to be modelled using the CR mechanisms described in Section 4.4. As expected, N_2^+ is produced mainly across the shock [11], where non-equilibrium between the two thermal modes is significant. Similarly, radiance from CN-Violet bands between $385 - 392$ nm and atomic N and O between $640 - 650$ nm is seen to increase in the non-equilibrium zone near the stagnation line. Further investigation of CR models for these species is therefore required to improve comparison with experimental data. For the V1 condition, in Figure 4.27b, the majority of the band radiation that is over or under estimated by the radiation codes actually occurs in the zone of thermal equilibrium, modelled using Boltzmann populations.

Out near the periphery of the flow, a short line of sight to the spectrometer would experience less absorption. However, a large portion of CN-Violet band radiation, for both conditions, seems to be produced close to the stagnation region ($x = 0$). It is therefore likely that, as previously hypothesised in Section 4.5.1, strong self-absorption of CN-Violet $\Delta v = 0$ radiation occurs along the line of sight, reducing intensity received by the spectrometer. This self-absorption seems to not be accounted for by NEQAIR, which results in an overestimation in the numerical spectra.

4.6 CONCLUSIONS

The generally successful comparison of numerical simulations with experimental data presented in this chapter are a step forward in proving the validity and reliability of computational aerothermodynamic tools. Through the completion of *Objective O.3*, strong shock layers formed around a decomposing model in Earth and Venus entry flows in X2 have been simulated for the first time, using CFD and radiation modelling. Differences between the numerical and experimental data have been identified and reasons for their existence hypothesised.

2D axisymmetric CFD simulations were performed to numerically simulate the flow around non-reacting steel and decomposing phenolic aeroshell models subjected to Venus (V1) and Earth (E1) hypersonic flows in the *X*2 expansion tube. A separate mesh was generated for each condition, with cells clustered at the shock and wall for the V1 case and just at the wall for the E1 case. A grid resolution study was conducted on both the final meshes using the translational-rotational temperature, T_{tr}, as the test parameter. In each case, the theoretical temperature at zero grid-spacing and the theoretical order of convergence were found to be within the required range to demonstrate convergence. Better convergence was achieved with the mesh used for the E1 case.

The thermal energy exchange and thermochemistry were then defined for each condition. This included selecting the relevant equation of state, thermal modes, energy exchange mechanisms, and chemistry models to best represent the state of thermochemical non-equilibrium in the shock layer. Two flowfield chemistry models were chosen and compared for each condition. A boundary condition was defined to model resin decomposition on the phenolic model surface, simulating oxidation and nitridation reactions using two separate finite-rate

models. Accurate modelling of shock layer transport properties required the use of collision integrals, some of which were not available in literature. New values were therefore calculated for neutral-neutral interactions, based on the Lennard Jones and Stockmayer potentials for non-polar and polar molecules respectively, coupled to empirical corrections. Good agreement was found for both polar and non-polar interactions when compared to similar values in literature.

For comparison with experimentally obtained spectra, the radiative transfer equation was solved along a line of sight in the CFD solution. This line was chosen to mimic the experimental line of sight, at a distance of approximately 0.1 mm from the stagnation point. Emission and absorption coefficients were calculated by coupling the calculation to a radiation database. A comparison of numerical and experimental spectra for the V1 condition showed the presence of the same spectral lines and good approximation of line shape as well as spectral radiance for the C_2 Swan band. On the other hand, CN Violet band intensities were heavily overestimated and are thought to be self-absorbed in experiment. At visible wavelengths, comparison was inconclusive, with the underestimation of peak intensities across the entire range. In general, spectra produced from flowfield solutions calculated using Johnston's reaction scheme resulted in stronger emission compared to those obtained using Park's reaction scheme. Use of kinetic models to simulate resin decomposition on the model surface had no effect on the calculated spectra.

For the E1 condition, comparisons were made in the IR, visible and UV wavelength ranges. Through the use of Abe's chemistry model, generated numerical spectra produced lower intensity values than those obtained using Park's model. Once again, the radiation in the visible wavelength range was underestimated by the both chemistry models, even though the presence of the same lines and similar line shape was noted. Comparisons in the IR were extremely successful, with simulations conducted using Park's chemistry model providing near-identical peak intensities and line shapes. Comparisons of UV radiation were the most interesting as decomposed resin from the phenolic model surface mixed with hot boundary layer gases to emit strong CN band radiation, not present in control measurements with a steel model. Use of Suzuki's nitridation rate resulted in lower levels of CN band radiation compared to Park's finite-rate surface kinetic model. N_2^+ band radiation was seen to be largely overestimated by both flowfield chemistry models, contaminating the numerical spectra and causing large over-predictions. This has been sourced to the use of the

combined vibrational and electronic thermal modes to control the N_2^+ reaction rates, which creates a spike in production via the Arrhenius model. After subtracting N_2^+ radiation from the numerical spectra, CN Violet band radiation calculated in the UV showed excellent comparison with experimental data.

Further work is required to understand the reasons behind visible discrepancies and whether they are due to the calculated temperature in the boundary layer, the reaction or energy exchange models selected or the radiation databases underestimating the radiative coefficients for the species involved. To reduce the effect of noise for the V1 condition, Boubert *et al.* [131] have suggested the use of a 70% CO_2 - 30% N_2 gas mixture which is said to significantly improve the emission signal to noise ratio while keeping the chemical kinetic processes the same as a traditional Martian or Venusian atmosphere. Different wavelength ranges, such as $300 - 400$ nm and $450 - 580$ nm, should be investigated in the future for a better understanding of the behaviour of the CN and C_2 band emissions in Venus flows. For the E1 condition, measuring radiation in the $340 - 390$ nm range would allow the further study of CN and N_2^+ radiation at this condition.

Accurate knowledge of the model surface temperature is essential for numerical rebuilding. With the aim of simulating phenolic pyrolysis with these models, the targeted temperatures would not be high enough to use the pyrometers in place at the facility for measurements. Careful placement of thermocouples below the model surface should give a reliable estimate. Many of the visible discrepancies stem from the error in calculation of freestream conditions. To reduce this error, better thermodynamic data is required at the nozzle exit.

Part II

INTERNAL HEAT TRANSFER

HEAT TRANSFER IN TPS MATERIALS: A REVIEW

A wide range of factors affect the design of a spacecraft's thermal protection system. The choice of material is dictated by the surface heating rates while the thickness is largely dependent on the heat load integrated over the vehicle's trajectory [32]. Laub [8] shows that the fraction of an entry vehicle's mass devoted to the TPS strongly correlates to total integrated heat load and performance characteristics, such as the optimal material strength and thermal conductivity. Typically, these properties are both proportional to material density, therefore requiring a trade-off between ablation, insulation performance and an acceptable mass penalty. Reducing the mass in favour of added payload weight allocation also brings into account the economics of the system. The Chinese, for example, successfully used a TPS made of oak wood, which was economical but resulted in a heavy vehicle [3, 133].

In addition to thermal stresses, it is critical to account for mechanical stresses during the design phase, such as severity of the shear environment. Manufacturability, ease of assembly of the heat shield tiles and size of the aeroshell must also be given due consideration. Smaller capsules such as Stardust have heat shields made of a single large piece of material, while larger capsules such as MSL need one composed of tiles of various sizes and thicknesses, increasing the complexity of assembly and qualification. The sizing of the material thickness is based on a selected threshold temperature which should be held constant at the bondline joining the aeroshell and the TPS. This temperature is usually dependent on the properties of the silicon glue used to join the two structures. These requirements are then validated using a combination of theoretical modelling (see Section 7.2.1), ground testing (explained in-depth in Section 2.1) and flight data from previous missions. Thermo-physical models are developed to predict and reproduce the TPS material's high temperature response, both on the surface and in-depth.

5.1 MODELLING ABLATION AND THERMAL RESPONSE

5.1.1 *A Historical Perspective*

In the early 1960s, rudimentary ablation modelling began by coupling the one-dimensional conduction equation to resin density decomposition, modelled using a single Arrhenius equation [134]. Soon after, Kendall *et al.* [135] added a modified surface energy balance (Equation 7.7, further detailed in Section 7.2.2) involving B' non-dimensional ablation rates, non-unity Prandtl and Lewis numbers as well as unequal heat and mass transfer coefficients. The single reaction Arrhenius model was improved upon by Goldstein [136] to include three reactions to describe the decomposition of the resin matrix.

This work culminated in the Charring Material Thermal Response and Ablation Program (CMA) [137], which remained industry and NASA's main ablation code for TPS sizing and design until the turn of the century. With most models for ablative materials developed and validated in the 1960s, progress stalled due to the lack of new ablative materials, the success of the implemented TPS designs, NASA's switch to reusable TPS with the advent of the Space Shuttle and often unfavourable cost-benefit analyses [138]. In 1999, Chen and Milos [65] developed the Fully Implicit Ablation and Thermal response program (FIAT), based on the same theory as CMA. The energy conservation equation is solved in one dimension using a fully implicit finite difference formulation, thereby improving numerical stability and convergence compared to CMA. This allows more complete and rigorous analysis of heat shield response coupled to CFD and radiation tools, currently making FIAT the primary analysis tool for analysis of heat shields for aerothermodynamic missions.

5.1.2 *Decomposition Kinetics*

Experimental test data provide thermal response models with material properties and decomposition kinetic parameters. Thermogravimetric analysis (TGA) measures the mass loss of the TPS material as a function of temperature. The highest specification systems can still only attain temperatures up to approximately 2100 K at a maximum heating rate of $100\,\mathrm{K\cdot s^{-1}}$ [5, 22]. Though unable to test the TPS materials within their full operating range, this methodology still allows the determination of decomposition kinetic constants for the Arrhenius equations.

Differential Scanning Calorimetry (DSC) is used to study the heat of reaction for pyrolysis as a function of temperature. Elemental compositions of the virgin material and pyrolysis gases are studied using mass spectroscopy and gas chromatography respectively. Gas enthalpies as well as specific heat and thermal conductivities of the virgin material are measured using specialised laboratory setups. Quantification of the char thermal conductivities and specific heats is much more complex. Covington *et al.* [139] tune the variables by matching model predictions to experimental arc-jet data. Till date, the majority of thermal response models still use thermochemistry data from the late 1960s, detailed by Sykes [140] and April, Pike and Del Valle [141]. A combination of the aforementioned experimental methods and theoretical developments were used to study the finite-rate chemistry and energy transfer due to reacting flow of pyrolysis gases in a charring ablator.

5.1.3 *State of the Art Models*

With the aim of reducing the TPS mass penalty on payload for interplanetary missions, there has been a recent push to develop higher fidelity ablation models, resulting in more than 25 codes throughout the community employing advanced thermo-physical and thermo-mechanical models of varying complexity, as summarised by Lachaud *et al.* [142]. Chen and Milos have recently expanded FIAT to allow for anisotropic material properties and heat transfer in two and three dimensions [143, 144]. While Dec and Braun [145] have exploited the advantage that finite element methods have in their ability to discretise and work with complex, three dimensional geometries when compared to finite difference methods. Ewing, Laker and Walker [146] present a unique model, incorporating the effect of material swelling and mechanical erosion in traditional models. Recently, Fu, Wenk and Martin [147] fully coupled mechanical and thermal response for ablative TPS to show the significant effect of temperature on mechanical performance and stress generation.

New high fidelity ablation tools such as PATO developed by Lachaud *et al.* [18] have implemented multi-dimensionality and applied Darcy's law to model flow of the pyrolysis gas through the pores. This is especially important given the decreasing material density of current and next generation TPS materials. The underlying equations used have been summarised in Section 7.2.1. Steps have been taken towards eliminating the cumbersome B' non dimensional ablation rates, in favour of calculating surface thermochemical ablation within the code.

In a separate study, Ferguson *et al.* [148] use a multiscale approach to investigate in depth oxidation and mass loss in PICA. Further research involving, amongst others, the inclusion of roughness effects, surface ablation and in-depth radiation is being encouraged and pursued [138].

5.2   INCORPORATING RADIATION

Radiative characterisation of morphologically complex macroporous media is of importance in a variety of applications and technologies including entry vehicle heat shields, combustion, solar energy conversion and chemical processing. Of special interest to this work is the radiative transfer through highly porous fibrous media containing loosely packed, randomly oriented fibres, thermoset in a polymeric resin matrix, which are employed in entry vehicle TPS. The extremely low effective conductivity of these media relates to their ability to suppress radiative energy transport by scattering and absorption [149]. To be able to study radiative heat transfer in these materials, it is imperative to have prior knowledge of their optical properties.

5.2.1   *Radiative Characterisation*

Legacy TPS materials absorbed the majority of incident radiation at the surface due to their high density. Experimental validation of in-depth radiative behaviour was therefore considered redundant. Recent adoption of low density porous ablators, however, suggests possible transmission and in-depth absorption of incident fluxes. White [36] used a solar tower to irradiate PICA samples according to incident fluxes simulated for lunar return trajectories. No evidence of in-depth transmission and absorption of PICA under radiative heating was found in the near infrared wavelength regime. There is a strong possibility that results would vary with heating rates and the selected wavelength range. Delmas, Le Foll and André [150] have recently validated an experimental methodology for the measurement of radiative properties of a silica ceramic between $800\,\mathrm{K}$ and $2000\,\mathrm{K}$. Similarly, Haussener *et al.* [151] estimated the extinction coefficient, via spectroscopy measurements, of a reticulate porous ceramic foam sample meant for high temperature processing.

Incoming radiation in the form of plane waves propagate as cylindrical waves upon interaction with the fibres. Highly porous fibrous materials are most often manufactured with an average separation between fibres larger than

the fibre diameter and wavelength of the incident radiation. This provides the scattered waves enough time to recover their prior phase and amplitude before being further attenuated [149]. Therefore, the scattering characteristics of any fibre are unaffected by other fibres in the medium, resulting in so-called independent scattering. This is not the case for high density insulations used as refractory combustion chamber liners, woven cloth heat shields and various types of fibre-reinforced matrix composites, which contain closely spaced aligned fibres and undergo dependent scattering. The assumption of independent scattering, in the materials of interest to this work, allows for relatively straightforward modelling via use of the radiative transfer equation (RTE).

Le Foll *et al.* [152] used a backward Monte Carlo method coupled to Mie theory to calculate the radiative properties for a single fibre in a TPS material, which were then homogenised over several fibres. When the typical length of the fibres is much greater than the wavelength of the incident radiation, the absorption and scattering characteristics of infinite cylinders can be used and their orientation set to isotropic, anisotropic or random [153]. Due to the two dimensional scattering behaviour of the fibres, their radiative properties vary heavily with orientation [154] due to their incident angle dependent extinction and scattering cross sections. According to Lee and Cunnington [155], the "major consideration" in evaluating the effective radiative properties is therefore the proper formulation of the RTE to account for sample morphology.

Recent advances in computational techniques allow for the incorporation of the exact morphology from 3D data obtained by imaging techniques such as computed tomography [156, 157, 158]. These investigations rely on volume averaging theory for the derivation of the homogenised RTEs [15, 16, 17]. The incorporated effective radiative properties can be obtained by using Monte Carlo techniques, in the limit of geometrical optics, as defined by Tancrez and Taine [159]. The theory has been derived for the most general case of multi-component media with semi-transparent homogeneous, isotropic single phases [15].

To date computational applications have assumed two phases, either transparent and opaque [15], or transparent and semi-transparent [17, 160, 161]. In a variety of applications however, there is a possibility of both phases being semi-transparent in the wavelength range of interest, or, for reacting media, during part of the reaction process [162]. The resulting macroscopic optical behaviour

is dependent on the material microstructure, bulk properties of the phases and inter-phase characteristics. Incorporating this macroscopic optical behaviour into a coupled multi-physics computation or investigation requires detailed knowledge of the effect of the different phases and their properties on the overall optical behaviour.

5.2.2   *Coupling Radiation and Conduction*

The effect of thermal radiation energy transport through highly porous insulators has historically been an active research topic, reviewed in depth by Lee and Cunnington [149]. Tong [163] explained that analytical solutions to the RTE are difficult to obtain due to spectral dependance of the radiative properties, as well as the complex mathematical nature of the equation system. Earlier studies, such as one by Banas [164], used a semi-empirical approach, quantifying the consequences of radiative heat transfer via an effective thermal conductivity. This effective conductivity always included a radiation conductivity term, which was based on empirical recordings determined on a best-fit basis from heat transfer data. However, this approach was far too limited, as experiments were necessary for each type of fibrous insulator to determine the empirical parameter.

Later studies such as those by Tong *et al.* [163] and Stark [165] solved Maxwell's equations to calculate the radiative properties of a single fibre. For the entire material, these properties are therefore equal to the sum of the properties of the individual fibres [149]. Scaling up in complexity to a composite material consisting of a fibre phase and a resin/gas phase, the effective radiative properties were obtained by calculating a weighted sum of the properties of each participating phase, based on the solid volume fraction [155]. These properties were then used in conjunction with approximate heat transfer models to evaluate the thermal response of the insulator in question. Due to their simplicity, the Rosseland diffusion approximation, used by Caps *et al.* [166] and Dombrovsky [167] and the two-flux method, used by Tong [163] and Lee [154], have achieved widespread use in one-dimensional engineering problems [168]. The method of discrete ordinates, spherical harmonics as well as the zonal and Monte Carlo methods can alternatively be used to solve radiative heat transfer in low density fibrous media [169].

5.2.3 *Including Radiation in TPS Thermal Response*

To be considered of value in a TPS sizing and design process, a numerical tool must be able to conduct the complex calculations required, as efficiently as possible. This includes solving the finite-rate species conservation equations and flow of gas through the pores and surface ablation. The effect of internal radiation has largely been ignored by traditional material response models. With the current recognition of ablation as a volumetric effect with in-depth consequences, this thinking has started to change.

To be able to maintain the required computational efficiency, Rosseland's diffusion approximation (Equation 7.5) is used to quantify radiative heat transfer in the TPS material in its high enthalpy surroundings. It uses a modified diffusion approximation, accounting for scattering by the fibrous medium, to formulate a radiative thermal conductivity, which is then applied to an equation similar to heat conduction. Traditionally, the diffusion approximation has the inherent assumption that radiation can be treated as a diffusion process in an absorbing, optically thick medium [168]. This assumption has been extended, by various researchers, to be valid for an absorbing and scattering medium [166, 170], but is not without its limitations.

Kaviany [171] remarked that the major limitation of this method is the difficulty of calculating the required radiative exchange factor, which is heavily dependent on the conductivity of the solid phase. The approximation is not valid near any surfaces, where higher-order derivatives of T^4 are required [172]. It is also only valid when the medium is linearly anisotropic [169].

Pinaud *et al.* [173] have used Airbus' proprietary ablation code, `Amaryllis`, to model the thermal response of ASTERM subjected to high enthalpy plasma in an arc-jet. The diffusion approximation with simplified radiative properties estimated via Mie theory is used to incorporate internal radiative effects. Daryabeigi *et al.* [174, 175] used a combination of experimentally and analytically derived radiative properties as an input to the diffusion approximation for a range of low density fibrous insulators. In order to study the anisotropic behaviour of fibre preforms, van Eekelen and Lachaud [176] developed a phenomenological model for effective radiative conductivity based on calculating the view factors using a Monte Carlo method. They show a dependence of radiative conductivity on temperature without linking it to fibre orientation. Subsequently, Nouri and

Martin [177] calculated a geometrical configuration factor for an artificial carbon fibre preform morphology, using a direct simulation method, to show the angular and temperature dependance of radiative conductivity. These models, however, are all based on either simplified or artificial structures and do not account for the true morphology of the medium.

More recently, radiative conductivities are being evaluated using several methodologies for exact 3D morphologies obtained via X-ray computed tomography. Nouri *et al.* [178] expand upon their previous work [177], by calculating a geometric configuration factor to compute radiative energy exchange on a polygonal mesh of fiberform (carbon preform used as a base for PICA), obtained from 3D micro-scale imaging. Vignoles and Ortona [179] implemented a hybrid Monte Carlo/random walk algorithm to calculate effective thermal conductivity of a digitised 3D sample of an open cell foam, obtained via computed tomography. They accounted for the coupling of the conduction in the solid phase and radiation in the pore space. They also find anisotropy of the effective thermal conductivity to decrease with temperature. Mendes *et al.* [180] used much simpler semi-analytical models to calculate effective thermal conductivity of open-cell metal foam samples at high temperatures obtained via micro-tomography. They claim that the effective properties needed for this calculation can be estimated efficiently using simple numerical tools, based solely on the data extracted from tomography data.

For engineers to be able to reduce design uncertainties, the aforementioned range of methods used to model TPS thermal response are in need of validation. This is usually achieved via comparison with experimental data obtained via ground testing. In some rare and exceptional cases, data recovered during flight by heat shield instrumentation is made available.

5.3   HEAT SHIELD FLIGHT DATA

At the height of the space race, in support of the Apollo program, numerous re-entry missions were instrumented to collect aeroheating and TPS performance data [32]. Calorimeters and radiometers were used on the Mercury and Gemini missions as well as on certain Apollo missions. The TPS on Fire II comprised several layers of beryllium and was equipped with forebody calorimeters, radiometers as well as afterbody thermocouples. Heat transfer sensors were included in early Space Shuttle missions, while later on, infrared imagery

of its reusable TPS was successfully conducted, providing the community with valuable data regarding turbulent transition and roughness effects [181]. Unfortunately, some of the data returned were either insufficient for comparison with simulations, or not critically evaluated.

Correct installation of instrumentation in entry vehicle thermal protection systems is mission critical and high risk. Therefore, a large proportion of past missions have little to no data of TPS performance during the entry, descent and landing (EDL) phase of the mission. In 2004, the Genesis sample return capsule failed to deploy its drogue chute and crashed into the ground. The minimal EDL data available about its carbon-carbon heat shield hindered the post-crash investigation [182]. Two years later, an assessment of the TPS performance was requested after the successful re-entry of the Stardust capsule. The lack of instrumentation once again impeded the engineers' ability to qualify the vehicle's aerothermal environment and TPS performance. As a result, instrumentation of all future atmospheric entry systems has been mandated by NASA.

5.3.1 *Past Instrumented Missions*

The majority of available flight data are for Earth re-entry type missions. However, TPS data from interplanetary entry vehicles does exist. These data are especially important, given the inability of ground-testing facilities to correctly reproduce representative surface heating rates in flows other than air [8]. In 1976, Viking I and II entry probes entered the Martian atmosphere after orbit insertion, due to concerns about its harsh entry environment [32]. The forebody of the TPS was not instrumented for both missions. However, each probe had two surface mounted afterbody thermocouples on the fibreglass inner cone and aluminium skin of the outer cone. Ingoldby *et al.* [183] compared the pre-flight afterbody heat flux estimated at approximately 3% of forebody heating to a value of 5% derived from flight data. Analytical techniques were used to derive the surface heat fluxes, which involved simplifying assumptions about the thickness and thermal response of the materials involved.

The Pioneer-Venus program included four entry probes with dense carbon phenolic heat shields, which entered Venus' atmosphere along different trajectories in 1978. Each probe employed two in-depth thermocouples in the forebody heat shield, at the nose and along the conical frustum [184]. Extremely high convective and radiative heating rates (in excess of $7000\,\mathrm{W{\cdot}cm^{-2}}$) were expected.

Pitts and Wakefield [184] compared the flight data to temperature calculations from NASA's legacy CMA code, based on the predicted heating rates and found them to be generally well matched.

In 1989, the Galileo probe entered Jupiter's atmosphere at $47\,km\cdot s^{-1}$, undergoing the most severe heating environment experienced by a planetary entry capsule. The vehicle was well instrumented, equipped with ten Analog Resistance Ablation Detector (ARAD) sensors, designed to measure TPS recession. In depth temperature measurements were provided by two resistance thermometers on the forebody and two more on the afterbody. Unfortunately, a software issue resulted in the overwriting of temperature data from early in the mission. Milos *et al.* [57] used a combination of ARAD data and calculations performed with FIAT to estimate a peak heating rate of $13\,400\,W\cdot cm^{-2}$ at the frustum. The same study showed that the design model overpredicted recession at the stagnation point but significantly underpredicted recession at the frustum [57]. This discrepancy has not been understood.

In 1997, the Mars Pathfinder mission entered the Martian atmosphere, equipped with six forebody and three afterbody thermocouples at different depths and locations. Milos *et al.* [185] conducted aerothermal and TPS response analyses for the entry vehicle using FIAT and compared their results to the flight data. Temperatures calculated for each thermocouple except those at the bondline seemed to match well with flight data. Mahzari [186] utilised inverse methods to reconstruct surface heating profiles at the stagnation point and shoulder as an input for updated aerothermal and TPS response simulations. This method resulted in much closer match with the flight data.

5.3.2 *Mars Science Laboratory*

In 2012, the Mars Science Laboratory (MSL) successfully entered Mars' atmosphere and used its sky crane to safely lower the Curiosity rover to the ground. MSL's thermal protection system composed of a PICA forebody heat shield, 4.5 m in diameter, which was instrumented with a temperature and pressure sensor system called MSL Entry, Descent, and Landing Instrumentation (MEDLI). The previous Mars missions assessed their drag and stability performance via observed initial states coupled with the on-board Inertial Measurement Unit (IMU) data [182]. This approach, however, does not allow total drag force to be decoupled into its aerodynamic and atmospheric contributions. MEDLI

provided the first in-depth understanding of Mars entry environments as well as the response of a PICA heat shield to that environment [182].

It consists of three subsystems: the MEDLI Integrated Sensor Plug (MISP) for temperature measurement, the Mars Entry Atmospheric Data System (MEADS) for pressure measurement and Sensor Support Electronics (SSE) [32]. A layout of MISP and MEADS instrumentation on MSL is provided in Figure 5.1. The plugs are placed at different locations across the capsule forebody, to account for the range of heat fluxes involved, depicted via the colour map in Figure 5.1. Each plug is composed of a combination of four sets of thermocouples (TC 1-4) placed at different depths and a Hollow Aerothermal Ablation and Temperature (HEAT) sensor to measure propagation of an isotherm. Every MEADS pressure sensor is in a high pressure, low heat flux region near the stagnation point and nose.
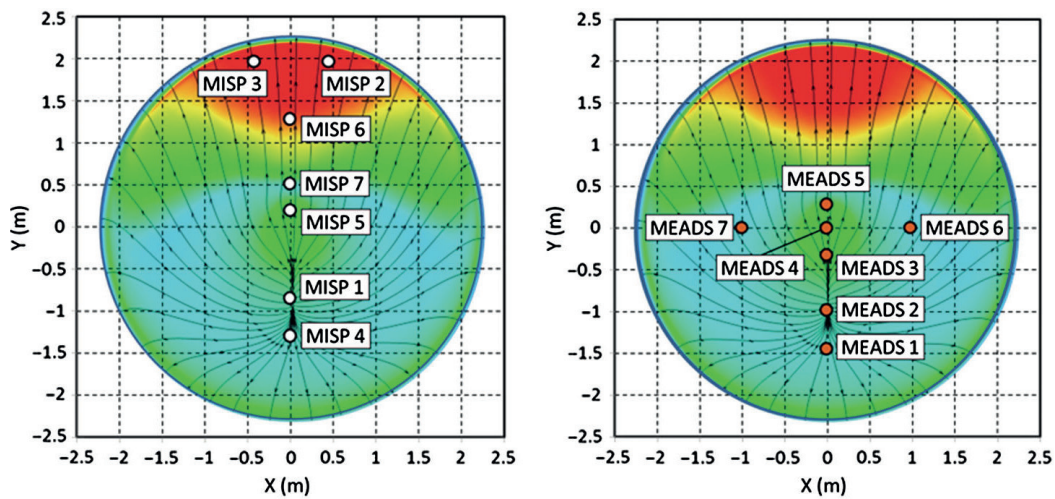
Figure 5.1: Layout of (a) MISP plugs and (b) MEDLI port locations on MSL heat shield from Bose *et al.* [187]. The distribution of heat fluxes is depicted via the colour map.

MEDLI data has been used to better understand the high temperature response of PICA along MSL's entry trajectory. White *et al.* [188] compared flight data with post-flight analysis and postulated the onset of roughness induced turbulent transition at the heat shield surface. Bose *et al.* [187] reconstructed the aerother-

mal environment surrounding MSL's heat shield and its consequent thermal response. They found that the models overpredict surface recession and temperatures in the leeside region, but underpredict temperature in the stagnation and apex regions. They also used inverse methods and a multi-parameter estimation framework to improve FIAT predictions of the MSL heat shield thermal response.

Omidy *et al.* [189] rebuilt the MISP thermocouple responses by using FIAT and PATO side by side to find that both codes give results within an error margin of 2%. The difference is likely due to the inclusion of gas species conservation equations in PATO. Using the shallowest thermocouple data as a temperature boundary condition, good accuracy was achieved for the two shallowest thermocouples. Low temperature peaks in data from TC3 and TC4, not reproduced in the numerical simulation, were later attributed to water phase change based effects [190]. Cruden *et al.* [191] investigated the effect of flowfield radiation on the MISP thermocouple responses. They found that radiative heating accounts for 43% of the heat load discrepancy.

5.3.3 *Future Instrumented Missions*

Plans were in place to instrument both the forebody and afterbody heat shields of the ESA Schiaparelli EDL module [192], which crash landed on the surface of Mars on 19th October 2016. It is unknown as of the time of writing whether any aerothermal data can or will be recovered from the entry vehicle. NASA's Mars 2020 mission will be instrumented with MEDLI 2, which will comprise of sensors on both the forebody and backshell, including 7 pressure transducers, 17 thermal plugs and 3 heat flux sensors, including a radiometer [193]. The shift towards frequent instrumentation of entry vehicle heat shields becoming common practice should provide substantial data for model validation in different environments and conditions.

5.4 SUMMARY

Accurate and efficient modelling and validation of TPS material response is a great challenge in the design and sizing of ablative heatshields for entry vehicles. This review investigated the decline and rebirth of research and development in the field of ablative TPS materials for space science missions, between 1976 and today. Reduction of TPS mass penalty for interplanetary missions is now a priority, leading to the use of new lower density porous ablators. These nascent

technologies require improved accuracy in modelling and ground testing before they can be flight qualified and entrusted with the safety of scientific or human payload. Many state of the art thermo-physical models are under development. Though the effects of thermal response on structural integrity and finite rate chemistry on pyrolysis are being investigated, the effects of internal radiation have often been hypothesised but rarely explored.

In-depth radiative effects are often overlooked due to the complexity involved in obtaining the accurate, spectrally resolved optical properties required in heat transfer calculations. Including the dependence of these properties on wavelength, fibre orientation, temperature and pressure could reduce the computational efficiency of the thermal response simulation, rendering it less appealing for use in the sizing process. Simplifying assumptions and semi-analytical expressions, such as the use of artificial geometries and property homogenisation over the material domain, are therefore used.

To improve accuracy and incorporate the significant morphology-based effects, however, radiative characterisation of porous media has recently been conducted using high resolution tomography data. This method has never been applied to two phase, low density TPS materials, such as modern lightweight carbon phenolics. Nevertheless, existing work provides a good basis for accurate calculation of these optical properties. The proposed numerical modelling, conducted to fulfil *Objective O.4*, will modify previous methodologies to account for the semi-transparency of both phases. The 3D structures of low density carbon phenolic and high density graphite will be digitised using high resolution synchrotron tomography and used for this investigation.

Legacy codes used for TPS design and sizing such as `CMA` and `FIAT` and even newer codes such as `PATO`, which use advanced thermochemical and thermo-mechanical models, avoid the evaluation of internal radiative heat transfer entirely. `Amaryllis` includes a low fidelity, simplified implementation of the diffusion approximation to model radiation in ASTERM. The diffusion approximation is an efficient, but limited methodology. A more rigorous and higher fidelity model is thus required and feasible due to improvements in computational power and efficiency. The development of numerical tools, proposed in *Objective O.5*, will calculate the divergence of the radiative flux using a path-length Monte Carlo method, based on the previous accurate calculation of optical properties of the TPS materials (in *Objective O.4*). Coupling of internal

radiation with ablative effects will be achieved via inclusion of the radiative divergence in the energy conservation equation in PATO.

Data specific to the problem of internal radiation in TPS materials are scarce. The best available method for evaluating this phenomenon is therefore via comparison with available flight data. Good quality data are available from the MEDLI experiment [182], which sent back time-resolved thermocouple data at different locations and depths from the MSL forebody heat shield. This data has previously been used for comparison with thermal response code simulations (without internal radiation), providing a good foundation for the comparison carried out in this work (*Objective O.6*).

RADIATIVE BEHAVIOUR OF ABLATIVE MATERIALS[1]

6.1 INTRODUCTION

This chapter aims to quantify the influence of the semi-transparent bulk phases on the macroscopic optical behaviour of a sample and to provide correlations based on single phase bulk material properties. These correlations are readily incorporated into macroscopic engineering simulations. The effective properties, calculated by applying the discrete-scale approach to the real 3D geometries of the samples obtained by computed tomography, are used to derive continuum radiative properties for a semi-infinite slab of the material sample. The two-phase media considered are a medium density carbon phenolic and a high density graphite reinforced polymer composite (Table C.1), each comprised of semi-transparent fluid and solid phases.

6.2 METHODOLOGY

This study considers quasi-steady radiative transfer in a medium consisting of two semi-transparent phases. The phase compositions are dependent on the extent of reaction (i.e. decomposition): (i) initially the sample consists of solid fibres bound by thermoset resin and an air filled gas phase, and (ii) after the heterogeneous reactions, the solid phase comprises solely of the fibres and the gas phase contains a mixture of strongly attenuating pyrolysis gases and air. The equations for the assessment of radiative transfer, given in the next section, are solved using Monte Carlo ray tracing. The method is subject to the following assumptions: (i) both phases are homogeneous and isotropic; (ii) each phase has constant, non-polarising optical properties; (iii) both phases are at local thermodynamic equilibrium; (iv) the characteristic length of each component is greater than the wavelengths of interest, validating the application of geometrical optics; (v) negligible diffraction; (vi) all components are at rest as compared to the speed

---

[1] Material from this chapter has been submitted for publication in the following article,

- N Banerji, P Leyland, S Haussener. Tomography based radiative characterisation of decomposing carbonaceous heat shield materials. Carbon, 2017.

of light and (vii) dependent-scattering effects are negligible. The main governing equations, derived by Lipiński *et al.* [15], are summarised in Section 6.2.1.

6.2.1 *Governing Equations and Implementation*

The quasi-steady homogenised RTEs for a multi-phase medium comprising of two semi-transparent phases are given by Equation 6.1, where the spectral subscript has been omitted for brevity. This set of equations is derived from the discrete-scale RTEs valid in the individual phases and the corresponding interphase boundary conditions [15]. I_i is the volume averaged local intensity, $I_{b,i}$ is the volume averaged blackbody intensity in vacuum, κ_i, $\sigma_{s,ij}$, $\Phi_{i,j}$ are the effective absorption and scattering coefficients and the scattering phase functions respectively.

$$\hat{s} \cdot \nabla I_i(\mathbf{x}, \hat{s}) = -\beta_i I_i(\mathbf{x}, \hat{s}) + \kappa_{d,i} I_{b,i}(\mathbf{x}, \hat{s}) + \frac{\sigma_{s,ii}}{4\pi} \int_{\Omega_i=0}^{4\pi} I_i(\mathbf{x}, \hat{s}_i)\Phi_{ii}(\hat{s}_i, \hat{s})d\Omega_i$$

$$+ \frac{\sigma_{s,ji}}{4\pi} \int_{\Omega_i=0}^{4\pi} I_j(\mathbf{x}, \hat{s}_i)\Phi_{ji}(\hat{s}_i, \hat{s})d\Omega_i, \qquad i, j = 1, 2; i \neq j \quad (6.1)$$

The effective properties, given in Equations 6.2 - 6.6, are a combination of single phase bulk material properties ($\beta_{d,i}$, $\kappa_{d,i}$, $\sigma_{d,s,i}$, $\Phi_{d,ij}$) and morphology-dependent properties ($\sigma_{refl,s,i}$ and $\sigma_{refr,s,i}$),

$$\sigma_{s,ii} = \sigma_{s,refl,i} + \sigma_{s,d,i} \tag{6.2}$$

$$\sigma_{s,ij} = \sigma_{s,refr,i} \tag{6.3}$$

$$\Phi_{ii} = \sigma_{s,ii}^{-1}(\Phi_{refl,i}\sigma_{s,refl,i} + \Phi_{d,i}\sigma_{s,d,i}) \tag{6.4}$$

$$\Phi_{ij} = \sigma_{s,ij}^{-1}\Phi_{refr,i}\sigma_{s,refr,i} \tag{6.5}$$

$$\beta_i = \beta_{d,i} + \sigma_{s,refl,i} + \kappa_{ij} \tag{6.6}$$

Simulations are conducted for 10 mm thick semi-infinite slabs, exposed to a diffuse beam parallel to the surface normal and a perfectly black boundary at the rear. Reflectance, R, is the integrated flux leaving the inlet surface and absorptance, $A = 1 - R - Tr$, where Tr is the slab transmittance, i.e. the integrated flux leaving the outlet surface. The two-phase morphology associated properties are determined by direct pore level simulations [159, 156, 194] applied to the real 3D geometries of the samples obtained by high resolution synchrotron computed tomography.

6.2.2 *Composite Sample Morphology*

To evaluate the feasibility of using the tomography-based approach for TPS materials, preliminary discrete-scale morphological and radiative characterisation of a highly porous alumina foam has been conducted, using low resolution, low flux tomography [195]. This investigation revealed several insufficiencies in the data quality, contrast and resolution, leading to difficulty in image segmentation. Higher beam energies and higher resolution were obtained via a campaign, conducted at the TOMCAT beamline of the SLS at the Paul Scherrer Institute [196]. The data were collected using an 18 keV photon energy, an exposure time of 130 ms, and a microscope allowing for a spatial resolution of 0.33 μm resulting in a field of view of $2560 \times 2560 \times 2160$ pixels ($845 \times 845 \times 713$ μm^3). In composite materials, the resin phase typically presents nanometre sized structural characteristics. It is therefore likely that the 0.33 μm pixel size is not sufficient to resolve these structures. The segmented microstructure is therefore an approximation of the gas-resin phase morphology, within the limits of the resolution of the imaging technique.

To examine the effect of material decomposition, the gas phase, occupying the pore space, is artificially adapted via image segmentation to (i) include only the air phase (virgin case) and to (ii) include air and resin phases where the resin phase is assumed decomposed and comprises of highly attenuating pyrolysis gases (decomposed case). In both cases, one phase combines two separate components along with their bulk properties. This approximation avoids the use of a three-phase model. This is shown in 3D surface renderings of the carbon phenolic and graphite samples in Figure 6.1a and 6.1b respectively. The front half each image portrays the material in its decomposed state, where complete gasification of the resin leaves a solid phase enveloped in attenuating gases. The back half of the samples portray the virgin state, where the solid phase is made up of the fibres and thermoset resin. The indices 1 and 2 are used for the gas and solid phase respectively.

6.3 RESULTS

6.3.1 *Morphological Characterisation*

Porosities are calculated by two-point correlations using a Monte Carlo method [197]. The porosity is seen to increase with decomposition (as expected due
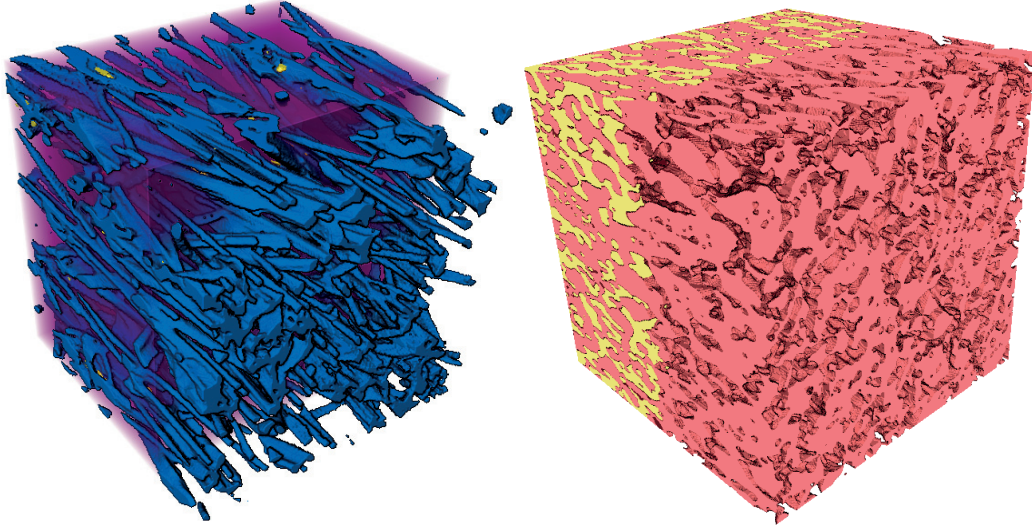
Figure 6.1: 3D renderings (425 µm edge length) of the discrete-scale sample geometries for (a) the decomposing medium porosity carbon phenolic composite sample (solid fibre phase in blue, resin phase in purple and air in yellow) and (b) the decomposing high density graphite reinforced polymer composite sample (solid phase in pink, resin phase in yellow and air is not visible due to low volume fraction).

to resin outgassing) from 0.5673 to 0.8114 for the carbon phenolic and from 0.0774 to 0.2779 for the graphite. The normalised pore-size distribution based on mathematical opening distributions with spherical structuring elements [198] is presented in Figure 6.2a. With all its resin reacted, the decomposed carbon phenolic sample shows the largest pores. Pore sizes increase very slightly with heating for the graphite sample. The mean pore size of the virgin samples are 11.39 and 7.59 µm for the carbon phenolic and graphite samples respectively. For the decomposed samples d_{pore} are 19.89 and 9.57 µm respectively. Figure 6.2b shows the normalised solid phase distributions, with a mean solid phase diameter, d_{solid} of 15.47 µm and 10.89 µm for the virgin and decomposed carbon phenolic respectively. For the virgin and decomposed graphite, d_{solid} is 24.82 µm and 21.74 µm respectively.

The representative elementary volume edge length (l_{REV}), describing the smallest volume for which continuum can be assumed, is estimated based on porosity calculations on subsequently growing sample sub-volumes and is assumed suf-

ficient when the solutions converge to the porosity within a band of ± 0.025. The edge length of a cubic REV, l_{REV}, for the four samples investigated are $0.11\,\mathrm{mm}$, $0.17\,\mathrm{mm}$, $0.16\,\mathrm{mm}$ and $0.15\,\mathrm{mm}$ respectively. For the discrete-scale calculations, a cubic sample of $0.27\,\mathrm{mm}$ edge length was used to ensure a constant domain size for all samples investigated, which lies well above the required REV size. All morphological characteristics and the reference size parameter used, if not otherwise indicated, are summarised in Table 6.1. The reference size parameter ($x_{ref} = \pi d_{pore}/\lambda$) is based on the calculated mean pore diameter for a wavelength of $1\,\mu\mathrm{m}$.

a) Opening size distribution of gas phase.   b) Opening size distribution of solid phase.
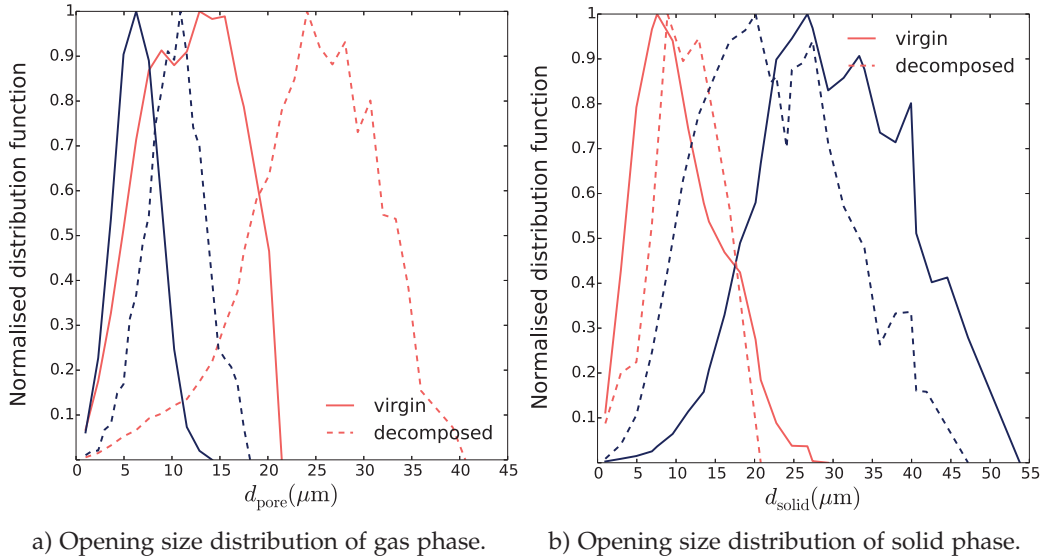
Figure 6.2: Morphological property distributions of the virgin (solid line) and decomposed (dashed line) forms of the carbon phenolic (grey) and graphite (black) samples.

6.3.2 *Effective Radiative Properties*

Calculations of the effective radiative properties are performed for a combination of bulk properties at size parameters between 5 and 500, corresponding to wavelengths between $0.041\,\mu\mathrm{m}$ and $16.39\,\mu\mathrm{m}$. Reflection and refraction are modelled by Fresnel's equations and the generalised form of Snell's law [168] at the specularly reflecting interfaces. Both phases are assumed to be semi-transparent, i.e. its bulk absorption and scattering coefficients, $\kappa_{d,i}$, $\sigma_{d,s,i}$ are equal to a non-zero value and its refractive indices do not equal 1. For cases such as the virgin

Table 6.1: Numerically determined porosity, mean solid and pore diameters, REV edge lengths and size parameters calculated for a reference wavelength of 1 μm for the four samples investigated.

	Carbon Phenolic		Graphite	
	Virgin	Decomposed	Virgin	Decomposed
Porosity	0.5673	0.8114	0.0774	0.2779
d_{pore} (mm)	11.39	19.89	7.59	9.57
d_{solid} (mm)	15.47	10.89	24.82	21.74
l_{REV} (mm)	0.11	0.17	0.16	0.15
Ref. size parameter, x_{ref}	35.78	62.49	23.84	30.07

graphite, where smallest pore diameters are on the order of the wavelength studied, wave effects estimated via Mie theory suggest values approximately 11% greater compared to those calculated using the current methodology based on geometrical optics. The assumption of independent scattering is confirmed using the criteria by Tien *et al.* [199] for the smallest observed size parameter, $x = 5$ and a pore volume fraction of $f_{\text{v}} = 0.08$.

Extinction Coefficient

The product of mean pore diameter and effective extinction coefficient, β_1, of the air or reactive gas-filled pore phase for all four samples is plotted against the normalised bulk extinction coefficient, $\beta_1 d_{\text{pore}}$, of the same phase and shown in Figure 6.3a. The behaviour can be divided into two separate responses. For low normalised bulk extinction coefficients ($\beta_1 d_{\text{pore}} < 0.01$), little attenuation in the gas phase is observed and the morphological effects dominate. The numerical value of β_1 in the limit of small $\beta_{d,1}$ depends only on the morphological properties of the samples. The simplest morphological characteristic, the porosity, shows a clear trend : the effective extinction coefficient is inversely proportional to sample porosity. The decomposed carbon phenolic, with the highest porosity, has the lowest effective extinction coefficient, β_1. The higher density virgin and decomposed graphite samples show significantly more extinction in the morphologically dominated response.
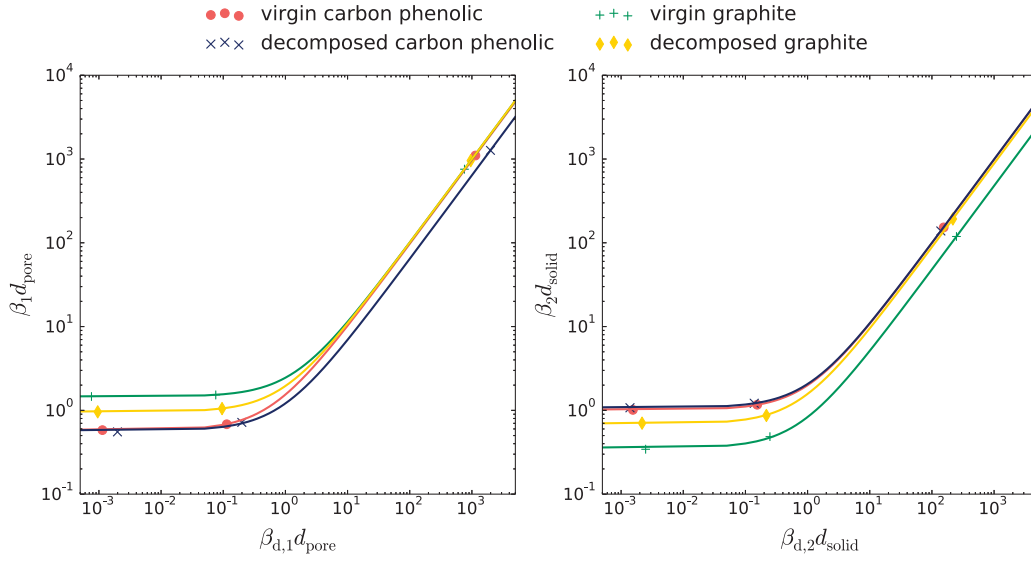
Figure 6.3: Normalised effective extinction coefficient, $\beta_i d_{\mathrm{mean},i}$, as a function of normalised bulk extinction coefficient of the (a) gas ($\beta_{\mathrm{d},1}d_{\mathrm{pore}}$), and (b) solid ($\beta_{\mathrm{d},2}d_{\mathrm{solid}}$) phases. The lines indicate the fits detailed in Table 6.2. Data is calculated for various combinations of size parameters and bulk material properties.

Once the product of mean pore diameter and normalised bulk extinction coefficient of the gas phase increases past a threshold ($\sim 10^{-1}$ for both the carbon phenolic and graphite), internal radiation starts to contribute heavily to the effective properties in a directly proportional manner, leading to a linear rise. A similar effect can be seen for β_2, shown in Figure 6.3b. However, in this case, the volume fraction of the solid phase is the relevant characteristic morphological property, with decreasing effective extinction coefficient for an increase in solid volume fraction.

A set of semi-empirical linear curve fitting functions for the data presented in Figure 6.3, is presented in Table 6.2, with a RMS value greater than 0.9999 for each fit. The curve fits can be used to estimate effective extinction coefficients of similar material samples and their corresponding changes with respect to reaction extent or wavelength (via changes in size parameter) by moving along the respective curve in Figure 6.3. These values hold true for any combination of wavelength and bulk material properties, both of which affect the bulk extinction coefficient.

Table 6.2: Dependence of the effective extinction coefficient of the gas and solid phase on the discrete-scale extinction coefficient of the gas and solid phase, respectively. The functions have been obtained by fitting the calculated data points, indicated in Figure 6.3, with a fit quality of RMS > 0.9999.

| | Carbon Phenolic | | Graphite | |
	Virgin	Decomposed	Virgin	Decomposed
$\beta_1 d_{\text{mean}}$	$0.9664\beta_{\text{d},1}d_{\text{pore}} + 0.576$	$0.6381\beta_{\text{d},1}d_{\text{pore}} + 0.572$	$0.9947\beta_{\text{d},1}d_{\text{pore}} + 1.457$	$0.9981\beta_{\text{d},1}d_{\text{pore}} + 0.956$
$\beta_2 d_{\text{mean}}$	$0.9802\beta_{\text{d},2}d_{\text{solid}} + 1.013$	$0.9896\beta_{\text{d},2}d_{\text{solid}} + 1.075$	$0.4779\beta_{\text{d},2}d_{\text{solid}} + 0.355$	$0.8826\beta_{\text{d},2}d_{\text{solid}} + 0.689$

Scattering

The normalised scattering coefficients $\sigma_{\text{refl,s},i}$ and $\sigma_{\text{refr,s},i}$, are shown in Figure 6.4a, as a function of the refractive index ratio (n_2/n_1) for the virgin carbon phenolic sample at $n_2 = 1, 2, 3$ and $n_1 = 1$. With increasing refractive index ratio, the radiation scattered within a single phase ($\sigma_{\text{refl,s},i}$) increases and the radiation scattered from one phase to another ($\sigma_{\text{refr,s},i}$) decreases due to a combination of total internal reflection and increased directional hemispherical reflectivity of the interface. Morphology does not significantly affect the scattering coefficients as the decomposed sample exhibits identical behaviour as do both graphite samples. This is consistent with previous observations of the relative scattering behaviour on the sample morphology [194]. No wavelength dependence is observed for the normalised scattering coefficients assuming the real part of the refractive index at a particular wavelength is given by the ratio indicated. The scattering phase function is presented in Figure 6.4b, as a function of the directional cosine of the scattering angle, $\mu_s = \cos(\theta)$. The assumption of perfectly reversible interface behaviour for photons scattered at the outer or inner boundary produces identical inter-phase scattering functions ($\Phi_{\text{refr},1} = \Phi_{\text{refr},2}$).

$\Phi_{\text{refr},i}$ show a peak in the forward direction, which becomes more pronounced with increasing ratio of refractive indices due to increased directional hemispherical reflectivity of the interface at a majority of incidence angles for $n_2/n_1 = 3$. The phase function, $\Phi_{\text{refr},i}$ drops to zero in the backward direction as total reflection limits the accessibility of angles below $\mu_s < -\sqrt{1 - \mu_{\text{refl,tot}}^2}$. Scattering due to reflection at the interface of the gas phase ($\Phi_{\text{refl},1}$) has access to all scattering angles and the scattering behaviour is generally isotropic, with a small peak in the forward direction. For the solid phase ($\Phi_{\text{refl},2}$), the phase function is flat in

the forward direction, and rapidly approaches zero in the backward direction due to total internal reflection limiting angles below $\mu_s < 1 - 2\mu_{refl,tot}^2$ [194]. The forward scattering, highly anisotropic behaviour for $\Phi_{refl,2}$ is consistent with the work of Lee [154] for fibrous insulations. The curves shown in Figure 6.4b are for the virgin carbon phenolic sample. However, no sensitivity of the effective scattering phase functions with respect to morphological differences or size parameter were observed and consequently these functions are valid for both samples in their virgin and decomposed states. Coefficients of the seventh order polynomial fit to the scattering phase functions are detailed in Table 6.3.

Along with the effective extinction coefficients calculated above, this scattering data can be supplied to the continuum-scale RTEs to accurately describe radiative heat exchange in two-phase media with known bulk material properties and of similar morphology to the samples considered in this paper. The RTEs can then be coupled to the energy equation and support the accurate solution of heat and mass transfer characteristics in complex macroporous reacting media.

a) Effective normalised scattering coefficients as a function of refractive index ratio (n_2/n_1) for virgin carbon phenolic.

b) Effective scattering phase function for scattering between different phases (phase 1: gas, phase 2: solid) for $n_2/n_1 = 2$ (red lines) and $n_2/n_1 = 3$ (black lines).
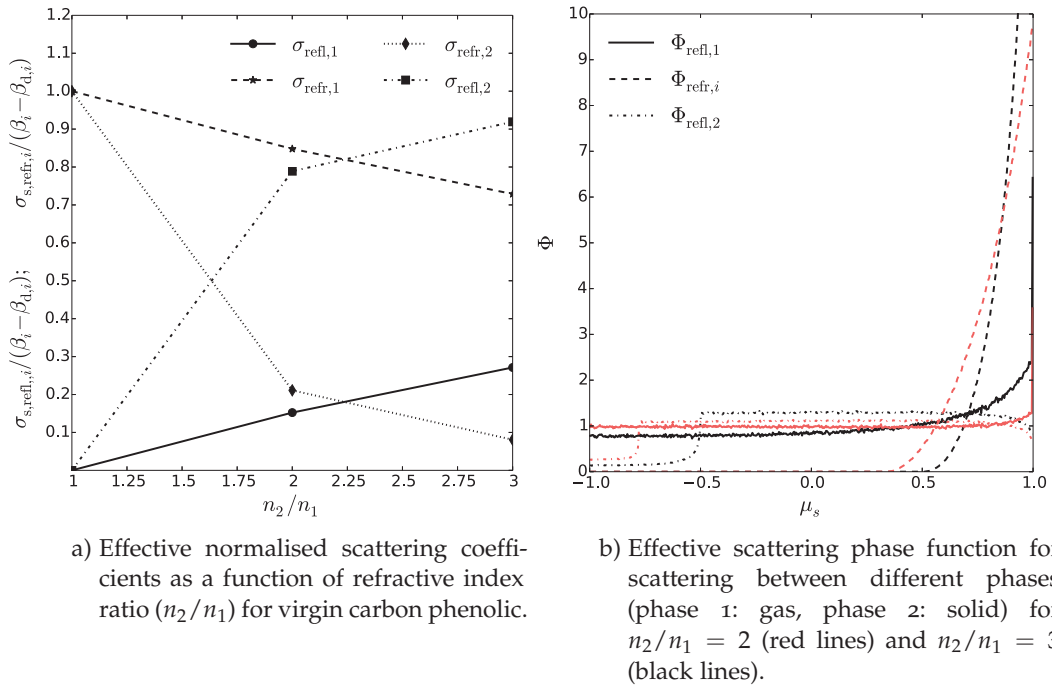
Figure 6.4: Effective scattering properties.

Table 6.3: Coefficients of the seventh order polynomial fit to the scattering phase functions $\Phi_{\mathrm{refl},1}$, $\Phi_{\mathrm{refr},i}$ and $\Phi_{\mathrm{refl},2}$ for all four sample morphologies.

n_2/n_1	$f(\mu)$	a_0	a_1	a_2	a_3	a_4	a_5	a_6	a_7	RMSE
3	$\Phi_{\mathrm{refl},1}$	0.8311	0.8164	-0.5952	-0.4015	0.4374	0.3561	0.1639	0.8369	0.025
	$\Phi_{\mathrm{refr},i}$	11.95	14.80	-4.116	-7.353	0.9844	1.167	-0.1128	-0.0334	0.071
	$\Phi_{\mathrm{refl},2}$ ($\mu_\mathrm{s} > -0.496$)	-5.31	6.666	0.3121	-2.498	0.2017	0.2053	0.0092	1.291	0.016
	$\Phi_{\mathrm{refl},2}$ ($\mu_\mathrm{s} < -0.496$)	37985.85	204757.75	469654.75	594114.19	447589.81	200803.33	49671.38	5226.6	0.029
2	$\Phi_{\mathrm{refl},1}$	0.3989	0.3937	-0.3803	-0.3207	0.1614	0.0784	-0.0301	0.9771	0.019
	$\Phi_{\mathrm{refr},i}$	-1.438	-1.724	3.993	7.127	2.634	-0.5232	-0.2954	-0.0047	0.036
	$\Phi_{\mathrm{refl},2}$ ($\mu_\mathrm{s} > -0.771$)	-1.363	0.1673	1.428	-0.1281	-0.4855	-0.0166	0.0559	1.111	0.014
	$\Phi_{\mathrm{refl},2}$ ($\mu_\mathrm{s} < -0.771$)	8.42	5.29×10^7	1.42×10^8	2.13×10^8	1.90×10^8	1.02×10^8	3.04×10^7	3.88×10^6	0.024

6.3.3 *Macroscopic Optical Properties*

General Solution

The dependency of absorptance on bulk extinction coefficient for each of the four investigated samples is shown in Figure 6.5, with $n_2/n_1 = 2$, $\sigma_{s,d,i} = 0$ and a wavelength of $1\,\mu m$ (i.e. x_{ref}).

For $\beta_{d,1} \leq 10^5\,m^{-1}$ and $\beta_{d,2}/\beta_{d,1} < 10^{-2}$, the decomposed carbon phenolic sample, which has the highest porosity of the four, shows the strongest absorptance and the high density virgin graphite sample shows the lowest absorptance. In this range the gas phase is dominating the absorption behaviour. The smaller $\beta_{d,1}$, the smaller this asymptotic absorption value. For increasing $\beta_{d,2}/\beta_{d,1}$ ratios, the solid phase starts to also contribute to absorption, increasing the absorptivity. For cases with low gas phase bulk absorption ($\beta_{d,1} < 10^4 m^{-1}$), the contribution of the solid phase becomes so significant that the absorptivity of the low porosity and high porosity sample cases cross and the virgin graphite sample, which has the lowest porosity of the four, shows the highest absorptance and the decomposed carbon phenolic sample shows the smallest absorptance.

This crossover is not visible for the cases with very large $\beta_{d,1}$, as with increasing $\beta_{d,2}/\beta_{d,1}$, k_2 grows, and if $k_2 > 1$, direct reflection by the solid phase at the inlet boundary starts to dominate the radiation behaviour. In this case (i.e. $\beta_{d,1} \geq 10^4 m^{-1}$ and for large $\beta_{d,2}/\beta_{d,1}$), the low porosity sample has the largest fraction of direct reflection and consequently the lowest absorptance. The dominance of the inlet face is also visible for the cases with lower $\beta_{d,1}$ leading to a decrease in calculated absorptance with increasing $\beta_{d,2}/\beta_{d,1}$ and eventually another cross of the low and high porosity cases and a drop in the absorptance for all cases.

For $\beta_{d,1} \geq 10^5\,m^{-1}$ and low $\beta_{d,2}/\beta_{d,1}$, direct reflection at the inlet boundary is observed, but this time due to the gas phase where $k_1 > 1$. Absorptance is therefore inversely proportional to porosity, with the high porosity decomposed carbon phenolic displaying low absorptance. Highest absorptance is seen in the virgin graphite sample due to its low gas phase volume fraction.

For cases where $\beta_{d,1} \geq 10\,m^{-1}$, slab transmittance is always zero for all investigated samples due to large sample thickness coupled with the presence of highly attenuating bulk phases. Everything that is not absorbed, is therefore
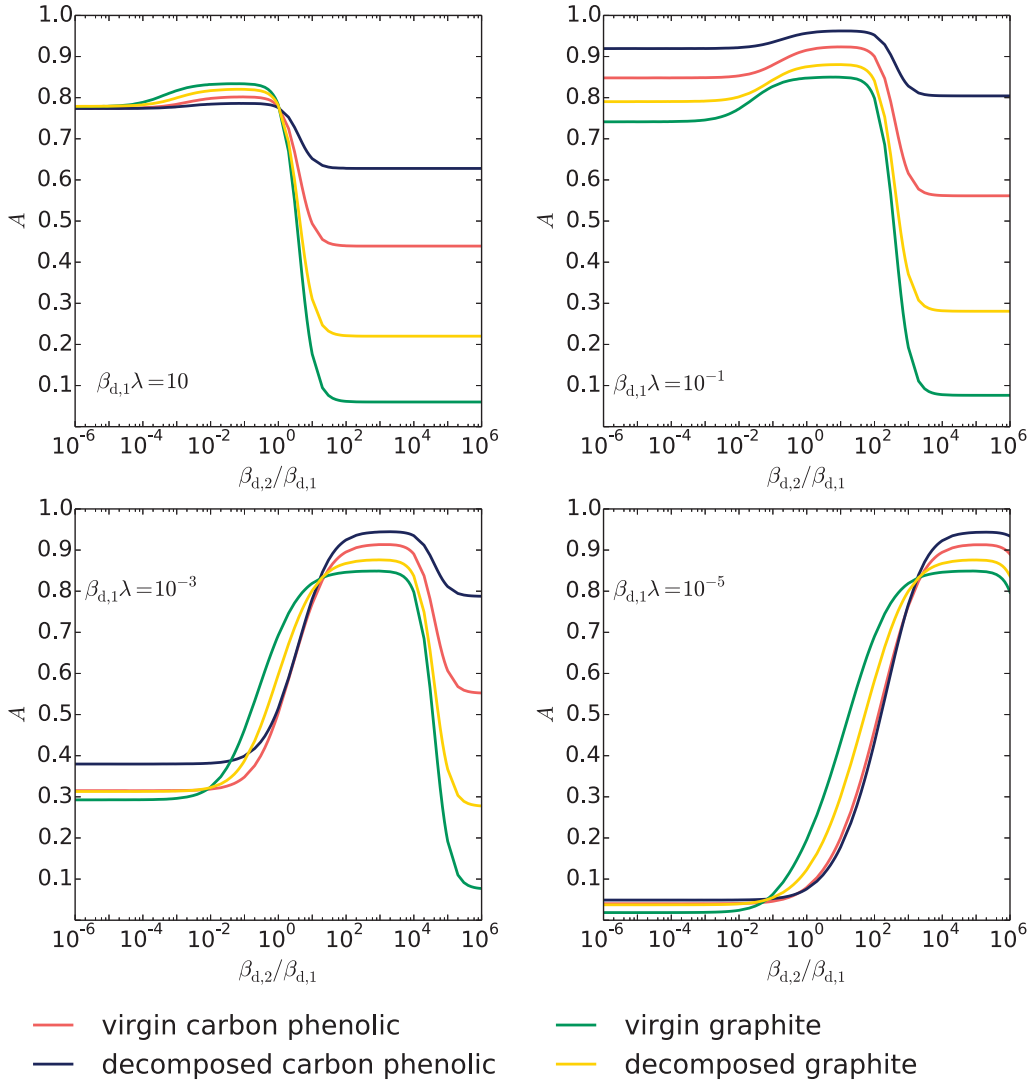
Figure 6.5: Absorptance of a 10 mm thick slab exposed to collimated irradiation at a wavelength of 1 μm (i.e. x_{ref}) composed of the four samples under consideration for different bulk extinction coefficients, $n_2/n_1 = 2$ and $\sigma_{s,d,i} = 0$.

reflected. However, for $\beta_{d,1} \leq 10\,\mathrm{m}^{-1}$, the virgin and decomposed graphite samples show up to 9% and 3% transmittance respectively, for the small values of $\beta_{d,2}/\beta_{d,1} < 1$, as shown in Figure 6.6. Due to the low volume fraction of the attenuating gas phase in both virgin and decomposed graphite, as well as
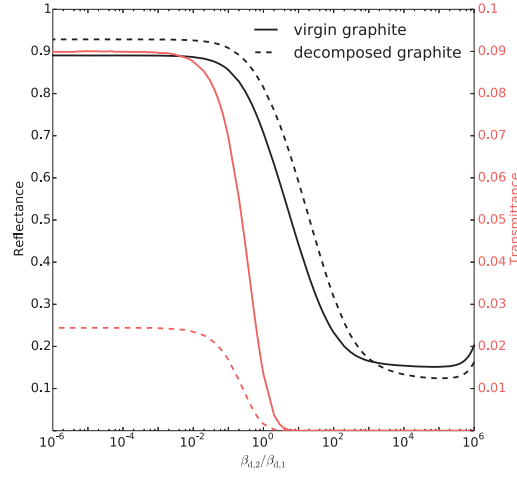
Figure 6.6: Fraction of incoming radiation, at a wavelength of $1\,\mu m$, that is reflected and transmitted by the virgin and decomposed graphite samples for $\beta_{d,1} = 10$ m^{-1}, $n_2/n_1 = 2$ and $\sigma_{s,d,i} = 0$.

extremely low solid phase bulk extinction coefficients, radiation is transmitted across the slab. The same phenomenon is insignificant ($Tr < 0.005$) for the carbon phenolic samples due to the increased presence of the gas phase.

The directional-hemispherical reflectivity at the phase boundary is shown in Figure 6.7a, as a function of incident angle for variations in k_i with $n_2/n_1 = 2$, i.e. for radiation travelling from phase 1 to phase 2. As observed previously in Figure 6.5, the larger the value of k_i (dependant on $\beta_{d,i}$), the higher the reflectivity, $\rho_{r,sp,i}$ across all angles of incidence. For extremely high values of k_i, total internal reflection is observed at values of $\theta_{in} < 85°$. For low values of k_i, reflectivity increases with an increase in incident angle. For radiation travelling from phase 2 (solid) to phase 1 (gas), a similar trend is reported in Figure 6.7b, showing an increase in reflectance with an increase in k_i. However, for values of $k_i > 1$, there is a dip in reflectance at higher angles of incidence.

Application to Thermal Protection Systems

The data in Figure 6.5 is usable for any two-phase medium with a similar morphology to the carbon phenolic or graphite samples. Here, the absorptance of a $10\,mm$ thick slab of the investigated TPS materials is calculated. Lee [155] computed the bulk extinction coefficient for a carbon fibre matrix as $9000\,m^{-1}$

a) From phase 1 (gas)
to phase 2 (solid),
$n_2/n_1 = 2$ for $n_1 = 1$.

b) From phase 2 (solid)
to phase 1 (gas),
$n_2/n_1 = 0.5$ for $n_1 = 2$.
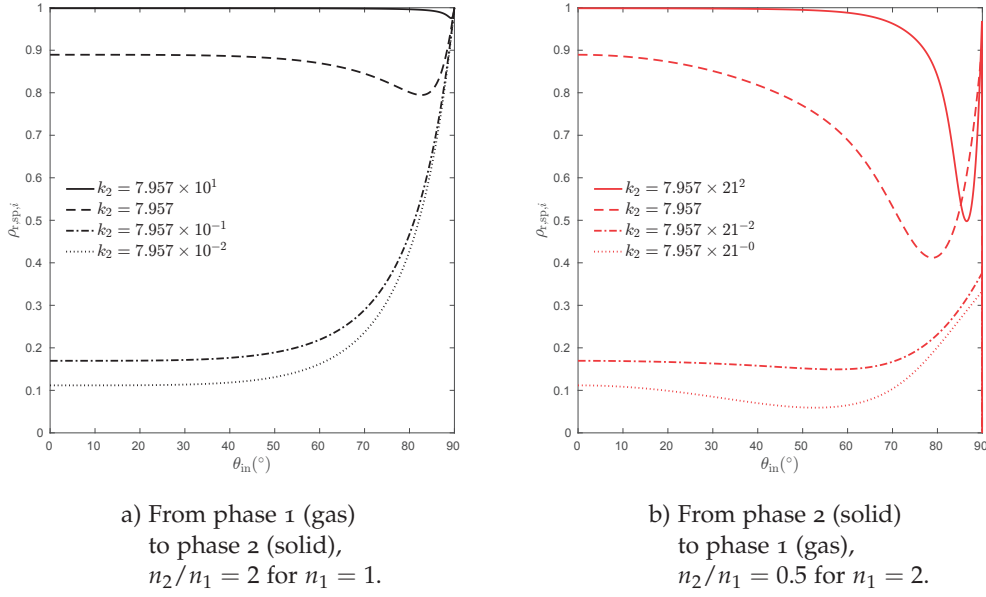
Figure 6.7: Directional-hemispherical reflectivity as a function of incident angle at the phase boundary for varying values of k_i.

while White [200] calculated the same from experimental measurements to be $7700\,\mathrm{m}^{-1}$ for a PICA material sample. Using a plasma radiation database, PARADE v3.2 [70], gas phase absorption coefficients are calculated for an equilibrium mixture of pyrolysis products given in Table 6.4) at room temperature (virgin case) and at 3000 K (decomposed case). In a wavelength range 50 - 5500 nm, the spectrally averaged absorption coefficients were estimated to be $10\,\mathrm{m}^{-1}$ and $10^5\mathrm{m}^{-1}$ for the virgin and decomposed cases respectively. Using Lee's estimation of the bulk extinction coefficient for the solid phase, the ratio, $\beta_{\mathrm{d},2}/\beta_{\mathrm{d},1} \sim 900$ can be calculated for the virgin case and $\beta_{\mathrm{d},2}/\beta_{\mathrm{d},1} \sim 0.09$ for the decomposed case.

Table 6.4: Equilibrium concentrations of phenolic products at 3000 K and 101 325 Pa.

Species	C	CO	H_2	C_2H_2	H	C_4H_2	C_2H
Mass fraction (n.d)	5.93×10^{-1}	2.98×10^{-1}	5.51×10^{-2}	4.44×10^{-2}	5.78×10^{-3}	2.21×10^{-3}	1.51×10^{-3}

From Figure 6.5, an increase is therefore observed, from 0.76 to 0.94, for absorption during decomposition of the carbon phenolic composite. The reflectance decreases from 0.24 to 0.06. Using the same ratios of bulk coefficients - on the assumption that the carbon fibre matrix would be similar, and any hydrocarbon based resin would decompose to form the same products at high temperatures - absorptance in decomposing graphite increases from 0.82 to 0.84, while reflectance decreases from 0.18 to 0.14. Radiation is not transmitted across either sample for all extents of decomposition. The change in macroscopic optical properties is more critical for the lower density carbon phenolic composite, compared to the higher density graphite. These findings are significant, especially given the desire, across the industry, to replace current TPS materials with ones of low to medium density.

Spectral Dependence

The spectral dependence of absorptance for the four samples under consideration is presented in Figure 6.8a, via evaluation at different size parameters $5 < x < 500$, with $n_2/n_1 = 2$, $k_2/k_1 = 0.01$ for $k_1 = 7.958 \times 10^{-2}$ and $\sigma_{s,d,i} = 0$. The absorptance increases with size parameter due to the increasing bulk extinction coefficient (while keeping n_2/n_1, k_2/k_1 and $\sigma_{d,s,i}$ constant). At these size parameters, with the given value for k_1, the gas phase exhibits opacity ($\beta_{d,1} d_{\mathrm{pore}} > 1$). The decomposed carbon phenolic sample, which has the highest porosity of the four samples, shows the strongest absorptance and the high density virgin graphite sample shows the lowest. For values of x below 50, a steep increase in absorptance, the rate of which is proportional to sample porosity, is observed. For $x > 150$, the absorptance attains a local asymptote.

A similar behaviour for the absorptance with respect to the size parameter is observed for $k_1 = 7.958 \times 10^{-5}$ as shown in Figure 6.8b. In this case, the gas phase extinction coefficient exhibits semi-transparent behaviour at small size parameters ($x < 500$). At large size parameters, the gas phase exhibits opaque behaviour, resulting in the high porosity carbon phenolic sample exhibiting the highest absorptance. It can be seen that at values of $x > 800$, the curves start to cross over, following the same trends observed for $k_1 = 7.958 \times 10^{-2}$ with the highest absorptance observed for highest porosity decomposed carbon phenolic. These curves are expected to asymptotically attain their local maxima at even higher size parameters.
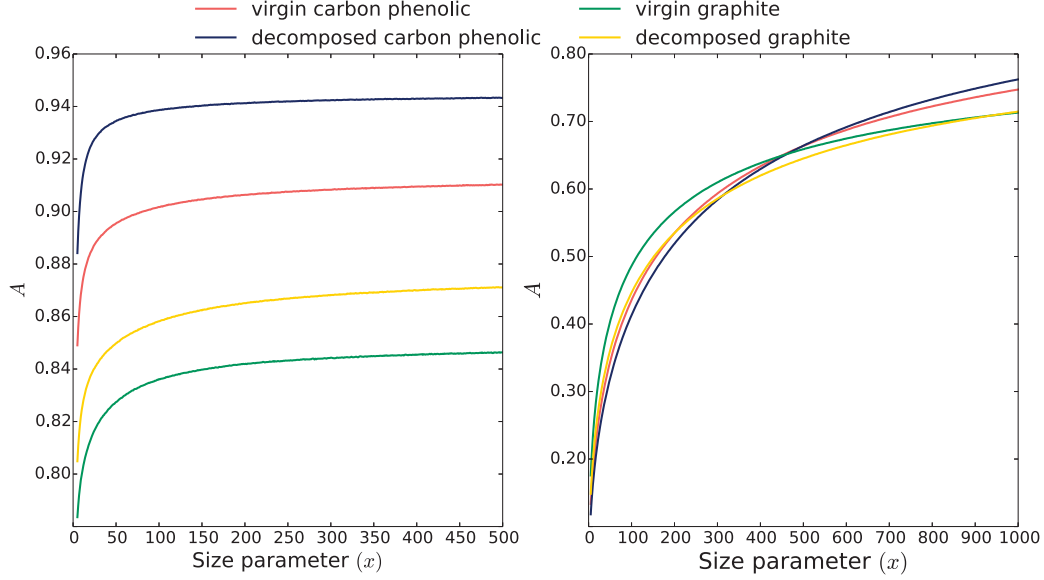
Figure 6.8: Absorptance of a 10 mm thick slab composed of the four samples exposed to collimated irradiation for different size parameters (x_{ref}), for $n_2/n_1 = 2$, $\sigma_{s,d,i} = 0$ and $k_2/k_1 = 0.01$ where (a) $k_1 = 7.958 \times 10^{-2}$ and (b) $k_1 = 7.958 \times 10^{-5}$.

At a temperature of approximately 3000 K, the possibility exists for a TPS material's gas phase to attenuate strongly compared to its solid phase. If both phases are strongly absorbing, from Figure 6.8a, it can be seen that the decomposed carbon phenolic composite would absorb approximately 88% of the incoming radiation at wavelengths in the near infrared and above ($\lambda \geq 1.25\,\mu m$ for $x < 50$). The decomposing graphite reinforced polymer composite would absorb less radiation at 81% due to the less absorbing solid phase making up the majority of its structure. For wavelengths in the ultraviolet and visible, absorption increases for both samples, attaining their local asymptotes at around 94% absorption for the carbon phenolic and 86% for the graphite.

Scattering Effects

The inclusion of scattering effects, by varying scattering albedos of both phases, marks a significant change in sample absorptance. Calculated absorptance is plotted in Figure 6.9 against gas phase scattering albedos ($\omega_{d,i} = \sigma_{d,s,i}/\beta_{d,i}$). From left to right, the columns present absorptance values calculated by also

including scattering within the solid phase, by selecting $\omega_{d,2}$ to be equal to 0, 0.5 or 1 with varying $\beta_{d,i}$ dependent on k_i and $\omega_{d,1}$. From top to bottom, each row represents a different selected size parameter used in the calculation, $x = 5$ and 500 to demonstrate any wavelength dependency.
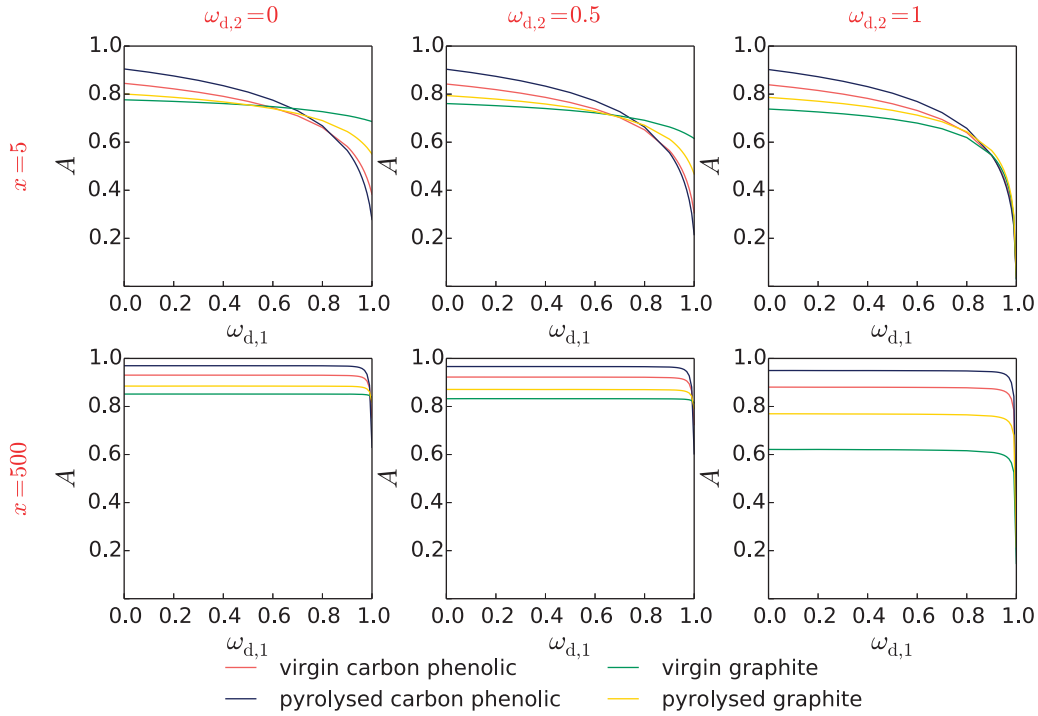
Figure 6.9: Absorptance of a $10\,\text{mm}$ thick slab exposed to diffuse irradiation. The slab is composed of the four samples under consideration for different gas-phase scattering albedos ($\omega_{d,1}$) with constant values for $k_1 = 7.958 \times 10^{-4}$ when $k_2/k_1 = 0.01$ and $n_2/n_1 = 2$. Across - variation of solid phase scattering albedo, $\omega_{d,2} = 0, 0.5, 1$; Down - variation of size parameter, $x = 5$ and 500.

For $x = 5$, all three plots show a decrease in absorptance for all samples with an increase in $\omega_{d,1}$. Sample porosity plays an influential role in these results. If the solid volume fraction is extremely high (i.e. virgin graphite sample), variations in scattering albedo $\omega_{d,1}$ do not significantly affect absorption for $\omega_{d,2} = 0$ and 0.5. This is due to the majority of the sample comprising of the solid phase and thus overall slab reflectance not being significantly augmented by scattering in the gas phase. However, when $\omega_{d,2}$ equals 1, high values of $\omega_{d,1}$ result in a substantial drop in absorptance. Conversely, absorptance in the high

porosity decomposed carbon phenolic sample is more significantly affected by increasing $\omega_{d,1}$, and drops even further by increasing $\omega_{d,2}$ due to cumulative scattering effects in both phases. For $x = 500$, discrete extinction coefficients $\beta_{d,i}$ are extremely high and invoke a stronger absorption coefficient $\kappa_{d,i}$ irrespective of the scattering albedos investigated. The absorptance values for each sample therefore remain constant for $0 > \omega_{d,1} > 0.9$ after which scattering in both phases dominates absorption, leading to a steep increase in reflectance.

Carbon fibres used in TPS materials are said to be highly scattering [155], selected to help transfer heat away from the payload via re-radiation. From Figure 6.9, it can be seen that for lower wavelengths ($x = 500$), slab absorptance is mainly based on sample porosity. The percentage of incoming radiation absorbed by the decomposed carbon phenolic sample remains constant at approximately 97% with variations in the solid phase scattering albedo ($\omega_{d,2}$). However, with an increase in scattering, samples with lower porosities begin to reflect more incoming radiation. A large drop in absorptance is thus seen for the decomposing graphite reinforced polymer composite. Absorption behaviour at higher wavelengths ($x = 5$) accounts for scattering in the gas phase in addition to the aforementioned variables. For very highly scattering gases, the decomposed carbon phenolic sample with the highest porosity reflects the largest amount of incoming radiation. Optimising a TPS for re-radiation behaviour therefore requires a compromise between density (porosity) and spectrally resolved scattering properties dependant on the relevant flight conditions.

The presented results can be used as a library of absorption data for a macroporous sample and be incorporated into any continuum modelling of chemically reacting media, such as a pyrolysing TPS material. The individual cells of the computational domain would have to be checked for the reaction convergence state or the composition of the pyrolysis gas at every time-step after which the radiative characteristics of the cell can be calculated based on the aforementioned correlations. For example during atmospheric entry, the increasing reaction front in the TPS material results in time-dependent (decomposition extent), variable optical properties in the TPS through its thickness.

6.4   CONCLUSIONS

Accurate radiative modelling and characterisation of reacting macroporous media consisting of at least two semi-transparent phases is essential for applications

in the space and solar-thermal industries. A multi-scale methodology based on computed tomography and Monte Carlo ray tracing was therefore used to determine the macroscopic optical properties of such samples. More specifically, the aim was to understand above which threshold individual bulk phase properties start to dominate overall absorption behaviour and the dependence of this dominance on sample morphology. The analysis was applied to two thermal protection system material samples, a medium density carbon phenolic composite and a high density graphite. The exact $3D$ morphology of the materials' complex porous structures were recorded using high resolution synchrotron computed tomography. Once digitalised and segmented, direct pore-level simulations were used to determine the effective radiative properties, namely, the effective extinction and scattering coefficients and the scattering phase functions.

The volume averaged radiative transfer equations were then used to determine the overall reflectance, absorptance and transmittance of semi-infinite slabs of the TPS materials. The effect of wavelength on these properties was evaluated for a range of size parameters from $5 < x < 1000$. Resin decomposition was seen to significantly affect the radiative behaviour of the TPS samples. Absorptance during pyrolysis increased from 0.76 to 0.94 for carbon phenolic and from 0.82 to 0.84 for graphite. Reflectance decreased from 0.24 to 0.04 and from 0.18 to 0.16 respectively. The increase in absorption was greater for the lower density carbon phenolic composite compared to the high density graphite. Scattering effects in both phases were also investigated. Optimising a TPS for good re-radiation behaviour was seen to involve a trade-off between material density and spectrally resolved scattering properties tuned for flight conditions.

This is a significant result, especially given the aim across the industry of replacing older, denser TPS materials with newer, more porous and lighter ones. Given knowledge of the bulk properties, the data presented can be incorporated in heat transfer calculations of macroporous media applied in the space or solar energy conversion domains, in order to quantify, design and optimise these applications.

RADIATIVE CONTRIBUTION TO MSL TPS HEATING

7.1 INTRODUCTION

Good quality data from the MEDLI experiment across seven plug locations (MISPs $1 - 7$), were successfully recorded and stored during atmospheric entry. For the shallowest thermocouple, TC1, peak temperatures ranged from 1094 K at MISP4 to 1322 K at MISP7. The variation in TC1 depth across the plugs, however, excludes the reasoning that plug 7 experienced highest heating. Depicted by the colour map in Figure 5.1, it can be seen that MISP2 is in the zone of peak convective heating and has been chosen as the test case [189]. Figure 7.3a presents the time resolved thermocouple data for MISP2.

In this chapter, flight data recovered from the forebody heat shield of the 2012 MSL mission is used for comparison with computational simulations. The state of the art material thermochemical response code, PATO, is used to resolve the time-resolved high temperature response of the four thermocouples embedded inside MISP2 on the leeside of the capsule. First, PATO temperature predictions based on heating environments estimated using CFD and flowfield radiation modelling are compared with the flight data. These include a effective conductivity term which is meant to account for radiative transfer inside the material domain. To be able to quantify the effects of internal radiation, effective properties, calculated in Chapter 6, are combined with volumetric view factors to evaluate the radiative fluxes. Section 7.2.1 describes the 1D model employed for this rebuilding.

7.2 METHODOLOGY

7.2.1 *Governing Equations*

PATO solves for the conservation of momentum, mass and energy inside the TPS material, the equations for which are derived and defined in detail by Lachaud *et al.* [18]. Due to the modifications employed on the internal energy equation in

this work, it will be briefly described here. It is based on a modified transient thermal conduction given in Equation 7.1.

$$\partial_t(\rho_t e_t) + \partial_x \cdot (f_v \rho_g h_g \mathbf{v_g}) + \partial_x \cdot \sum_{k=1}^{N_g}(\mathcal{Q}_k) = \partial_x \cdot (\underline{\underline{\mathbf{k}}} \cdot \partial_x T)$$
$$+ \mu f_v^2 (\underline{\underline{\mathbf{K}}}^{-1} \cdot \mathbf{v_g}) \cdot \mathbf{v_g} + \nabla \cdot \dot{q}_{rad,t} \tag{7.1}$$

The first term on the left hand side (LHS) describes the total storage energy, e_t, of the TPS material, which is defined as the sum of the specific energy of its phases (fibre and gas). Convective heat transfer inside the material is defined by the second term on the LHS, with f_v being the volume fraction of the gas phase, ρ_g its density and h_g its absolute enthalpy. The convection velocity of the gas phase, $\mathbf{v_g}$, is calculated by solving the volume averaged equation for conservation of momentum, detailed by Lachaud *et al.* [18]. The last term on the LHS models diffusive heat transfer, with $\mathcal{Q}_k$ being the effective diffusive heat flux. The second term on the right hand side (RHS) describes the energy dissipated by viscous effects in the Darcian regime [18], with $\underline{\underline{\mathbf{K}}}$ being the permeability tensor and μ the dynamic viscosity. This term is most often small enough to be neglected. The first term on the RHS defines effective conductivity, which is the main mode of heat transport. The second order tensor, $\underline{\underline{\mathbf{k}}}$, accounts for conduction in the solid and gas, radiative heat transfer and possible coupling terms between the two modes. Thermal equilibrium is assumed between phases, following conditions defined by Puiroux *et al.* [201] whereby the Peclet number for diffusion of heat within the pores is small.

To be able to evaluate and explicitly quantify the radiative contribution to the in-depth response of MISP2's thermocouples, it must be decoupled from the effective conductivity tensor, $\underline{\underline{\mathbf{k}}}$, applied by PATO. Using the effective radiative properties characterised in Chapter 6, the radiative flux divergence, $\nabla \cdot \dot{q}_{rad,j}$, can be solved for each cell, j, across the domain, using Equation 7.2. This term then comprises the last term in the energy equation (Equation 7.1). The spatial domain is discretised into N_e finite volumes, with N_b boundary area elements.

$$\nabla \cdot \dot{q}_{rad,j} = 4\kappa\sigma T_j^4 - \underbrace{\sum_{i=1}^{N_e}(4\kappa\sigma T_i^4 G_{ij}\frac{V_i}{V_j})}_{\text{internal finite volumes}} - \underbrace{\sum_{l=1}^{N_b}(H_{lj}\dot{q}_{in,j}\frac{A_l}{V_j})}_{\text{boundary elements}} \tag{7.2}$$

The G_{ij} and H_{lj} tensors are defined as discrete analogues to view factors used in the enclosure method [169, 202]. The G_{ij} tensor accounts for volumetric

absorption by cell j, based on volumetric emission from cell i, either directly or after any number and type of reflections. The H_{lj} tensor accounts for similar volumetric absorption of energy emitted by area element l on the boundary. The first term on the RHS accounts for grey body emission, with κ being the absorption coefficient and σ the Stefan-Boltzmann constant. Both tensors depend on geometry, boundary conditions and optical properties of the material domain. By assuming the temperature and wavelength independence of optical properties, it is possible to decouple the temperature from the computationally intensive Monte Carlo ray tracing method employed to calculate both tensors. They are therefore calculated only once rather than at each time step, implying a significant gain in computational efficiency. Radiative divergence can then be solved at each iteration for any given temperature.

In Chapter 6, it was seen that the extent of the pyrolysis reaction played a major role in determining the effective radiative properties of each phase. This can be taken into account while calculating the radiative divergence for the entire TPS, via Equation 7.3,

$$\nabla \cdot \dot{q}_{\text{rad,t}} = \tau \cdot \nabla \cdot \dot{q}_{\text{rad,v}} + (1 - \tau) \cdot \nabla \cdot \dot{q}_{\text{rad,c}} \tag{7.3}$$

where τ is the mass fraction of virgin material in a mixture of virgin material (ρ_{v}) and char (ρ_{c}) that yields the correct local density [143] in Equation 7.4.

$$\tau = \frac{\rho_{\text{v}}(\rho - \rho_{\text{c}})}{\rho(\rho_{\text{v}} - \rho_{\text{c}})} \tag{7.4}$$

This calculation requires evaluation of a set of G and H tensors for both virgin and char states. The radiative contribution, k_r was calculated using the Rosseland diffusion approximation, (Equation 7.5) and subtracted from the effective conductivity tensor, $\underline{\mathbf{K}}$, to avoid overestimating the effects of internal radiation. A literature value of $\beta = 9000$ m^{-1} for PICA, was applied for the extinction coefficient [200].

$$k_{\text{r}} = \frac{16\sigma T^3}{3\beta} \tag{7.5}$$

7.2.2   Boundary Conditions and Mesh

In order to predict surface convective heating for use as a boundary condition for PATO, CFD simulations were performed by Bose *et al.* [187] along MSL's best

estimated trajectory, incorporating data retrieved from the MEADS and IMU experiments on board. It must be noted that surface convective heat flux, presented in Figure 7.1, is not a direct input to PATO. The surface pressure, heat transfer coefficient and enthalpy are extracted at each plug's location from the CFD solutions. Before being provided to the thermal response code, these variables are time-resolved via fitting to tight monotonic splines [32]. These data are supplied by Omidy *et al.* [189] for MISP2. The surface energy balance is then performed as follows,

$$C_H(H_r - h_w) + \dot{m}_g h_g + \dot{m}_c h_c - (\dot{m}_g + \dot{m}_c)h_w \qquad (7.6)$$
$$+\alpha_w q_{rad} - \sigma \epsilon_w (T_w^4 - T_{BL}^4) - q_{cond} = 0$$

where the first term describes the convective heat rate using heat transfer coefficient, C_H and recovery and wall enthalpies, H_r and h_w. The sum of the second, third and fourth terms represents the total chemical energy at the surface resulting from pyrolysis and ablation. Mass flux and enthalpies of the gas and char at the surface are represented by $\dot{m}$ and h terms respectively. The fifth and sixth terms represent the incoming radiative heat rate absorbed by the material (with absorptance represented by α_w) and the re-radiation to the environment (controlled by wall emittance, ϵ_w). The last term represents heat conducted into the material from the surrounding environment.

The calculation is performed using properties from the fictitious *Theoretical Ablative Composite for Open Testing* (TACOT) [203] material. This material has been defined to support validation of ablation modelling without infringement of security or patent restrictions. Subsequently, this means that the present model has inherent inaccuracies compared to data generated in studies based on PICA, making it difficult to ascertain the accuracy of the radiation calculation. Re-radiation is modelled with an effective temperature kept constant along the entire trajectory, $T_{BL} = 202.6$ K, as specified in the test case by Omidy *et al.* [189]. A one dimensional grid with 100 cells is refined to the flow facing boundary. The initial temperature through the domain is defined based on the flight data initial temperatures.

White *et al.* [188] suggested that better comparison with flight data is achieved by simulating the thermochemical response of both the TPS and its substructure. This is possible in PATO via use of the inbuilt subMat parameter, which allows the specification of a multilayer stack of isotropic materials (with the surface heating boundary condition fixed on the TPS material front wall), through which

residual energy can flow. To include the radiative divergence term in the energy equation, G and H tensors, by definition, require entries for all control volumes absorbing radiative energy. Unfortunately, use of the `subMat` feature was limited by the size of the resulting matrices required by this larger domain. Instead, an analytical solution (Equation 7.7) for transient conductive heat transfer at the interface of two semi-infinite materials was applied to the TPS material back wall. The material selected to interface with the back wall was RTV Silicone glue, as per specifications of MSL's heat shield [188], whose thermal properties are given in Table 7.1.

Table 7.1: Thermal properties of RTV Silicone glue.

	k_{RTV} (W·m^{-1}·K^{-1})	ρ (kg·m^{-3})	C_p (J·kg^{-1}·K^{-1})	α (m^2·s^{-1})
RTV Silicone glue	0.844	1290	1460	4.48×10^{-7}

The conductive heat flux from the TPS domain to its back wall can be equated with the semi-infinite analytical solution. Therefore, using the thermal properties of the RTV Silicone glue, it is possible via Equation 7.7 to calculate the temperature of the interface between the two materials, T_s.

$$k_{\mathrm{TPS}}\frac{T_i - T_s}{\Delta x} = k_{\mathrm{RTV}}\frac{(T_s - T_{\mathrm{capsule}})}{\sqrt{\alpha \pi t}} \tag{7.7}$$

$$\alpha = \frac{k}{\rho C_p}$$

$$T_s = T_i\frac{k_{\mathrm{TPS}}}{\Delta x} + \frac{k_{\mathrm{TPS}}}{\Delta x} + T_{\mathrm{capsule}}\frac{k_{\mathrm{RTV}}}{\sqrt{\alpha \pi t}} + \frac{k_{\mathrm{RTV}}}{\sqrt{\alpha \pi t}} \tag{7.8}$$

T_{capsule} is the temperature inside the capsule, T_i is the temperature of the last cell in the computational domain for the TPS material, k is thermal conductivity and α, thermal diffusivity. This temperature is then imposed upon the back wall of the computational domain.

Identical spatial discretisation was used to solve the RTE, keeping cell size and distribution constant between both solvers. Reflection and refraction were modelled by Fresnel's equations and the generalised form of Snell's law [168], at the specularly reflecting interfaces. At the incoming boundary, a radiative heat

flux given in Figure 7.1, was applied, as calculated by Cruden *et al.* [191] using a combination of numerical modelling via NEQAIR and shock tube experiments. Further details are given in Appendix A. By coupling the divergence of the radiative flux to the energy equation, terms involving radiation were removed from Equation 7.7, to ensure they were not duplicated. The methodology followed for the numerical simulations of the thermal response of the MSL heat shield is summarised in Figure 7.2.

Using the correlations provided in Table 6.2, effective extinction coefficients were calculated for both virgin and char material, selecting bulk properties (listed in Table 7.2) to obtain maximum effect. To evaluate the feasibility of this methodology and any advantage of explicitly evaluating internal radiative effects, a simplified approach was adopted, ignoring scattering. For the Monte Carlo simulation, the computational domain was said to comprise of a single non-participating material, with radiative properties calculated by weighting the contributions of fibre and gas phases by volume fraction. A refractive index of $n = 2$ was chosen at the domain boundaries. Using porosities for virgin and char (provided in Table 6.1), the complex part of the refractive index was calculated using $k = \beta_{\mathrm{eff}} \cdot \lambda / 4\pi$ [169]. For the virgin material, $k_v = 4.06 \times 10^{-3}$ and for the char, $k_c = 3.36 \times 10^{-3}$.

Table 7.2: Phase-dependant bulk properties used for Monte Carlo simulation.

	Gas Phase		Fibre Phase	
	Virgin	Char	Virgin	Char
β_{d} (m^{-1})	1	9000	15000	9000
β_{eff} (m^{-1})	5.06×10^4	3.77×10^4	5.17×10^4	6.16×10^4
λ (m)		1.0×10^{-6}		
k	4.02×10^{-3}	3.0×10^{-3}	4.12×10^{-3}	4.9×10^{-3}
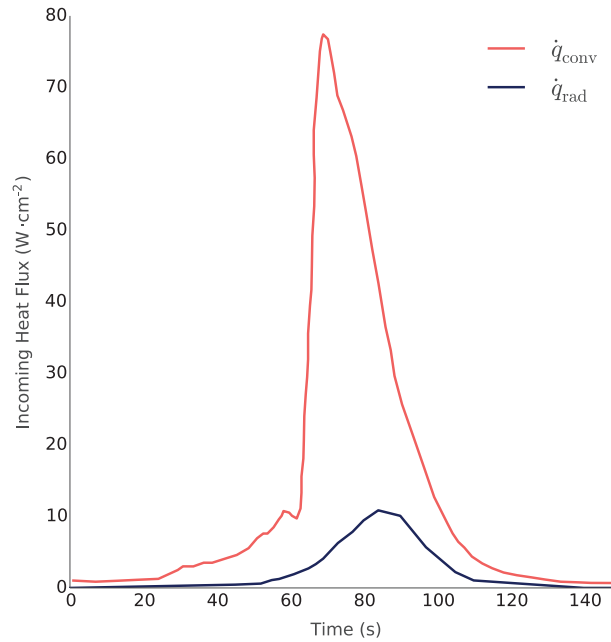
Figure 7.1: Convective and radiative heat fluxes applied at the boundary wall to simulate the thermal response of MISP2 [187, 191].
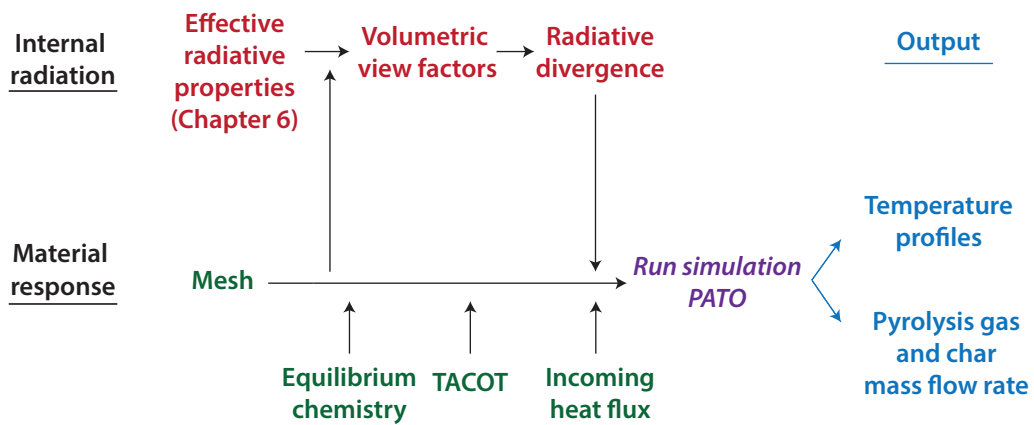
Figure 7.2: Methodology for numerical simulations of the MSL heat shield thermal response along its trajectory using PATO, including effective radiative properties calculated in Chapter 6 and volumetric view factors.

7.3   RESULTS

7.3.1   *Internal Radiation*

A key observation made from the flight data presented in Figure 7.3a is the absence of any near-surface thermocouple burnout for MISP2. This indicates that the TPS did not recede beyond the shallowest thermocouple, TC1, which had a nominal depth of 2.68 mm below the unablated surface (see Table 7.3). In the event that the thermocouple survived TPS recession past its surface, it would have been exposed to the significantly hotter boundary layer flow, giving much higher readings than those recovered. The peak temperature read by TC1 is 1230 K. Thermocouple response simulated using PATO under purely convective heating is shown in Figure 7.3b. When compared against the flight data (Figure 7.3a), it is evident that the model significantly overpredicts peak temperature and temperature rise. The reason for this overestimation could be that transition to turbulence happened later than expected in flight, leaving less time for the predicted increase in surface heating [32]. Temperature augmentation in flight due to turbulent transition was therefore less than model predictions. The simulations also predict TC1 burnout due to recession, which did not occur in flight as previously discussed. The equilibrium chemistry models used to define gas-surface interactions are known to be inaccurate for the low heating rates experienced by MSL and tend to overpredict recession [204]. Combined with the overestimated surface heating rates this is the main cause of this discrepancy [32, 187, 191].

Replacing the equilibrium model with finite-rate calculations should provide a more accurate value for wall enthalpy. Any increase in wall enthalpy should result in a reduction of energy removal via ablation, thereby improving comparison with MISP2's thermal response in flight. PATO has the ability to replace the equilibrium model with finite-rate chemistry calculations, which should be used for similar studies in the future. Accurate predictions of surface recession are critical for improved modelling of in-depth thermocouple response, which should increase in temperature with increasing proximity to the TPS material surface.

For the remaining simulations, recession was therefore excluded from the model. The resulting temperature profiles at all four thermocouple locations are shown in Figure 7.3c, with and without the inclusion of radiative heating
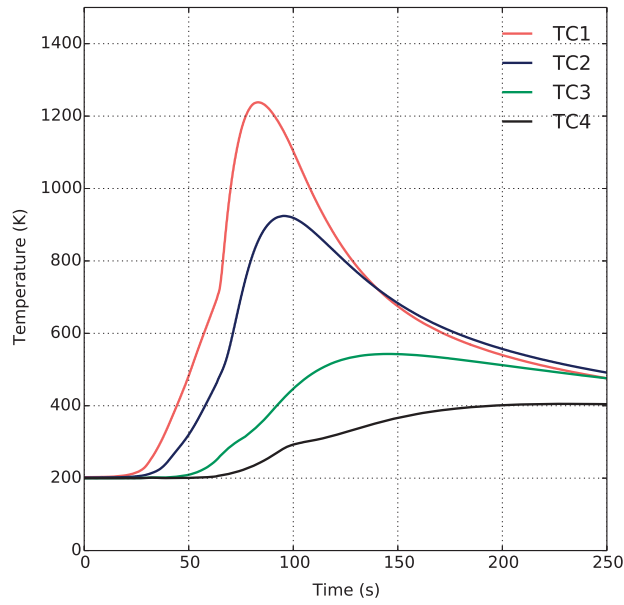
a) Flight data.
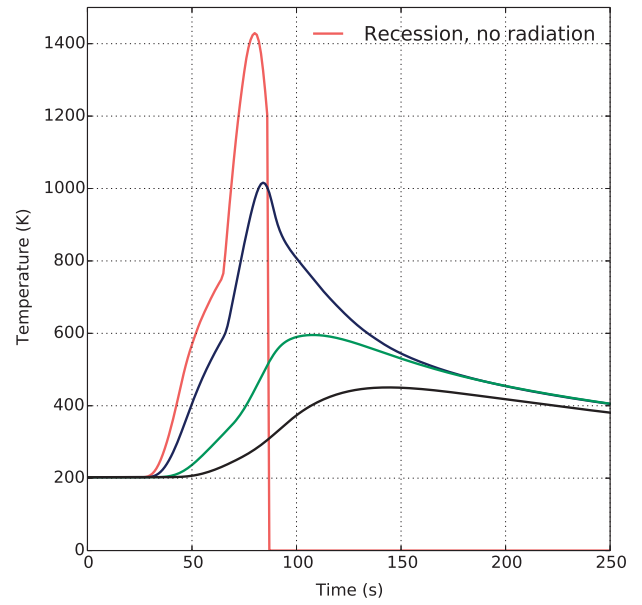
b) Combined effect of recession and convective heating on thermocouples.
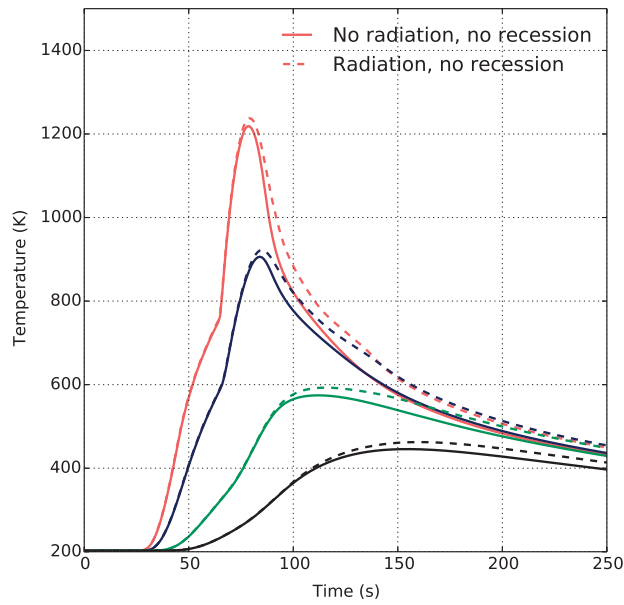
c) No recession, purely convective (solid lines) and total heating (dashed lines).
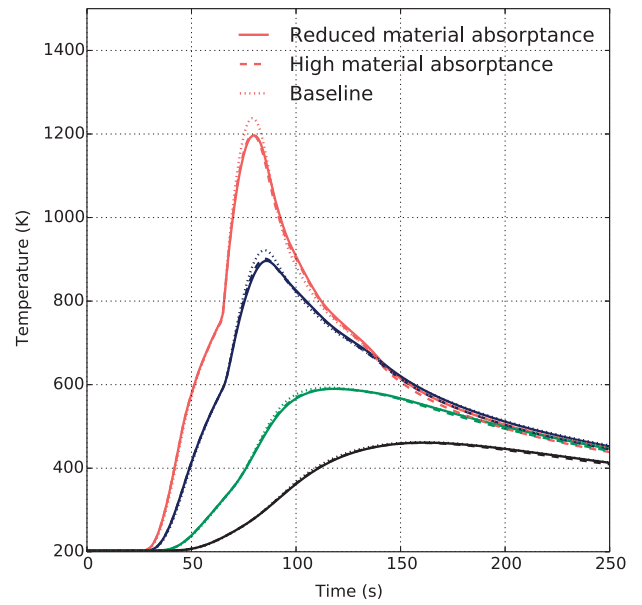
d) No recession, baseline model (dotted), including internal radiative effects with low (solid) and high absorptance (dashed).

Figure 7.3: Comparison of MISP2 flight data with PAT0 simulations using a boundary layer approximation.

Table 7.3: X-ray measured depths of thermocouples in MISP2 [187].

	TC1	TC2	TC3	TC4	Total plug depth
Depth (mm)	2.68	5.16	11.57	17.77	29

at the wall. Straight away, it is noticeable that by excluding recession, the peak temperature measured by TC1 reduces to approximately 1212 K using purely convective heating at the wall. The temperature across all thermocouples is underpredicted at the end of cool-down, compared to flight values. Cruden *et al.* suggest an overprediction in turbulent heating at MISP2 resulting in an excessive recession prediction [191]. This hypothesis is backed up by the fact that the numerical model obtains very similar values to peak temperature during flight in the absence of recession. The inclusion of radiative heating at the boundary improves model predictions significantly and is therefore used as the baseline model for later comparisons. Peak temperature for TC1 increases to 1233 K, overpredicting flight values by just 3 K. Similarly, TC2 peaks at 916 K, similar to flight. Compared to the case applying purely convective heating at the wall, higher temperatures are predicted for the end of cool-down, improving similarity to recorded data. However, values are still underpredicted compared to flight, especially for the shallow thermocouples (TC1 and TC2). Overall temperature profiles are broadened across all thermocouples, showing closer resemblance to flight profiles.

The through-thickness temperature response of MISP2 is plotted in Figure 7.4 for when peak radiative heating occurs along MSL's trajectory (i.e. between 75−90 s, as per Figure 7.1). It can be seen that, compared to the baseline simulation, the majority of the incoming radiation is absorbed within the first 0.2 mm by the TPS material's strongly absorbing phases. There is a delay in cool-down compared to the baseline case, as the energy is not conducted inwards upon the arrival of the incoming heat flux. It is first absorbed and only then is it transferred inwards. In Figure 7.3d, thermocouple results from simulations incorporating strongly absorbing phases inside the TPS domain are plotted against the baseline model. Values used for material extinction coefficients are listed in Table 7.4. A decrease in peak temperature is noted for all thermocouples compared to the baseline model and flight. This is due to the majority of radiative fluxes being absorbed within the first 0.2 mm as seen in
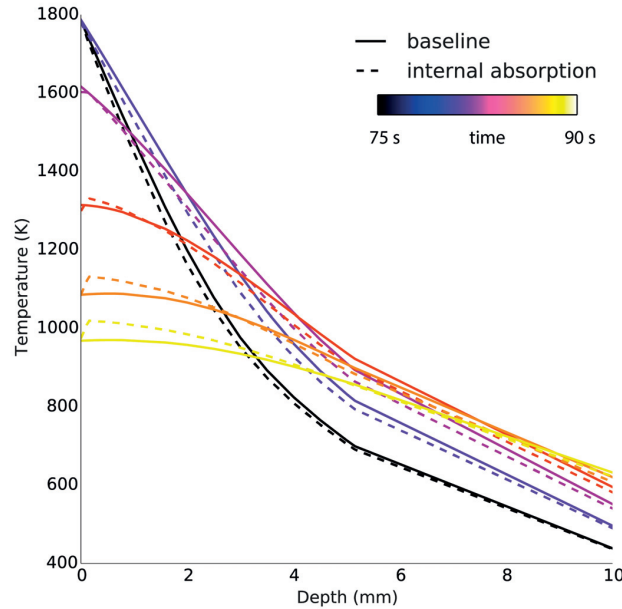
Figure 7.4: Through thickness temperature response of MISP2 (limited to the first 10 mm), comparing PATO simulations without (solid) and with (dashed lines) internal radiative effects.

Figure 7.4, while the first thermocouple is nominally located 2.68 mm from the surface.

During cool-down, later in the trajectory, slight broadening of the profiles for TC1 and TC2 is seen, which compares favourably with flight. As most of the radiative energy is stored at the surface of the material domain, it takes longer for it to conduct into the material and arrive at the thermocouples. This delayed conduction leads to the broadening of these thermocouple response profiles. The high absorption case is plotted against PATO baseline and flight data in Figure 7.5, concentrating on the end of the flight trajectory during cool-down. It is noted that by including highly absorptive behaviour of the TPS material phases, a drop in temperature is seen throughout the trajectory. For TC4, this is favourable, as it brings the temperature reading closer to the values measured in flight.

In solving Equation 7.2 for the strongly absorbing materials considered (Table 7.4), the majority of the incoming radiation is absorbed by the first cell in

Table 7.4: TPS material absorption coefficients.

	Low absorptance	High absorptance
κ_v (m^{-1})	3580	6300
κ_c (m^{-1})	9000	15000
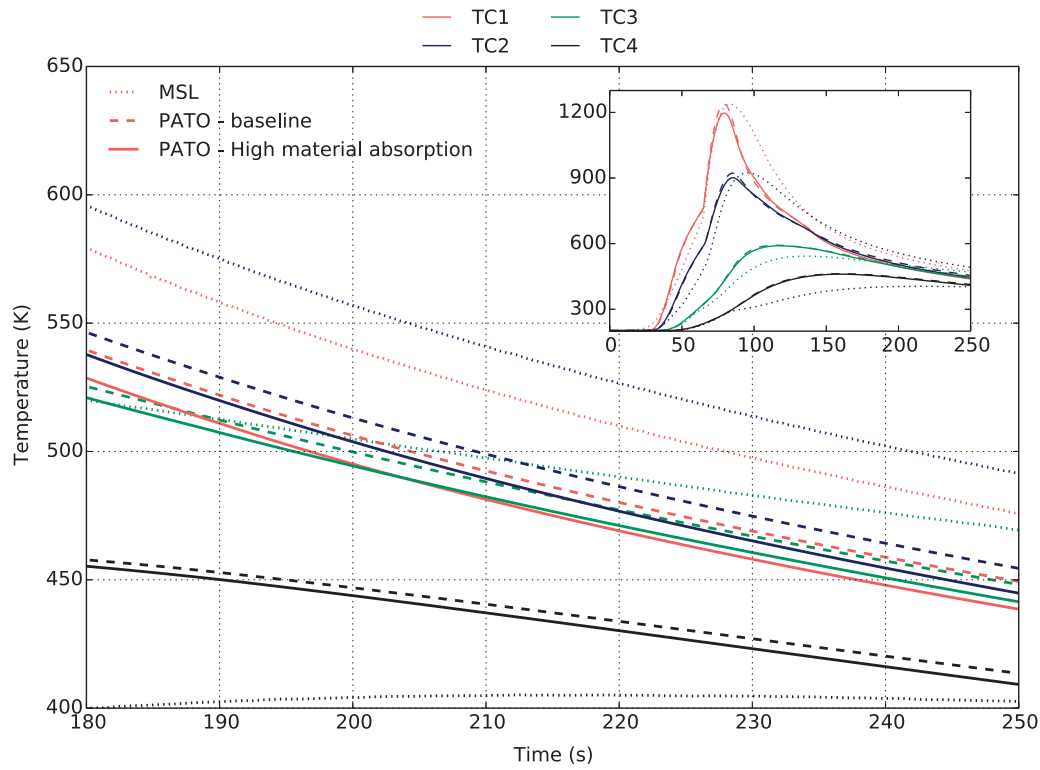
Figure 7.5: Detailed view of thermocouple response during cool-down, comparing MSL flight data (dotted) to PATO simulations with (solid) and without (dashed lines) internal radiative effects.

the TPS domain. Given that the reference temperature controlling re-radiation (T_∞) is kept constant at 202.6 K in the test-case specified boundary conditions (Appendix A), there is an increase in energy dissipated via re-radiation with

every increase in wall temperature. Similarly, most of the energy emitted by a cell is absorbed before it reaches the cell boundaries.

Combined with the fact that energy is increasingly dissipated outwards soon after being absorbed, it is not given the chance to conduct through the domain and affect thermocouple response. It is therefore recommended to modify this re-radiation controlling temperature with time, providing realistic boundary layer temperatures through empirical correlations, so that the energy is given the chance to dissipate inwards. MISP1 is subjected to lower convective heating than MISP2 but higher radiative heating. It would therefore be interesting to rebuild MISP1's response for strongly absorbing solid and gas phases, as a higher proportion of the energy would be delivered through radiation. A test case with significantly higher radiative heating (i.e. Stardust [72]) is also recommended to be able to visualise the effects of internal absorption on temperature.

Defining the TPS material as a 1D participating medium and limiting the radiation to a single wavelength was deemed sufficient to assess the importance of quantifying the radiative contribution to TPS material response. However, these simplifications underestimate the overall effect. Optical properties are heavily dependent on both wavelength and temperature, as shown in Chapter 6. They must therefore be taken into account for a more detailed analysis. Work is currently underway to solve Equation 6.1 in a 3D domain, for both participating fibre and gas phases. The strongly forward scattering nature of both phases (Figure 6.4b) should help transfer the energy obtained via surface radiative heating deeper into the material, thereby affecting the thermal response.
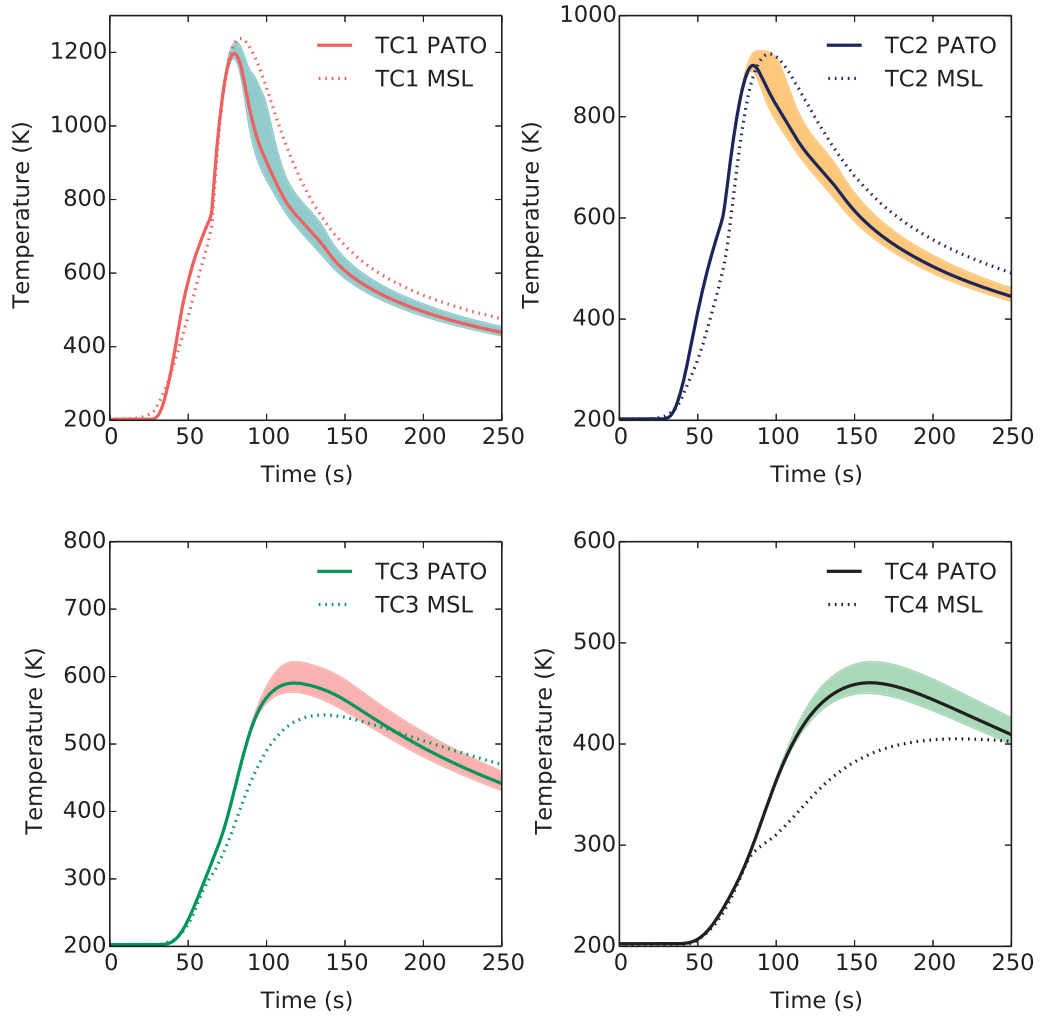
Figure 7.6: Comparison of flight data with simulations incorporating internal radiative effects ($\beta_v = 6300$ m^{-1}, $\beta_c = 15000$ m^{-1}), with an uncertainty interval based on applying 50% and 200% of the incoming radiative heat flux boundary condition, keeping convective heating the same. Note the difference in scale in y-axis for each subplot.
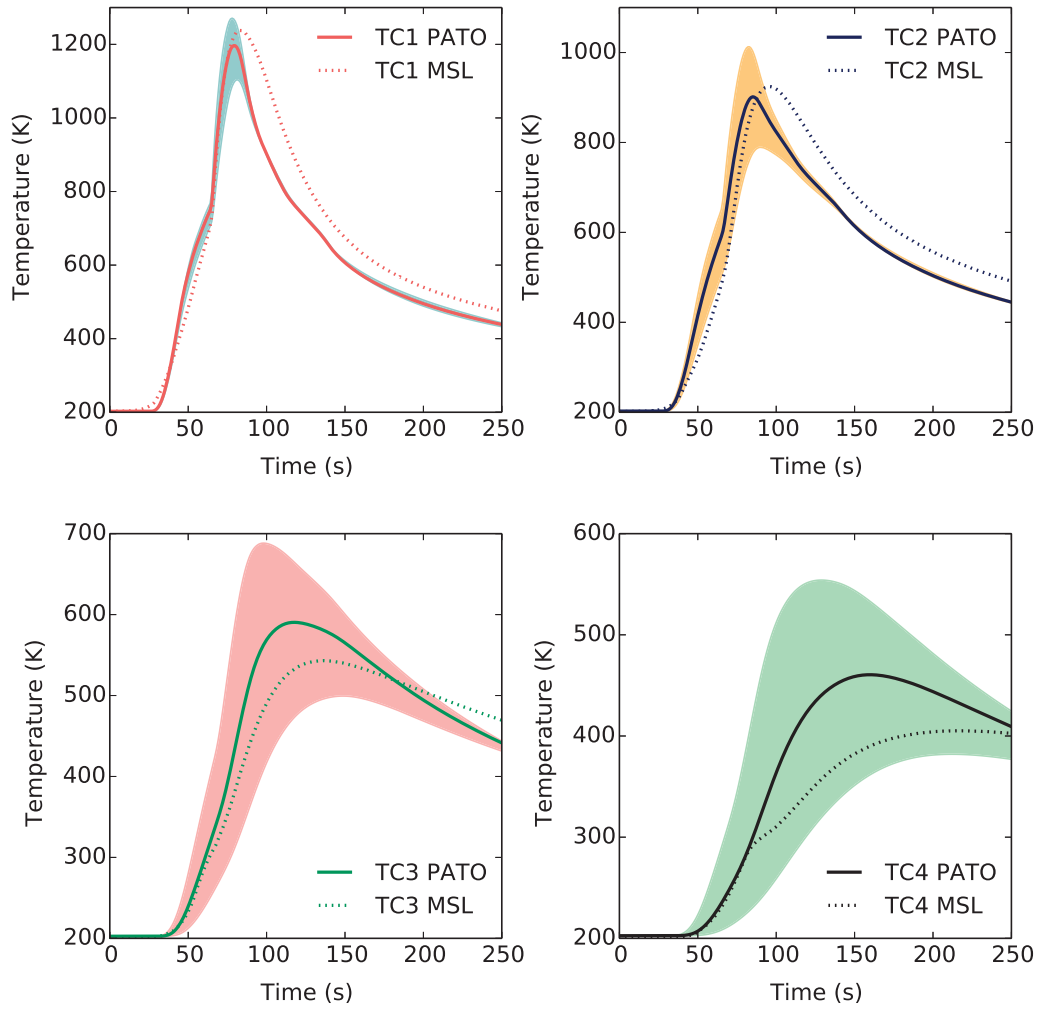
Figure 7.7: Comparison of flight data with simulations incorporating internal radiative effects ($\beta_v = 6300$ m^{-1}, $\beta_c = 15000$ m^{-1}), with an uncertainty interval based on varying the virgin and char conductivities, k_v and k_c, by 50% and 200% of its database value. Note the difference in scale in y-axis for each subplot.

7.3.2 *Sensitivity Analysis*

Uncertainty intervals were calculated based on 50% and 200% of radiative heating experienced by MISP2. These are plotted in Figure 7.6 for each thermocouple for a highly absorbing TPS material ($\beta_v = 6300$ m^{-1}, $\beta_c = 15000$ m^{-1}). Modifications in radiative heating at the surface have a significant effect on surface and in-depth thermocouple temperature profiles. For TC1 and TC2, doubling the radiative heating results in matching the peak temperatures experienced in flight and reduces the error between simulation and flight temperatures during the cool-down period. Similarly, an increase in incoming radiation improves prediction of TC3's thermal response, but increases discrepancy between numerical results and flight data for TC4.

Model accuracy is also affected by uncertainties in high temperature properties, for example, thermal conductivity which is difficult to characterise accurately in controlled environments. The effect of varying thermal conductivity on temperature profiles was evaluated by running simulations using 50% and 200% of k values provided by *TACOT*. This data is presented in Figure 7.7. A large uncertainty interval can be seen for the shallow thermocouples (TC1 and TC2) concentrated around their peak temperature values. The deeper thermocouples (TC3 and TC4), are affected by a large uncertainty throughout the simulation time, based on varying thermal conductivity.

7.4 CONCLUSIONS

The implementation of a simplified model accounting for internal absorption in a charring ablator, presented in this chapter, meets Objectives O.5 and O.6 and sets the foundation for more in-depth analysis of internal radiative effects. The material response code PATO was used to simulate the one-dimensional temperature profiles of thermocouples embedded at varying depths inside the MISP2 plug on MSL's ablative heat shield. Assuming optical properties of the material to be independent of wavelength and temperature, volumetric view factors were calculated using a Monte Carlo ray tracing method. This allowed the calculation of a time resolved radiative flux divergence, which was supplied to the energy equation and dependant on the extent of the pyrolysis reaction.

Surface recession was excluded from the models due to overprediction by equilibrium ablation models for low heating rates such as those experienced by

MSL. Recession is, however, critical to obtaining accurate predictions of material response. Inclusion of radiative heating at the surface improved thermocouple response prediction, broadening the profiles and matching peak temperatures for shallow thermocouples (TC1 and TC2). Good comparison was not seen for in-depth thermocouples (TC3 and TC4). At the end of cool-down, temperatures were heavily underestimated for all but the deepest thermocouple, for which temperature was overestimated. Including the internal radiation term for highly absorbing materials decreased the peak temperatures across all thermocouples but broadened the profiles due to increased absorption at the TPS surface and delayed material cool-down. The majority of the radiative flux was seen to be absorbed at a depth of approximately 0.2 mm. Improved comparison with flight was seen for the deepest thermocouple at the end of the cool-down period. Increasing the absorption coefficient in the material resulted in a further decrease in temperature.

Inaccuracies in this flight rebuild stem from a multitude of variables. The fictional *TACOT* material database used does not contain the exact properties of PICA, used on MSL's heat shield. High temperature thermal properties included in these databases are notoriously hard to measure accurately. The boundary conditions employed were developed using CFD simulations, radiation modelling and experiments and contain the inherent uncertainties. The controlling temperature for re-radiation included in the boundary conditions heavily influences and overestimates energy dissipated away from the material. An uncertainty analysis showed large fluctuations in calculated temperatures across all thermocouples for changes in surface radiative heating as well as virgin and char thermal conductivities.

The assumption of a non-scatting medium underestimates the overall effect of internal radiation on TPS material response. Work is therefore underway to quantify this phenomenon by solving the coupled volume averaged RTEs for each strongly forward scattering phase, using radiative properties calculated in the previous chapter.

8

CONCLUSIONS

By addressing the objectives set out in Section 1.4, this thesis evaluated the role played by thermal radiation in both the high temperature response of ablative heat shields and their surrounding aerothermal environment. With the end goal of improving the understanding of the complex physics of the strongly radiating shock and the fidelity of prediction methods for radiative heating of the TPS in different atmospheres, a study combining computational aerothermodynamic simulations and expansion tube testing of composite aeroshells was detailed and analysed in *Part I* of this work. In *Part II*, the contribution of radiation to heat transfer inside charring ablators was gauged and quantified using numerical simulations based on computed tomography data.

8.1 MAJOR FINDINGS

During the course of this thesis, progress was made with regards to experimental testing of TPS materials for entry into multiple atmospheres, filling in a niche in the testing envelope. Based on previous studies, it was seen that ablation testing is largely conducted in arc-jet facilities and occasionally using solar towers. These facilities have the ability to test the material for long durations at representative heating rates. However, they cannot faithfully reproduce extra-terrestrial atmospheres and flight-equivalent radiative heating, both critical parameters for demanding trajectories planned for future missions. Expansion tube ablation testing can help fill this gap, but is comparatively new and still maturing as a methodology. Previously, ablation testing in X2 was limited to air, for non-flight geometries and/or conditions. In addition, ground testing of ablative materials provides the opportunity to establish data sets for the validation of computational aerothermodynamic tools. Numerical rebuilding of X2 experiments remains rare due to its difficulty, but helps quantify unmeasurable flow parameters while providing a benchmark for state of the art codes.

In *Chapter* 3, Earth and Venus (re-)entry conditions were chosen and characterised for expansion tube testing. Based on a fibre-glass inner shell, a

methodology was established to manufacture reusable composite aeroshells in the laboratory. In this case, the shell was layered with a mixture of phenolic resin and chopped carbon fibres, to replicate current generation ablative materials such as PICA. The sphere-cone geometry was chosen for its similarity to entry vehicles as well as the ease of numerical rebuilding due to rotational symmetry of the flow around the model centreline. Limited success was achieved with the electrical pre-heating method, which was a favoured idea for replicating pyrolysis, due to the brittleness and low thermal shock resistance of the phenolic resin. Pyrolysis was instead achieved through aerodynamic heating of the model during the experiment with model surface temperatures reaching approximately 600 K for both flows during the steady test time. The boundary layer radiation was then investigated for different atmospheres in the presence of pyrolytic species.

In *Chapter* 4, CFD simulations were conducted and coupled to radiation databases, solving the RTE along a line of sight chosen to mimic the experiments. A different structured grid was used to simulate each condition. It was found that due to the small model size, a more converged, stable solution could be obtained by using an increased number of cells in the x-direction, clustered just to the wall, rather than to both the wall and the shock. This new mesh, used to simulate the Earth flow, reduced simulation time and the effect of the carbuncle on the heat flux calculations. Two reaction schemes, three radiation databases and two surface kinetic rates were used for each atmospheric condition, to determine which combination produced the best comparison to experiment. Relevant collision integrals were evaluated when not available in literature, for calculation of flow transport properties. It was seen that for both conditions, reaction schemes proposed by Park showed greater agreement with the experimental results. Applying Suzuki's reduced nitridation efficiency to the reacting surface boundary condition produced results most similar to experiment. Similarly, the solution provided by the NEQAIR radiation database seemed to have the closest fit.

Overall, comparisons in the visible spectrum were inconclusive for both conditions, with numerically generated spectra severely underestimating the noisy experimental data. For the Venus condition, C_2-Swan features in the UV were well reproduced, matching line shape and intensity across the spectrum. CN-Violet features were severely overestimated. These bands are thought to have undergone strong self-absorption in experiment which was not well

modelled by the radiation codes. Very good comparison was found for the Earth condition in the IR matching line shape and intensity well for all atomic oxygen and nitrogen features. In the UV, overproduction of N_2^+ by the reaction models contributed to inflation of spectra magnitudes of other species, contaminating the desired result. Once N_2^+ was removed from the data, excellent comparison was found for the CN Violet $v = +1$ band. CN Violet $v = 0$ features were still slightly overestimated. Therefore, *Part I* of this thesis created two unique datasets, for Earth and Venus entry, through experiment and numerical analysis.

Current interest in developing low density ablators for thermally challenging atmospheric entry trajectories, coupled to the recent detection of the volumetric nature of ablation makes understanding internal radiation a priority. In *Chapter* 5, the common use of oversimplifications in the form of the Rosseland diffusion approximation or analytical models with artificial geometries to define internal radiation in composites was noted. More often than not, radiation is assumed implicit in the conductivity term of the energy equation, which is empirically evaluated. Recent advances in computing have allowed the use of stochastic, mesh-less methods to evaluate effective radiative properties of real 3D sample geometries for use in macroscopic heat transfer calculations. However, existing literature concentrates on porous ceramics or fibre felts and not fibre-resin composites used in charring ablators. It is therefore now possible, and of interest, to include TPS material radiation models in a state of the art thermal response code. Thermocouple data from the MSL heat shield was selected to validate this coupled methodology.

In *Chapter* 6, a multi-scale methodology was used to characterise the effective radiative properties of samples of two TPS materials, carbon phenolic and graphite. The exact 3D morphologies of the two samples were recorded using high resolution synchrotron tomography, digitised and then segmented to manipulate the extent of pyrolysis and create datasets of both virgin and charred samples. Conducting direct pore-level simulations on these datasets using a Monte Carlo method allowed the characterisation of morphological and spectrally resolved effective radiative properties across both fibre and resin phases. Unlike existing studies, both phases were assumed semi-transparent, which is likely at certain wavelengths during pyrolysis. The calculated properties, such as extinction and scattering coefficients and scattering phase function, were later used in *Chapter* 7 to incorporate radiation in TPS thermochemical response using PATO. They were also used to calculate macroscopic optical

properties of a 10 mm thick semi-infinite slab of both materials, by solving the coupled volume-averaged RTEs. Slab absorptance was seen to increase during pyrolysis from 0.76 to 0.94 for carbon phenolic and from 0.82 to 0.84 for graphite. Optimising a TPS for good re-radiation behaviour was seen to involve a trade-off between material density and spectrally resolved scattering properties tuned for specific flight conditions. Given the industry-wide aim to replace denser materials with lightweight charring ablators, it is imperative to account for this significant change in absorption for low density ablators.

In *Chapter* 7, thermocouple data recovered from MSL's entry into the Martian atmosphere was used for comparison with coupled radiation-material response calculations. PATO was used to simulate the temperature profiles of all four thermocouples embedded inside MISP2 at varying depths. Due to a combination of overestimated turbulent surface heating rates and erroneous equilibrium chemistry models, surface recession was significantly overestimated and therefore not used for the simulations. The inclusion of radiative heating at the surface improved comparison with flight data by matching peak temperatures for the shallow thermocouples and broadening the temperature profiles. This dataset was therefore used as the baseline model.

Assuming the TPS material to be non-scatting but strongly absorbing and its optical properties to be independent of temperature and wavelength, specular view factors were calculated using the Monte Carlo method. These values were used to calculate the temperature-dependent radiative flux divergence and supplied to the energy equation included in PATO. Including internal radiation decreased peak temperatures for all thermocouples but broadened their profiles as the majority of the incoming radiative heat flux was absorbed near the TPS material surface. Temperature prediction was improved for the deepest thermocouple at the end of the trajectory. Given that internal radiation seems to have a demonstrable effect, even for such a strongly absorbing material, it should be considered in future material response calculations.

8.2 RECOMMENDATIONS FOR FUTURE WORK

It is imperative to improve the experimental methodology and modelling techniques for a better grasp of the response of low density ablators to strongly radiating shock waves. The electrical pre-heating method is currently limited by the brittleness of the phenolic resin. A novel technique therefore needs to

be developed to reduce the thermal stresses in the aeroshell during heating. A ceramic aeroshell with a heated RCC strip set into a groove across the stagnation point is conceivable and would give the ability to attain higher temperatures in a controlled fashion. A scaled Hayabusa or Stardust geometry and condition should be selected for comparison with published flight data. For the Venus flow, the use of a 70% CO_2 - 30% N_2 gas mixture as suggested by Boubert *et al.* [131] is recommended to decrease the noise in spectral measurements. Better measurement of flow parameters would also be of great use for an improved understanding of the physical processes and numerical rebuilding. Using a mount with a pitot rake mounted under the model, similar to that currently used on the LENS-XX expansion tube [205] could help identify shot-specific flow parameters.

Another priority would be to investigate radiation across different spectral regions. For Venus flow, strong C_2 bands should be visible between $400 - 600$ nm. The expansion of X2's imaging capabilities is ongoing, with the introduction of mid IR spectroscopy systems. These systems could be applied for the measurement of CO_2 and CO released during pyrolysis. For Earth flow, it would be interesting to probe lower UV wavelengths for CN band radiation. Accessing the VUV spectral region would increase experimental complexity significantly, but would be important for quantification of CO Fourth-Positive radiation and therefore surface oxidation rates. For radiation bands that show poor comparison between numerically generated and experimentally obtained spectra, it is important to investigate the radiation data sets further and minimise this error. Given the low fidelity of N_2^+ modelling by existing reaction schemes, the creation of tuned rates for N_2^+ is recommended, similar to work conducted by Johnston [102] for CN using the EAST facility. For small geometries, the use of high density meshes is recommended for their increased simplicity, efficiency, stability and convergence. Refinement of the mesh along the line of sight can be improved for better resolution of the calculated spectra.

Having applied a multi-scale methodology to explicitly quantify radiation in TPS material response for the first time, a foundation has been laid for future research to improve upon. Due to the similarity in the chemical composition and thus X-ray absorption of both fibres and the resin matrix, phase segmentation in carbon phenolics is difficult. It would be interesting to conduct a tomography campaign using a low density SiC composite ablator, such as SLA-56l, where the difference in chemical compositions should allow more accurate phase segmentation and post-processing. At present, the coupled simulations involving

internal radiative effects and material thermal response assume the TPS to be non-scattering. This simplification underestimates the overall effect that absorption has on material response. It is therefore important to account for all effective radiative properties calculated in Chapter 6, including the scattering coefficients and phase functions. Work is currently underway to quantify this phenomenon by solving the coupled volume averaged RTEs for each semi-transparent phase. Ideally, an improved understanding of the effects of thermal radiation on the TPS and its surrounding environment will lead to better sizing, margining and optimisation of the structure, allowing an increase in useful payload for frequent and safe deployment in space exploration.

REFERENCES

[1] J D Anderson. *Hypersonic and high temperature gas dynamics*. AIAA, 2000.

[2] D S F Portree. Project FIRE Redux: Interplanetary Reentry Tests (1966). https://www.wired.com/2012/07/interplanetary-reentry-tests-1966/, 2012. Accessed: 2016-11-22.

[3] T Rivell. Notes on earth atmospheric entry for mars sample return missions. Technical Report TP–2006-213486, NASA, 2006.

[4] L S Swenson Jr, J M Grimwood, and C C Alexander. *This New Ocean: A History of Project Mercury*. NASA, 1998.

[5] G Duffa. *Ablative thermal protection systems modeling*. American Institute of Aeronautics and Astronautics, 2013.

[6] M Stackpoole, S Sepka, I Cozmuta, and D Kontinos. Post-flight evaluation of stardust sample return capsule forebody heatshield material. *AIAA paper*, 1202:2008, 2008.

[7] N Mansour, F Panerai, A Martin, D Y Parkinson, A A MacDowell, A Fast, G Vignoles, and J Lachaud. A new approach to light-weight ablators analysis: from micro-tomography measurements to statistical analysis and modeling. In *44th AIAA Thermophysics Conference*, volume 2768, San Diego, CA, 2013.

[8] B Laub and E Venkatapathy. Thermal protection system technology and facility needs for demanding future planetary missions. In *Planetary Probe Atmospheric Entry and Descent Trajectory Analysis and Science*, volume 544, pages 239–247, 2004.

[9] H Tran, C Johnson, D Rasky, F Hui, Y K Chen, and M Hsu. Phenolic impregnated carbon ablators (PICA) for Discovery Class missions. *AIAA Paper*, 1911:1996, 1996.

[10] R A S Beck, H H Hwang, M J Wright, D M Driver, and E M Slimko. The Evolution of the Mars Science Laboratory Heatshield (Part II). 7th International Planetary Probe Workshop, 2010.

[11] E J Fahy. *Superorbital Re-entry Shock Layers: Flight and Laboratory Comparisons*. PhD thesis, The University of Queensland, 2017.

[12] D Hunt and R Morgan. Simulated atmospheric entry ablation in superorbital flows. In *38th Aerospace Sciences Meeting and Exhibit*, page 502, Reno, NV, 2000.

[13] F Zander, R G Morgan, U Sheikh, D R Buttsworth, and P R Teakle. Hot-wall reentry testing in hypersonic impulse facilities. *AIAA journal*, 51(2):476–484, 2012.

[14] S W Lewis, R G Morgan, T J McIntyre, C R Alba, and R B Greendyke. Expansion tunnel experiments of earth reentry flow with surface ablation. *Journal of Spacecraft and Rockets*, pages 1–13, 2016.

[15] W Lipiński, J Petrasch, and S Haussener. Application of the spatial averaging theorem to radiative heat transfer in two-phase media. *Journal of Quantitative Spectroscopy and Radiative Transfer*, 111(1):253–258, 2010.

[16] W Lipiński, D Keene, S Haussener, and J Petrasch. Continuum radiative heat transfer modeling in media consisting of optically distinct components in the limit of geometrical optics. *Journal of Quantitative Spectroscopy and Radiative Transfer*, 111(16):2474–2480, 2010.

[17] J Petrasch, S Haussener, and W Lipiński. Discrete vs. continuum-scale simulation of radiative transfer in semitransparent two-phase media. *Journal of Quantitative Spectroscopy and Radiative Transfer*, 112(9):1450–1459, 2011.

[18] J Lachaud, A J van Eekelen, J B Scoggins, T E Magin, and Nagi N Mansour. Detailed chemical equilibrium model for porous ablative materials. *International Journal of Heat and Mass Transfer*, 90:1034–1045, 2015.

[19] C Park. *Nonequilibrium Hypersonic Aerothermodynamics*. NASA, 1989.

[20] R Gollan. *Computational Modelling of High-Temperature Gas Effects with Application to Hypersonic Flows*. PhD thesis, The University of Queensland, 2008.

[21] P A Gnoffo, K J Weilmuenster, H H Hamilton, D R Olynick, and E Venkatapathy. Computational aerothermodynamic design issues for hypersonic vehicles. *Journal of Spacecraft and Rockets*, 36(1):21–43, 1999.

[22] M Natali, J M Kenny, and L Torre. Science and technology of polymeric ablative materials for thermal protection systems and propulsion devices: A review. *Progress in Materials Science*, 84:192–275, 2016.

[23] ASTM. 285-80. standard test method for oxyacetylene ablation testing of thermal insulation materials. *Annual Book of ASTM Standards*, 15(03), 2008.

[24] B Laub, J Balboni, and H Goldstein. Ground test facilities for tps development. Technical Report TM-2002-211400, NASA, 2002.

[25] P Agrawal, D T Ellerby, M R Switzer, and T H Squire. Multidimensional testing of thermal protection materials in the arcjet test facility. In *10th AIAA/ASME Joint Thermophysics and Heat Transfer Conference*, Chicago, IL, 2010.

[26] S Loehle, T Staebler, T Reimer, and A Cefalu. Photogrammetric surface analysis of ablation processes in high-enthalpy air plasma flow. *AIAA Journal*, 53(11):3187–3195, 2015.

[27] B Helber, C O Asma, Y Babou, A Hubin, O Chazot, and T E Magin. Material response characterization of a low-density carbon composite ablator in high-enthalpy plasma flows. *Journal of Materials Science*, 49(13):4530–4543, 2014.

[28] M E MacDonald, C M Jacobs, C O Laux, F Zander, and R G Morgan. Measurements of air plasma/ablator interactions in an inductively coupled plasma torch. *Journal of Thermophysics and Heat Transfer*, 29(1):12–23, 2014.

[29] A Martin, S C C Bailey, F Panerai, R S C Davuluri, H Zhang, A R Vazsonyi, Z S Lippay, N N Mansour, J A Inman, B F Bathel, et al. Numerical and experimental analysis of spallation phenomena. *CEAS Space Journal*, pages 1–8, 2016.

[30] E Venkatapathy, B Laub, G J Hartman, J O Arnold, M J Wright, and G A Allen. Thermal protection system development, testing, and qualification for atmospheric probes and sample return missions: Examples for saturn, titan and stardust-type sample return. *Advances in Space Research*, 44(1):138–150, 2009.

[31] Scott C Splinter, Kim S Bey, Jeffrey G Gragg, and Amy Brewer. Comparative measurements of earth and martian entry environments in the NASA

Langley HYMETS Facility. In *49th AIAA Aerospace Sciences Meeting*, volume 1014, pages 4–7, Orlando, FL, 2011.

[32] M Mahzari. *Inverse estimation methodology for the analysis of aeroheating and thermal protection system data*. PhD thesis, Georgia Institute of Technology, 2013.

[33] S Del Papa, L Suess, and B Shafer. The Development of a CO2 Test Capability in the NASA JSC Arc Jet for Mars Entry Simulation. In *8th International Planetary Probe Workshop*, Portsmouth, VA, 2011.

[34] J Baumgart, T Magin, P Rini, G Degrez, and O Chazot. Simulation of entry in the true martian atmosphere. In *Fifth European Symposium on Aerothermodynamics for Space Vehicles*, volume 563, page 593, Cologne, Germany, 2005.

[35] G Herdrich and T Marynowski. Mars and Venus entry simulation capabilities of IRS plasma wind tunnel PWK3. *Applied Physics Research*, 4(1):146, 2012.

[36] S White. Solar tower radiation testing of phenolic impregnated carbon ablator. *Journal of Spacecraft and Rockets*, 49(5):889–893, 2012.

[37] S Sepka, M Gasch, R A Beck, and S White. Testing of candidate rigid heatshield materials at lhmel for the entry, descent, and landing technology development project. *Adv Ceram Coat Mater Extrem Environ II*, 33(3):129–157, 2012.

[38] W Congdon. Thermostructural Testing of Scaled Ablative-Aeroshell Systems Using the Sandia Solar Tower Facility. In *40th AIAA Thermophysics Conference*, volume 3909, Seattle, WA, 2008.

[39] A F Gollnick Jr. Thermal effects on a transpiration cooled hemisphere. *Journal of the Aerospace Sciences*, 29(5):583–590, 1962.

[40] G E Kaattari. The effect of simulated ablation-gas injection on the shock layer of blunt bodies at mach numbers of 3 and 5. Technical Report NASA-TN-D-2954, NASA, 1965.

[41] R G Morgan. Radiation measurements in simulated ablation layers. Technical Report FA23860914144, AFOSR, 2010.

[42] E J Fahy, D Buttsworth, and R G Morgan. Scaled earth re-entry experiments in the x2 expansion tube. In *7th Asia-Pacific International Symposium on Aerospace Technology*, Cairns, Australia, 2015.

[43] PA Jacobs, TB Silvester, RG Morgan, MP Scott, RJ Gollan, and TJ McIntyre. Superorbital expansion tube operation: estimates of flow conditions via numerical simulation. In *43rd AIAA Aerospace Sciences Meeting*, pages 10–13, Reno, NV, 2005.

[44] E J Fahy, R J Gollan, D Buttsworth, P A Jacobs, and R G Morgan. Expansion tube and computational fluid dynamics studies of superorbital earth re-entry. In *46th AIAA Thermophysics Conference*, Washington D.C, USA, 2016.

[45] T N Eichmann. *Radiation Measurements in a Simulated Mars Atmosphere*. PhD thesis, The University of Queensland, 2012.

[46] H Porat. *Measurement of radiative heat transfer in simulated Titan and Mars atmospheres in expansion tubes*. PhD thesis, The University of Queensland, 2016.

[47] G de Crombrugghe, D Gildfind, F Zander, T J McIntyre, and R G Morgan. Design of Test Flows to Investigate Binary Scaling in High Enthalpy CO2 N2 Mixtures. In *19th Australasian Fluid Mechanics Conference*, Melbourne, Australia, 2014.

[48] C M James, D E Gildfind, S W Lewis, and R G Morgan. Implementation of a state-to-state analytical framework for the calculation of expansion tube flow properties. 2017. *submitted to Shock Waves*.

[49] D E Gildfind, R G Morgan, and P A Jacobs. Expansion Tubes in Australia. In *Experimental Methods of Shock Wave Research*, pages 399–431. Springer, 2016.

[50] U A Sheikh, R G Morgan, and T J McIntyre. Vacuum ultraviolet spectral measurements for superorbital earth entry in x2 expansion tube. *AIAA Journal*, 53(12):3589–3602, 2015.

[51] D. R Buttsworth, M. D'Souza, D. Potter, T. Eichmann, N. Mudford, M. McGilvray, T. J McIntyre, P. Jacobs, and R. Morgan. Expansion tunnel radiation experiments to support hayabusa re-entry observations. In *48th AIAA Aerospace Sciences Meeting*, pages 2010–634, 2010.

[52] R G Morgan, A Sasoh, B Littleton, A Bishop, T J McIntyre, J Hoogland, and A Gardner. Simulation of ablative mixing layers in superorbital flows. In *22nd International Symposium on Shock Waves*, volume 22, pages 727–732. University of Southampton, 1999.

[53] Jason Hoogland. *Simulation of ablation in a superorbital expansion tube*. PhD thesis, The University of Queensland, 2012.

[54] S W Lewis. Hypervelocity Shock-Layer Emission Spectroscopy with High Temperature Ablating Models. Private communication, 2017.

[55] J Mora-Monteros, P Leyland, G Hannema, U Sheikh, E J Fahy, R G Morgan, and T J McIntyre. Analysis and Rebuilding of Experiments on a heated graphite model in X2 Expansion Tube. In *46th AIAA Thermophysics Conference*, Washington, D.C, 2016.

[56] M K Lockwood, B R Starr, J W Paulson Jr, D A Kontinos, Y K Chen, B Laub, J Olejniczak, M J Wright, N Takashima, and C G Justus. Systems Analysis for a Venus Aerocapture Mission. Technical Report TM-2006-214291, NASA, 2006.

[57] F S Milos. Galileo probe heat shield ablation experiment. *Journal of Spacecraft and Rockets*, 34(6):705–713, 1997.

[58] G A Bird. *Molecular gas dynamics and the direct simulation of gas flows*. Clarendon, 1994.

[59] M Panesi. *Physical models for nonequilibrium plasma flow simulations at high speed re-entry conditions*. PhD thesis, von Kàrmàn Institute for Fluid Dynamics, 2009.

[60] J O Hirschfelder, C F Curtiss, R B Bird, and M G Mayer. *Molecular theory of gases and liquids*, volume 26. Wiley New York, 1954.

[61] G E Palmer and M J Wright. Comparison of methods to compute high-temperature gas viscosity. *Journal of Thermophysics and Heat Transfer*, 17(2):232–239, 2003.

[62] A Laricchiuta, D Bruno, M Capitelli, C Catalfamo, R Celiberto, G Colonna, P Diomede, D Giordano, C Gorse, S Longo, et al. High temperature Mars atmosphere. Part I: transport cross sections. *The European Physical Journal D*, 54(3):607–612, 2009.

[63] M J Wright, H H Hwang, and D W Schwenke. Recommended collision integrals for transport property computations part II: Mars and Venus entries. *AIAA journal*, 45(1):281–288, 2007.

[64] C Park, R L Jaffe, and H Partridge. Chemical-kinetic parameters of hyperbolic earth entry. *Journal of Thermophysics and Heat Transfer*, 15(1):76–90, 2001.

[65] Y-K Chen and F S Milos. Ablation and thermal response program for spacecraft heatshield analysis. *Journal of Spacecraft and Rockets*, 36(3):475–483, 1999.

[66] S Muppidi, M Barnhardt, and N N Mansour. Toward ablative material response coupling in dplr. In *11th AIAA/ASME Joint Thermophysics and Heat Transfer Conference*, page 2120, Atlanta, GA, 2014.

[67] S V Zhluktov and T Abe. Viscous shock-layer simulation of airflow past ablating blunt body with carbon surface. *Journal of Thermophysics and Heat Transfer*, 13(1):50–59, 1999.

[68] P A Gnoffo. Planetary-entry gas dynamics. *Annual Review of Fluid Mechanics*, 31(1):459–494, 1999.

[69] D Potter. *Modelling of radiating shock layers for atmospheric entry at Earth and Mars*. PhD thesis, The University of Queensland, 2011.

[70] A Smith, J Beck, M Fertig, H Liebhart, and L Marraffa. Plasma radiation database parade v3. 1. *ESA Contract Rept. TR28/96 No*, 8, 2011.

[71] A M Brandis, C O Johnston, B A Cruden, D Prabhu, and D Bose. Validation of high speed earth atmospheric entry radiative heating from 9.5 to 15.5 km/s. *AIAA paper*, 2012.

[72] Y Liu, D Prabhu, K A Trumble, D Saunders, and P Jenniskens. Radiation modeling for the reentry of the stardust sample return capsule. *Journal of Spacecraft and Rockets*, 47(5):741–752, 2010.

[73] M Winter, B Butler, Z Diao, F Panerai, A Martin, S C C Bailey, P M Danehy, and S Splinter. Characterization of ablation product radiation signatures of pica and fiberform. In *46th AIAA Thermophysics Conference*, page 3233, Washington D.C, 2016.

[74] R J Gollan and P A Jacobs. About the formulation, verification and validation of the hypersonic flow solver eilmer. *International Journal for Numerical Methods in Fluids*, 73(1):19–57, 2013.

[75] F S Milos and Y K Chen. Ablation and thermal response property model validation for phenolic impregnated carbon ablator. *Journal of Spacecraft and Rockets*, 47(5):786–805, 2010.

[76] D M Driver, J E Carballo, R Beck, D Prabhu, J A Santos, A Cassell, K Skokova, C Tang, H H Hwang, E Slimko, et al. Arcjet testing in shear environment for mars science laboratory thermal protection system. *Journal of Spacecraft and Rockets*, 51(4):1151–1166, 2014.

[77] W Zhang, A Lani, and M Panesi. Analysis of non-equilibrium phenomena in inductively coupled plasma generators. *Physics of Plasmas (1994-present)*, 23(7):073512, 2016.

[78] J A Fay and F R Riddell. Theory of stagnation point heat transfer in dissociated air. *Journal of the Aerospace Sciences*, 25(2):73–85, 1958.

[79] F Sanson, N Villedieu, F Panerai, O Chazot, P M Congedo, and T E Magin. Quantification of uncertainty on the catalytic property of reusable thermal protection materials from high enthalpy experiments. *Experimental Thermal and Fluid Science*, 2016.

[80] T Gökçen, Y K Chen, K A Skokova, and F S Milos. Computational analysis of arc-jet wedge tests including ablation and shape change. *AIAA Paper*, 4644:2010, 2010.

[81] R S C Davuluri, H Zhang, and A Martin. Numerical study of spallation phenomenon in an arc-jet environment. *Journal of Thermophysics and Heat Transfer*, 30(1):32–41, 2015.

[82] V Wheatley, D Bond, D Pullin, and R Samtaney. Two-fluid plasma richtmyer-meshkov instability. *Bulletin of the American Physical Society*, 61, 2016.

[83] G Palmer, D Prabhu, A Brandis, and T J McIntyre. Numerical simulation of radiation measurements taken in the X2 facility for Mars and Titan gas mixtures. In *42nd AIAA Thermophysics Conference*, volume 3768, page 12, Honolulu, HI, 2011.

[84] C R Alba, R B Greendyke, S W Lewis, R G Morgan, and T J McIntyre. Numerical modeling of earth reentry flow with surface ablation. *Journal of Spacecraft and Rockets*, 53(1):84–97, 2015.

[85] T Suzuki, K Fujita, and T Sakai. Graphite Nitridation in Lower Surface Temperature Regime. *Journal of Thermophysics and Heat Transfer*, 24(1):212–215, 2010.

[86] B Kraetzig, D R Buttsworth, F Zander, and S Löhle. Temperature and Heat Flux Measurement on Hot Models in Short-Duration Facilities. *Journal of Thermophysics and Heat Transfer*, 29(1):37–46, 2014.

[87] K Sutton and R A Graves Jr. A general stagnation-point convective heating equation for arbitrary gas mixtures. Technical Report NASA-TR-R-376, NASA, 1971.

[88] J Canny. A computational approach to edge detection. *IEEE Transactions on pattern analysis and machine intelligence*, PAMI-8(6):679–698, 1986.

[89] C Jacobs. *Radiation in low density hypervelocity flows*. PhD thesis, The University of Queensland, 2011.

[90] S W Lewis, R G Morgan, and T J Mcintyre. Shock Layer Radiation Measurements with Sublimating Graphite Models in an Expansion Tunnel. In *Radiation and High Temperature Gases Workshop*, St. Andrews, Scotland, 2014.

[91] A Kramida, Yu Ralchenko, J Reader, and and NIST ASD Team. NIST Atomic Spectra Database (ver. 5.3), [Online]. Available: http://physics.nist.gov/asd. National Institute of Standards and Technology, Gaithersburg, MD., 2015. Accessed: 2016-12-20.

[92] C O Laux, T G Spence, C H Kruger, and R N Zare. Optical diagnostics of atmospheric pressure air plasmas. *Plasma Sources Science and Technology*, 12(2):125, 2003.

[93] J W Slater. Examining spatial (grid) convergence. *Public tutorial on CFD verification and validation, NASA Glenn Research Centre, MS*, 86, 2006.

[94] P J Roache, K N Ghia, and F M White. Editorial policy statement on the control of numerical accuracy. *Journal of Fluids Engineering*, 108(1):2–2, 1986.

[95] C Park. Assessment of two-temperature kinetic model for ionizing air. *Journal of Thermophysics and Heat Transfer*, 3(3):233–244, 1989.

[96] C Park, J T Howe, R L Jaffe, and G V Candler. Review of chemical-kinetic problems of future NASA missions. II-Mars entries. *Journal of Thermophysics and Heat transfer*, 8(1):9–23, 1994.

[97] C Park and H K Ahn. Stagnation-point heat transfer rates for pioneer-venus probes. *Journal of thermophysics and heat transfer*, 13(1):33–41, 1999.

[98] R C Millikan and D R White. Systematics of vibrational relaxation. *The Journal of chemical physics*, 39(12):3209–3213, 1963.

[99] C Park. Review of chemical-kinetic problems of future nasa missions. i-earth entries. *Journal of Thermophysics and Heat transfer*, 7(3):385–398, 1993.

[100] L Landau and E Teller. Theory of sound dispersion. *Physikalische zeitschrift der Sowjetunion*, 10(34):34–43, 1936.

[101] J P Appleton and K N C Bray. The conservation equations for a non-equilibrium plasma. *Journal of Fluid Mechanics*, 20(04):659–672, 1964.

[102] C O Johnston and A M Brandis. Modeling of nonequilibrium CO Fourth-Positive and CN Violet emission in CO_2–N_2 gases. *Journal of Quantitative Spectroscopy and Radiative Transfer*, 149:303–317, 2014.

[103] R N Gupta and J M Yos. A review of reaction rates and thermodynamic and transport properties for an 11-species air model for chemical and thermal nonequilibrium calculations to 30000 K. Technical Report TM-101528, NASA, 1990.

[104] K Suzuki, K Fujita, and T Abe. Chemical Nonequilibrium Viscous Shock-Layer Analysis over Ablating Surface of Superorbital Re-Entry Capsule. *The Institute of Space and Astronautical Science Report*, 2003.

[105] F G Blottner. Prediction of electron density in the boundary layer on entry vehicles with ablation. Technical Report SP-252, NASA, 1970.

[106] C H Lewis and D J Song. Hypersonic-finite rate chemically reacting viscous flows over an ablating carbon surface. *Journal of Spacecraft and Rockets*, 23(1):47–54, 1986.

[107] C K Westbrook, W J Pitz, and P A Urtiew. Chemical kinetics of propane oxidation in gaseous detonations. *Progress in Aeronautics and Astronautics*, 94, 1984.

[108] J Heicklen. Gas-phase chemistry of re-entry. *AIAA Journal*, 5(1):4–15, 1967.

[109] M L Da Silva, V Guerra, and J Loureiro. Two-temperature models for nitrogen dissociation. *Chemical Physics*, 342(1):275–287, 2007.

[110] C E Treanor and P V Marrone. Effect of dissociation on the rate of vibrational relaxation. *Physics of Fluids (1958-1988)*, 5(9):1022–1026, 1962.

[111] C Park. The limits of two-temperature model kinetic model in air. In *48th AIAA Aerospace Sciences Meeting*, volume 911, Orlando, FL, 2010.

[112] R Savajano. *Modelling and validation of planetary (re-)entry phenomena*. Phd thesis, Ecole Polytechnique Fédérale de Lausanne, 2014.

[113] J Mora-Monteros. Ablation-radiation coupling in hypersonic re-entries. Master's thesis, Ecole Polytechnique Fédérale de Lausanne, 2014.

[114] F J Krieger. *The viscosity of polar gases*. Rand Corporation, 1951.

[115] J G Kim, O J Kwon, and C Park. A high temperature elastic collision model for dsmc based on collision integrals. *AIAA paper*, 3803:2006, 2006.

[116] R A Svehla. Estimated viscosities and thermal conductivities of gases at high temperatures. Technical Report NASA-TR-R-132, NASA, 1962.

[117] R J Kee, F M Rupley, J A Miller, M E Coltrin, J F Grcar, and E Meeks. Chemkin Collection. Technical report, Reaction Design Inc., San Diego, 2000.

[118] M J Wright, D Bose, G E Palmer, and E Levin. Recommended Collision Integrals for Transport Property Computations Part 1: Air Species. *AIAA Journal*, 43(12):2558–2564, 2005.

[119] J B Scoggins and T Magin. Development of MUTATION++: MUlticomponent Thermodynamics And Transport properties for Ionized gases library in C++. In *11th AIAA/ASME joint thermophysics and heat transfer conference*, volume 2966, Atlanta, GA, 2014.

[120] A Bellemans and T Magin. Calculation of collision integrals for ablation species. In *8th European Symposium on Aerothermodynamics for Space Vehicles*, 2015.

[121] B McBride and S Gordon. NASA-Glenn Chemical Equilibrium Program 17192, 2000.

[122] J D Ramshaw and C H Chang. Ambipolar diffusion in two-temperature multicomponent plasmas. *Plasma chemistry and plasma processing*, 13(3):489–498, 1993.

[123] G V Candler. Nonequilibrium processes in hypervelocity flows: an analysis of carbon ablation models. In *50th AIAA Aerospace Sciences Meeting*, pages 2012–0724, 2012.

[124] R W MacCormack. The Carbuncle CFD Problem. In *49th AIAA Aerospace Sciences Meeting*, Orlando, FL, 2011.

[125] C O Johnston. *Nonequilibrium shock-layer radiative heating for Earth and Titan entry*. PhD thesis, Virginia Tech, 2006.

[126] A Thorne, U Litzén, and S Johansson. *Spectrophysics: principles and applications*. Springer Science & Business Media, 1999.

[127] B A Cruden. Absolute radiation measurements in earth and mars entry conditions. Technical Report STO-AVT-218-VKI, NATO, 2014.

[128] C O Johnston. Improved exponential integral approximation for tangent-slab radiation transport. *Journal of Thermophysics and Heat Transfer*, 24(3):659–661, 2010.

[129] G Palmer, G Allen, C Tang, and J Brown. Coupled fluids-radiation analysis of a high-mass mars entry vehicle. *AIAA Paper*, 3495:2011, 2011.

[130] N Joiner, J Beck, M Capitelli, M Fertig, G Herdrich, A Laricchiuta, H Liebhart, M Lino da Silva, L Marraffa, P Reynier, et al. Validation of aerothermal chemistry models for re-entry applications: Theoretical and computational synthesis. In *8th European Symposium on Aerothermodynamics for Space Vehicles*, Lisbon, Portugal, 2015. European Space Agency.

[131] P Boubert and C Rond. Nonequilibrium radiation in shocked martian mixtures. *Journal of Thermophysics and Heat Transfer*, 24(1):40–49, 2010.

[132] B A Cruden, R Martinez, J H Grinstead, and J Olejniczak. Simultaneous vacuum ultraviolet through near IR absolute radiation measurement with spatiotemporal resolution in an electric arc shock tube. In *41st AIAA Thermophysics Conference*, page 4240, San Antonio, TX, 2009.

[133] K Kruszelnicki. Space oddities. `https://www.newscientist.com/article/mg14619738-300-space-oddities/`, 1995. Accessed: 2016-11-21.

[134] T R Munson and R J Spindler. Transient Thermal Behavior of Decomposing Materials. Part 1. General Theory and Application to Convective Heating. Technical Report RAD-TR-61-10, AVCO Corp. Wilmington MA. Research and Advanced Development Division., 1961.

[135] R M Kendall, E P Bartlett, R A Rindall, and C B Moyer. *An analysis of the coupled chemically reacting boundary layer and charring ablator*. National Aeronautics and Space Administration (NASA), 1968.

[136] H E Goldstein. Kinetics of nylon and phenolic pyrolysis. Technical report, Lockheed Missiles and Space Co. Inc. Sunnyvale CA., 1965.

[137] Anon. User's Manual, Aerotherm Charring Material Thermal response and Ablation Program (CMA87). Technical Report UM-87-11/ATD, Acurex Corporation, Aerotherm Division, Mountain View, CA., 1987.

[138] B Laub. Ablator modeling: why not much has changed over the past 45 plus years. 4th AF/SNL/NASA Ablation Workshop, 2011.

[139] M A Covington, J M Heinemann, H E Goldstein, Y K Chen, I Terrazas-Salinas, J A Balboni, J Olejniczak, and E R Martinez. Performance of a low density ablative heat shield material. *Journal of Spacecraft and Rockets*, 45(2):237–247, 2008.

[140] G F Sykes Jr. Decomposition Characteristics of a Char-Forming Phenolic Polymer Used for Ablative Composites. Technical Report TN D-3810, NASA, 1967.

[141] G C April, R W Pike, and E G Del Valle. Modeling reacting gas flow in the char layer of an ablator. *AIAA Journal*, 9(6):1113–1119, 1971.

[142] J Lachaud, T E Magin, I Cozmuta, and N N Mansour. A Short Review of Ablative-Material Response Models and Simulation Tools. In *7th Aerothermodynamics Symposium*. European Space Agency, 2011.

[143] Y-K Chen and FS Milos. Two-dimensional implicit thermal response and ablation program for charring materials. *Journal of Spacecraft and Rockets*, 38(4):473–481, 2001.

[144] Y K Chen and Frank Milos. Three-Dimensional Ablation and Thermal Response Simulation System. In *38th AIAA Thermophysics Conference*, Fluid Dynamics and Co-located Conferences. American Institute of Aeronautics and Astronautics, jun 2005.

[145] J A Dec, R D Braun, and B Lamb. Ablative thermal response analysis using the finite element method. *Journal of thermophysics and heat transfer*, 26(2):201–212, 2012.

[146] M E Ewing, T S Laker, and D T Walker. Numerical modeling of ablation heat transfer. *Journal of Thermophysics and Heat Transfer*, 27(4):615–632, 2013.

[147] R Fu, H Weng, J Wenk, and A Martin. Application of A New Thermal-Mechanical Coupling Solver for Ablation. In *46th AIAA Thermophysics Conference*, page 4432, Washington D.C, 2016.

[148] J C Ferguson, F Panerai, J Lachaud, A Martin, S C Bailey, and N N Mansour. Modeling the oxidation of low-density carbon fiber material based on micro-tomography. *Carbon*, 96:57–65, 2016.

[149] S C Lee and G R Cunnington. Theoretical models for radiative transfer in fibrous media. *Annual review of heat transfer*, 9(9), 1998.

[150] A Delmas, S Le Foll, and F André. Identification of radiative properties of fibrous insulation for high temperature applications. In *13ème Journéess d'études des Milieux Poreux*, 2016.

[151] S Haussener, P Coray, W Lipiński, P Wyss, A Steinfeld, et al. Tomography-based heat and mass transfer characterization of reticulate porous ceramics for high-temperature processing. *Journal of Heat Transfer*, 132(2):023305, 2010.

[152] S Le Foll, F André, A Delmas, J M Bouilly, and Y Aspa. Radiative transfer modelling inside thermal protection system using hybrid homogenization method for a backward Monte Carlo method coupled with Mie theory. *Journal of Physics: Conference Series*, 369(1):12–28, 2012.

[153] L A Dombrovsky and D Baillis. *Thermal radiation in disperse systems: an engineering approach*. Begell House New York, 2010.

[154] S C Lee. Effect of fiber orientation on thermal radiation in fibrous media. *International journal of heat and mass transfer*, 32(2):311–319, 1989.

[155] S C Lee, S White, and J A Grzesik. Effective radiative properties of fibrous composites containing spherical particles. *Journal of thermophysics and heat transfer*, 8(3):400–405, 1994.

[156] J Petrasch, P Wyss, and A Steinfeld. Tomography-based Monte Carlo determination of radiative properties of reticulate porous ceramics. *Journal of Quantitative Spectroscopy and Radiative Transfer*, 105(2):180–197, 2007.

[157] S Haussener, W Lipiński, P Wyss, A Steinfeld, et al. Tomography-based analysis of radiative transfer in reacting packed beds undergoing a solid-gas thermochemical transformation. *Journal of Heat Transfer*, 132(6):061201, 2010.

[158] S Haussener, M Gergely, M Schneebeli, and A Steinfeld. Determination of the macroscopic optical properties of snow based on exact morphology and direct pore-level heat transfer modeling. *Journal of Geophysical Research: Earth Surface*, 117(F3), 2012.

[159] M Tancrez and J Taine. Direct identification of absorption and scattering coefficients and phase function of a porous medium by a monte carlo technique. *International Journal of Heat and Mass Transfer*, 47(2):373–383, 2004.

[160] M Chahlafi, F Bellet, F Fichot, and J Taine. Radiative transfer within non beerian porous media with semitransparent and opaque phases in non equilibrium: Application to reflooding of a nuclear reactor. *International Journal of Heat and Mass Transfer*, 55(13):3666–3676, 2012.

[161] V Leroy, B Goyeau, and J Taine. Coupled upscaling approaches for conduction, convection, and radiation in porous media: theoretical developments. *Transport in porous media*, 98(2):323–347, 2013.

[162] R Viskanta and M P Mengüç. Radiation heat transfer in combustion systems. *Progress in Energy and Combustion Science*, 13(2):97–160, 1987.

[163] T W Tong and C L Tien. Radiative heat transfer in fibrous insulations—Part I: analytical study. *Journal of Heat Transfer*, 105(1):70–75, 1983.

[164] R P Banas and G R Cunnington. Determination of effective thermal conductivity for the Space Shuttle Orbiter's Reusable Surface Insulation/RSI. In *1st AIAA/ASME Joint Thermophysics and Heat Transfer Conference*, Boston, MA, 1974.

[165] C Stark and J Fricke. Improved heat-transfer models for fibrous insulations. *International journal of heat and mass transfer*, 36(3):617–625, 1993.

[166] R Caps, H P Ebert, M C Arduini-Schuster, and J Fricke. Optimization of Inorganic and Organic Fibers for Maximal Thermal Radiation Extinction. *Thermal Conductivity*, 22:725–735, 1994.

[167] LA Dombrovsky. Quartz-fiber thermal insulation: infrared radiative properties and calculation of radiative-conductive heat transfer. *Journal of Heat Transfer*, 118(2):408–414, 1996.

[168] J R Howell, M P Mengüç, and R Siegel. *Thermal radiation heat transfer*. CRC press, 2010.

[169] Michael F Modest. *Radiative heat transfer*. Academic press, 2013.

[170] V A Petrov. Combined radiation and conduction heat transfer in high temperature fiber thermal insulation. *International Journal of Heat and Mass Transfer*, 40(9):2241–2247, 1997.

[171] M Kaviany. *Principles of heat transfer in porous media*. Springer Science & Business Media, 2012.

[172] S Penner. *Radiation and Reentry*. Elsevier, 2012.

[173] G Pinaud, JM Bouilly, J Barcena, S Florez, B Perez, W Fisher, V Leroy, D Bernard, T Massuti, G Herdrich, et al. HYDRA: Macroscopic modelling of hybrid ablative thermal protection system. In *5th International Conference on Porous Media and its Applications in Science and Engineering, ICPM5, Kona, HI*, 2014.

[174] L Daryabeigi, G R Cunnington, and J R Knutson. Combined heat transfer in high-porosity high-temperature fibrous insulation: Theory and experimental validation. *Journal of thermophysics and heat transfer*, 25(4):536–546, 2011.

[175] K Daryabeigi, G R Cunnington, and J R Knutson. Heat transfer modeling for rigid high-temperature fibrous insulation. *Journal of Thermophysics and Heat Transfer*, 27(3):414–421, 2013.

[176] A J van Eekelen and J Lachaud. Numerical validation of an effective radiation heat transfer model for fiber preforms. *Journal of Spacecraft and Rockets*, 48(3):534–537, 2011.

[177] N Nouri and A Martin. Three dimensional radiative heat transfer model for the evaluation of the anisotropic effective conductivity of fibrous materials. *International Journal of Heat and Mass Transfer*, 83:629–635, 2015.

[178] N Nouri, F Panerai, K A Tagavi, N N Mansour, and A Martin. Evaluation of the anisotropic radiative conductivity of a low-density carbon fiber material from realistic microscale imaging. *International Journal of Heat and Mass Transfer*, 95:535–539, 2016.

[179] G L Vignoles and A Ortona. Numerical study of effective heat conductivities of foams by coupled conduction and radiation. *International Journal of Thermal Sciences*, 109:270–278, 2016.

[180] Miguel AA Mendes, Valeria Skibina, Prabal Talukdar, Rhena Wulf, Ulrich Gross, Dimosthenis Trimis, and Subhashis Ray. Experimental validation of simplified conduction–radiation models for evaluation of effective thermal conductivity of open-cell metal foams at high temperatures. *International Journal of Heat and Mass Transfer*, 78:112–120, 2014.

[181] T J Horvath, D M Tomek, K T Berger, S C Splinter, J N Zalameda, P W Krasa, S Tack, R J Schwartz, D M Gibson, and A B Tietjen. The HYTHIRM project: flight thermography of the space shuttle during hypersonic reentry. *AIAA Paper*, 241, 2010.

[182] F M Cheatwood, D Bose, C D Karlgaard, C A Kuhl, J A Santos, and M J Wright. Mars science laboratory (MSL) entry, descent, and landing instrumentation (MEDLI): Complete flight data set. Technical Report TM-2014-218533, NASA, 2014.

[183] R N Ingoldby, F C Michel, T M Flaherty, M G Doryand, B Preston, K W Villyard, and R D Steele. Entry Data Analysis for Viking Landers 1 and 2 Final Report. Technical Report TM-3770218, Martin Marietta Corp., 1976.

[184] W C Pitts and R M Wakefield. Performance of entry heat shields on pioneer venus probes. *Journal of Geophysical Research: Space Physics*, 85(A13):8333–8337, 1980.

[185] F S Milos, Y K Chen, W M Congdon, and J M Thornton. Mars pathfinder entry temperature data, aerothermal heating, and heatshield material response. *Journal of Spacecraft and Rockets*, 36(3):380–391, 1999.

[186] M Mahzari, R D Braun, and T R White. Reconstruction of mars pathfinder aeroheating and heat shield response using inverse methods. *Journal of Spacecraft and Rockets*, 50(6):1171–1182, 2013.

[187] D Bose, T White, M Mahzari, and K Edquist. Reconstruction of aerothermal environment and heat shield response of mars science laboratory. *Journal of Spacecraft and Rockets*, 51(4):1174–1184, 2014.

[188] T R White, M Mahzari, D Bose, and J A Santos. Post-flight analysis of the mars science laboratory entry aerothermal environment and thermal protection system. In *44th AIAA Thermophysics Conference*, San Diego, CA, 2013.

[189] A D Omidy, F Panerai, I Cozmuta, A Martin, J R Lachaud, and N N Mansour. Code-to-Code Comparison, and Material Response Modeling of Stardust and MSL using PATO and FIAT. Technical Report CR-2015-218960, NASA, 2015.

[190] A D Omidy, F Panerai, J R Lachaud, N N Mansour, and A Martin. Effects of water phase change on the material response of low-density carbon-phenolic ablators. *Journal of Thermophysics and Heat Transfer*, pages 473–478, 2016.

[191] B A Cruden, A M Brandis, T R White, M Mahzari, and D Bose. Radiative heating during mars science laboratory entry: Simulation, ground test, and flight. *Journal of Thermophysics and Heat Transfer*, pages 1–9, 2016.

[192] J M Bouilly, F Bonnefond, L Dariol, P Jullien, and F Leleu. Ablative thermal protection systems for entry in Mars atmosphere. A presentation of materials solutions and testing capabilities. In *The 4th International Planetary Probe Workshop, Pasadena, CA*, 2006.

[193] H H Hwang, D Bose, T R White, H S Wright, M Schoenenberger, C A Kuhl, D Trombetta, J A Santos, T Oishi, C D Karlgaard, et al. Mars 2020 entry, descent and landing instrumentation 2 (medli2). In *46th AIAA Thermophysics Conference*, Washington, D.C, 2016.

[194] S Haussener, W Lipiński, J Petrasch, P Wyss, and A Steinfeld. Tomographic characterization of a semitransparent-particle packed bed and determination of its thermal radiative properties. *Journal of Heat Transfer*, 131(7):072701, 2009.

[195] N Banerji, P Leyland, and S. Haussener. Coupling internal radiation to material response of thermal protection systems. In *8th European Symposium on Aerothermodynamics for Space Vehicles*, 2015.

[196] M Stampanoni, A Groso, A Isenegger, G Mikuljan, Q Chen, A Bertrand, S Henein, R Betemps, U Frommherz, P Böhler, et al. Trends in synchrotron-based tomographic imaging: the sls experience. In *SPIE Optics+ Photonics*, pages 63180M–63180M. International Society for Optics and Photonics, 2006.

[197] J G Berryman and S C Blair. Use of digital image analysis to estimate fluid permeability of porous materials: Application of two-point correlation functions. *Journal of Applied Physics*, 60(6):1930–1938, 1986.

[198] H J Vogel. Morphological determination of pore connectivity as a function of pore size using serial sections. *European Journal of Soil Science*, 48(3):365–377, 1997.

[199] C Tien and BL Drolen. Thermal radiation in part1culate media with dependent and independent scattering. *Annual Review of Heat Transfer*, 1(1), 1987.

[200] S White. Radiation Testing of PICA at the Solar Power Tower. In *10th AIAA/ASME Joint Thermophysics and Heat Transfer Conference*, volume 28, Chicago, IL, 2010.

[201] N Puiroux, Marc Prat, and Michel Quintard. Non-equilibrium theories for macroscale heat transfer: ablative composite layer systems. *International Journal of Thermal Sciences*, 43(6):541–554, 2004.

[202] D Y S Perraudin and S Haussener. Numerical quantification of coupling effects for radiation-conduction heat transfer in participating macroporous

media: Investigation of a model geometry. *International Journal of Heat and Mass Transfer*, 2017.

[203] J Lachaud, A Martin, T van Eekelen, and I Cozmuta. Ablation Workshop Test Case. http://ablation2014.engineering.uky.edu/files/2014/02/AblationTestCase3_V2.0-bis.pdf, 2014. Accessed: 2017-3-4.

[204] F S Milos, Y K Chen, and T Gokcen. Nonequilibrium ablation of phenolic impregnated carbon ablator. *Journal of Spacecraft and Rockets*, 49(5):894–904, 2012.

[205] A Dufrene, M MacLean, and M Holden. High enthalpy studies of capsule heating in an expansion tunnel facility. In *43rd AIAA Thermophysics Conference*, page 2998, New Orleans, LA, 2012.

[206] Cellobond Resin J2027L. http://www.hexion.com/products/technicaldatasheet.aspx?id=30503. Accessed: 2017-4-20.

[207] Torayca T700S Data Sheet. http://www.toraycfa.com/pdfs/T700SDataSheet.pdf. Accessed: 2017-4-20.

[208] Block Resistance Wire. http://uk.rs-online.com/web/p/multicore-industrial-cable/7496354/. Accessed: 2017-4-20.

[209] Mersen CALCARB HD. https://www.mersen.com/uploads/tx_mersen/3-CALCARB-rigid-carbon-thermal-insulation-mersen_04.pdf. Accessed: 2017-4-20.

APPENDICES

A

PATO BOUNDARY CONDITION

The boundary condition for the MSL test case with radiative heating is provided via a text file, attached to the electronic version of this document. To my knowledge this attachment can unfortunately only be accessed via Adobe Acrobat and Okular (Linux) and not Preview/Skim (for Mac).

B

RADIATION CODE COMPARISON

The numerically generated spectra in the UV wavelength range, for a line of sight taken 0.1 mm from the model surface is presented in Figure B.1. Compared to the experimental spectra, given in Figure 3.9, it can be seen that NEQAIR produces the best match, while the other two codes used significantly overestimate spectral radiance. Obtaining the closest results to measured data is the logic used for presenting only the NEQAIR results in the thesis document.
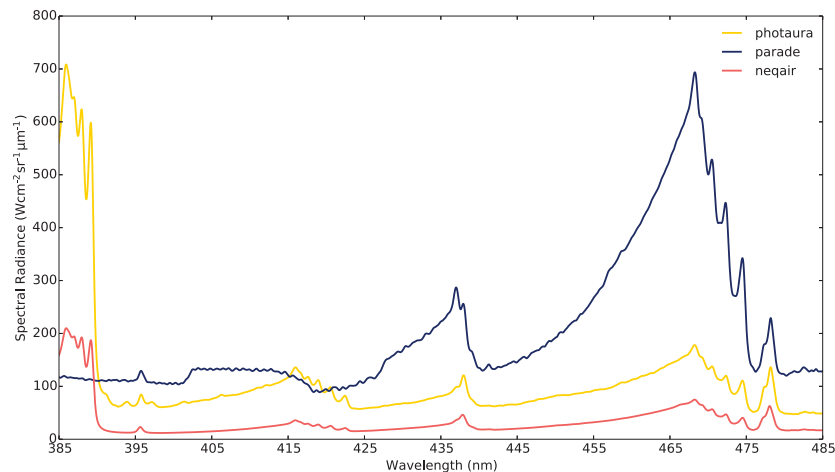
Figure B.1: Comparison of spectral radiances calculated by NEQAIR, Photaura and PARADE for the V1 condition in the UV wavelength range.

C

BULK MATERIALS

Table C.1: Summary of the bulk materials used to manufacture the phenolic aeroshells and materials investigated during the tomography campaign.

Material	Provider	Reference
Cellobond resin J2027L	Hexion	[206]
T700S carbon fibre	Torayca	[207]
Nichrome wire	RS Components	[208]
Graphite reinforced polymer composite (CALCARB)	Mersen	[209]
Carbon phenolic composite (ASTERM)	Airbus DS	[192]

D

TECHNICAL DRAWINGS

The schematics provide details for the manufacture of (i) steel aeroshell models, (ii) the mould used to create the phenolic models and (iii) the dimensions of the grooves and holes required in the phenolic models.

60

18.1
18

23.23

R 19.5
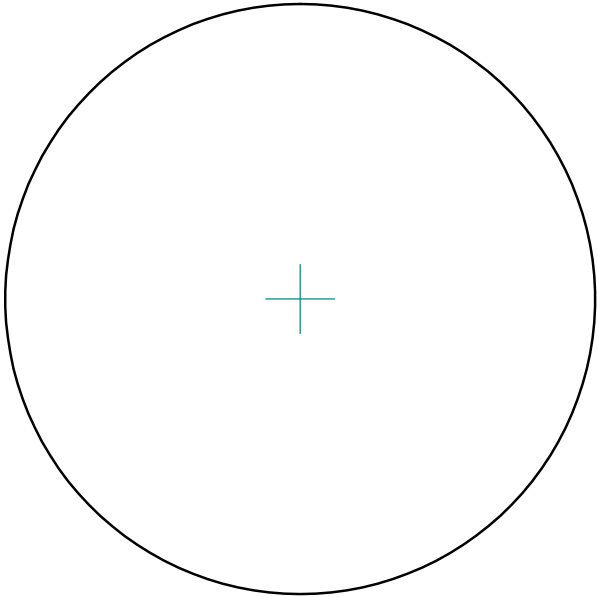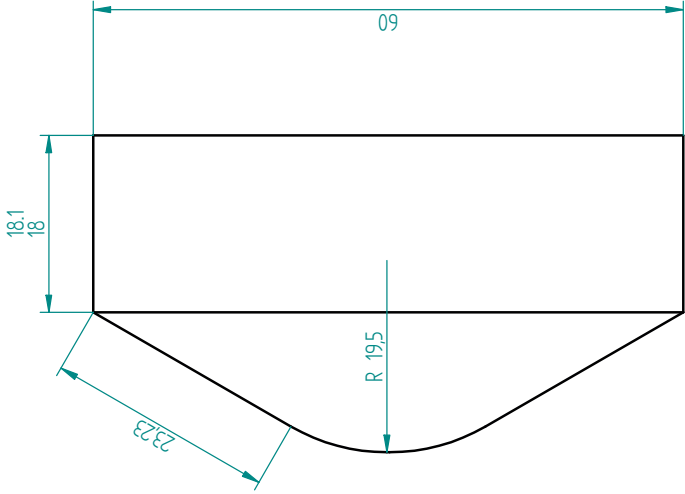
Notes :

- Cold wall sphere-cone (diameter 60mm, nose radius 19.5mm)

- 2x parts required

- Material – Low carbon steel

- Contact details: Nikhil Banerji,
office 50-C110, nikhil.banerji@uq.edu.au

39.2

1°   1°

20

14.2

5

30°

R 20

23.09

SECTION A-A

A

A

Ø 60

Ø 60.7

Ø 70

Notes :

- Sphere-cone (diameter 60mm, nose radius 20mm)

- 1x part required

- Material – Stainless Steel

- Contact details: Nikhil Banerji,
office 50-C110, nikhil.banerji@uq.edu.au

48

46.8

24

10

Ø5

Ø5

60

1°

1°

24

R 20

1

COLLISION INTEGRAL DATA SETS

Table A1: Reduced collision integral $\Omega^{(1,1)\star}$ as a function of temperature for ablative Earth, Mars and Venus entry.

Collisions	Temperature (K)					Collisions	Temperature (K)				
	2000	4000	8000	16000	32000		2000	4000	8000	16000	32000
C–C	0.5319	0.4040	0.3063	0.2319	0.1755	C–C$_2$	0.6075	0.4626	0.3516	0.2667	0.2020
C–C$_3$	0.6525	0.4973	0.3785	0.2875	0.2180	C–CO$_2$	0.6075	0.4626	0.3516	0.2667	0.2020
C–CO	0.5757	0.4379	0.3325	0.2520	0.1908	C–CN	0.5674	0.4315	0.3275	0.2482	0.1879
C–C$_2$H$_2$	0.6104	0.4649	0.3534	0.2681	0.2031	C–C$_2$H	0.6527	0.4975	0.3787	0.2876	0.2181
C–CH	0.5638	0.4287	0.3254	0.2465	0.1866	C–H	0.5392	0.4097	0.3107	0.2353	0.1781
C–H$_2$	0.5582	0.4244	0.3220	0.2440	0.1847	C–HCN	0.6547	0.4990	0.3798	0.2886	0.2188
C–HCO	0.6491	0.4948	0.3765	0.2860	0.2168	C–N$_2$	0.5654	0.4300	0.3263	0.2473	0.1872
C–N	0.5654	0.4300	0.3263	0.2473	0.1872	C–NO	0.5857	0.4457	0.3385	0.2566	0.1943
C–O	0.5819	0.4428	0.3362	0.2549	0.1930	C–O$_2$	0.5819	0.4428	0.3362	0.2549	0.1930
C$_2$–C$_2$	0.7316	0.6128	0.5172	0.4388	0.3741	C$_2$–C$_3$	0.7886	0.6583	0.5558	0.4722	0.4032
C$_2$–CO$_2$	0.7317	0.6128	0.5172	0.4389	0.3742	C$_2$–CO	0.6931	0.5809	0.4898	0.4151	0.3536
C$_2$–CN	0.6832	0.5726	0.4827	0.4090	0.3483	C$_2$–C$_2$H$_2$	0.7353	0.6158	0.5197	0.4410	0.3761
C$_2$–C$_2$H	0.7889	0.6586	0.5560	0.4724	0.4033	C$_2$–CH	0.6789	0.5690	0.4796	0.4063	0.3460
C$_2$–H	0.6157	0.4690	0.3565	0.2705	0.2050	C$_2$–H$_2$	0.6723	0.5634	0.4747	0.4021	0.3424

Collisions	Temperature (K)				
	2000	4000	8000	16000	32000
C_2–HCN	0.7915	0.6606	0.5576	0.4739	0.4046
C_2–N_2	0.6809	0.5706	0.4810	0.4075	0.3470
C_2–NO	0.7051	0.5909	0.4984	0.4226	0.3600
C_2–O_2	0.7006	0.5871	0.4952	0.4198	0.3576
C_3–CO_2	0.7886	0.6584	0.5558	0.4722	0.4032
C_3–CN	0.7345	0.6151	0.5192	0.4406	0.3756
C_3–C_2H	0.8616	0.7089	0.5972	0.5078	0.4342
C_3–H	0.6614	0.5040	0.3838	0.2916	0.2212
C_3–HCN	0.8663	0.7112	0.5990	0.5093	0.4356
C_3–N_2	0.7318	0.6130	0.5174	0.4390	0.3743
C_3–NO	0.7587	0.6347	0.5358	0.4550	0.3882
C_3–O_2	0.7537	0.6307	0.5324	0.4520	0.3856
CO_2–CO	0.6931	0.5809	0.4898	0.4151	0.3536
CO_2–C_2H_2	0.7353	0.6158	0.5198	0.4411	0.3761
CO_2–CH	0.6790	0.5690	0.4796	0.4063	0.3460
CO_2–H_2	0.6723	0.5634	0.4748	0.4021	0.3424
CO_2–HCO	0.7843	0.6550	0.5529	0.4698	0.4010
CO_2–N	0.6451	0.4916	0.3741	0.2841	0.2154
CO_2–O	0.6637	0.5059	0.3852	0.2927	0.2220
CO–CO	0.6570	0.5503	0.4635	0.3925	0.3340
CO–C_2H_2	0.6964	0.5837	0.4922	0.4172	0.3554

Collisions	Temperature (K)				
	2000	4000	8000	16000	32000
C_2–HCO	0.7842	0.6549	0.5529	0.4698	0.4010
C_2–N	0.6450	0.4916	0.3741	0.2841	0.2154
C_2–O	0.6637	0.5058	0.3852	0.2927	0.2220
C_3–C_3	0.8611	0.7086	0.5969	0.5076	0.4340
C_3–CO	0.7453	0.6239	0.5267	0.4471	0.3813
C_3–C_2H_2	0.7927	0.6616	0.5585	0.4746	0.4052
C_3–CH	0.7297	0.6112	0.5159	0.4377	0.3731
C_3–H_2	0.7224	0.6053	0.5107	0.4333	0.3693
C_3–HCO	0.8538	0.7049	0.5939	0.5050	0.4317
C_3–N	0.6933	0.5281	0.4024	0.3060	0.2323
C_3–O	0.7140	0.5434	0.4141	0.3152	0.2393
CO_2–CO_2	0.7317	0.6128	0.5172	0.4389	0.3742
CO_2–CN	0.6832	0.5726	0.4827	0.4090	0.3483
CO_2–C_2H	0.7889	0.6586	0.5560	0.4724	0.4034
CO_2–H	0.6157	0.4690	0.3566	0.2705	0.2050
CO_2–HCN	0.7915	0.6606	0.5577	0.4739	0.4046
CO_2–N_2	0.6809	0.5706	0.4810	0.4075	0.3470
CO_2–NO	0.7051	0.5909	0.4984	0.4226	0.3601
CO_2–O_2	0.7006	0.5871	0.4952	0.4198	0.3576
CO–CN	0.6476	0.5424	0.4567	0.3866	0.3290
CO–C_2H	0.7456	0.6241	0.5269	0.4472	0.3814

Collisions	Temperature (K)				
	2000	4000	8000	16000	32000
CO–CH	0.6435	0.5389	0.4537	0.3840	0.3268
CO–H$_2$	0.6373	0.5336	0.4491	0.3801	0.3234
CO–HCO	0.7415	0.6207	0.5239	0.4447	0.3792
CO–N	0.6114	0.4657	0.3540	0.2686	0.2035
CO–O	0.6291	0.4794	0.3646	0.2767	0.2097
CN–CN	0.6378	0.5338	0.4495	0.3805	0.3239
CN–C$_2$H	0.7347	0.6153	0.5194	0.4407	0.3758
CN–H	0.5752	0.4376	0.3322	0.2518	0.1906
CN–HCN	0.7408	0.6171	0.5203	0.4416	0.3766
CN–N$_2$	0.6363	0.5327	0.4484	0.3794	0.3228
CN–NO	0.6588	0.5519	0.4649	0.3936	0.3350
CN–O$_2$	0.6547	0.5484	0.4619	0.3910	0.3328
C$_2$H$_2$–C$_2$H	0.7930	0.6618	0.5587	0.4747	0.4054
C$_2$H$_2$–H	0.6187	0.4713	0.3583	0.2719	0.2060
C$_2$H$_2$–HCN	0.7956	0.6639	0.5604	0.4762	0.4067
C$_2$H$_2$–N$_2$	0.6842	0.5734	0.4834	0.4096	0.3488
C$_2$H$_2$–NO	0.7085	0.5937	0.5009	0.4247	0.3619
C$_2$H$_2$–O$_2$	0.7040	0.5900	0.4977	0.4219	0.3595
C$_2$H–CH	0.7300	0.6115	0.5161	0.4378	0.3733
C$_2$H–H$_2$	0.7227	0.6055	0.5109	0.4334	0.3694
C$_2$H–HCO	0.8543	0.7052	0.5941	0.5052	0.4319

Collisions	Temperature (K)				
	2000	4000	8000	16000	32000
CO–H	0.5835	0.4440	0.3372	0.2556	0.1936
CO–HCN	0.7483	0.6260	0.5285	0.4486	0.3826
CO–N$_2$	0.6454	0.5405	0.4551	0.3852	0.3278
CO–NO	0.6683	0.5599	0.4718	0.3996	0.3402
CO–O$_2$	0.6640	0.5564	0.4687	0.3969	0.3379
CN–C$_2$H$_2$	0.6866	0.5754	0.4851	0.4111	0.3501
CN–CH	0.6338	0.5306	0.4467	0.3781	0.3217
CN–H$_2$	0.6283	0.5259	0.4425	0.3744	0.3185
CN–HCO	0.7319	0.6118	0.5161	0.4380	0.3734
CN–N	0.6028	0.4590	0.3488	0.2645	0.2004
CN–O	0.6202	0.4725	0.3593	0.2726	0.2066
C$_2$H$_2$–C$_2$H$_2$	0.7389	0.6188	0.5223	0.4432	0.3780
C$_2$H$_2$–CH	0.6822	0.5718	0.4820	0.4084	0.3478
C$_2$H$_2$–H$_2$	0.6756	0.5661	0.4771	0.4042	0.3441
C$_2$H$_2$–HCO	0.7883	0.6581	0.5556	0.4721	0.4031
C$_2$H$_2$–N	0.6481	0.4940	0.3760	0.2855	0.2165
C$_2$H$_2$–O	0.6669	0.5083	0.3871	0.2942	0.2231
C$_2$H–C$_2$H	0.8621	0.7091	0.5974	0.5080	0.4344
C$_2$H–H	0.6616	0.5042	0.3839	0.2917	0.2212
C$_2$H–HCN	0.8668	0.7114	0.5992	0.5095	0.4357
C$_2$H–N$_2$	0.7321	0.6132	0.5175	0.4391	0.3744

Collisions	Temperature (K)				
	2000	4000	8000	16000	32000
C$_2$H–N	0.6936	0.5283	0.4025	0.3062	0.2324
C$_2$H–O	0.7143	0.5435	0.4143	0.3153	0.2394
CH–CH	0.6299	0.5273	0.4438	0.3756	0.3196
CH–H$_2$	0.6243	0.5225	0.4396	0.3719	0.3164
CH–HCO	0.7267	0.6079	0.5129	0.4352	0.3710
CH–N	0.5989	0.4560	0.3465	0.2628	0.1990
CH–O	0.6163	0.4695	0.3569	0.2708	0.2052
H–H	0.5467	0.4155	0.3151	0.2387	0.1807
H–HCN	0.6636	0.5058	0.3851	0.2926	0.2220
H–N$_2$	0.5732	0.4360	0.3310	0.2509	0.1899
H–NO	0.5937	0.4519	0.3433	0.2603	0.1971
H–O$_2$	0.5899	0.4489	0.3410	0.2586	0.1958
H$_2$–HCN	0.7249	0.6073	0.5125	0.4348	0.3706
H$_2$–N$_2$	0.6261	0.5240	0.4409	0.3730	0.3173
H$_2$–NO	0.6483	0.5430	0.4572	0.3870	0.3293
H$_2$–O$_2$	0.6442	0.5395	0.4542	0.3844	0.3271
HCN–HCO	0.8693	0.7098	0.5960	0.5065	0.4330
HCN–N	0.6958	0.5299	0.4038	0.3071	0.2331
HCN–O	0.7166	0.5452	0.4155	0.3163	0.2402
HCO–HCO	0.8517	0.7020	0.5908	0.5022	0.4294
HCO–N	0.6897	0.5254	0.4003	0.3044	0.2310

Collisions	Temperature (K)				
	2000	4000	8000	16000	32000
C$_2$H–NO	0.7590	0.6349	0.5360	0.4551	0.3883
C$_2$H–O$_2$	0.7540	0.6309	0.5326	0.4522	0.3857
CH–H	0.5716	0.4347	0.3300	0.2501	0.1894
CH–HCN	0.7347	0.6131	0.5171	0.4388	0.3742
CH–N$_2$	0.6322	0.5293	0.4455	0.3769	0.3207
CH–NO	0.6547	0.5484	0.4619	0.3910	0.3328
CH–O$_2$	0.6505	0.5449	0.4589	0.3884	0.3306
H–H$_2$	0.5659	0.4303	0.3266	0.2475	0.1874
H–HCO	0.6579	0.5015	0.3818	0.2900	0.2200
H–N	0.5732	0.4360	0.3310	0.2509	0.1899
H–O	0.5899	0.4489	0.3410	0.2586	0.1958
H$_2$–H$_2$	0.6181	0.5172	0.4351	0.3680	0.3130
H$_2$–HCO	0.7187	0.6021	0.5081	0.4309	0.3673
H$_2$–N	0.5931	0.4515	0.3430	0.2601	0.1970
H$_2$–O	0.6103	0.4648	0.3533	0.2680	0.2030
HCN–HCN	0.8985	0.7199	0.6016	0.5106	0.4366
HCN–N$_2$	0.7344	0.6151	0.5191	0.4405	0.3756
HCN–NO	0.7617	0.6368	0.5376	0.4565	0.3895
HCN–O$_2$	0.7564	0.6328	0.5343	0.4536	0.3572
HCO–N$_2$	0.7280	0.6098	0.5147	0.4366	0.3722
HCO–NO	0.7547	0.6314	0.5331	0.4526	0.3861

Collisions	Temperature (K)				
	2000	4000	8000	16000	32000
HCO–O	0.7102	0.5406	0.4120	0.3135	0.2381
N$_2$–N$_2$	0.6340	0.5308	0.4468	0.3781	0.3216
N$_2$–NO	0.6565	0.5500	0.4632	0.3922	0.3338
N$_2$–O$_2$	0.6524	0.5465	0.4602	0.3896	0.3316
N–NO	0.6220	0.4739	0.3603	0.2734	0.2072
N–O	0.6181	0.4708	0.3580	0.2716	0.2058
N–O$_2$	0.6399	0.4877	0.3711	0.2817	0.2136
O–O	0.6359	0.4846	0.3686	0.2799	0.2121
O$_2$–O$_2$	0.6712	0.5624	0.4740	0.4014	0.3418

Collisions	Temperature (K)				
	2000	4000	8000	16000	32000
HCO–O$_2$	0.7497	0.6274	0.5297	0.4496	0.3835
N$_2$–N	0.6007	0.4574	0.3475	0.2636	0.1996
N$_2$–O	0.6181	0.4708	0.3580	0.2716	0.2058
N–N	0.6007	0.4574	0.3475	0.2636	0.1996
N–O	0.6181	0.4708	0.3580	0.2716	0.2058
NO–NO	0.6798	0.5697	0.4802	0.4068	0.3464
NO–O$_2$	0.6755	0.5661	0.4771	0.4041	0.3441
O–O$_2$	0.6359	0.4846	0.3686	0.2799	0.2121

Table A2: Reduced collision integral $\Omega^{(2,2)\star}$ as a function of temperature for ablative Earth, Mars and Venus entry.

Collisions	Temperature (K)				
	2000	4000	8000	16000	32000
C–C	0.6400	0.4917	0.3769	0.2885	0.2208
C–C$_3$	0.7621	0.5902	0.4551	0.3497	0.2681
C–CO	0.6857	0.5283	0.4056	0.3108	0.2379
C–C$_2$H$_2$	0.7209	0.5567	0.4282	0.3285	0.2516
C–CH	0.6735	0.5184	0.3979	0.3048	0.2332
C–H$_2$	0.6677	0.5138	0.3942	0.3019	0.2310

Collisions	Temperature (K)				
	2000	4000	8000	16000	32000
C–C$_2$	0.7180	0.5543	0.4264	0.3270	0.2504
C–CO$_2$	0.7180	0.5544	0.4264	0.3270	0.2504
C–CN	0.6773	0.5215	0.4002	0.3066	0.2347
C–C$_2$H	0.7624	0.5903	0.4553	0.3499	0.2682
C–H	0.6478	0.4979	0.3817	0.2923	0.2237
C–HCN	0.7643	0.5919	0.4565	0.3508	0.2690

Collisions	Temperature (K)				
	2000	4000	8000	16000	32000
C–HCO	0.7589	0.5876	0.4530	0.3481	0.2668
C–N	0.6752	0.5198	0.3989	0.3056	0.2339
C–O	0.6922	0.5334	0.4097	0.3140	0.2404
C_2–C_2	0.8449	0.7205	0.6171	0.5301	0.4571
C_2–CO_2	0.8450	0.7205	0.6171	0.5301	0.4571
C_2–CN	0.7992	0.6803	0.5809	0.4979	0.4287
C_2–C_2H	0.8993	0.7645	0.6564	0.5656	0.4887
C_2–H	0.7262	0.5610	0.4317	0.3312	0.2537
C_2–HCN	0.9019	0.7664	0.6581	0.5671	0.4901
C_2–N_2	0.7969	0.6782	0.5791	0.4963	0.4272
C_2–NO	0.8200	0.6988	0.5975	0.5126	0.4416
C_2–O_2	0.8158	0.6950	0.5941	0.5096	0.4390
C_3–CO_2	0.8990	0.7643	0.6562	0.5654	0.4886
C_3–CN	0.8476	0.7228	0.6191	0.5319	0.4586
C_3–C_2H	0.9486	0.8117	0.6967	0.6020	0.5216
C_3–H	0.7706	0.5970	0.4606	0.3541	0.2715
C_3–HCN	0.9494	0.8139	0.6984	0.6036	0.5231
C_3–N_2	0.8451	0.7207	0.6172	0.5302	0.4572
C_3–NO	0.8703	0.7418	0.6362	0.5473	0.4723
C_3–O_2	0.8655	0.7379	0.6327	0.5441	0.4695
CO_2–CO	0.8086	0.6887	0.5885	0.5046	0.4345

Collisions	Temperature (K)				
	2000	4000	8000	16000	32000
C–N_2	0.6752	0.5198	0.3989	0.3056	0.2339
C–NO	0.6960	0.5365	0.4122	0.3159	0.2418
C–O_2	0.6922	0.5334	0.4097	0.3140	0.2404
C_2–C_3	0.8990	0.7643	0.6562	0.5654	0.4885
C_2–CO	0.8086	0.6887	0.5885	0.5046	0.4345
C_2–C_2H_2	0.8483	0.7234	0.6197	0.5325	0.4591
C_2–CH	0.7950	0.6766	0.5776	0.4950	0.4261
C_2–H_2	0.7886	0.6708	0.5725	0.4904	0.4221
C_2–HCO	0.8946	0.7611	0.6534	0.5628	0.4862
C_2–N	0.7550	0.5843	0.4504	0.3460	0.2652
C_2–O	0.7728	0.5988	0.4621	0.3553	0.2725
C_3–C_3	0.9485	0.8115	0.6965	0.6018	0.5215
C_3–CO	0.8577	0.7314	0.6268	0.5389	0.4649
C_3–C_2H_2	0.9031	0.7673	0.6589	0.5678	0.4907
C_3–CH	0.8432	0.7190	0.6157	0.5289	0.4560
C_3–H_2	0.8363	0.7131	0.6104	0.5241	0.4518
C_3–HCO	0.9468	0.8078	0.6935	0.5992	0.5190
C_3–N	0.8007	0.6209	0.4801	0.3697	0.2838
C_3–O	0.8200	0.6358	0.4921	0.3794	0.2914
CO_2–CO_2	0.8450	0.7206	0.6171	0.5301	0.4571
CO_2–CN	0.7992	0.6803	0.5810	0.4979	0.4287

Collisions	Temperature (K)				
	2000	4000	8000	16000	32000
CO_2–C_2H_2	0.8484	0.7235	0.6197	0.5325	0.4591
CO_2–CH	0.7951	0.6766	0.5777	0.4950	0.4261
CO_2–H_2	0.7886	0.6708	0.5725	0.4905	0.4221
CO_2–HCO	0.8947	0.7611	0.6534	0.5628	0.4862
CO_2–N	0.7550	0.5844	0.4505	0.3460	0.2652
CO_2–O	0.7728	0.5988	0.4621	0.3553	0.2725
CO–CO	0.7735	0.6574	0.5605	0.4799	0.4129
CO–C_2H_2	0.8118	0.6915	0.5910	0.5069	0.4365
CO–CH	0.7599	0.6454	0.5499	0.4706	0.4048
CO–H_2	0.7540	0.6399	0.5451	0.4663	0.4011
CO–HCO	0.8538	0.7281	0.6239	0.5363	0.4626
CO–N	0.7219	0.5576	0.4289	0.3291	0.2520
CO–O	0.7394	0.5718	0.4403	0.3380	0.2589
CN–CN	0.7503	0.6380	0.5444	0.4663	0.4014
CN–C_2H	0.8478	0.7230	0.6193	0.5321	0.4588
CN–H	0.6853	0.5279	0.4053	0.3106	0.2377
CN–HCN	0.8462	0.7206	0.6181	0.5319	0.4592
CN–N_2	0.7530	0.6390	0.5443	0.4656	0.4005
CN–NO	0.7751	0.6589	0.5619	0.4812	0.4140
CN–O_2	0.7713	0.6554	0.5587	0.4783	0.4115
C_2H_2–C_2H	0.9034	0.7675	0.6591	0.5680	0.4909

Collisions	Temperature (K)				
	2000	4000	8000	16000	32000
CO_2–C_2H	0.8993	0.7645	0.6564	0.5656	0.4887
CO_2–H	0.7262	0.5610	0.4317	0.3312	0.2537
CO_2–HCN	0.9019	0.7664	0.6581	0.5671	0.4901
CO_2–N_2	0.7969	0.6783	0.5791	0.4963	0.4273
CO_2–NO	0.8200	0.6988	0.5975	0.5127	0.4416
CO_2–O_2	0.8158	0.6950	0.5941	0.5097	0.4390
CO–CN	0.7639	0.6489	0.5531	0.4734	0.4073
CO–C_2H	0.8580	0.7316	0.6270	0.5390	0.4650
CO–H	0.6938	0.5348	0.4108	0.3148	0.2410
CO–HCN	0.8598	0.7331	0.6285	0.5404	0.4663
CO–N_2	0.7620	0.6472	0.5514	0.4720	0.4060
CO–NO	0.7846	0.6673	0.5693	0.4877	0.4197
CO–O_2	0.7805	0.6636	0.5661	0.4848	0.4172
CN–C_2H_2	0.8024	0.6831	0.5835	0.5002	0.4307
CN–CH	0.7474	0.6351	0.5416	0.4637	0.3990
CN–H_2	0.7448	0.6318	0.5379	0.4601	0.3957
CN–HCO	0.8417	0.7176	0.6150	0.5287	0.4561
CN–N	0.7133	0.5505	0.4233	0.3246	0.2486
CN–O	0.7307	0.5646	0.4346	0.3335	0.2554
C_2H_2–C_2H_2	0.8518	0.7264	0.6223	0.5348	0.4612
C_2H_2–CH	0.7982	0.6794	0.5802	0.4972	0.4281

Collisions	Temperature (K)				
	2000	4000	8000	16000	32000
C_2H_2-H	0.7292	0.5634	0.4336	0.3327	0.2548
C_2H_2-HCN	0.9060	0.7695	0.6608	0.5696	0.4923
$C_2H_2-N_2$	0.8001	0.6811	0.5817	0.4986	0.4292
C_2H_2-NO	0.8233	0.7017	0.6001	0.5149	0.4437
$C_2H_2-O_2$	0.8190	0.6979	0.5967	0.5119	0.4410
C_2H-CH	0.8434	0.7192	0.6159	0.5290	0.4561
C_2H-H_2	0.8366	0.7133	0.6106	0.5243	0.4519
C_2H-HCO	0.9470	0.8081	0.6937	0.5993	0.5192
C_2H-N	0.8009	0.6211	0.4802	0.3698	0.2839
C_2H-O	0.8202	0.6359	0.4923	0.3795	0.2915
$CH-CH$	0.7442	0.6321	0.5387	0.4611	0.3967
$CH-H_2$	0.7408	0.6282	0.5347	0.4573	0.3933
$CH-HCO$	0.8377	0.7143	0.6119	0.5258	0.4534
$CH-N$	0.7095	0.5474	0.4209	0.3227	0.2471
$CH-O$	0.7268	0.5615	0.4321	0.3315	0.2539
$H-H$	0.6556	0.5042	0.3866	0.2961	0.2266
$H-HCN$	0.7727	0.5987	0.4620	0.3553	0.2724
$H-N_2$	0.6832	0.5262	0.4040	0.3095	0.2369
$H-NO$	0.7041	0.5431	0.4174	0.3200	0.2450
$H-O_2$	0.7003	0.5400	0.4149	0.3181	0.2435
H_2-HCN	0.8387	0.7151	0.6122	0.5258	0.4532

Collisions	Temperature (K)				
	2000	4000	8000	16000	32000
$C_2H_2-H_2$	0.7918	0.6736	0.5750	0.4927	0.4241
C_2H_2-HCO	0.8987	0.7641	0.6560	0.5652	0.4884
C_2H_2-N	0.7580	0.5868	0.4524	0.3476	0.2664
C_2H_2-O	0.7759	0.6013	0.4641	0.3569	0.2737
C_2H-C_2H	0.9487	0.8120	0.6969	0.6022	0.5218
C_2H-H	0.7708	0.5972	0.4608	0.3543	0.2716
C_2H-HCN	0.9495	0.8142	0.6986	0.6038	0.5232
C_2H-N_2	0.8454	0.7209	0.6174	0.5304	0.4573
C_2H-NO	0.8705	0.7420	0.6364	0.5475	0.4725
C_2H-O_2	0.8658	0.7381	0.6329	0.5443	0.4697
$CH-H$	0.6815	0.5249	0.4029	0.3087	0.2363
$CH-HCN$	0.8422	0.7177	0.6154	0.5293	0.4568
$CH-N_2$	0.7489	0.6353	0.5411	0.4628	0.3981
$CH-NO$	0.7711	0.6553	0.5587	0.4783	0.4115
$CH-O_2$	0.7672	0.6517	0.5555	0.4755	0.4091
$H-H_2$	0.6756	0.5202	0.3992	0.3058	0.2341
$H-HCO$	0.7674	0.5944	0.4585	0.3525	0.2702
$H-N$	0.6832	0.5262	0.4040	0.3095	0.2369
$H-O$	0.7003	0.5400	0.4149	0.3181	0.2435
H_2-H_2	0.7346	0.6227	0.5299	0.4530	0.3896
H_2-HCO	0.8328	0.7100	0.6076	0.5216	0.4496

Collisions	Temperature (K)					Collisions	Temperature (K)				
	2000	4000	8000	16000	32000		2000	4000	8000	16000	32000
H_2–N_2	0.7426	0.6298	0.5361	0.4586	0.3943	H_2–N	0.7035	0.5426	0.4170	0.3197	0.2448
H_2–NO	0.7649	0.6497	0.5537	0.4739	0.4077	H_2–O	0.7207	0.5566	0.4281	0.3284	0.2515
H_2–O_2	0.7608	0.6460	0.5504	0.4711	0.4052	HCN–HCN	0.9727	0.8156	0.6969	0.6027	0.5230
HCN–HCO	0.9558	0.8092	0.6937	0.5996	0.5199	HCN–N_2	0.8475	0.7227	0.6191	0.5319	0.4586
HCN–N	0.8029	0.6227	0.4815	0.3708	0.2847	HCN–NO	0.8727	0.7436	0.6379	0.5489	0.4738
HCN–O	0.8224	0.6375	0.4936	0.3805	0.2924	HCN–O_2	0.8681	0.7400	0.6346	0.5458	0.4078
HCO–HCO	0.9475	0.8036	0.6897	0.5959	0.5163	HCO–N_2	0.8415	0.7176	0.6144	0.5277	0.4550
HCO–N	0.7973	0.6183	0.4779	0.3679	0.2824	HCO–NO	0.8663	0.7385	0.6333	0.5447	0.4701
HCO–O	0.8164	0.6331	0.4899	0.3776	0.2900	HCO–O_2	0.8618	0.7348	0.6299	0.5416	0.4673
N_2–N_2	0.7507	0.6370	0.5425	0.4641	0.3991	N_2–N	0.7112	0.5488	0.4220	0.3236	0.2477
N_2–NO	0.7731	0.6570	0.5602	0.4796	0.4127	N_2–O	0.7285	0.5629	0.4332	0.3324	0.2546
N_2–O_2	0.7690	0.6534	0.5569	0.4768	0.4102	N–N	0.7112	0.5488	0.4220	0.3236	0.2477
N–NO	0.7324	0.5661	0.4357	0.3344	0.2561	N–O	0.7285	0.5629	0.4332	0.3324	0.2546
N–O_2	0.7285	0.5629	0.4332	0.3324	0.2546	NO–NO	0.7958	0.6773	0.5783	0.4956	0.4266
NO–O	0.7500	0.5803	0.4472	0.3435	0.2632	NO–O_2	0.7917	0.6736	0.5750	0.4926	0.4240
O–O	0.7461	0.5771	0.4446	0.3414	0.2616	O–O_2	0.7461	0.5771	0.4446	0.3414	0.2616
O_2–O_2	0.7875	0.6699	0.5716	0.4897	0.4215						

Nikhil Banerji

Education

Ecole Polytechnique Fédérale de Lausanne (EPFL) 2017
PhD, Mechanical Engineering

University of Bath, United Kingdom 2012
MEng (Hons.), Aerospace Engineering with French

Core Experiences

Interdisciplinary Aerodynamics Group, EPFL 2013 – 2017
PhD Researcher. *Effects of Radiation on Ablative Heat Shields During Atmospheric Entry*. Using experimental and numerical methods, successfully characterised heat transfer in lightweight materials in extreme environments. Validated results against flight data from NASA's 2012 Mars Science Laboratory mission.

Interdisciplinary Aerodynamics Group, EPFL 2013 - 2016
Research Engineer, European Space Agency (ESA) Ablation-Radiation Coupling Project. Coupled Computational Fluid Dynamics simulations to thermodynamic analyses. Co-authored technical reports and presented progress and results to ESA and collaborating institutes.

Centre for Hypersonics, The University of Queensland, Australia 2015
Researcher. Designed and manufactured lightweight models for high temperature testing in wind tunnels. Integrated novel electrical pre-heating system into models. Interfaced with suppliers and workshop. Measured shock layer radiation via emission spectroscopy.

Institut Supérieur de l'Aéronautique et de l'Espace, France 2012
Master Thesis. Analysed the propagation of delamination due to vibrational stresses in an aircraft panel using finite element methods via **SAMCEF**. Validated results against experimental data.

ITER Organization, France 2010 - 2011
R&D position in Diagnostics Division. Structural and risk analyses for X-ray and vacuum ultraviolet spectroscopy systems. Finite element design studies on diagnostic window assemblies and mounting systems using **ANSYS**.

Additional Experience

Institute of Mechanical Engineering, EPFL 2013 – 2016
Teaching assistant. Lectured and corrected exams for Master level course, "*Introduction to Planetary Sciences*". Co-supervision of 5 master theses and 10 semester projects. Developed innovative project topics, aiding the student with code development and implementation, resulting in several publications.

Logitech, S.A., Switzerland 2010
Project Management Intern. Helped manage *Leadership Development Project*, researching change and supply chain management strategies.

Airbus Aircraft Design Project, University of Bath 2009
Technical Integrator. Interfaced with departments such as electronics, structure and aerodynamics and developed final aircraft design to JAF and ICAO standards. Led engineering team to deliver the final design on time and under budget.

Languages

English, Hindi, Bengali (mother tongue); *French* – Speaking and Understanding (C2), Writing (C1); *Spanish* – Speaking and Understanding (B2), Writing (A2).

Technical skills

Engineering: Heat Transfer, Experimental Testing, Finite Element Analysis, Computational Fluid Dynamics, CAD, Mechanical Design, Project Documentation.

Interdisciplinary: Effective communicator, excellent analytical and problem solving skills, adept at working in a team, good presenter, excellent time management, used to pressure, independent, highly adaptive, resourceful and creative.

IT Skills: Linux (Ubuntu, Fedora), Mac OS X, Microsoft Office, MATLAB, Python, FORTRAN, LaTeX, bash and Git.

Extracurricular activities

Playing electric guitar and composing music – Bands in Switzerland (2005 – 2007) and the UK (2008-2012), having released 2 albums and played over 10 live concerts. Playing football in local amateur teams and leagues (since 1998). Snowboarding, hiking, cycling and squash.

Personal Information

Born: 27. October 1988; *Nationality*: Swiss; Swiss Driving License (Cat. B).